

MEASUREMENT TECHNIQUES FOR IR SPECTROSCOPIC
BLOOD GLUCOSE DETERMINATION

Ralf Marbach
VDI Verlag GmbH
Heinrichstr. 24
Postfach 8228
40239 Duesseldorf
Tel. 011-49-211-6188-0

Published as a so-called Fortschritt Bericht
Series 8: Measurement and Control Technology, Nr. 346

Duesseldorf, 1994

translated by Mark S. Benak
Rio Grande Medical Technologies, Inc.
copyright ©1993, U.S.A.

March 28, 1994

Contents	
1 Introduction	4
2 Medical Aspects and State of the Technology	6
3 Infrared Spectroscopy	10
3.1 Measurement Principle	10
3.2 Basic Physical Concepts	13
3.3 Fourier Transform Spectroscopy	18
3.3.1 Basic Concepts	18
3.3.2 The Bruker IFS-66 Spectrometer	22
3.3.3 Systematic Errors	24
3.3.4 Noise	28
3.3.5 Selection of the Measurement Parameters	35
4 Multivariate Signal Processing	37
4.1 Model Generation	37
4.2 The Parameter Estimation	44
4.2.1 The PCR Estimator	45
4.2.2 The PLS Estimator	48
4.3 Practical Model Generation and Examples	54
5 Procedures for Liquid Blood	65
5.1 Problems of Biotic Liquid Samples	65
5.2 Data Set for the Liquid Blood Analysis	68
5.3 ATR Measurements in the Mid IR	74
5.3.1 Experimental Details	74
5.3.2 Results	79
5.4 Transmission Measurement in the Near IR	88
5.4.1 Experimental Details	88
5.4.2 Results	91

6 Noninvasive Measurement Procedure	98
6.1 The Skin	98
6.2 Monte Carlo Simulation of the Optical Characteristics of Skin in the Near IR	101
6.3 Development of the Measurement Accessory	109
6.4 Diffuse Reflection Measurement of the Lip	119
6.4.1 Single Person Experiment with Oral Glucose Tolerance Test	120
6.4.2 Experiment with Larger Patient Population	126
6.4.3 Single Person Experiment with Random Blood Glucose Levels	130
7 Summary and Outlook	134
Appendices	137
A Effective Optical Throughput	137
B Definitions for Random Vectors	139
C Certainty of the Clinical-Chemical Reference Method	140
D Results of the Spectroscopic Analysis of Further Substrates in Blood Plasma	141
9 Bibliography	144

Index of Important Abbreviations and Symbols

Large bold letters represent matrices (e.g. \mathbf{A}), vectors are printed small and bold (e.g. \mathbf{b}); estimated values have a diacritical mark above them (e.g. $\hat{\mathbf{b}}$).

In this work, no differences are made between the stochastic values and their realizations through the notation; stochastic variables are either with a diacritical sign above them ($\hat{\mathbf{b}}$) or are named explicitly (e.g. the error vector \mathbf{e}).

$E[\mathbf{e}]$ expected value of a stochastic variable
 $E[\mathbf{e}_1|\mathbf{e}_2]$ conditional expected value of \mathbf{e}_1 given \mathbf{e}_2

$\text{COV}[\mathbf{e}_1, \mathbf{e}_2] = E[(\mathbf{e}_1 - E[\mathbf{e}_1])(\mathbf{e}_2 - E[\mathbf{e}_2])^T]$
 $\text{COV}[\mathbf{e}] = \text{COV}[\mathbf{e}, \mathbf{e}]$

$\text{rg}(\mathbf{A})$ rank of the matrix \mathbf{A}
 $\det(\mathbf{A})$ determinant of the symmetric matrix \mathbf{A}
 $\text{spur}(\mathbf{A})$ sum of the diagonal elements of the symmetric metric matrix \mathbf{A} (sum of the eigenvalues)

$\|\mathbf{v}\|$ euclidian normal of the vector \mathbf{v}
 $\text{diag}(\mathbf{v})$ diagonal matrix with the elements of the vector \mathbf{v}

$x \sim y$ y proportional to x
 $x * y$ x convoluted with y
 $x \doteq y$ equal by definition
 i imaginary unit ($i^2 = -1$)

$\Pi_T \doteq \begin{cases} \frac{1}{T} & -\frac{T}{2} \leq x \leq \frac{T}{2} \\ 0 & \text{otherwise} \end{cases}$

$\text{si}(x) \doteq \frac{\sin(x)}{x}$

1 Introduction

The concentration of glucose in capillary blood ("blood sugar") is an important parameter in medical diagnostics. Inside the complicated biological system, which keeps the energy production in the human in line, glucose takes on a central role; it can be called the *fuel of life*. In healthy humans, the blood glucose concentration is nearly constant at a value approximately 1 wt. %. In patients with diabetes mellitus, the control mechanisms for blood sugar are disturbed. As a result, metabolic problems occur which can lead to death in a matter of months without therapeutic measures. For the diabetes therapy, the concentration of the blood glucose must be determined at regular intervals. The goal is the complete normalization of the blood sugar such that atherosclerotic problems, possibly resulting from increased average blood glucose values over long periods of time from years to decades, can be avoided.

More than 10 percent of all examinations in a hospital laboratory deal with glucose in capillary blood which means that this is the most often determined component of the blood [1]. A larger number of measurements are conducted by the patients on themselves. In this case, a drop of capillary blood is placed on a test strip where a chemical reaction with the glucose can be processed visually through changing color or with the help of a small, commercially available, pocket-size device for self-monitoring of the blood sugar (see Ch. 2). How often the measurement is made depends on the severity of the disease and on the willingness of the patient to use the equipment; a max. of 8 measurements per day are conducted.

Optical spectroscopy in the infrared (IR) spectral region allows improvements in the current state of technology for blood glucose measurements in two ways. These define both of the goals of this work:

1) The Reagentless Determination of Glucose in Biotic Liquid Samples Using IR Spectroscopy

The goal of the development is novel automated analysis processes for the clinical-chemical laboratory which can replace the current devices that use large amounts of chemicals; the advantage of a physical, i.e. reagentless, measurement technique lies in the savings of operating costs.

According to earlier results [2,3], the possibilities of optical spectroscopy in the mid IR spectral region for the quantitative analysis of biotic liquid samples, such as blood, plasma, serum, etc., are being further developed. Based on the economic aspect of the development goal, a simultaneous determination of glucose and a few further blood parameters often medically required is desired. In order to achieve determination errors in the region of clinical acceptance, the measurement conditions as well as the algorithm for the multivariate signal processing were optimized.

Furthermore, the information content of the spectra in the near infrared region (NIR) were examined which to date have not been used successfully for the analysis of glucose. Here, optimized techniques for quantitative signal processing are also used. The successful glucose calibration of the NIR spectra of liquid samples is a requirement for the development of a non-invasive measurement technique.

2) The Non-invasive Determination of Glucose in the Near Infrared Spectral Region

The goal is the development of small, inexpensive, and robust pocket-size photometers for the noninvasive measurement of blood glucose through the skin. These should replace the current methods of blood glucose self-monitoring in which blood is drawn, whereby the willingness to make measurements more often with many patients, especially with children, can be significantly increased. Through regular use, even a quasi-closed control loop for glucose with feedback through the patients themselves is realizable. The intervals between two measurements that are necessary for this lie in the region of a few hours to minimally about 30 minutes after eating. The economic advantages are the avoidance of costs for test strips, which at this time lie at approximately 1.50 DM (ca. \$0.90 US) per measurement as well as the long term reduction of the handling costs of potentially resulting damage by diabetes later.

The examination of the possibilities for a noninvasive NIR spectroscopic determination of blood glucose represent the main point of this work. According to the results of quantitative analyses in liquid blood samples and from theoretical estimates of the optical characteristics of biological tissue, the realization possibilities for a noninvasive measurement using Monte Carlo simulations were estimated. For the selected measurement technique, transcutaneous diffuse reflection in the long-wave NIR spectral region, an optimized optical apparatus was developed. The technique was tested with single person experiments as well as with a larger patient collective, whereby the diffuse reflection spectra of the inner lip were used for the calibration.

2 Medical Aspects and State of the Technology

In the framework of a balanced diet, approximately 50% of the human calorie requirement is provided through carbohydrates. These are divided into compound sugars (e.g. plant and animal starches), double sugars (e.g. sucrose, maltose, milk sugar) as well as single sugars (e.g. grape sugar and fructose). Higher valued carbohydrates are broken down through enzymes in the digestive channel of the body into grape sugar, the so-called D(+)-glucose. This then passes through the intestinal wall into the blood stream such that every body cell can be provided with glucose for energy consumption. The main consumer of glucose is the muscle tissue. Above the actual energy requirement of the body, approximately 75 g of glucose can be stored in the liver and can be given to the blood stream between meals as necessary. Stationary values of the blood glucose concentration lie in the region around 80-120 mg/dl for healthy people. After the breakdown of the carbohydrates, this value is temporarily increased, however, the blood sugar level should sink approximately two hours after eating to its stationary rest value [4]. The blood sugar reduction is initiated by the hormone insulin which is produced by the so-called β -cells of the pancreas depending on the actual blood glucose concentration. This closed control loop for holding the glucose concentration constant in the blood reacts very quickly to a blood sugar increase with an insulin secretion that was measured to occur within one minute [5]. Insulin fulfills many tasks in the framework of the human metabolism, the most important of which includes allowing the glucose to pass through the cell walls from the blood.

In the Federal Republic of Germany, ca. 4-5% of the population suffers from diabetes mellitus (from Greek: dia = through, bain = to go and Latin: litos = honey sweet) [4]. The sugar disease arises through a lack of insulin which leads to an increase in the blood sugar concentration. At blood sugar values of ca. 160-180 mg/dl, the kidney level for glucose is surpassed such that the glucose is removed in the urine and is no longer available for energy consumption. In cases of absolute lack of insulin, the body's own fat and protein must be burned for energy consumption; as a result of the products which arise during the breakdown of fat (e.g. acetone), an acidosis of the organism can result, i.e. a diabetic coma. Approximately 0.3-0.7% of the population suffers from the so-called Type I diabetes which is associated with a complete shutdown of the body's own insulin production [5]. The majority of the patients suffer from Type II diabetes ("age sugar") with which an insulin production exists, however, the blood sugar reducing action of the insulin is limited through a so-called insulin resistance. The most important factor for the initiation of Type II diabetes is obesity. Therefore, diabetes can also be termed a disease of the civilization whose diagnosis and treatment is meanwhile a large portion of the necessary work conducted in clinical and chemical laboratories.

The usual processes for glucose analysis use biochemical methods with glucose oxidation, glucose hexokination, or glucose dehydrogenation [6]. Through the enzymatic reaction with glucose, colored reaction products are generated which can be photometrically measured and processed in special automatic analysis devices. The disadvantages of the biochemical techniques are the necessity to draw blood and the consumption of expensive chemicals.

The goal of the medical treatment of diabetes is to normalize the blood sugar level as much as possible. Therefore, patients are advised to avoid the consumption of quickly resorbing single and double sugars in order to avoid peaks in the blood sugar concentration. For Type I diabetics,

the therapy always consists of insulin injections; the administering of insulin in tablet form is not possible, since insulin is a protein which would be destroyed in the digestive track. A Type II diabetes is treated according to the severity of the disease either alone with diet, with tablets in order to increase the insulin production, or with insulin injections. A diabetes which is not treated over a longer period of time can result in the diabetic consequences mentioned above [4,7]. These consist of blockage, especially of the smaller blood passageways, through increased sugar conglomeration in the passage wall. The consequences are damages especially to the retina, the kidneys, the nerves, and the lower extremities. High blood sugar values can lead to arterial sclerosis independent of other risk factors such as high blood pressure, obesity, metabolic disturbances, and nicotine consumption.

The adjustment of the blood sugar is especially difficult for the insulin dependent diabetic, since the closed control loop in healthy humans for holding the blood glucose concentration constant reacts very sensitively to its complete opening through the absence of insulin. For example, the consumption of a relatively small amount of carbohydrate in a roll (ca. 25 g) causes an increase in blood sugar of ca. 100 mg/dl in a Type I diabetic. The amount of carbohydrates in the food must be exactly known in order to determine the amount of insulin that must be injected such that after eating, a normal blood sugar resting value can be reached again. An overdose of the applied insulin amount causes a reduction of the sugar level to below the normal region; symptoms of hypoglycemia (blood sugar < 50 mg/dl) are feelings of weakness and a ravenous appetite, and with the secretion of blood sugar increasing hormones, the body decreases the risk of losing consciousness. As a result of the body's own counter reaction which also functions in a diabetic, an unpermissibly high blood sugar value results again. An additional difficulty arises during the determination of the necessary amount of the injection such that the insulin requirement of a person changes, e.g. shortly before physical strains or through the appearance of a cold with fever and long term through a change in weight.

In the year 1984, the introduction of devices for the self-monitoring of blood sugar led to an essential advance in the controlled dosing of insulin. These are handy, pocket-sized photometers used by the patient which measure the enzymatic color reaction of a test strip upon which a drop of capillary blood must be placed. The upper limits are approximately $\pm 15\%$ variation from the actual value. Since lower blood sugar values must be better known than high values for the initiation of medically correct reactions, a relative error tolerance is prescribed [8]. The measurement time of the photometric system is typically 1-2 min. Alternately, devices have been recently offered which function electrochemically with enzyme electrodes (test strips as the source of current). The advantages are the smaller size of the device (format of a check card or a ball point pen) as well as the measurement time of typically 20 s. Through repeated self-monitoring, it is possible for the patient to determine the required amount of insulin more flexibly and to sink the average blood sugar value further into the normal region without significantly increasing the risk of hypoglycemia. The disadvantage of the current methods for self-monitoring of blood sugar lies in the necessity to draw blood which is generally associated with the puncture of the fingertip. Due to the high dynamics of the blood glucose concentration with time constants of approximately 30 min (see [9] and the references cited there), the realization of a quasi-closed control loop is not possible, since the short time intervals required between measurements are not practically achievable.

An improvement in the current state of diabetes therapy is strived for from the medical side through a transplantation of foreign β -cells. Technically speaking, large amounts of effort have flown into the development of an artificial closed loop pancreas system which consists of an implantable component glucose sensor and an insulin depot/pump. A principle problem for both devices is the body's own immune reaction against implanted foreign objects. While appropriate insulin pumps have already been realized, the implantable enzymatic glucose sensors cannot hold their functionality over a longer period of time [10-12]. Therefore, the realization of needle shaped glucose sensors has been recently initiated which can be inserted by the patient him- or herself at equidistant locations underneath the skin; a functional period of approximately 5-7 days is seen as marketable and can already be achieved with the existing sensors [5]. The glucose concentration of the subcutaneous tissue fluid in the stationary state is identical to that in the blood plasma and for dynamic changes, a time delay of only ca. 5 min arises [13,14]. The principle difficulty in the realization of these "half-invasive" sensors arises is that the glucose sensors after implantation require a stabilizing phase of approximately 3-4 h and afterwards must be newly calibrated for blood glucose. The output signals of these sensors lie on the order of 1.5 to 15 nA per 100 mg/dl glucose [5]. The disadvantages of this measurement technique are the lack of reliability through the often occurring changes in the measurement condition and the arising medical dangers, e.g. through infection.

The *non-invasive glucose measurement* offers an essential improvement in diabetes therapy, i.e. the unbloody measurement through the skin. Here, spectroscopic methods, which use the reaction of electromagnetic beams with material, contain the potential possibilities. In connection with an implanted insulin pump, a quasi-closed control loop with feedback through the patient can be realized with such a method. Up to now, a non-invasive measurement could only be conducted with nuclear magnetic resonance spectroscopy which is, however, not appropriate for use in the self-monitoring of blood sugar due to the extremely large size of the apparatus. The most promising method with chance for a practical realization is optical spectroscopy in the infrared region which can deliver substance specific information with relatively small technical effort.

The requirement for the non-invasive measurement is a successful application of IR spectroscopy to the analysis of liquid blood samples (see [15-19]). The development of spectroscopic automated analysis devices for the clinical-chemical laboratory will receive great economic meaning, since these present a large cost advantage in comparison to the current biochemical methods with the use of chemicals. Since the IR spectrum of the blood is the sum of the superimposed spectra of the individual substances in the blood, quantitative processing of the information is problematic due to the complexity of the blood contents, the variability of the different contents as well as the small concentration of glucose. The determination of the blood glucose concentration requires quantification of a very small signal with a large changing background spectrum and could be demonstrated for a larger patient population for the first time in the framework of our study. The average errors in determination lay at 20 mg/dl in blood [2] and 22 mg/dl in plasma [3], significantly above the certainties that can be achieved with the current clinical-chemical methods ([20], see also Ch. 5.2).

The cited studies with IR-spectroscopy use the molecule specific absorption in the so-called mid IR spectral region (wave length ca. 2.5-25 μm), whereby the maxima of the glucose signals lie in the region around 9.6 μm . A basic problem for non-invasive measurement using IR spectroscopy

is the high absorption of the beam by water in the tissue. The spectral region of the mid IR is, therefore, not appropriate for a non-invasive measurement, since only an insufficient penetration depth of the beam into the skin can be achieved [21]. As a result, the use of radiation in the near IR spectral region (NIR: 0.8–2.5 μm) for a non-invasive measurement of blood glucose has been discussed [22,23]. When approaching the visible spectral region, the absorption of water decreases such that NIR spectroscopy has been routinely used for quite some time, e.g. for the non-invasive measurement of the oxygen saturation level of the blood [24]. Recently, even the determination of the cerebral oxygen saturation using transmission spectroscopy through the heads of newly born infants was reported, whereby only approximately a 10^{-10} portion of the radiated power can be detected [25]. Because of the essentially small size and specificity of the absorption signals in the near IR, the quantitative determination of glucose for the NIR spectra of liquid blood samples is already very difficult and could be first shown in the framework of this work [26]. An advantage of NIR spectroscopy is the more simple, more inexpensive, and more robust hardware in comparison to the mid IR.

A series of suggestions for the noninvasive NIR spectroscopic measurement of blood glucose have been published as patents [27–29] or have been introduced at conferences [30,31]. A conclusive critique of these diverse methods is not possible at the present time, since no scientific publications on this subject exist.

3 Infrared Spectroscopy

3.1 Measurement Principle

Infrared spectroscopy is one of the most important investigation methods in analytical chemistry and is at the same level of importance as nuclear resonance, mass, and ultraviolet spectroscopy. Its major significance is attributed to the large information content of the IR spectra, to the many possibilities for sample preparation, as well as to the relatively small effort for a measurement [32]. The basic physical concept is the absorption of electromagnetic radiation with wavelengths in the region of approximately 0.8 to 500 μm with which the atoms in a molecule can be excited into oscillation. As a result, substance specific signals can be measured with IR spectroscopy that are characteristic for the type and the geometric placement of the atoms in a molecule. The qualitative analysis of samples is a major area of application where the main goal lies in the constitution explanation of organic molecules. The appropriateness of substance identification is given through the high number of absorption bands and the good reproducibility of the measurement. Moreover, there exists a large number of comparison spectra which have been collected into various data banks and, through the development of electronic data processing, are available today on-line in many laboratories [33]. In Fig. 3.1, the principle construction for the measurement of an IR absorption spectrum is sketched.

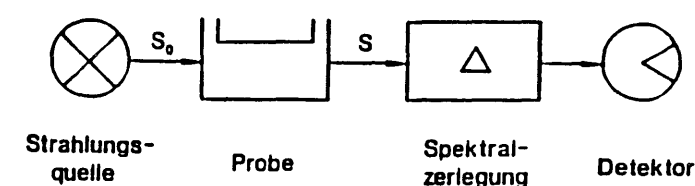


Fig. 3.1: Block Diagram of an IR Spectrometer.

The radiation power density S_R emitted from an IR source passes through the sample to be examined. Broad-banded temperature radiators are used as radiation sources whose frequency dependent output spectrum $S_R(\tilde{\nu})$ approaches that of a black body radiator. As the IR radiation passes through the sample, it is damped according to the substance; the exiting radiation $S(\tilde{\nu})$ is separated spectrally and measured by a power detector. In modern IR spectrometers, mainly Michelson interferometers are normally used as the spectral devices (Ch. 3.3) which have replaced the earlier monochromators frequently used with prisms and gratings.

Essential for absorption spectroscopy is that the substance specific information is contained in the radiation damping. In order to become independent of the frequency dependent characteristics of the applied radiation source, of the optical components in the spectrometer, etc., a reference measurement is, therefore, necessary with which the transfer function of the "empty" spectrometer $S_R(\tilde{\nu})$ is determined after the sample has been removed from the measurement path. The transmission $T(\tilde{\nu})$ can be calculated from the so-called single beam spectra $S(\tilde{\nu})$ and $S_R(\tilde{\nu})$ with the help of the Lambert-Bouguer Law, which is valid for homogeneous samples, as follows:

$$T(\tilde{\nu}) \doteq \frac{S(\tilde{\nu})}{S_R(\tilde{\nu})} = e^{-\alpha(\tilde{\nu})d} \quad (3.1)$$

Here, $\alpha(\tilde{\nu})$ is the sample specific absorption coefficient [mm^{-1}] and d is the sample thickness subject to the IR radiation. Analogous to the usual unit for power damping in electrical engineering, the decibel, the extinction $A(\tilde{\nu})$ (absorbance) is defined with the negative decade logarithm. However, it is common to use the "unit" AU (absorbance unit) for extinction where 1 AU is equal to 10 dB.¹

$$A(\tilde{\nu}) \doteq -\log_{10} T(\tilde{\nu}) = \frac{\alpha(\tilde{\nu})d}{2.303} \quad (3.2)$$

In Fig. 3.2, the extinction spectrum of crystalline glucose is shown as an example that was measured with the KBr-pellet technology in the mid IR spectral region [32:p. 116ff]. The extinction A [AU] is displayed versus the frequency f [THz] ($1 \text{ THz} = 10^{12} \text{ Hz}$). Due to the uncomfortably large numbers, the so-called *wavenumber* $\tilde{\nu}$ [cm^{-1}] is used instead of the frequency f which is defined with the help of the speed of light in a vacuum $c_0 = 2.9979 \times 10^{10} \text{ cm/s}$.

$$\tilde{\nu} \doteq \frac{f}{c_0} \quad [\text{cm}^{-1}] \quad (3.3)$$

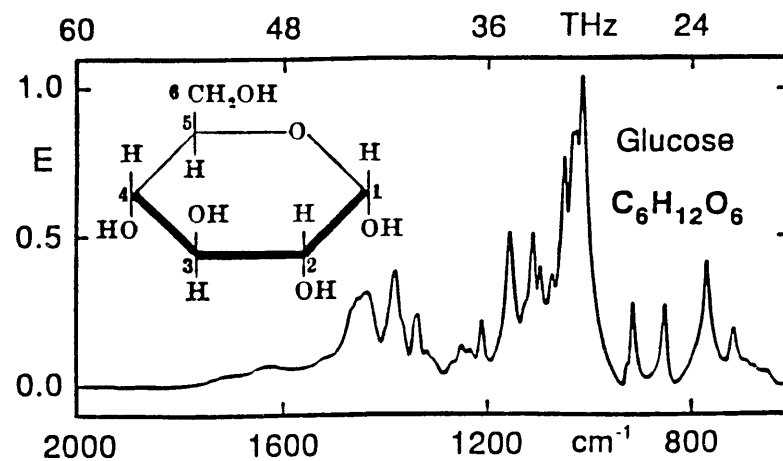


Fig. 3.2: Extinction spectrum of dehydrated, crystalline glucose.

¹Normally, the absorption coefficient α is given as the decade logarithm.

The wavenumber is the number of waves which fit on a centimeter in the vacuum. Although $\tilde{\nu}$ does not have the dimensions of inverse time, the concepts of "wave number" and "frequency" are often used synonymously. The location, form, and intensity of the absorption bands in Fig. 3.2 are characteristic for the glucose molecule displayed. The largest absorption signals of glucose are found in the region $1200\text{--}950 \text{ cm}^{-1}$ (8.3 to $10.5 \mu\text{m}$) in the mid IR. The spectrum of glucose in liquid solution, e.g. in blood, displays essentially broader absorption bands as compared to that in crystalline form and shows an overall smoother form with less structure (cf. Fig. 4.2).

The empirically determined Beer's Law is the basic concept for quantitative spectroscopic investigations. According to it, the radiation damping is proportional to the substance specific extinction coefficients $\epsilon_i(\tilde{\nu})$ [m^2/mol] and to the number of particles in the radiated volume, i.e., the concentration c [mol/m^3]. If the sample contains a mixture of k different substances, Beer's law is:

$$\alpha(\tilde{\nu}) = \epsilon_1(\tilde{\nu})c_1 + \epsilon_2(\tilde{\nu})c_2 + \dots + \epsilon_k(\tilde{\nu})c_k \quad (3.4)$$

According to Eq. 3.4 and Eq. 3.2, the extinction $A(\tilde{\nu})$ is a linear function of the substance concentration in the examined sample. However, Beer's law is not always valid. Deviations of basic nature can occur through the chemical affects of the sample substances themselves, i.e. the individual extinction coefficients $\epsilon_i(\tilde{\nu})$ in Eq. 3.4 are dependent on the concentration c_i ($i = 1, 2, \dots, k$). These so-called "matrix effects" occur frequently in highly concentrated solutions in which the densely packed sample molecules affect each other adversely. In addition, deviations from Beer's law occur through radiation losses resulting from various physical effects of the sample. A term $A_F(\tilde{\nu})$, e.g. through Fresnel losses on the cuvette windows, occurs which is weakly dependent on the concentrations c_i and the frequency $\tilde{\nu}$. Further distorting affects are the diffusely scattered light and the insufficient homogenization of the sample (for further details, see e.g. [34:p. 524ff,35]). Finally, the linearity of Beer's law is also disturbed through the non-ideal behavior of the spectrometer, e.g. through nonlinear detectors (Ch. 3.3.3) and through a spectral resolution of the measurement that is too small. The convolution of the single beam spectra with the finite resolution function of the spectral apparatus $h(\tilde{\nu})$ (cf. Eq. 3.13) also causes a nonlinear dependence of the measured extinction $A_{\text{app}}(\tilde{\nu})$ on the true value due to the logarithmic expression for the extinction:

$$A_{\text{app}}(\tilde{\nu}) = -\log_{10} \frac{S(\tilde{\nu}) \star h(\tilde{\nu})}{S_R(\tilde{\nu}) \star h(\tilde{\nu})} \quad (3.5)$$

Due to the broad absorption bands of the blood spectra, the spectral resolution of the measurements conducted was chosen to be 4 cm^{-1} in the mid IR and 32 cm^{-1} in the near IR so that this effect is negligible [36].

In this work, no absolute measurements of the extinction coefficients of the blood components were attempted, rather, the unknown concentrations c_i were determined quantitatively using the IR spectra of the given blood samples. Here, high reproducibility of the measurement and a good signal-to-noise ratio (S/N) are necessary. Due to the small concentration of glucose and other substrates examined in blood, only relatively small changes in the IR spectra (inverse measurement problem) are shown regardless of the large individual oscillations of these medical parameters. Eq. 3.4 can be interpreted as a Taylor series truncated after the first term which describes changes in $\alpha(\tilde{\nu})$ according to changes in the substrate concentrations c_i around the operating point of

“average blood.” The linear relationship between the extinction $A(\bar{\nu})$ and the concentrations c_i , which is important for the quantitative analysis, can be assumed to be a good approximation.

3.2 Basic Physical Concepts

An electromagnetic wave is damped through various physical effects as it passes through a medium, whereby a difference is made between outer unquantized and inner quantized effects. The latter explains the inner structure of the material and, therefore, must be described with the help of quantum theory. An overview is given in Fig. 3.3. S_F describes the part of the radiation power lost on the various bordering areas through the outer effect of the Fresnel reflection. The cause is the unmatched wave resistances of the sequentially occurring materials which mainly arise through differences in the refraction indices. If the wave resistance inside the sample is also statistically varying through inhomogeneities, a portion S_D is scattered, i.e. deflected in new, random directions. The size and direction characteristics of S_D are dependent on the spatial distribution of the scattering particles in the samples and on the relationship of the particle diameter d to the wave length λ ; S_D is largest if both characteristics lie approximately on the same order of magnitude. In physics, various outer scattering effects are differentiated depending on the size relationship, e.g. Mie scattering ($d \approx \lambda$) or Rayleigh scattering of molecules ($d \gg \lambda$). A very weak inner scattering effect is the Raman scattering with which information about the inner structure of the scattering particles is gained from the wave length modulation of a part of the scattering radiation.

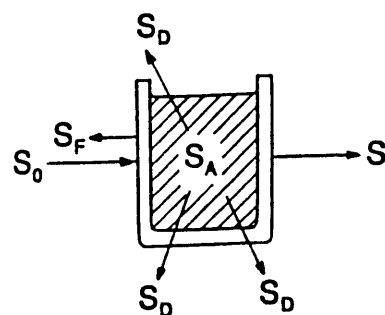


Fig. 3.3: Damping losses during throughput of an electromagnetic wave through a sample; see text for details.

The most important inner effect is the radiation absorption S_A by the molecules of the sample. The molecules absorb energy from the electromagnetic wave and are transported from one energy state E_A into another excited energy state E_B where they give off another type of energy, most

often heat, and fall back again into the ground state E_A . Since these processes take place in atomic and molecular dimensions, only such energy portions $\Delta E = E_B - E_A$ can be absorbed according to the laws of quantum physics corresponding to the transfer allowed between two discrete energy levels of the molecules. With the relationship

$$\Delta E = hf \quad (3.6)$$

in which small h is the Planck constant [$J s$] and f is the oscillation frequency [s^{-1}], the discrete frequencies $f_i = E_i/h$ are determined at which the molecular absorption bands can arise. One can imagine that a molecule is a spatial arrangement of mass points (atoms) which are connected with springs (chemical bonds). The atoms can divert oscillations around their equilibrium state whose eigenfrequencies are determined through the distribution of mass and the bonding forces corresponding to the discrete absorption frequencies f_i . The examination of the location and the intensity of molecule specific absorption bands is the task of IR spectroscopy.

The energy transfer through absorption of electromagnetic radiation functions for molecules in the IR spectral region, such as in the region of technical frequencies and the signal transmission to antennas, through excitation of dipole oscillations, i.e. through periodic changes in the direction and/or size of the dipole moment vector. The size of the absorption is dependent on the absolute value of the dipole moment change and on the direction of the dipole relative to the applied field. The previously mentioned effect does not normally occur in IR spectroscopy, since the orientation of the dipole point for isotropic sample materials is stochastically distributed throughout all spatial directions such that no directional dependence exists. For the simple case of a two atom molecule with a permanent dipole moment, the different possible forms of the dipole oscillation of the molecule are schematically shown in Fig. 3.4 [37:p. 11]

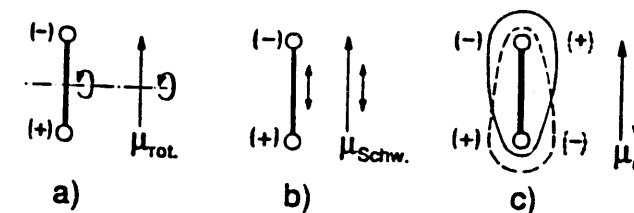


Fig. 3.4: Change of the molecular dipole moment vector μ through (a) molecule rotation, (b) molecular framework oscillation, and (c) electron excitation.

Dipole oscillations of a molecule are possible through rotation of the entire molecule, through oscillations of the atoms against each other in the molecular structure, and through oscillation

(deformation) of the electron shell. The resonant frequencies of the three forms of oscillation are found in different optical spectral regions. With energy-rich radiation in the visible and ultraviolet frequency region, the excitation of valence electrons is, for example, possible, while substance specific structure oscillations are excited with infrared radiation. These relationships are summarized in Table 3.1 [37:p.14]:

Table 3.1: Division of the Optical Spectral Region

Interaction	Electron Spectra			Rotation-Oscillation Spectra		Rotation Spectra	
	σ -electr.	π, n -elekr.		Upper Osc.	Molecular Osc.	Molecular Rotation	
Spectral Region	Vacuum-UV	UV	VIS	near IR	mid IR	far IR	Microwaves
λ [μm]	0.01	0.2	0.4	0.8	2.5	25	500
$\tilde{\nu}$ [cm^{-1}]				12500	4000	400	20
f [THz]				3750	1200	120	6

The division of the spectral region is oriented not only to the molecular change of state but also to the technical boundary conditions, i.e. to the available spectrometers and accessories. The Fourier transform spectrometer (Ch. 3.3) used in this work could be used for measurements in the near and mid IR. For an application in the far IR, where limitations regarding the applicable optical materials arise, it was not properly equipped.

As shown in Fig. 3.2, the spectrum of glucose in the mid IR does not consist of discrete absorption lines, rather, it displays a smooth, continuous shape. In solid and liquid samples, the discrete energy levels are smeared by changes between the molecules at broad energy bands, i.e., the lines become absorption bands. Only for gaseous samples can the pure rotation or the rotation oscillation spectra of single molecules be measured, where the natural line width of the gas spectra are determined through the thermal movement of the molecules (Doppler effect) and through the probability of collisions (pressure propagation).

The high information content of the spectra in the mid IR is explained by the large number of possible molecule oscillations. To clearly determine the spatial structure of a molecule with N atoms, $3N$ independent coordinates are required, i.e., a molecule has 3 degrees of freedom of movement. Here, three of the degrees of freedom correspond to translation in the three spatial directions. The number of degrees of freedom for the molecule rotation is dependent on the geometric structure of the molecule. Normally, there are three degrees of freedom of rotation about the three main inertial axes; there are two for linearly structured molecules. As a result, there remains $3N-6$ (linear molecules: $3N-5$) degrees of freedom for the *normal oscillations*² of the atoms against each other in the molecular structure. One separates these into the $N-1$ *valence oscillations*, for which primarily the separations of the atoms connected to each other change, and the typically lower frequency $2N-5$ (linear molecules: $2N-4$) *deformation oscillations*, for which primarily the bonding angles between the atoms change. Whether the normal oscillation also causes a dipole moment

²The definition of a normal oscillation is: (1) All atoms of the molecule oscillate toward each other with the same frequency and fixed phase; and (2) Normal oscillations can be excited independent of each other, i.e. they transfer no energy. The oscillations occur with a relatively small amplitude of about 10% of the atomic separations [38:0.15].

change of the molecule and, hence, can be excited through the absorption of electromagnetic radiation is dependent on the spatial symmetry of the molecule; typically, the majority of normal oscillations are "IR active" [39]. Above 1500 cm^{-1} , the valence oscillations of hydrogen as well as the atom groups with compound bonds absorb for which the characteristic frequency bands for individual so-called functional groups can be given (e.g. [40:p. 49ff]). Below ca. 1500 cm^{-1} , practically all deformation oscillations of the molecule structure can be found in addition to the valence oscillations of the heavy atoms. The absorption signals in this *fingerprint region* are, therefore, very characteristic for a molecule (cf. Fig. 3.2).

The NIR spectral region ($0.8-2.5 \mu\text{m}$) takes on a known special place for which the H-F valence oscillation of its lower frequency limit lies at $2.526 \mu\text{m}$ (3959 cm^{-1}). This is the normal oscillation with the highest frequency due to the small mass of hydrogen and the large electronegativity of fluorine. As a result of the unharmonicity of the molecule oscillations, absorptions are also observed in the near IR. In Fig. 3.5, the experimentally determined form of the potential energy as a function of the atomic separation is displayed for the valence oscillation of the H-Cl molecule, where the proportional wave number $\tilde{\nu}$ was selected as a measure for the energy E (from [41]).

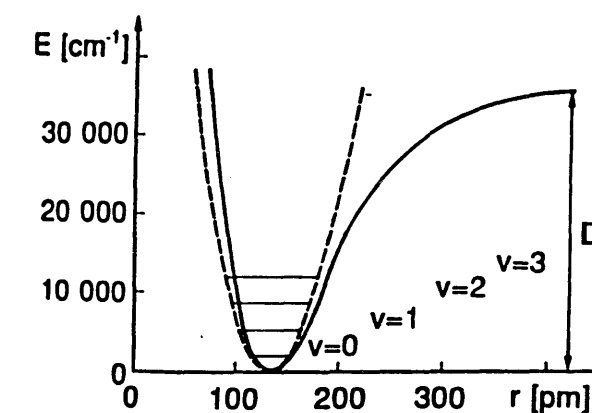


Fig. 3.5: Potential curve (—), harmonic approximation (---), and oscillation levels of the valence oscillation of H-Cl (v oscillation quantum number, D disassociation energy).

For a small deflection around the resting position, the potential curve can be approximated by a parabola $E = \frac{1}{2}k(r - r_0)^2$, i.e. the oscillation is harmonic with the returning force $-k(r - r_0)$ proportional to the deflection. In this case, the energy levels allowed by quantum theory are equidistant, and only transfers between neighboring levels with changes in the oscillation quantum number (cf. Fig. 3.5) around $\Delta v = \pm 1$ are allowed, i.e. in the harmonic case, only a single absorption band of the frequency $\Delta E/h$ arises. In reality, an unharmonic oscillation is expelled whose potential curve for large atomic separations flattens off. As a result, the energy levels allowed are no longer equidistant, and the quantum theory also allows level transfers with $\Delta v = \pm 2, \pm 3, \dots$, the so-called *overtone*s. In addition, two different unharmonic oscillations of a molecule

can also divide the energy of an absorbed photon for a shared excitation; this leads to the so-called *combination oscillation*. Due to the quickly falling transfer possibilities between the higher energy levels and their lower population densities, the intensity of the absorption bands of combination tones and overtones decreases very quickly. The NIR spectra of glucose and a few other blood substrates are shown in Fig. 3.6. The strongest NIR signals of glucose can be found around $1.6 \mu\text{m}$. In comparison to the mid IR, these extinction signals are essentially smaller (ca. 2000 times) and above all, very much broader with less structure ("entropy-poorer").

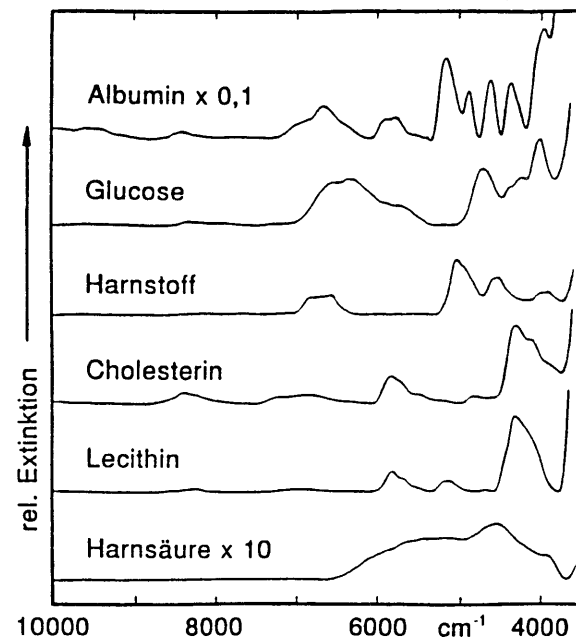


Fig. 3.6: NIR extinction spectra of various blood substrates as pure crystalline material in KBr-pellet technology; the signals are scaled relative to each other corresponding to the average physiological concentrations in blood plasma [3] (Lecithin was chosen as the model substance for the triglycerides).

The molecular oscillations do not only allow themselves to be excited through absorption of electromagnetic waves of identical frequency, rather, also through unrealistic collisions with light quanta of higher energy. In addition to IR spectroscopy, there exists a second important method for the observation of molecular oscillations, Raman spectroscopy, for which a monochromatic laser beam (e.g. diode laser at 800 nm or $\tilde{\nu}_{\text{las}} = 12500 \text{ cm}^{-1}$) is directed onto the sample. The scattered light spectrum of the sample S_D (cf. Fig. 3.3) consists of excitation lines at $\tilde{\nu}_{\text{las}}$ through the elastic Rayleigh scattering and from the molecule specific spectrum $S_{D,\text{Raman}}$ at $\tilde{\nu}_{\text{las}} \pm \tilde{\nu}_{\text{mol}}$ (Raman scattering, see e.g. [39]). There is no experience for the quantitative analysis of biotic samples in the concentration region that is proposed here. As a result of the large technical effort required, Raman spectroscopy appears to only be slightly appropriate for routine blood analysis; furthermore, the necessity arises to radiate biotic samples with relatively high laser powers. For these reasons, this method was not used for a non-invasive measurement through the skin.

3.3 Fourier Transform Spectroscopy

3.3.1 Basic Concepts

Two parameters are important for the judgement of the function of the spectral apparatus, namely the spectral resolution and the effective optical throughput which determines the magnitude of the radiation power that falls onto the detector. There is an inverse relationship between the two parameters. The throughput is dependent on the geometric design and the efficiency of the optical elements used (see App. A). Since in the IR spectral region either the additive detector noise or the photon noise of the radiation source dominates (Ch. 3.3.4), the signal-to-noise ratio of the spectroscopic measurement increases with the radiation power on the detector, e.g. with increasing throughput.

Up to and into the 1980s, IR spectrometers were built with monochromatic sources which contained dispersive elements, prisms, or gratings [34]. With monochromatic sources, the spectral resolution is set through the mechanical adjustment of the width of the exit slit so that the universally valid inverse relationship between resolution and throughput becomes very apparent here. With prisms, typical resolutions in the mid IR of 2 to 20 cm^{-1} were achieved [32], whereby the value for measurements over broad IR spectral regions varied due to the dispersion of the prism. After the production of inexpensive echelette gratings³ became possible through the development of modern reproduction technology, the prisms in the IR spectrometers were replaced with diffraction gratings. For identical measurement conditions (wavelength and resolution), improvements of about an order of magnitude in the effective throughput were achieved [42] such that commercial devices typically achieved a resolution of 0.2 cm^{-1} [32]. The disadvantages of grating monochromators were the increased scattered light values and the necessity to separate the overlapping of dispersion spectra of different order through supplemental spectral filtering.

To improve the signal-to-noise ratio, the measurement beam in dispersive spectrometers was mechanically modulated through chopper wheels, and the detector signal was made phase-sensitively constant with a lock-in amplifier; due to the inertia of the thermal detectors available, only very low chopper frequencies of typically 5 – 30 Hz could be used. The disadvantages of these low modulation frequencies were the proximity to $1/f$ noise, the difficulty of the measurement with a single bandwidth typically $f_{\text{max}} = f_{\text{chop}}/10$, and the susceptibility to the so-called slow spectrometer drifts from which the reproducibility of the measurement suffers (see e.g. [34:p. 148] as well as Ch. 3.3.3).

Today, the measurements of IR spectra are almost entirely made with Fourier transform spectrometers [43] which instead of a dispersive element, use the 1882 two-beam interferometer developed by A. A. Michelson, consisting of a beam splitter and two planar mirrors [44] (see Fig. 3.7). The emitted power S_R from an IR radiation source is made parallel with collimator optics C_1 and reaches the beam splitter with a reflection degree R and a transmission degree T ; real beam splitters are approximately free of losses, e.g. $R + T = 1$. The part $R S_R$ is reflected back from the fixed mirror M_1 such that the power $T R S_R$ reaches the detector. An equally sized portion $R T S_R$ reaches the detector through the second arm of the interferometer after reflection from the

³Echelette gratings display "sawtooth"-formed lines. As a result, the percentual portion of the radiation power reflected in the direction of the exit slit is significantly increased, and the efficiency of the gratings becomes comparable to that of prisms [34:p. 154].

movable mirror M_2 . The portion $(R_2 + T_2) S_R$ is imaged back onto the radiation source and is lost for the measurement.⁴

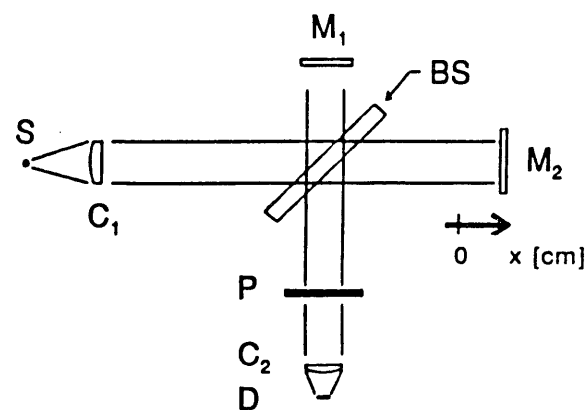


Fig. 3.7: Principle of the FT spectrometer (S radiation source, C_1 collimator, BS beam splitter, M_1 fixed mirror, M_2 movable mirror, P sample, C_2 condenser, D detector).

For examining the interferences that arise, the time signal $E(t)$ of the electric field strength $[V/m]$ is observed which enters the interferometer as a planar wave with beam cross-sectional area $Q [m^2]$. With the thermal radiation sources that are normally used, $E(t)$ is a realization of a random process arising from the overlaying of a very large number of finite length wave trains that are sent from the source molecules independent of each other as a result of spontaneous emission. From the central value theorem, it follows that $E(t)$ is an unpolarized gaussian random process [45] that can be assumed to be ergodic for stationary operating conditions of the source [46:p. 72].

Both time signals $k_1 E(t)$ and $k_2 E(t + \tau)$ reach the detector,⁵ whereby the path time difference $\tau = 2x/c_0$ (cf. Fig. 3.7) is generated through both arms of the interferometer with a deflection of the movable mirror M_2 from the so-called *ZPD position* (zero path difference). The damping during transmission through both arms of the interferometer can be described with the coefficients k_1 and k_2 . In the ideal case, k_1 and k_2 are real and constant $k_1 = k_2 = 0.5$ over the entire frequency region of $E(t)$. This extends into the IR from about 30 THz ($10 \mu m$) to 300 THz ($1 \mu m$). With today's detectors, electric field strengths from about 0.5 THz can be measured time-resolved [47:p. 30], for higher frequencies, only power detectors are available whose output signals are proportional to the radiation power that hits the detector:

$$p(t, \tau) = \frac{1}{2} \epsilon_0 c_0 Q |k_1 E(t) + k_2 E(t + \tau)|^2 [W] \quad (3.7)$$

⁴The efficiency $2 * R * T$ of a beam splitter reaches the maximum value of 50% for $R = T = 0.5$.

⁵The speed of light in the interferometer can be set equal to that in a vacuum $c_0 \approx 3 \times 10^{10}$ cm/s.

Except for a proportionality factor with dimensions independent of the detector type used, the detector signal is given by:

$$i(\tau) = \frac{1}{T_D} \int_{T_D} p(t, \tau) dt [W] \quad (3.8)$$

where T_D is the response time of the detector. Even the fast IR detectors made of semiconductor material have response times of typically $1 \mu s$ such that they function as ideal integrators in the infrared frequency region. With the definition of the *autocorrelation function* $\Gamma(\tau)$

$$\Gamma(\tau) \doteq \lim_{T \rightarrow \infty} \frac{1}{T} \int_T E(t) E(t + \tau) dt \quad (3.9)$$

the detector signal, the so-called *interferogram*, is given by

$$\begin{aligned} i(\tau) &= \frac{1}{2} \epsilon_0 c_0 Q \frac{1}{T_D} \int_{T_D} \{k_1^2 E(t)^2 + k_2^2 E(t + \tau)^2 + 2k_1 k_2 E(t) E(t + \tau)\} dt \\ &= \frac{1}{2} \epsilon_0 c_0 Q \{(k_1^2 + k_2^2) \Gamma(0) + 2k_1 k_2 \Gamma(\tau)\} \\ &\doteq i_{DC} + i_{AC}(\tau) \end{aligned} \quad (3.10)$$

According to the Wiener-Kinchine Theorem, the power spectral density of the signal $E(t)$ can be determined through Fourier transformation of $i_{AC}(\tau)$ (e.g., [48]); the proportionality constants that arise cancel each other during the calculation of the transmission from the single beam spectra of the sample and reference and remain negligible for absorption spectroscopy. In practice, the informationless DC portion of the interferogram is eliminated through a highpass filter and the variable portion is preamplified, A/D-converted, and transformed to the desired single beam spectrum with the help of a discrete Fourier transformation

$$S(f) \doteq F[i_{AC}(\tau)] = \int_{-\infty}^{\infty} i_{AC}(\tau) e^{-i2\pi f \tau} d\tau \left[\frac{W}{Hz} \right] \quad (3.11)$$

where $f \doteq 1/\tau$ [Hz]. With the relationship $\tau = 2x/c_0$ and the variable substitutions

$$\begin{aligned} l &\doteq 2x \\ \bar{\nu} &\doteq \frac{1}{l} \end{aligned} \quad (3.12)$$

The Fourier transform can be written with the typical units for IR spectroscopy of optical path difference l [cm] and the wave number $\bar{\nu}$ [cm^{-1}]:

$$S_l(\bar{\nu}) \doteq F_l[i_{AC}(l)] = \int_{-\infty}^{\infty} i_{AC}(l) e^{-i2\pi \bar{\nu} l} dl \left[\frac{W}{cm^{-1}} \right] \quad (3.11a)$$

where $S_l(\bar{\nu}) = S(f/c_0)$. The spectral resolution $\Delta \bar{\nu}$ is determined through the maximum deflection of the movable mirror $x_{max} = 1/2l_{max}$ in FT spectroscopy. This corresponds to a multiplication of the interferograms with a rectangular function or a convolution of the spectra with a Si-function:

$$\int_{-l_{max}}^{l_{max}} \frac{e^{-i2\pi \bar{\nu} l}}{2l_{max}} dl = \frac{\sin(2\pi \bar{\nu} l_{max})}{2\pi \bar{\nu} l_{max}} \doteq \text{si}(2\pi \bar{\nu} l_{max}) \quad (3.13)$$

The nominal resolution $\Delta\tilde{\nu}$ of an FT measurement is defined as:

$$\Delta\tilde{\nu} \doteq \frac{1}{l_{\max}} \quad (3.14)$$

In practice, the interferograms are often multiplied with other so-called *apodization functions* (from Greek: without feet), whereby the disturbing secondary maxima of the rectangular apodization of the Si function that arise are eliminated at the cost of a somewhat decreased resolution (e.g., [49,50]). The Fourier transform is conducted with a computer on which the control software, the spectrometer, and the diverse programs for the processing are also installed. The sample times for the interferogram are defined by the cosine shaped interferogram of a laser whose beam is supplementally fed with the IR measurement radiation through the interferometer and is registered on a separate detector. The HeNe laser that is used emits in the red region at 632.8 nm or $\tilde{\nu}_{\text{las}} = 15800 \text{ cm}^{-1}$ [51:p. 587]; the large coherence length of single mode lasers allows resolutions of the FT spectrometer on the order of 0.001 cm^{-1} [32]. Typically, both zero crossings (per cycle) of the laser interferogram are detected with a Schmitt-Trigger such that a sampling frequency of approximately 31600 cm^{-1} without supplemental electronics is available.

With the so-called *slow-scan* IR spectrometers, the mirror M_2 is driven either in discrete steps or very slowly with a constant mirror velocity of typically $4 \mu\text{m/s}$; as with dispersive spectrometers, the beam is modulated with a mechanical chopper. For various reasons, it is better for the regions of the near and mid-IR (cf. [43:p. 47]) to measure so-called rapid-scan interferograms with a constant mirror velocity with approximately $c_M = 0.05\text{-}5 \text{ cm/s}$ and to improve the S/N ratio of the spectra for large measurement times, a large number of interferograms ("scans") are summed up and averaged in the computer. With the variables of the mirror movement of the same form (at the turnaround points of the mirror, the data acquisition is interrupted)

$$\begin{aligned} t_M &\doteq \frac{x}{c_M} \\ f_M &\doteq \frac{1}{t_M} \end{aligned} \quad (3.15)$$

the important relationship between the optical frequencies f_M [Hz] and $\tilde{\nu}$ [cm^{-1}] and the signal frequency at the detector exit f_M [Hz] becomes:

$$f_M = 2 \frac{c_M}{c_0} f = 2c_M \tilde{\nu} \quad (3.16)$$

Through the scaling $t_M = (c_0/2c_M)\tau$, the rapid scan interferometer transforms the optical frequencies from the THz region into a technically appropriate order of magnitude:

$$F[i_{\text{AC}}(t_M)] = \frac{2c_M}{c_0} S\left(\frac{2c_M}{c_0} f\right) = \frac{2c_M}{c_0} S(f_M) \quad (3.11b)$$

The maximum frequencies at the detector exit are typically smaller than $f_M = 100 \text{ KHz}$. When using fast semiconductor detectors, the frequency region of an FT-IR measurement is limited through the A/D converter and the mechanical inertia of the interferometer.⁶

⁶In the following, the optical frequencies will be noted with $\tilde{\nu}$ [cm^{-1}] such that the indices of the variables t_M and f_M are no longer necessary for the technical frequencies.

FT spectrometers possess a much improved S/N ratio compared with dispersive devices. On the one hand, this is due to the fact that the optical throughput with the circularly shaped field stops and apertures is larger than that with slits in the monochromator [42]. A comparative study of two commercial devices showed that approximately one hundred times more radiation power is available at the detector as compared with grating spectrometers through this so-called *Jacquinot advantage* for comparable measurement conditions in the mid-IR ($\tilde{\nu} = 2000 \text{ cm}^{-1}$) with FT spectrometers [52]. The second reason for the better performance of the interferometer is the so-called *Fellgett advantage*. With FT spectrometers, the entire spectrum $S(\tilde{\nu})$ falls onto the detector simultaneously whereby with the monochromatic device, the N spectral elements $N = (\tilde{\nu}_{\max} - \tilde{\nu}_{\min})/\Delta\tilde{\nu}$ must be measured sequentially. The advantage of FT devices through the better use of the available measurement time can be formulated in two equivalent ways [53]: (1) For a constant total measurement time, the measurement time per spectral element with FT devices is a factor N larger; the noise in the spectrum is reduced by a factor of \sqrt{N} (Multiplex advantage); (2) In order to achieve identical S/N ratios, FT spectrometers require a $1/N$ times smaller measurement time (time advantage) in comparison to a dispersive device. Both of the aforementioned advantages of the FT device fold out their full efficiency for the case that the S/N ratio of the measurement is limited through the additive detector noise (cf. Ch. 3.3.4).

3.3.2 The Bruker IFS-66 Spectrometer

Commercial FT spectrometers have been obtainable since the 1970s. The motivations were the re-discovery of the FFT algorithm by Cooley and Tukey [54] as well as the development of minicomputers, HeNe lasers, fast-IR detectors, and mechanical components with which the movable mirror can be pushed along the optical axis of the interferometer with very small tilts (order of magnitude $< 1 \mu\text{rad}$) [43]. Fig. 3.8 shows a schematic diagram of the Bruker IFS-66 spectrometer that was used [55]:

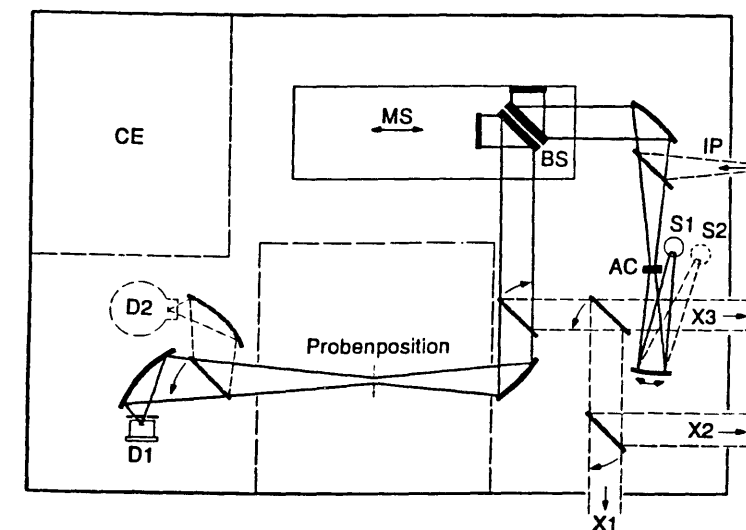


Fig. 3.8: The Bruker IFS-66 spectrometer (- standard; - - optional; S_1/S_2 radiation sources; AC field aperture exchanger; BS beam splitter; MS movable mirrors; D_1/D_2 detectors; IP IR inputs; $X_1 - X_3$ IR outputs; CE control electronics).

The IFS-66 is a portable table device with dimensions $74 \times 54 \times 22$ cm ($B \times T \times H$) that is equipped with accessories for measurements in the near and mid IR. Through two movable mirrors, each of two detectors and IR sources can be chosen by the software. For the beam sources, a tungsten-halogen glow lamp in the near IR and a globar⁷ in the near IR are available. Both sources are cooled through an external water circulation. Liquid nitrogen cooled semiconductor elements can be used as detectors. By cooling to 77°K, the noise and the response behavior of the detectors are influenced positively. For the measurements in this work, a photovoltaic InSb element ($\phi = 4$ mm) in the near IR and a photoconductive MCT element ($\square = 1 \times 1$ mm) in the mid IR were used.⁸ In the mid IR, an approximately $0.4 \mu\text{m}$ thick Ge layer is used as the beam splitter which is steamed onto a KBr-substrate. For the optical phase compensation (symmetry of the interferometer arms), a second KBr-plate with equal thickness is fixed before the Ge. In the near IR, a ca. $0.17 \mu\text{m}$ thick Si layer brought onto a CaF_2 substrate was used. A change of the beam splitters is possible by hand through the housing lid.

The heart of the device is a Michelson interferometer with two planar mirrors in a 90° arrangement, whereby the movable mirror is positioned on an air bearing with a rectangular cross section. The diameter of the collimated IR beam is ca. 40 mm. The unexpanded He-Ne laser beam for the definition of the sampling times ($\phi \approx 1$ mm) is centrally merged into the interferometer; the sample period is automatically set by the operating software of the IFS-66 according to the requirements of the sampling theorem. The maximum obtainable resolution is given as better than 0.1 cm^{-1} . Due to a nearly one-sided deflection of the movable mirror around the ZPD position, the symmetry of the interferograms $i_{\text{AC}}(l) = i_{\text{AC}}(-l)$ can be used in such a way that quasi the total mechanical mirror path contributes to the spectral resolution. The radiation flow can be controlled through field apertures "AC" (see Fig. 3.8) with various diameters. The apertures "AC" are imaged into the sample focus by two identical off-axis paraboloid mirrors (fulfillment of the sine condition through common subtraction of both paraboloids [34].) Through the location of the sample behind the interferometer, the emission spectrum of the sample generates solely a DC component on the detector such that this false light signal can be filtered off. In the IFS-66, there is a sample compartment available, i.e. both of these signal beam spectra for the sample and reference must be sequentially measured. The detector optics consist each of a single off-axis ellipsoid mirror with a reduction of about 5:1. The collimated beam from the interferometer can be deflected to the off-side through further movable mirrors such that additional measurement accessories with a separate detector can be connected to the IFS-66 (see Ch. 6.3).

During operation, the housing of the IFS-66 is purged with gaseous nitrogen (consumption typically 600 L/h) in order to force the disturbing IR absorbers, water vapor and carbon dioxide, out of the beam path. The sample compartment is reachable from above through a lid in order not to disturb the purge of the device during a sample exchange. In the focus of the sample, experiments with standard accessories such as e.g. transmission cuvettes were conducted. The air bearing of the movable mirror is also filled with gaseous nitrogen (ca. 150 L/h; pressure = 1-2 bar)

⁷A globar is an electrically heated SiC column which approximates the emission spectrum of a black radiator at an operating temperature of approximately 1500°K.

⁸Photovoltaic detectors contain a PN transition and function electrically as current sources when radiated such that preamplifiers with low impedance inputs can be connected to them. Photoconductive elements change their electrical resistance when radiated; for fixed current inputs, the changes in the voltage through the element can be detected with high impedance preamplifiers.

which is fed through a cleaning filter before the bearing due to the small thickness of the supporting air layer in the micrometer region.

The detector signal is preamplified, then bandpass filtered, and sampled with a 16-bit A/D converter. After choosing the velocity of the mirror c_M , the limit frequencies of the bandpass filter with $f_{\text{HP/LP}} = 2 c_M \tilde{\nu}_{\text{min/max}}$ can be adjusted to the bandwidth of the IR spectrum (cf. Eq. 3.16 and Ch. 3.3.5). Through a permanently connected high pass filter of the first order with $f_{\text{HP}} \approx 16$ Hz before the bandpass filter, the DC portion of the interferogram which contains no information is eliminated before the A/D conversion.

3.3.3 Systematic Errors

Two single beam spectra $S_1(\tilde{\nu})$ and $S_2(\tilde{\nu})$ which were taken under identical measurement conditions with an FT spectrometer also display systematic differences in addition to stochastic noise which is responsible for the so-called *drifting of the baselines* $S_1(\tilde{\nu})/S_2(\tilde{\nu})$. Spectrometer drifts arise, for example, as a result of small misalignments of the interferometer through oscillations in the room temperature. In this work, the single beam spectra (typically 1000 scans) were taken with measurement times of approximately 1-2 min and at time intervals between samples and references of approximately 1-6 min such that stochastic changes with time constants on the order of magnitude of a few minutes must be calculated with the systematic errors, since on the one hand, these are not averaged out during a measurement and on the other hand, can be noticed between two measurements.

One can derive the systematic errors in FT spectroscopy whether they primarily influence the amplitude of the single beam spectra or influence their position on the wave number axis. The first group includes, e.g. oscillations in the emission of the radiation source, the sensitivity of the detector as well as the modulation efficiency of the interferometer as a result of small misalignments. In order to re-unite both of the radiation halves after passing through the interferometer such that interference of the electric fields takes place, the components of the interferometer must be exactly mechanically aligned for a portion of the wavelengths used. For both angles under which the beam splitter is met by the area normals of both interferometer mirrors, only differences on the order of $\Theta \approx 10^{-5}$ rad are allowed. The modulation efficiency of a Michelson interferometer is reduced by a factor $2J_1(n\pi)/(n\pi)$ with $n = \Theta\phi_M/\lambda$ through the so-called tilt error where ϕ_M is the illuminated diameter of the interferometer mirrors and the J_1 is the Bessel function of first order. For $\phi_M = 40$ mm and $\lambda = 1 \mu\text{m}$, an angle error of $\Theta = 1.25 \cdot 10^{-5}$ rad already yields a mirror tilt of half a wavelength $n = 1/2$ and a reduction of the modulation efficiency $2J_1(1/2\pi)/(1/2\pi) = 0.72$ [47:p. 110]. Modulation losses also arise through stochastic changes in the flatness of the optical surface areas; for a KBr beam splitter, this loss factor for wavelengths of $\lambda = 10.9 \mu\text{m}$ (916 cm^{-1}) is given as 0.671 [56].

Systematic translations of the single beam spectra along the frequency axis arise if the IR radiation is not directed into the interferometer parallel to the optical access. According to Eq. 3.11, the relationship between the interferogram⁹ $i(l)$ and the spectra $S(\tilde{\nu})$ for a Michelson interferometer

⁹In further discussion, only DC-corrected interferograms appear such that $i(l) = i_{\text{AC}}(l)$ will be written.

reads:

$$i_{\text{ideal}}(l) = \int_{-\infty}^{\infty} S(\tilde{\nu}) \cos(2\pi\tilde{\nu}l) d\tilde{\nu} \quad (3.11c)$$

where the plane symmetry $S(\tilde{\nu}) = S(-\tilde{\nu})$ was considered in the calculation of the Fourier cosine transformation. The ideal relationship Eq. 3.11c is exactly valid only for FT spectrometers for which the radiation source and the detector can be approximated as infinitesimal points on the optical axis of the interferometer. For real devices, the finite expansion of both of these areas must be integrated, i.e. these must also be considered, which according to the laws of geometric optics, run along their path from the source to the detector skewed through the interferometer. One can easily show that a beam with angle γ to the optical axis after passing through a Michelson interferometer can receive an optical path difference $l_\gamma = l \cos \gamma$ during re-uniting at the detector. The summation of the skew beams takes place under use of the axial symmetry of the optics through integration over the space angle Ω_S which spans the finite expanded beam source S for the collimator optics C_1 . Modern FT spectrometers work almost entirely with collimated radiation, i.e. the radiation source S is located in the focus of C_1 and is imaged into infinity (see Fig. 3.9). The space angle Ω_S of a cone with a half opening angle γ_{max} is defined as the area which the cone cuts out of the surface area of the unit sphere (radius = 1):

$$\Omega_S = \int_0^{\gamma_{\text{max}}} 2\pi \sin(\gamma) d\gamma = 2\pi(1 - \cos(\gamma_{\text{max}})) \quad [\text{sr}] \quad (3.17)$$

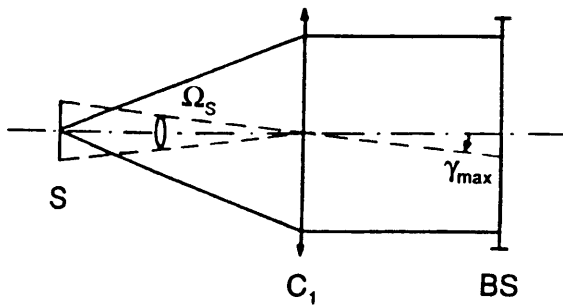


Fig. 3.9: The effect of a finitely expanded radiation source.

For Lambert radiation sources, the radiation power is equally distributed over the space angle Ω_S . Furthermore, if the emissions of different area elements of the source are uncorrelated and the sensitivity of the detector is also constant and uncorrelated over its radiated surface area, the integration can be conducted as follows [47]:

$$i_{\text{real}}(l) = \frac{1}{\Omega_S} \int_0^{\Omega_S} \int_{-\infty}^{\infty} S(\tilde{\nu}) \cos\left(2\pi\tilde{\nu}l\left(1 - \frac{\Omega}{2\pi}\right)\right) d\tilde{\nu} d\Omega$$

$$= \int_{-\infty}^{\infty} S(\tilde{\nu}) \text{si}\left(\frac{1}{2}\Omega_S\tilde{\nu}l\right) \cos\left(2\pi\tilde{\nu}l\left(1 - \frac{\Omega_S}{4\pi}\right)\right) d\tilde{\nu} \quad (3.18)$$

The interpretation of Eq. 3.18 is difficult due to the dependence of the integrands on l and $\tilde{\nu}$; the measurement of the single beam spectrum is influenced regarding the amplitude as well as the position on the wave number axis. These effects become clearer for the Fourier transformed $S_{\text{real}}(\tilde{\nu}'; \tilde{\nu})$ of $i_{\text{real}}(l; \tilde{\nu})$ where $\tilde{\nu}'$ and $l = 1/\tilde{\nu}'$ now build the Fourier-Paar of independent variables, and $\tilde{\nu}$ is a fixed parameter of the transformation:

$$\begin{aligned} S_{\text{real}}(\tilde{\nu}'; \tilde{\nu}) &= \int_{-\infty}^{\infty} i_{\text{real}}(l; \tilde{\nu}) \cos(2\pi\tilde{\nu}'l) dl \\ &= \int_{-\infty}^{\infty} S(\tilde{\nu}) \int_{-\infty}^{\infty} \text{si}\left(\frac{1}{2}\Omega_S\tilde{\nu}l\right) \cos\left(2\pi\tilde{\nu}l\left(1 - \frac{\Omega_S}{4\pi}\right)\right) \cos(2\pi\tilde{\nu}'l) dl d\tilde{\nu} \\ &= \int_{-\infty}^{\infty} S(\tilde{\nu}) \prod_{\frac{\Omega_S}{2\pi}} \left(\tilde{\nu}' - \tilde{\nu}\left(1 - \frac{\Omega_S}{4\pi}\right)\right) d\tilde{\nu} \end{aligned} \quad (3.19)$$

A single emission line with a Dirac spectrum $S(\tilde{\nu}) = \delta(\tilde{\nu} - \tilde{\nu}_0)$ is measured in an FT spectrometer as a rectangle of width $\tilde{\nu}_0\Omega_S/2\pi$ and height $2\pi/\tilde{\nu}_0\Omega_S$ that is centered around the frequency $\tilde{\nu}_0(1 - \Omega_S/4\pi)$; the corresponding interferogram $\text{si}(1/2\Omega_S\tilde{\nu}_0l) \cos(2\pi\tilde{\nu}_0l(1 - \Omega_S/4\pi))$ is damped with a Si function for longer path differences l . Hence, the effect is also known as self-apodization [57], although it does not include the usual convolution of the single beam spectrum, since the form of the rectangle is dependent on its position on the wave number axis. In commercial FT spectrometers, no attempts are made to correct the systematic errors according to Eq. 3.19, since the effects are normally small. In the Bruker IFS-66, the largest selectable field aperture "AC" (see Fig. 3.8) has, for example, a diameter of 12 mm, and the focal length of the off-axis paraboloid for collimation is $f_{C1} = 152.44$ mm; hence, the maximum space angle of the source can be determined in good approximation to be $\Omega_{S,\text{max}} = \pi^2/152.4^2 = 4.9 \cdot 10^{-3}$ sr. For measurements in the near IR with frequencies up to $\tilde{\nu}_{\text{max}} = 10000 \text{ cm}^{-1}$ and a spectral resolution of $\Delta\tilde{\nu} = 1/l_{\text{max}} = 32 \text{ cm}^{-1}$, a maximum modulation loss of $\text{si}(1/2\Omega_{S,\text{max}}\tilde{\nu}_{\text{max}}l_{\text{max}}) \approx 0.91$ and a frequency displacement of $-\tilde{\nu}_{\text{max}}\Omega_{S,\text{max}}/4\pi = -3.9 \text{ cm}^{-1}$. The systematic errors through finitely expanded sources and detectors become stronger for larger wave numbers $\tilde{\nu}_{\text{max}}$ and mirror paths l_{max} .¹⁰ One can show that the effects can be minimized through the use of collimated radiation in the interferometer [58].

For the quantitative analysis of the IR spectra, a high S/N ratio and a good reproducibility of the measurement is necessary. For the determination of glucose in whole blood, it is, therefore, not possible to take the reference spectrum with an empty sample cuvette. This procedure would, of course, reduce the experimental effort (in this work, water was used as the reference, cf. Ch. 5), however a field aperture "AC" with $\Omega_{\text{Ref}} < \Omega_{\text{Sample}}$ would have to be used before each reference measurement in order to avoid nonlinearities through saturation of the detector in addition to saturation of the A/D converter. In the Bruker IFS-66, the field screens are set through rotation of an angle-encoded disk with inserted circular screens. The switching prevents the danger that the screens not be used reproducibly and that the IR measurement radiation as a whole runs skew

¹⁰The usual criterium reads: $\Omega_{S,\text{max}} = \pi \cdot \Delta\tilde{\nu} / \tilde{\nu}_{\text{max}} = \pi / (\tilde{\nu}_{\text{max}} l_{\text{max}})$ [46]. For the space angle $\Omega_{S,\text{max}}$, the axis parallel beams and the beams of largest skewness γ_{max} interfere at a frequency $\tilde{\nu}_{\text{max}}$ at first destructively: $l_{\text{max}}(1 - \cos \gamma_{\text{max}}) = l_{\text{max}}\Omega_{S,\text{max}}/(2\pi) = 1/(2\tilde{\nu}_{\text{max}}) = 1/2\lambda_{\text{min}}$.

through the interferometer. A tilting of the IR radiation measurement of γ rad relative to the optical axis of the HeNe laser, which is directed into the interferometer with separate optics in order to define the sampling times, causes a frequency displacement of the single beam spectrum that is linear in $\tilde{\nu}$ of $\Delta\tilde{\nu} = -1/2\tilde{\nu}\gamma^2$ wave numbers.¹¹ Through these effects, systematic errors arise in the extinction spectra which depend on the true extinction $A_{\text{true}}(\tilde{\nu}) = -\log_{10}(S(\tilde{\nu})/S_R(\tilde{\nu}))$ as well as on the single beam spectrum $S_R(\tilde{\nu})$ of the "empty" spectrometer, as a Taylor series expansion shows:

$$\begin{aligned} A(\tilde{\nu}) &= -\log_{10}\left(\frac{S(\tilde{\nu} + \Delta\tilde{\nu})}{S_R(\tilde{\nu})}\right) \approx -\log_{10}\left(\frac{S(\tilde{\nu})}{S_R(\tilde{\nu})}\right) - \frac{\partial}{\partial\tilde{\nu}}(\log_{10}(S(\tilde{\nu})))\Delta\tilde{\nu} \\ &= A_{\text{true}}(\tilde{\nu}) + \left[\frac{\partial A_{\text{true}}(\tilde{\nu})}{\partial\tilde{\nu}} - \frac{\partial}{\partial\tilde{\nu}}(\log_{10} S_R(\tilde{\nu}))\right]\Delta\tilde{\nu} \end{aligned} \quad (3.20)$$

The reproducibility of the measurement is mainly influenced in the region of the steep flanks of the background spectrum S_R and strong absorption bands, where errors $\delta A/\delta\tilde{\nu}$ similar to dispersion occur. Particularly critical are the transmission measurements of blood plasma in the near IR, since glucose in the region of 6000–6600 cm^{-1} must be determined on the flank of a water band (Ch. 5.4). For the layer thickness used of 1 mm, the water absorption increases at 6300 cm^{-1} (≈ 0.3 AU) with a slope of about $5 \cdot 10^{-4}$ AU/ cm^{-1} . An angle error of $\gamma = 0.1$ deg causes at 6300 cm^{-1} a $\Delta\tilde{\nu} \approx -0.015$ cm^{-1} and an extinction error of about $-7 \cdot 10^{-6}$ AU in the region of the glucose bands whose peak heights lie at ca. $7 \cdot 10^{-5}$ AU for a concentration of 100 mg/dl. Angle errors can occur through transversal displacements of the radiation source (field apertures), the detector, and the sample. In a NIR transmission experiment, the diameter of the beam focus in the measurement cuvette is, for example, only 0.5 mm such that the "effective" sample position can be affected by air bubbles in the sample.

A further important cause for systematic errors is the nonlinearity of the semiconductor detectors used. With the radiation powers available in FT spectrometers, semiconductor detectors can typically be so far saturated that no modulation of the interferogram is measurable. The determination of the maximum valid radiation power for a special experiment occurs in practice through successive enlargement of the field aperture "AC"; nonlinearities in the measurement of the corresponding interferograms lead to additive terms through the Fourier transformation that result from a (possibly multiple) convolution of the single beam spectra with themselves. This effect can be particularly well observed on the lower frequency side of the spectra where the sensitivity of the semiconductor with band gap $E_{\text{gap}}[J]$ for wave numbers $\tilde{\nu} < \tilde{\nu}_{\text{gap}} = E_{\text{gap}}/(hc_0)$ abruptly sink and no signal appears in linear operation; the appearance of nonlinearities as a change in form of the steep flanks at $\tilde{\nu}_{\text{gap}}$ can be demonstrated [59].

A correction for the nonlinearities is not possible in FT spectrometers using software, since the nonlinear effects in the interferogram cannot be separated from the so-called phase errors [59]. These are responsible for the case that the real interferograms are asymmetric to the ZPD position:

$$i_{\text{real}}(l) = \int_{-\infty}^{\infty} S(\tilde{\nu}) \cos(2\pi\tilde{\nu}l + \phi(\tilde{\nu})) d\tilde{\nu} \quad (3.21)$$

In the derivation of Eq. 3.10, the coefficients k_1 and k_2 were assumed to be real and constant for the transmission through both of the interferometer arms. In practice, the coefficients $|k_1|e^{i\phi_1(\tilde{\nu})}$ and

¹¹ $l, \tilde{\nu} = l \cos \gamma \tilde{\nu} = l(1 - 1/2\gamma^2)\tilde{\nu} = l\tilde{\nu}_\gamma = l(\tilde{\nu} - 1/2\tilde{\nu}\gamma^2)$

$|k_2|e^{i\phi_2(\tilde{\nu})}$ are complex and frequency dependent such that phase errors $\phi(\tilde{\nu}) = \phi_1(\tilde{\nu}) - \phi_2(\tilde{\nu})$ occur. The beam splitter contributes a major portion through multiple reflections in the dielectric layer. The second important source for phase errors is the analog electronics for the preamplification and bandpass filtering of the detector signal whose transfer function $H(f) = |H(f)|e^{i\phi_H(f)}$ adds the additional phase $\phi_H(f) = \phi_H(\tilde{\nu}/2c_M)$ to the cosines in Eq. 3.21. The asymmetric interferograms undergo a so-called phase correction before the Fourier transformation [60]. For this purpose, the movable mirror is not only deflecting in one direction from the ZPD position, rather a portion of the interferogram is symmetrically sampled around the interferogram maximum. Since the phase $\phi(\tilde{\nu})$ displays a relatively smooth structureless form, for which its measurement requires only a small spectral resolution, this short symmetric portion can already achieve a good approximation of the phase correction through a complex Fourier transformation. The phase correction takes place through interpolation corresponding to the spectral resolution of the entire measurement which is determined through the maximum one-sided deflection of the mirror according to the well-known algorithms of Forman [61] and Mertz ([62], see also [63,64]).

Through detector nonlinearities, the maximum of the interferogram in the region of the ZPD position is damped. For ideal symmetric interferograms, this would mean that negative values in the frequency region $\tilde{\nu} < \tilde{\nu}_{\text{gap}}$ would occur in the single beam spectra (damping of the DC portion and the lower frequency Fourier components of $S(\tilde{\nu})$). The asymmetry of real interferograms can be either amplified or diminished through detector nonlinearities according to the phase error. The phase correction interprets the entire resulting asymmetry as phase error and corrects the calculation of the single beam spectra such that positive as well as negative values in the region $\tilde{\nu} < \tilde{\nu}_{\text{gap}}$ can occur [59]. In practice, semiconductor detectors in FT-IR spectrometers are often so used that very small nonlinearities cannot be avoided. Systematic drift errors, which primarily affect the average amplitude of the single beam spectra, also influence the lower frequency Fourier components of $S(\tilde{\nu})$ due to the change in the degree of the nonlinearity. Through nonlinearities, the reproducibility of the baseline is above all worsened while the finer local structures in the spectra are influenced less. In recent times, suggestions for improved preamplifiers have been made in which the sensitivity of the photoconductive MCT detectors is linearized for the mid IR by a feedback to the detector element [65,66]. However, these are not yet commercially available and were not used in this work.

3.3.4 Noise

The S/N ratio of single beam spectra $S(\tilde{\nu}) = S_{\text{true}}(\tilde{\nu}) + n(\tilde{\nu})$ is defined in IR spectroscopy as the ratio of the linearly averaged signal amplitude to the square root of the squared average noise amplitude [62:p. 28]:

$$\begin{aligned} SNR &\doteq \frac{S_{\text{av}}}{n_{\text{rms}}} \\ \text{where: } S_{\text{av}} &\doteq \frac{1}{B_S} \int_{B_S} S(\tilde{\nu}) d\tilde{\nu} \doteq \frac{l_{p-p}}{B_S} \left[\frac{W}{\text{cm}^{-1}} \right] \\ n_{\text{rms}}^2 &\doteq \frac{1}{B_n} \int_{B_n} n(\tilde{\nu})^2 d\tilde{\nu} \left[\frac{W^2}{\text{cm}^{-2}} \right] \end{aligned} \quad (3.22)$$

where B_S is the bandwidth of the single beam spectrum [cm^{-1}] and B_n is the effective noise bandwidth [cm^{-1}] which is determined from the analog bandpass filter in the preamplifier and is normally larger than B_S ; l_{p-p} is the peak-to-peak amplitude [W] of the interferogram at the ZPD position.¹²

The Parseval Theorem yields the relationship between the rms noise amplitude in the spectrum and in the interferogram:

$$n_{\text{rms}}^2 B_n = n_{l,\text{rms}}^2 l_{\text{max}} \quad (3.23)$$

where $n_{l,\text{rms}}$ is the rms noise in the interferogram domain [W] and l_{max} is the length of the interferogram [cm]. With the help of the number of resolved spectral elements $N = B_S l_{\text{max}}$ (see Eq. 3.14), a clear relationship between the S/N of the single beam spectrum and the so-called interferogram dynamics are described by Eq. 3.22 and Eq. 3.23 which is defined as the ratio of the maximum signal amplitude l_{p-p} to the rms noise amplitude $n_{l,\text{rms}}$:

$$SNR = \frac{S_{\text{av}}}{n_{\text{rms}}} = \sqrt{\frac{B_n}{B_S N}} \frac{l_{p-p}}{n_{l,\text{rms}}} \quad (3.24)$$

During sampling of the interferogram, it must be determined that the noise of the interferogram is digitized at least by the least significant bit of the A/D converter, since the SNR of the single beam spectrum would not otherwise be improved by the accumulation of many interferogram scans (e.g. [67]). In other words, the dynamic range of the A/D converter must be larger than that of the interferogram. In the IFS-66 spectrometer with a 16-bit quantization, the maximum allowed dynamics lie at $l_{p-p}/n_{l,\text{rms}} = 2^{15} = 32768$ (noise is sampled only in the last bit), and with $B_S = B_N$ and a typical value of $N = 500$ resolved spectral elements, an $SNR = 1465$ results for the single beam spectrum. This value can be increased by a factor of the \sqrt{M} through accumulation of M scans by the computer, whereby the theoretical limit of the word length of the computer is determined (Bruker Aspect 1000:2*24 = 48 bit). In addition, the IFS-66 has an available "8x gain-ranging", i.e. the interferogram $i(l)$ runs through a software-controlled analog switching amplifier before sampling with

$$i_{gr}(l) = \begin{cases} i(l) & |l| \leq l_{gr} \\ i(l) \times B & |l| > l_{gr} \end{cases} \quad (3.25)$$

such that the flatter, outer portion of the interferogram is apparently sampled with an additional 3 bits (see [68] for details); l_{gr} must be entered by the user. The main reason for the use of rapid-scan interferometers in the mid and near IR is that the dynamics of the interferogram can be reduced through an increase in the mirror velocity c_M and the available possibilities of the A/D conversion can be adjusted appropriately (increase in noise per sample point).

For the measurement of the radiation power density $S(\bar{\nu})$ in the optical frequency region, the noise occurs through an overlaying of various independent disturbance sources. These can be divided into the three following classes according to their dependence on the rms noise amplitude of the magnitude of the detector radiation power [62:p. 8ff]:

¹²Due to the fact that the rms signal amplitude is difficult to see, the usual definition for time signals of $SNR \doteq S_{\text{rms}}/n_{\text{rms}}$ is not used.

1) Photon Noise

The rms amplitude of this noise is proportional to the square root of the detected radiation power and fundamentally limits the maximum achievable S/N ratio for the measurement of electromagnetic radiation. The cause is the discretization of the radiation power in a "photon flow". If a power $l_0[W]$ of radiation at wave number $\bar{\nu}$ [cm^{-1}] is received on average, this corresponds to an average photon transfer rate $\bar{r}(\doteq E[r])$:

$$\bar{r} = \frac{l_0}{hc_0\bar{\nu}} \quad [\text{s}^{-1}] \quad (3.26)$$

The actual number p of the photons transferred in a time period τ oscillates statistically around the average value $\bar{p} = \bar{r}\tau$. In the visible and near IR spectral region, a Poisson distribution of p can be assumed as a good approximation¹³ [69:p. 16ff] for which $\sigma_p^2 = \bar{p}$ is valid (e.g. [70]). For the variance of the photon rate of $r = p/\tau$, it follows:

$$\sigma_r^2 = \frac{\sigma_p^2}{\tau^2} = \frac{\bar{r}}{\tau} \quad [\text{s}^{-2}] \quad (3.27)$$

In semiconductor detectors, centered photons are registered through the generation of additional free charge carriers. The average signal flow is

$$\bar{i} = wq\bar{r} \quad [A] \quad (3.28)$$

where q is the elementary charge [$A s$] and w is the so-called quantum efficiency ($0 \leq w \leq 1$) which yields the probability of detection of a charge carrier after photon absorption. The rms amplitude of the flow noise σ_i for the signal bandwidth $\Delta f = 1/(2\tau)$ [Hz] is determined with the well-known Schottky formula [71:p. 91]:

$$\sigma_i^2 = w^2 q^2 \frac{\bar{r}}{\tau} = 2wq\bar{i}\Delta f \quad [A^2] \quad (3.29)$$

The portion of the photon noise (shot noise) of the entire noise increases for shorter wavelengths, and for the spectroscopic wave measurement of intense radiation sources of the near IR, the photon noise is usually dominant. This can be explained in that the total power of a small number of energy-rich photons is transferred; the "discretization" of the radiation power increases. The SNR of the single beam spectra $SNR = \bar{p}/\sigma_p = (\bar{p})^{0.5}$ increases for photon noise only with the square root of the signal power and is only weakly dependent through the quantum efficiency on the detector type used. The multiplex advantage of FT spectrometers becomes nullified due to the increase in σ_i with $(\bar{i})^{0.5}$, the Jacquinot advantage is correspondingly weakened.

Photon noise also occurs for thermal IR detectors in which the impinging radiation power is transferred into heat and an electrical effect that is correlated with the increase in temperature is measured (e.g. Resistance-Bolometer, Seebeck thermo elements, etc.). The discrete nature of the

¹³The Poisson approximation is strictly valid only for coherent light (e.g. laser). If the photons are emitted from a black radiator of temperature T , p follows a Bose-Einstein distribution with an enlarged variance

$$\sigma_p^2 = \bar{p} \exp\left(\frac{hf}{kT}\right) / \left\{ \exp\left(\frac{hf}{kT}\right) - 1 \right\}$$

which with frequencies $hf \gg kT$ becomes the Poisson result.

relationship between the radiation and detector is observed as so-called temperature noise (not to be confused with Johnson noise from the electrical resistances). The variance in the temperature noise of a thermal detector with heat capacity $H[J K^{-1}]$, which is connected with an unlimited heat sink of temperature T by the heat conduction value $G[W K^{-1}]$, is [69,p. 137]:

$$\sigma_T^2 = \frac{4kGT^2\Delta f}{G^2 + (2\pi fH)^2} \quad [K^2] \quad (3.30)$$

For thermal detectors, it is generally valid that a high cut-off frequency $f_{\text{ther}} = G/H$ is only achievable at the cost of reduced sensitivity. In comparison to semiconductors, they display increased response times and a poorer S/N ratio and, therefore, were not used for this work.

2) Additive Noise

All of the noise sources which are independent of the detector radiation power fall under this category. This noise occurs e.g. in the analog preamplifier electronics (Johnson noise, $1/f$ noise, etc. [72]) and through the additive "digital noise sources". The last source refers to the roundoff errors in the calculation of the discrete Fourier transformation and the logarithms for the extinction spectra [73] as well as the quantization noise of the A/D converter whose variance can be given as a good approximation by $LSB^2/12$. As already mentioned in the comment to Eq. 3.24, the quantization noise in a correctly conducted FT-IR experiment is never the dominant noise source.

The most important source for additive noise in FT-IR measurements is the detector element itself [75] which in the mid IR is more dominant than the photon noise [76]. In this case, the multiplex and the Jacquinot advantages become very important. The physical causes for the detector noise are dependent on the detector type used. It is important that the standard deviations in a series of additive noise sources of thermal and quantum mechanical detectors increase proportionally with the square root of the sensitive detector area [77,34]. This is also valid for the additive sources to the photon noise to be calculated through the background temperature radiation of usually 300°K in the spectrometer.

3) Fluctuation Noise

The rms amplitude of this noise is directly proportional to the detector radiation power, i.e. fluctuations are random modulations of the measurement radiation. These occur, e.g. through atmospheric flimmering in measurements for monitoring the air quality through smoke stacks. Through an appropriate choice of the measurement frequency region (mirror velocity) and through an adjustment of the bandpass filter in the preamplifier, the effect of the "sidebands" of the single beam spectrum arising through fluctuation noise can be minimized. In laboratory experiments, fluctuation noise should never dominate, since the Jacquinot advantage is nullified and the multiplex advantage even becomes a disadvantage. In order to use the latter in FT-IR measurements, the relative fluctuations are only allowed to lie on the order of magnitude of 10^{-6} - 10^{-7} [35]. An example of fluctuation noise especially for FT spectrometers is the so-called "sampling noise" which occurs through uncertainties in the definition of the sampling times during the mirror movement. Through the application of HeNe lasers, whose light is also fed into the interferometer together with the IR measurement radiation, this noise can almost be entirely eliminated [78,79]. Random modulations of the optical path differences in the interferometer through oscillations in the refraction index of air depending on the temperature and pressure are reduced between the laser

frequency $\tilde{\nu}_{\text{Las}} \approx 15800 \text{ cm}^{-1}$ and the measurement frequencies in the IR through this technology, except for small dispersion effects, such that "sampling noise" in modern FT devices is not dominant. More disturbing than the stochastic fluctuations are currently the modulations of the detector signal through *systematic* errors such as eigen-oscillations of the interferometer housing resulting from mechanical or acoustic excitation or electromagnetic interferences (50 Hz and overtones) [80]. As long as these disturbances are incoherent with the scan, their size decreases as the rms amplitude of the stochastic fluctuations through accumulation with the square root of the number of interferogram scans. However, this is not valid for the very slow systematic errors due to the aforementioned baseline drifts (Ch. 3.3.3) in comparison to the length of a scan which, in practice, limits the maximum measurement time for the data accumulation.

Distribution Function of the Noise

In FT spectroscopy, it is possible to determine the statistical distribution of the noise in the spectral region independent from the characteristics of the noise in the interferogram region. According to a useful theorem from Brillinger, the noise of the single beam spectra through the discrete Fourier transformation of the noisy interferogram is asymptotically uncorrelated and normally distributed with increasing number of sampled data points [81:p. 94ff]. In FT-IR spectroscopy, the discrete FT calculations are conducted with at least a few hundred data points such that the asymptotic nature of the aforementioned theorem becomes effective. Furthermore, the Fourier transform acts in cases in which the rms amplitude of the interferogram noise is dependent on the position of the movable mirror, e.g. for dominating photon noise, to level the noise in the spectral region to a constant value $n_{\text{rms}} = \text{const}(\tilde{\nu})$. Only a dependence of the interferogram noise on the frequency remains undisturbed by the Fourier transformation due to the direct proportionality of the optical frequency $\tilde{\nu} [\text{cm}^{-1}]$ to signal frequency $f [\text{Hz}]$ at the detector exit (Eq. 3.16); e.g. the spectrum $S(\tilde{\nu})$ would be mainly disturbed through $1/f$ noise in the region of smaller wavenumbers. Through selection of the mirror velocity c_M and adjustment of the bandpass filter in the preamplifier, the $1/f$ noise in FT spectroscopy is usually eliminated. The remaining noise sources display constant power densities over the frequency region of the FT measurements $f_{\text{min/max}} = 2c_M\tilde{\nu}_{\text{min/max}}$ (cf. Eq. 3.16) such that for the noise of the $N = (\tilde{\nu}_{\text{max}} - \tilde{\nu}_{\text{min}})/\Delta\tilde{\nu}$ resolved elements of a direct single beam spectrum, the following approximation is valid:

$$n(\tilde{\nu}_i) \sim \text{Normal} \left\{ \begin{array}{l} E[n(\tilde{\nu}_i)] = 0; E[n(\tilde{\nu}_i)n(\tilde{\nu}_j)] = \begin{cases} n_{\text{rms}}^2 = \text{const.} & \tilde{\nu}_i = \tilde{\nu}_j \\ 0 & \text{sonst} \end{cases} \end{array} \right\} \quad i, j = 1 \dots N \quad (3.31)$$

Error Propagation

For the quantitative processing of the IR spectra, the extinction spectra are used in which the concentrations of the components are linear (cf. Eq. 3.4). The aforementioned noise sources appear in the sample spectrum $S(\tilde{\nu}) = S_{\text{true}}(\tilde{\nu}) + n_S$ as well as in the reference spectrum $S_R(\tilde{\nu}) = S_{R,\text{true}}(\tilde{\nu}) + n_R$. Since the S/R ratios of both single beam spectra in FT-IR experiments lie at least at 10^4 , the noise in the extinction spectra can be calculated in good approximation with the Gaussian error propagation law which, for both statistically independent variables n_S and n_R , reads [82]:

$$A(\tilde{\nu}) = -\log_{10} \left(\frac{S_{\text{true}}(\tilde{\nu}) + n_S}{S_{R,\text{true}}(\tilde{\nu}) + n_R} \right) = A_{\text{true}}(\tilde{\nu}) + n_A(\tilde{\nu})$$

$$\begin{aligned}
\text{with } A_{\text{true}}(\bar{\nu}) &= -\log_{10} \left(\frac{S_{\text{true}}(\bar{\nu})}{S_{R,\text{true}}(\bar{\nu})} \right) \\
n_{A,\text{rms}}(\bar{\nu}) &= \sqrt{\left(\frac{\partial A}{\partial S} \right)_{\text{true}}^2 n_{S,\text{rms}}^2 + \left(\frac{\partial A}{\partial S_R} \right)_{\text{true}}^2 n_{R,\text{rms}}^2} \\
&= \frac{1}{2.303} \sqrt{\left(\frac{-1}{S_{\text{true}}(\bar{\nu})} \right)^2 n_{S,\text{rms}}^2 + \left(\frac{-1}{S_{R,\text{true}}(\bar{\nu})} \right)^2 n_{R,\text{rms}}^2} \\
&\doteq \frac{1}{2.303} \sqrt{SNR_S(\bar{\nu})^{-2} + SNR_R(\bar{\nu})^{-2}}
\end{aligned} \tag{3.32}$$

The extinction spectrum is estimated as expected with an rms noise amplitude $n_{A,\text{rms}}(\bar{\nu})$ which is dependent on the local S/R ratios, $SNR_S(\bar{\nu})$ and $SNR_R(\bar{\nu})$, of both single beam spectra (see Eq. 3.32 for definitions). An optimization of the conditions for the quantitative analysis of IR signals requires a maximization of the extinction simultaneously in order to minimize the noise. In spectroscopy, this condition is deciding e.g. in the choice of the sample layer thickness in a transmission experiment: An improvement in the $SNR_S(\bar{\nu})$ can only be achieved through an increase in the radiation power to the detector, i.e. through the smallest possible layer thickness of the sample; in this fashion, the actual useful signal is reduced, namely the radiation damping through the sample absorption. An exacter treatment is possible through the definition of the "signal"/noise ratio in the extinction region:

$$SNR_A(\bar{\nu}) \doteq \frac{A(\bar{\nu})}{n_{A,\text{rms}}} = \frac{2.303 A(\bar{\nu})}{\sqrt{\left(\frac{n_{S,\text{rms}}}{S_{\text{true}}(\bar{\nu})} \right)^2 + \left(\frac{n_{R,\text{rms}}}{S_{R,\text{true}}(\bar{\nu})} \right)^2}} \tag{3.33}$$

In the case that additive detector noise dominates, Eq. 3.33 with $n_{S,\text{rms}} = n_{R,\text{rms}}$ can be simplified to:

$$\begin{aligned}
SNR_A(\bar{\nu}) &= \frac{2.303 A(\bar{\nu})}{\sqrt{\left(\frac{n_{R,\text{rms}}}{S_R(\bar{\nu})} 10^{-A(\bar{\nu})} \right)^2 + \left(\frac{n_{R,\text{rms}}}{S_R(\bar{\nu})} \right)^2}} \\
&= 2.303 SNR_R(\bar{\nu}) \frac{A(\bar{\nu})}{\sqrt{10^{2A(\bar{\nu})} + 1}}
\end{aligned} \tag{3.34}$$

For an optimal measurement of the sample extinction, the layer thickness of the sample must be chosen according to Eq. 3.34 such that $A_{\text{opt}} = 1/2.303 = 0.434$; this corresponds to a transmission of the sample $T_{\text{opt}} = e^{-1} = 36.8\%$ and an $SNR_{A,\text{opt}} = 0.345 SNR_R$.

In the case of dominating photon noise, larger layer thicknesses must be selected, since the extinction measurement is then optimized for somewhat smaller detector powers. In practice, the sample $S(\bar{\nu})$ as well as the reference $S_R(\bar{\nu})$ are measured "shot noise limited" such that the noise amplitude of both single beam spectra $n_{S,\text{rms}}$ and $n_{R,\text{rms}}$ are proportional to $\sqrt{S_{\text{av}}}$ and $\sqrt{S_{R,\text{av}}}$. Substitution into Eq. 3.33 yields:

$$SNR_A(\bar{\nu}) = 2.303 SNR_R(\bar{\nu}) \frac{A(\bar{\nu})}{\sqrt{\left(\frac{S_{\text{av}}}{S_{R,\text{av}}} \right) 10^{2A(\bar{\nu})} + 1}} \tag{3.35}$$

The theoretically optimal relationships for the S/N ratio of the extinction are achieved for a spectroscopic measurement with dominating photon noise and radiation sources with small bandwidths (e.g. lasers). In this case, $S_{\text{av}}/S_{R,\text{av}} \approx S(\bar{\nu})/S_R(\bar{\nu})$ is valid and Eq. 3.35 yields:

$$SNR_A(\bar{\nu}) = 2.303 SNR_R(\bar{\nu}) \frac{A(\bar{\nu})}{\sqrt{10^{A(\bar{\nu})} + 1}} \tag{3.35a}$$

For Eq. 3.35a, the optimal transmission lies at $T_{\text{opt}} = e^{-2} = 13.5\%$ i.e. in comparison to Eq. 3.34, $A_{\text{opt}} = 0.869$ as well as $SNR_{A,\text{opt}} = 0.691 SNR_R$ were doubled. In Fig. 3.10, SNR_A in dependence on transmission of the sample $T = 10^{-A}$ is displayed normalized for both cases in Eq. 3.34 and Eq. 3.35a. Both curves display a flat form in the region of the maxima such that the choice of the exact sample thickness is relatively uncritical. In the case of dominant additive noise, an approximately optimal function in the region of $T = 20-60\%$ is achieved, for Eq. 3.35a; this is valid for about $T = 3-30\%$. For FT-IR experiments with broadband radiation sources in the near IR, SNR_A follows a curve between both of the displayed curves.

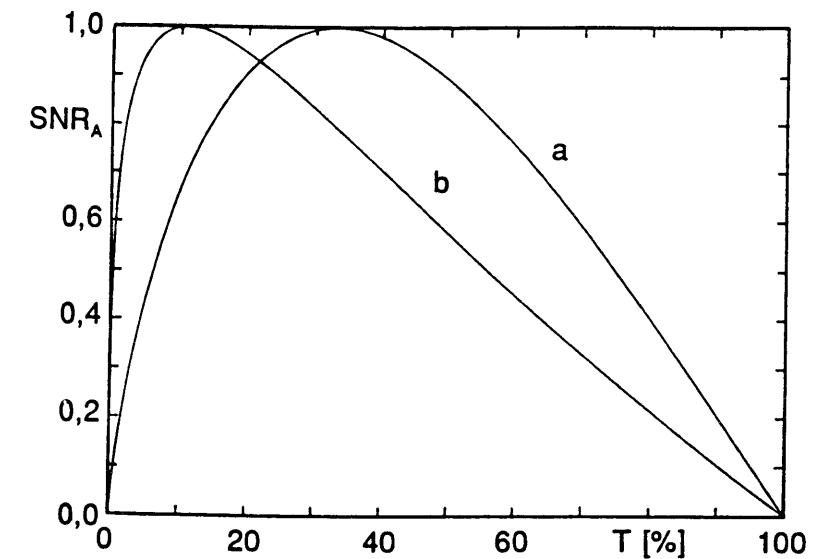


Fig. 3.10: Normalized representation of the S/N ratio in the extinction region versus the sample transmission T [%] for (a) dominant additive detector noise and (b) dominant photon noise and narrow band radiation source.

The noise $n_A(\bar{\nu})$ in the extinction region is uncorrelated and normally distributed like the noise of the single beam spectra n_S and n_R (cf. Eq. 3.31). This arises directly from the application of the Gaussian error propagation law which uses a linearization of the function $A(\bar{\nu}) = -\log_{10}(S(\bar{\nu})/S_R(\bar{\nu}))$ by a Taylor series expansion. Actually, the normal distribution of $n_A(\bar{\nu})$ can also be assumed for very strongly noisy single beam spectra with S/N ratios down to about $SNR_S(\bar{\nu}) = SNR_R(\bar{\nu}) \approx 10$ as long as no negative values arise during the calculation of $T(\bar{\nu}) = S(\bar{\nu})/S_R(\bar{\nu})$ [83:p. 139]. The amplitude of the extinction noise is not constant for the IR spectroscopic examination of blood, rather $n_{A,\text{rms}}(\bar{\nu})$ takes on larger values according to Eq. 3.33 in the region of stronger background absorption bands of water.

3.3.5 Selection of the Measurement Parameters

In the following, it was attempted to list the individual steps in short form for the optimization of the measurement conditions of FT-IR experiments. This should give an overview of the procedure used in this work, and simultaneously, a few of the identically selected parameters in all experiments will be named. For further technical details, please see the experimental portion of this work (Ch. 5 and Ch. 6).

1. After determining the spectral region of the measurement, the IR radiation source, beam splitter, optical accessories for sampling, and IR detector were appropriately chosen. The selection principle was to set up an optical transmission path with ideal bandpass behavior in order to use the available dynamic region of the A/D converter as full as possible for sampling the information-containing signal portions of the interferogram (cf. Eq. 3.24). Steep flanks of the bandpass (e.g. in the band gap frequency of semiconductor detectors) should not be set too close to a signal region in order to keep the susceptibility of systematic errors small. Special optical (interference) bandpass filters were not used, since these are firstly, relatively narrow banded and secondly, display high losses in the throughput region. During selection and construction of the optical sample accessories, it was, furthermore, important that the S/N ratio in the extinction region (SNR_A) is optimized through the layer thickness of the sample.
2. In the next step, the selection of the size of the field aperture "AC" (see Fig. 3.8) as well as through manipulations of the power supply of the IR radiation source were set to yield the maximum IR radiation for which the detector shows linear behavior during measurement of the sample and reference. This took place using the methods described by Chase [59] in Ch. 3.3.3.
3. Next, the mirror velocity c_M of the movable mirror was determined for the transformation of the optical frequencies into the region of the technical frequencies $f_{\min/\max} = 2c_M \tilde{\nu}_{\min/\max}$ (Eq. 3.16). By increasing c_M , susceptibility to slower drift appearances is reduced; by reducing c_M , the percent time requirement for the direction change of the mirror of the total scan length is reduced, i.e. the temporal use efficiency (duty cycle) of the measurement is increased. Further points of importance are the frequency dependence of the sensitivity of various IR detectors and the limits of the A/D converter. All interferograms in this work were sampled in one direction of the mirror motion (with a fast return). Sampling in both directions was not used, since the "duty cycle" of the IFS-66 spectrometer could not be increased for lower spectral resolutions $\Delta\tilde{\nu} = 1/l_{\max}$.
4. In the preamplifier, the cutoff frequencies of the electronic bandpass filter were adjusted through hardware manipulations to the bandwidth of the IR spectrum $f_{\min/\max} = 2c_M \tilde{\nu}_{\min/\max}$.
5. The amplification factor of the preamplifier was set such that the dynamic region of the A/D converter was almost completely used.
6. Finally, appropriate values for the diverse software parameters were determined, which include the apodization, the amplification (Eq. 3.25), phase correction, among others. The so-called Blackman-Harris 3-Term Function [84] was always used for the apodization in this work, and

for phase correction, the Mertz Method was applied [62]. Further details are given in the experimental portion of this work (Ch. 5 and Ch. 6).

4 Multivariate Signal Processing

While for the qualitative analysis of IR spectra for constitution explanation the examination of the dominating absorption bands regarding frequency, half value width, and relative intensities is sufficient, an exact measurement of the signal amplitude is required for the quantitative analysis. The requirements regarding the S/N ratio and the reproducibility of the measurement increase significantly as a result, especially if small extinction signals on top of a large background absorption should be measured so that the sample layer thickness cannot be adjusted to the actual useful signal (for glucose in water, cf. Fig. 5.1). Up to now, the applications of quantitative analysis are still limited to cases in which a so-called "analytical wave number" could be found for a material that was to be examined; what is meant here is an absorption band which is not overlaid with extinction signals from other sample components with variable concentration (e.g. [85]). For the determination of glucose in biotic fluids, there does not exist a specific absorption band of this type, since the spectra of a large number of various blood components are overlaid and these spectra are relatively unspecific in the fluid phase, i.e. structureless or "band weak" (cf. Fig. 4.1 and Fig. 5.15 for the situation in the mid and near IR respectively). For a successful glucose determination, a multivariate procedure must, therefore, be used for the quantitative signal analysis which in the last few years has experienced a considerable increase in interest through the introduction of the IR spectrometer and through the availability of fast computers [86]. These algorithms use information from broad spectral regions where the separation of overlaid spectra is possible and simultaneously the analysis certainty is increased through suppression of the spectral noise and the baseline drift.

4.1 Model Generation

IR spectra deliver information about the chemical makeup of the examined sample where the concentrations c_i of the IR active components occur linearly according to the Lambert-Beer Law in the extinction spectra (Ch. 3.1):

$$A(\tilde{\nu}) = \epsilon_1(\tilde{\nu})d(\tilde{\nu})c_1 + \epsilon_2(\tilde{\nu})d(\tilde{\nu})c_2 + \dots + \epsilon_K(\tilde{\nu})d(\tilde{\nu})c_K \quad (4.1)$$

For transmission experiments, the layer thickness of the sample is given by the measurement cuvette $d(\tilde{\nu}) = d_{\text{cuv}}$; for other measurement techniques, $d(\tilde{\nu})$ can be frequency dependent (cf. Ch. 5 and Ch. 6).

Let $k_i(\tilde{\nu}) = \epsilon_i(\tilde{\nu})d(\tilde{\nu})$ be the extinction per concentration unit through the i th medium of the sample ($i = 1, \dots, K$) and let the pure component spectrum k_i be a known N -dimensional (column) vector that arises through the sampling of $k_i(\tilde{\nu})$ at N discrete wavenumbers. The Lambert-Beer Law Eq. 4.1 in matrix notation reads:¹⁴

$$\begin{aligned} \mathbf{a} &= \mathbf{k}_1 c_1 + \mathbf{k}_2 c_2 + \dots + \mathbf{k}_K c_K + \mathbf{e} \\ &= \mathbf{K}_{N \times K} \mathbf{c}_{K \times 1} + \mathbf{e} \end{aligned} \quad (4.2)$$

The error vector \mathbf{e} represents stochastic measurement noise as well as an eventual systematic error in the model (see below). We are looking for the concentrations c_i with which the pure component

¹⁴In the following, matrices are written in large boldfaced type and vectors are written in small boldfaced type.

spectra k_i , appropriately weighted can be summed up to a measured mixture spectrum \mathbf{a} . The solution with the usual method of least squares reads:

$$\hat{\mathbf{c}}_{\text{LS}} = (\mathbf{KTK})^{-1} \mathbf{KTa} \quad (4.3)$$

and minimizes the sum of the squared errors $\text{SSE} = (\mathbf{a} - \mathbf{K}\hat{\mathbf{c}})^T(\mathbf{a} - \mathbf{K}\hat{\mathbf{c}})$ of the fit; with the definition $\hat{\mathbf{c}} = \hat{\mathbf{c}}_{\text{LS}} + \Delta\mathbf{c}$, it immediately results that the matrix \mathbf{KTK} is positive definite:¹⁵

$$\begin{aligned} \text{SSE} &= (\mathbf{a} - \mathbf{K}\hat{\mathbf{c}})^T(\mathbf{a} - \mathbf{K}\hat{\mathbf{c}}) \\ &= \mathbf{a}^T \mathbf{a} - \mathbf{a}^T \mathbf{K}(\mathbf{KTK})^{-1} \mathbf{KTa} + \Delta\mathbf{c}^T \mathbf{KTK} \Delta\mathbf{c} \end{aligned} \quad (4.4)$$

In order to judge the result of the fit in the spectral region also regarding the quality with which the solution $\hat{\mathbf{c}}$ estimates the true vector \mathbf{c} , it is necessary to make a few assumptions about the stochastic distribution of the error vector \mathbf{e} . The determination of the statistical moments of first and second order $E[\mathbf{e}]$ and $\text{COV}[\mathbf{e}]$ (see Appendix B) is sufficient for all of the following algebraic operations conducted, and for the usual assumptions for \mathbf{e} , the so-called physical model reads:

$$\mathbf{a} = \mathbf{Kc} + \mathbf{e}; \quad E[\mathbf{e}] = 0; \quad \text{COV}[\mathbf{e}] = \sigma^2 \mathbf{I} \quad (4.5)$$

For the case that the statistics in Eq. 4.5 correctly describe the error vector \mathbf{e} , the LS solution Eq. 4.3 is an optimal estimator in the sense that $\hat{\mathbf{c}}_{\text{LS}}$ displays the minimum error variance of all unbiased estimators with $E[\hat{\mathbf{c}}] = \mathbf{c}$ [87]. This is the well-known Gauss-Markov Theorem

$$E[(\hat{\mathbf{c}}_{\text{LS}} - \mathbf{c})^T(\hat{\mathbf{c}}_{\text{LS}} - \mathbf{c})] = \text{Min} \{ (\hat{\mathbf{c}} - \mathbf{c})^T(\hat{\mathbf{c}} - \mathbf{c}) \mid E[\hat{\mathbf{c}}] = \mathbf{c} \} \quad (4.6)$$

whose assumptions for validity in detail are [88]:

1. The regressors (columns of \mathbf{K}) are linearly independent, i.e. $\text{rg}(\mathbf{K}) = K$;
2. There exists no information a priori about the value of the model parameter \mathbf{c} and σ^2 ;
3. $\text{COV}[\mathbf{e}] = \sigma^2 \mathbf{I}$;
4. $E[\mathbf{e}] = 0$, i.e. the algebraic of Eq. 4.2 correctly describes the true model.

Except for the first point, the assumptions of the Gauss-Markov Theorem are not fulfilled for the physical model in Eq. 4.5. It is then e.g. a priori known that $c_i > 0$ is valid for the concentrations to be determined. Also, the variance of the extinction noise is not constant (Eq. 3.32), rather, a more realistic assumption would be ($n = 1, 2, \dots, N$):

$$\begin{aligned} \text{COV}[\mathbf{e}] &= \Sigma_{\text{spec}} = \sigma^2 \text{diag}[(10^{2\mathbf{a}(n)} + 1)^{1/2}] \quad \text{additive noise} \\ &= \Sigma_{\text{spec}} = \sigma^2 \text{diag}[(10^{\mathbf{a}(n)} + 1)^{1/2}] \quad \text{photon noise} \end{aligned} \quad (4.7)$$

¹⁵Due to $\text{rg}(\mathbf{KTK}) \equiv \text{rg}(\mathbf{K})$, the $(K \times K)$ matrix \mathbf{KTK} is only positive definite if the $(N \times K)$ matrix \mathbf{K} contains a complete column rank; it is required then that the pure component spectra k_i , in Eq. 4.2 are linearly independent.

each with an unknown parameter σ^2 ; however, the Gauss-Markov estimator can be adjusted to special measurement problems and more universally reads for $\text{COV}[\mathbf{e}] = \Sigma_{\text{spec}}$.¹⁶

$$\hat{\mathbf{c}}_{\mathbf{G}-\mathbf{M}}(\mathbf{K}^T \Sigma_{\text{spec}}^{-1} \mathbf{K})^{-1} \mathbf{K}^T \Sigma_{\text{spec}}^{-1} \mathbf{a} \quad (4.8)$$

The largest limitation for the practical use of the physical model arises in not being able to fulfill the four aforementioned assumptions for the Gauss-Markov Theorem. In reality, not all absorbing components are known for a highly complex system such as blood such that the true model Eq. 4.5 must be split into known and unknown components:

$$\mathbf{a} = [\mathbf{K}_b \ \mathbf{K}_u] \begin{bmatrix} \mathbf{c}_b \\ \mathbf{c}_u \end{bmatrix} + \mathbf{e}; \quad E[\mathbf{e}] = 0; \quad \text{COV}[\mathbf{e}] = \Sigma_{\text{spec}} \quad (4.9)$$

By neglecting the unknown components \mathbf{K}_u , the incorrect model

$$\mathbf{a} = \mathbf{K}_b \mathbf{c}_b + \mathbf{e}_f \quad (4.10)$$

is generated whose solutions with the method of least squares

$$\hat{\mathbf{c}}_{\text{LS},f} = (\mathbf{K}_b^T \mathbf{K}_b)^{-1} \mathbf{K}_b^T \mathbf{a} \quad (4.11)$$

displays the following expected value:

$$\begin{aligned} E[\hat{\mathbf{c}}_{\text{LS},f}] &= (\mathbf{K}_b^T \mathbf{K}_b)^{-1} \mathbf{K}_b^T E[\mathbf{a}] \\ &= (\mathbf{K}_b^T \mathbf{K}_b)^{-1} \mathbf{K}_b^T (\mathbf{K}_b \mathbf{c}_b + \mathbf{K}_u \mathbf{c}_u) \\ &= \mathbf{c}_b + (\mathbf{K}_b^T \mathbf{K}_b)^{-1} \mathbf{K}_b^T \mathbf{K}_u \mathbf{c}_u \end{aligned} \quad (4.12)$$

For the realistic case that the extinction spectra for the known and unknown components are overlaid in the spectral region used, $\mathbf{K}_b^T \mathbf{K}_u \neq 0$, there exists a systematic error or *bias* in the estimation of the parameter \mathbf{c} . This error does not only occur in practice through the unknown components, rather also through the so-called "matrix effects" for which the form of the individual pure component spectra k_i change through the dependence of the molecular state on the chemical makeup of the entire sample, e.g. through the building of hydrogen bonds (cf. discussion of Eq. 3.4). Matrix effects can be partly handled in that not the pure component spectra, rather the extinction spectra of known sample mixtures, are used as the regressors. After the special fit, the concentrations of the individual contents are determined through summing up the estimated mixtures. Such a physical model was successfully used for the quantitative analysis of various egg whites (albumin, immunoglobulin-G, and fibrinogen) in watered solutions [89]. Total protein in blood is the strongest absorber after water and about a hundred times more concentrated than glucose. As a result, the blood spectra display a few strong bands which can be directly connected to the protein such that the application of physical models for the protein analysis in blood is also imaginable, although the difficulties in the model generation would increase due to the biological variability of the samples.

¹⁶ Corresponds to the LS solution for minimizing the *weighted* sums of the squared error:

$$(\mathbf{a} - \mathbf{K} \hat{\mathbf{c}}_{\mathbf{G}-\mathbf{M}})^T \Sigma_{\text{spec}}^{-1} (\mathbf{a} - \mathbf{K} \hat{\mathbf{c}}_{\mathbf{G}-\mathbf{M}}) = \min$$

The application of physical models for the analysis of blood glucose is, in comparison, not sensible. Here, a model must be constructed whose systematic errors $\mathbf{K}_u \mathbf{c}_u$ are small in comparison to the average blood glucose extinction. This requirement is not fulfilled especially for measurements in the near IR. There is only one known attempt at a glucose calibration with physical model, and in spite of the fact that the largest glucose signals in the region of 1185–1000 cm^{-1} were used, the calibration line versus a clinical reference method displayed large systematic variations from the ideal 45° line (slope of 28° and y -intercept of 35 mg/dL [90]). The superiority of the following described statistical models is documented in [2] where a successful determination of glucose was conducted with the data set from [90].

The goal of quantitative spectroscopic analysis is mostly not a complete explanation of the chemical composition of the sample examined, rather the concentration determination of individual components. In a statistical corollary, absolutely no considerations regarding the functional relationships between spectrum and medium concentration are made, rather, the dependence is expressed solely through statistical correlations. For this purpose, the blood spectrum \mathbf{a} (sampled from N wavenumbers) and the corresponding true glucose concentrations c are summarized into an $(N+1)$ -dimensional random vector $[c, \mathbf{a}^T]$. By determining the distribution function of this vector (and at least its first two statistical moments), a so-called statistical model is defined which e.g. for a normal distribution reads ($\mu_c \doteq E[c]; \mu_a \doteq E[\mathbf{a}]$):

$$\begin{bmatrix} c \\ \mathbf{a} \end{bmatrix} \sim \text{Normal} \left\{ \begin{bmatrix} \mu_c \\ \mu_a \end{bmatrix}, \begin{bmatrix} \sigma_{cc}^2 & \text{COV}[\mathbf{a}, c]^T \\ \text{COV}[\mathbf{a}, c] & \text{COV}[\mathbf{a}] \end{bmatrix} \right\} \quad (4.13)$$

Using the model distribution function, the glucose concentration of a newly measured IR spectrum is predicted as a conditional expected value (see below). It is solely assumed that the random vector $[c, \mathbf{a}^T]_{\text{new}}$ also belongs to the model population which means e.g. that the IR spectra must be sampled under identical measurement conditions. In practice, the relevant criterium for the judgment of the quality of the prediction is the mean squared error $\text{MSE} = E[(\hat{c} - c)^2]$. An important advantage of the statistical model is that the best linear prediction in the MSE sense can be analytically given with the statistical moments of first and second order from Eq. 4.13:

$$\begin{aligned} \hat{\mathbf{c}}_{\text{opt},W} &= \mu_c + (\mathbf{a} - \mu_a)^T \mathbf{b}_{\text{opt}} \\ \text{where: } \mathbf{b}_{\text{opt},W} &= \text{COV}[\mathbf{a}]^{-1} \text{COV}[\mathbf{a}, c] \end{aligned} \quad (4.14)$$

The vector $\mathbf{b}_{\text{opt},W}$ represents the known Wiener filter from signal processing (e.g. [91]). The size of the MSE prediction error and the optimality of the Wiener filter is immediately determined with the definition $\mathbf{b} = \mathbf{b}_{\text{opt},W} + \Delta \mathbf{b}$:

$$\begin{aligned} \text{MSE} &\doteq E[(\hat{c} - c)^2] \\ &= \sigma_{cc}^2 - \text{COV}[\mathbf{a}, c]^T \text{COV}[\mathbf{a}]^{-1} \text{COV}[\mathbf{a}, c] + \Delta \mathbf{b}^T \text{COV}[\mathbf{a}] \Delta \mathbf{b} \end{aligned} \quad (4.15)$$

where $\text{COV}[\mathbf{a}]$ is positive (semi-)definite. An exception to the assumed normal distribution in Eq. 4.13 does not influence the results in Eq. 4.14 and Eq. 4.15, since the determination of the statistical moments of first and second order suffices for the description of the linear prediction estimator. In the case of a normally distributed random vector $[c, \mathbf{a}^T]$, it can, furthermore, be shown that the Wiener filter Eq. 4.14 is even *globally* the best estimator in the MSE sense (not only the best linear). This arises for the normal distribution from the linearity of the conditional

expected value $E[c | \mathbf{a}_{\text{new}}]$ which represents the global minimum of the MSE criterium [91:p. 13]. For the multivariate analysis of extinction signals, the linear relationship between c and \mathbf{a} is guaranteed through Beer's law such that for this special application case, the Wiener prediction (Eq. 4.14) is always *globally* the best estimator in the MSE sense, independent from the actual distribution of the vector $[c, \mathbf{a}^T]^T$!

In reality, the statistics of first and second order of the model (Eq. 4.13) are unknown and must be estimated through measurement of a finite number of so-called "standards". A standard consists of an IR spectrum \mathbf{a}_m ($m = 1, \dots, M$) and the corresponding "true" glucose concentration c_m which is determined with the help of a current clinical-chemical reference method. The desired statistics can be estimated with:¹⁷

$$\mu_c \approx c_{\text{av}} = \frac{c_1 + c_2 + \dots + c_M}{M} \quad (4.16a)$$

$$\mu_a \approx \mathbf{a}_{\text{av}} = \frac{\mathbf{a}_1 + \mathbf{a}_2 + \dots + \mathbf{a}_M}{M} \quad (4.16b)$$

$$\text{COV}[\mathbf{a}, c] \approx \frac{(\mathbf{a}_1 - \mathbf{a}_{\text{av}})(c_1 - c_{\text{av}}) + \dots + (\mathbf{a}_M - \mathbf{a}_{\text{av}})(c_M - c_{\text{av}})}{M} \quad (4.16c)$$

$$\text{COV}[\mathbf{a}] \approx \frac{(\mathbf{a}_1 - \mathbf{a}_{\text{av}})(\mathbf{a}_1 - \mathbf{a}_{\text{av}})^T + \dots + (\mathbf{a}_M - \mathbf{a}_{\text{av}})(\mathbf{a}_M - \mathbf{a}_{\text{av}})^T}{M} \quad (4.16d)$$

The judgement of the quality of the estimates (Eq. 4.16c-d) is difficult and is only possible with the help of statistics of the fourth order of $[c, \mathbf{a}^T]$ [91:p. 24]. In practice, the goal of MSE minimization by the Wiener filter in the statistical model (Eq. 4.13) is maintained, however, for the examination of the arising difficulties, another model is used, the so-called inverse regression model:

$$\begin{bmatrix} c_1 \\ \vdots \\ c_M \end{bmatrix} = \begin{bmatrix} \mathbf{a}_1^T \\ \vdots \\ \mathbf{a}_M^T \end{bmatrix} \mathbf{b} + \mathbf{e} = \mathbf{A}_{M \times N} \mathbf{b} + \mathbf{e}; \quad E[\mathbf{e}] = 0; \quad \text{COV}[\mathbf{e}] = \sigma^2 \mathbf{I} \quad (4.17)$$

In Eq. 4.17, the roles of the dependent and independent variables in Beer's law are exchanged such that now the extinction spectra are the input values and the concentrations are the output values. This corollary is allowed due to the linearity of Beers Law and from a statistical standpoint is more efficient than the physical model, since in Eq. 4.17, the measured data \mathbf{A} can be regressed against the desired data $\mathbf{c} \doteq [c_1, c_2, \dots, c_M]^T$.

The meaning of the vectors \mathbf{c} and \mathbf{e} in Eq. 4.17 has changed in comparison to the physical model Eq. 4.5: The vector \mathbf{c} now contains the concentration values only for individual components of the medium, e.g. glucose, which are determined for all M standard spectra in the matrix \mathbf{A} with a clinical-chemical reference method, and the vector \mathbf{e} weights all arising errors of the reference method in the inverse model.¹⁸ We are looking for an estimate for the parameter vector \mathbf{b} with which the standard spectra in \mathbf{A} can be formed through scalar multiplication into the reference

¹⁷For normally distributed vectors $[c, \mathbf{a}^T]$ the scaling factor $1/M$ implies that Eq. 4.16 is an ML (maximum-likelihood) estimator. ML estimators are, with increasing number of standards, (asymptotically) unbiased, consistent, efficient, and normally distributed; i.e. for large sets of data, the ML solutions are statistically optimal [91:p. 79ff]. For the variances in Eq. 4.16c-d, the exact unbiased estimates are also used with the factor $1/(M-1)$.

¹⁸These definitions of \mathbf{c} and \mathbf{e} will be maintained in the following, since the inverse model will be solely used.

concentrations \mathbf{c} approximately, $\hat{\mathbf{c}} = \mathbf{A} \hat{\mathbf{b}}$, and with which the prediction of newly measured spectra can be conducted: $\hat{\mathbf{c}}_{\text{new}} = \mathbf{A}_{\text{new}} \hat{\mathbf{b}}$. The vector $\hat{\mathbf{b}}$ corresponds to a linear predictor of the universal statistical model Eq. 4.13.

Through the construction of an inverse model, the systematic errors during the parameter estimation are avoided, i.e. also for real models, $E[\mathbf{e}] = 0$ is valid. For a correct experimental completion of the measurements, the errors \mathbf{e} are uncorrelated for the individual standards such that the assumption $\text{COV}[\mathbf{e}] = \sigma^2 \mathbf{I}$ is also realistic. The problem with the estimation of the parameter vector \mathbf{b} in the inverse model is the breakdown of the first aforementioned assumption for the Gauss-Markov Theorem which requires linearly independent regressors. The LS estimator from Eq. 4.17:

$$\hat{\mathbf{b}}_{\text{LS}} = (\mathbf{A}^T \mathbf{A})^{-1} \mathbf{A}^T \mathbf{c} \quad (4.18)$$

displays a variance

$$\begin{aligned} \text{COV}[\hat{\mathbf{b}}_{\text{LS}}] &= E\{[(\hat{\mathbf{b}}_{\text{LS}} - E[\hat{\mathbf{b}}_{\text{LS}}]) (\hat{\mathbf{b}}_{\text{LS}} - E[\hat{\mathbf{b}}_{\text{LS}}])^T] \\ &= E\{[(\mathbf{A}^T \mathbf{A})^{-1} \mathbf{A}^T (\mathbf{c} - E[\mathbf{c}]) (\mathbf{c} - E[\mathbf{c}])^T \mathbf{A} (\mathbf{A}^T \mathbf{A})^{-1}] \\ &= (\mathbf{A}^T \mathbf{A})^{-1} \mathbf{A}^T E[\mathbf{e} \mathbf{e}^T] \mathbf{A} (\mathbf{A}^T \mathbf{A})^{-1} \\ &= \sigma^2 (\mathbf{A}^T \mathbf{A})^{-1} \end{aligned} \quad (4.19)$$

which is decisively dependent on the invertibility of the matrix $\mathbf{A}^T \mathbf{A}$. The better the matrix is numerically conditioned, the more precise is the statistical estimation by $\hat{\mathbf{b}}_{\text{LS}}$ [92]. In practice, it is shown that the inverse models (Eq. 4.17) are very poorly conditioned, i.e. that the matrices $\mathbf{A}^T \mathbf{A}$ are (nearly) singular. From this, it follows that minimal changes in the measured data, e.g. through noise in the standard spectra \mathbf{A} , can significantly influence the solution $\hat{\mathbf{b}}_{\text{LS}}$. The effect of the variance amplification occurs visibly through the smooth form of the extinction spectra which are typically measured with a spectral resolution $\Delta \tilde{\nu}$ that is smaller than that which would be necessary for the correct sampling of the band form. The absorption value at a particular point in the spectrum can be determined, therefore, in good approximation by interpolation of neighboring points, i.e. the regressors (columns of \mathbf{A}) are "nearly linearly dependent" or "collinear". An additional amplification of the collinearity can occur through the similarity of the standards (rows of \mathbf{A}) amongst each other whose chemical composition is often only slightly different. For these reasons, the "physical" rank of the matrix $\mathbf{A}_{M \times N}$ (ideal measurement without noise and baseline drifts) is normally smaller than the number of the regressors N . Numerical tests for determining the *mathematically* exact rank \mathbf{A} most often yield the maximum value $\text{rg}(\mathbf{A}) = \min(M, N)$ as the result due to the spectral noise such that the calculation of $\hat{\mathbf{b}}_{\text{LS}}$ is possible with the mathematically exact inverses $(\mathbf{A}^T \mathbf{A})^{-1}$ for overdetermined systems of equations with $M > N$ numerically. However, this does not represent a practical solution to the problem, since the result is statistically unusable due to the extremely large variance.

The quantitative analysis is a two-step process. After the model generation, the individual model parameters are estimated in the second step. In the physical model, the danger exists of carrying along a high bias already in the first step which can no longer be eliminated. This method remains, therefore, limited to simple systems which are comprised of small well-known components; for such systems, the physical model yields the concentrations of all components of the sample simultaneously. The inverse model must then always be used if the measured extinction spectra cannot be determined with sufficient certainty from the spectra of individual known components,

e.g. for the determination of glucose in blood. An unbiased estimation with the LS method is often not applicable for the inverse models due to the aforementioned variance problem. However, the possibility exists for the user to reduce the systematic errors and the variance of the estimator $\hat{\mathbf{b}}$ against each other in the parameter estimation. This leads to the criterium of the total squared estimation error:

$$\begin{aligned} Q(\hat{\mathbf{b}}) &= E[(\hat{\mathbf{b}} - \mathbf{b})^T(\hat{\mathbf{b}} - \mathbf{b})] \\ &= \text{spur}\{\text{COV}[\hat{\mathbf{b}}]\} + \text{bias}(\hat{\mathbf{b}})^T \text{bias}(\hat{\mathbf{b}}) \end{aligned} \quad (4.20)$$

for which the variances and the (squared) bias terms of all elements of the vector $\hat{\mathbf{b}}$ are summed up. The practical task for the parameter estimation in inverse models is to find a solution $\hat{\mathbf{b}}$ which distances itself from the LS solution $\hat{\mathbf{b}}_{\text{LS}}$ at the cost of a small bias, however, allows a large reduction of the variance.

At this point, an important note must be made about the possibility of the estimation of the parameter vector \mathbf{b} also in cases of singular matrices $\mathbf{A}^T\mathbf{A}$. The estimator vector $\hat{\mathbf{b}}$ should be used for the prediction of new spectra:

$$\hat{\mathbf{c}}_{\text{new}} = \mathbf{A}_{\text{new}} \hat{\mathbf{b}} \quad (4.21)$$

From the spectra \mathbf{A}_{new} , it is assumed that they belong to the same population belong as the calibration standards \mathbf{A} (cf. comment on the statistical model Eq. 4.13). For the inverse regression model, this means that the spectra \mathbf{A}_{new} also follow the model Eq. 4.17:

$$\hat{\mathbf{c}}_{\text{new}} = \mathbf{A}_{\text{new}} \mathbf{b} + \mathbf{e}_{\text{new}}; E[\mathbf{e}_{\text{new}}] = 0; \text{COV}[\mathbf{e}_{\text{new}}] = \sigma^2 \mathbf{I} \quad (4.22)$$

In the solution of the inverse model, the error of the parameter estimation $Q(\hat{\mathbf{b}})$ should not be minimized, rather analogous to the MSE criterium of the statistical model, the prediction error for the spectra \mathbf{A}_{new} :

$$\begin{aligned} Q_{\text{pred}}(\hat{\mathbf{b}}) &= E[(\hat{\mathbf{c}}_{\text{new}} - \mathbf{c}_{\text{new}})^T(\hat{\mathbf{c}}_{\text{new}} - \mathbf{c}_{\text{new}})] \\ &= E[(\mathbf{A}_{\text{new}}(\hat{\mathbf{b}} - \mathbf{b}) - \mathbf{e}_{\text{new}})^T(\mathbf{A}_{\text{new}}(\hat{\mathbf{b}} - \mathbf{b}) - \mathbf{e}_{\text{new}})] \end{aligned} \quad (4.23)$$

From $\text{COV}[\mathbf{e}, \mathbf{e}_{\text{new}}] = 0$ and the fact that the stochastic part of $\hat{\mathbf{b}}$ is only dependent on \mathbf{e} it immediately follows that $\text{COV}[\hat{\mathbf{b}}, \mathbf{e}_{\text{new}}] = 0$. With this, Eq. 4.23 simplifies to:

$$Q_{\text{pred}}(\hat{\mathbf{b}}) = E[(\hat{\mathbf{b}} - \mathbf{b})^T \mathbf{A}_{\text{new}}^T \mathbf{A}_{\text{new}} (\hat{\mathbf{b}} - \mathbf{b})] + E[\mathbf{e}_{\text{new}}^T \mathbf{e}_{\text{new}}] \quad (4.24)$$

The optimization of the criterium $Q_{\text{pred}}(\hat{\mathbf{b}})$ takes place through minimization of the first sums. From Eq. 4.24, the important conclusion can be made that the prediction relative portion \mathbf{b} of the true parameter vector also remains estimatable for singular regression problems. One can think of the calibration spectra (rows of $\mathbf{A}_{M \times N}$) as N -dimensional vectors that all approximately display the same "direction" in vector space \mathbf{R}^N due to the high collinearity. The larger the number M of the calibration standards, the denser this "vector bundle" samples the linear subspace that is spanned by the spectra and the better the spectra \mathbf{A}_{new} through \mathbf{A} are represented in the future. Through the collinearity of the spectra, the matrix \mathbf{A} displays a non-empty null space (for a $\mathbf{b}_N \in \text{null space}(\mathbf{A})$, $\mathbf{A}\mathbf{b}_N = 0$ is valid [93]) which is the orthogonal complement of the aforementioned vector bundle. In the inverse regression model (Eq. 4.17), a portion \mathbf{b}_N of the

true vector $\mathbf{b}_{\text{true}} = \mathbf{b} + \mathbf{b}_N$ is not observable, and as a result, is also not estimatable. However, exactly this portion \mathbf{b}_N is irrelevant for the prediction of new spectra, since it is guaranteed with Eq. 4.22 that every new spectrum \mathbf{A}_{new} is also orthogonal to \mathbf{b}_N . In practice, it must be determined through statistical tests that the new spectra \mathbf{A}_{new} are located inside of the spectra bundle of \mathbf{A} , e.g. through the Mahalanobis distance to the average value of the calibration spectra [94]. With this, the identity of the estimatable portion of \mathbf{b} of the parameter vector (subspace of the rows of \mathbf{A}) are practically determined with the prediction relevant portion (subspace of the rows of \mathbf{A}_{new}).

The quality of the prediction estimator $\hat{\mathbf{b}}$ depends strongly on whether future spectra \mathbf{A}_{new} are well represented through the calibration spectra \mathbf{A} . At this point, the relationship to the statistical model Eq. 4.13 becomes clear again which can be generated at any time through interpretation of the calibration standards as a small sample from a larger sample population. On the basis of the finite number of available standards, the optimal solution of the inverse regression model in the $Q_{\text{pred}}(\hat{\mathbf{b}})$ sense represents an approximation to the desired Wiener filter of the statistical model.

The optimal estimator of the model Eq. 4.17 in the Q_{pred} sense can be given analytically and reads [87]:

$$\mathbf{b}_{\text{opt}} = \mathbf{b}\mathbf{b}^T \mathbf{A}^T (\mathbf{A}\mathbf{b}\mathbf{b}^T \mathbf{A}^T + \sigma^2 \mathbf{I})^{-1} \mathbf{c} \quad (4.25)$$

It is important to note that \mathbf{b}_{opt} is dependent on the desired true vector \mathbf{b} such that Eq. 4.25 is only theoretically of interest. This problem arises as soon as the requirement of an unbiased estimator with $E[\hat{\mathbf{b}}] = \mathbf{b}$ is given up. In the search for \mathbf{b}_{opt} , therefore, one helps himself in practice with so-called "estimator classes". These define a smaller number of solutions $\hat{\mathbf{b}}$ which depend on the existing data \mathbf{A} and \mathbf{c} as well as from a "search parameter" that can be controlled from the user. One can imagine an estimator class as a guideline with which the environment of the unbiased solution $\hat{\mathbf{b}}_{\text{LS}}$ is searched for the optimal estimator in the Q_{pred} sense. A universal statement of the form "Estimator class A is better than Estimator class B" is not possible, since the comparison of the best results for various data sets can result differently. In the selection of an estimator class, practical considerations also play a role, such as e.g. the computer effort or the problematics in finding the best estimator of the class.

4.2 The Parameter Estimation

With the algorithms described in the following section, poorly conditioned linear regression problems can be approximately solved with the Q_{pred} criterium (cf. Eq. 4.23) of the total squared prediction error. Principally, methods can be used that are based on the physical as well as on the inverse model. Normally, the physical models are so well conditioned that unbiased parameter estimations deliver satisfactory solutions with the usual least squares methods (cf. Eq. 4.3 and Eq. 4.8). However for inverse regressions, due to the arising variance amplification through collinearity, one must stray away from the Q_{pred} criteria whose optimal solution can only be found approximately through the use of estimator classes (e.g. [95,98]). With these, modifications of the matrix $\mathbf{A}^T\mathbf{A}$ can be made before the calculation of $(\mathbf{A}^T\mathbf{A})^{-1}$ such that a numerically stable and statistically inexpensive inversion is possible (large variance reduction at the cost of a small bias). Older examples are the ridge estimator ($\mathbf{A}^T\mathbf{A} \rightarrow \mathbf{A}^T\mathbf{A} + \tau\mathbf{I}$ with $\tau \geq 0$) (e.g. [96,97]) or the various methods of regressor selection (e.g. [98,99]) for which columns of matrix \mathbf{A} are eliminated before the inversion according to differing criteria. A comparison of various classes using a Monte

Carlo study with simulated data can be found in [100]. Through the availability of large computer capacities and through the development of software for the numerically stable handling of large matrices, the algorithms that are preferably used today are based on a data orthogonalization. These try to describe the variance of the available calibration spectra through an (approximated) eigenvector decomposition such that an appropriate division of the measurement problem into a solvable "better conditioned" and a not useful "poor conditioned" portion takes place whereby the latter due to the orthogonality of both of the data subspaces can be eliminated before the inversion. Here, mainly two estimator classes compete with each other: on the one hand, the PCR (principal component regression) estimator which is typically used in statistics whose algebraic characteristics are very appropriate for describing the problem of poorly conditioned systems of equations, and on the other hand, the up-to-now nearly solely used quantitative spectroscopy PLS (partial least squares) estimator. Both methods are algorithmically related and use an orthogonal decomposition of the matrix \mathbf{A} such that an inversion of the regression problem is possible iteratively and user controlled.

4.2.1 The PCR Estimator

This algorithm orthogonalizes the regression problem with the singular value decomposition (SVD) of the matrix \mathbf{A} ([101], numerical details in [102]):

$$\mathbf{A} = (\mathbf{u}_1 \ \mathbf{u}_2 \ \dots \ \mathbf{u}_{R_T}) \begin{pmatrix} s_1 & & & \\ & s_2 & & \\ & & \ddots & \\ & & & s_{R_T} \end{pmatrix} \begin{pmatrix} \mathbf{v}_1^T \\ \mathbf{v}_2^T \\ \vdots \\ \mathbf{v}_{R_T}^T \end{pmatrix} \quad (4.26)$$

$$= \mathbf{U}_{(M \times R_T)} \mathbf{S}_{(R_T \times R_T)} \mathbf{V}_{(R_T \times N)}^T$$

The diagonal elements $s_i > 0$ of the matrix \mathbf{S} are the singular values of \mathbf{A} and the \mathbf{u}_r and \mathbf{v}_r are the orthonormal left and right singular vectors, respectively:

$$\mathbf{U}^T \mathbf{U} = \mathbf{V}^T \mathbf{V} = \mathbf{I}_{(R_T \times R_T)} \quad (4.27)$$

According to the usual conventions, the singular values are ordered according to their size: $s_1 \geq s_2 \geq \dots \geq s_{R_T} > 0$. The SVD represents a universal representation of the eigenvalue decomposition of quadratic matrices which is used for matrices of optional dimension $(M \times N)$ and optional ranges $0 \leq R_T \leq \min(M, N)$. For the mathematically exact rank R_T of the matrix \mathbf{A} , the following is valid:

$$s_r = 0 \text{ for } r = R_T + 1, R_T + 2, \dots, R_{\max} = \min(M, N) \quad (4.28)$$

The SVD is the most numerically reliable method for determining the rank of a matrix with which problems also arise due to the roundoff errors in the computer. In use with regression problems, the determination of a number R_T "significant" modes¹⁹ is however uncritical, since the measurement noise of the data \mathbf{A} is very much larger than the noise from roundoff error. Therefore, the matrix \mathbf{A} can be decomposed without numerical problems up to a rank for which the modes only represent measurement noise.

¹⁹The concept "mode" stands for a singular value s_r and its corresponding singular vectors \mathbf{u}_r and \mathbf{v}_r .

With the SVD of \mathbf{A} , the inverse model Eq. 4.17:

$$\mathbf{c} = \mathbf{U} \mathbf{S} \mathbf{V}^T \mathbf{b} + \mathbf{e} \\ = \sum_{r=1}^{R_T} s_r (\mathbf{v}_r^T \mathbf{b}) \mathbf{u}_r + \mathbf{e} \quad (4.29)$$

The collinearity of the matrix \mathbf{A} is shown as very small singular values so that the corresponding modes of the vector \mathbf{b} can be irreversibly damped on the order of magnitude of the error vector \mathbf{e} . The PCR estimator class is defined with the help of a "PCR inverse"

$$\mathbf{A}_{R, \text{PCR}}^i = \mathbf{V}_R \mathbf{S}_R^{-1} \mathbf{U}_R^T \quad (4.30)$$

where the index R refers to an optional amount of R modes which can be chosen from a total of R_T modes—this is the search parameter determined by the user. The use of all R_T modes in Eq. 4.30 yields the so-called Moore–Penrose Inverse \mathbf{A}^+ which yields a Gauss–Markov estimator of $\hat{\mathbf{c}}_{\text{new}}$ under the assumptions for Eq. 4.22²⁰ [103]. The PCR estimator in comparison uses only a smaller subset of the modes for the inversion of the model Eq. 4.17:

$$\hat{\mathbf{b}}_{R, \text{PCR}} = \mathbf{A}_{R, \text{PCR}}^i \mathbf{c} \\ = \sum_r \frac{1}{s_r} (\mathbf{u}_r^T \mathbf{c}) \mathbf{v}_r \\ = \sum_r \frac{1}{s_r} (\mathbf{u}_r^T \mathbf{c}_{\text{true}}) \mathbf{v}_r + \sum_r \frac{1}{s_r} (\mathbf{u}_r^T \mathbf{e}) \mathbf{v}_r \quad (4.31)$$

where the summation index r runs through the R selected PCR modes. The first summation in Eq. 4.31 approximately inverts the algebraically exact relationship $\mathbf{c}_{\text{true}} = \mathbf{A} \mathbf{b}$, i.e. the non-stochastic portion of the regression model; this term describes the systematic error in the estimation of the parameter vector

$$\text{bias}[\hat{\mathbf{b}}_{R, \text{PCR}}] = E[\hat{\mathbf{b}}_{R, \text{PCR}}] - \mathbf{b} \\ = \mathbf{A}_{R, \text{PCR}}^i \mathbf{c}_{\text{true}} - \mathbf{b} \\ = - \sum_j \frac{1}{s_j} (\mathbf{u}_j^T \mathbf{c}_{\text{true}}) \mathbf{v}_j \quad (4.32)$$

where the summation index j runs over the $(R_T - R)$ modes not selected. The second summation in Eq. 4.31 contains the stochastic error vector \mathbf{e} for which in the model Eq. 4.17, $\text{COV}[\mathbf{e}] = \sigma^2 \mathbf{I}$ is valid, and this term describes the occurrence of the variance in the parameter estimation

$$\text{COV}[\hat{\mathbf{b}}_{R, \text{PCR}}] = E[\mathbf{A}_{R, \text{PCR}}^i \mathbf{e} \mathbf{e}^T \mathbf{A}_{R, \text{PCR}}^{iT}] \\ = \sigma^2 \mathbf{V}_R \mathbf{S}_R^{-2} \mathbf{V}_R^T \\ = \sigma^2 \sum_r \frac{1}{s_r^2} \mathbf{v}_r \mathbf{v}_r^T \quad (4.33)$$

²⁰Algebraically, the Moore–Penrose Inverse yields the least-squares solution with a minimum Euclidian norm (the LS solution $\hat{\mathbf{b}}_+ = \mathbf{A}^+ \mathbf{c}$ remains completely in the linear subspace of the rows of \mathbf{A}).

$$\mathbf{A}[\mathbf{w}_1 \mathbf{w}_2 \dots \mathbf{w}_\Omega] = [\mathbf{p}_1 \mathbf{p}_2 \dots \mathbf{p}_\Omega] \begin{bmatrix} l_{p1} & l_{w2} & & & & \\ & l_{p2} & l_{w3} & & & \\ & & \ddots & \ddots & & \\ & & & \ddots & \ddots & \\ & & & & \ddots & l_{w\Omega} \\ & & & & & l_{p\Omega} \end{bmatrix} \quad (4.37b)$$

The first column of Eq. 4.37b yields the left Lanczos vector \mathbf{p}_1

$$l_{p1}\mathbf{p}_1 = \mathbf{A}\mathbf{w}_1 \quad (4.38)$$

where the scaling factor l_{p1} is required for the normalization of the Euclidian length of the vector \mathbf{p}_1 . This is universally valid for l_{pr} and l_{wr} of the following PLS factors with which

$$l_{wr}\mathbf{w}_r = \mathbf{A}^T\mathbf{p}_{r-1} - l_{pr-1}\mathbf{w}_{r-1} \quad (r = 2, 3, \dots, \Omega) \quad (4.39a)$$

$$l_{pr}\mathbf{p}_r = \mathbf{A}\mathbf{w}_r - l_{wr}\mathbf{p}_{r-1} \quad (4.39b)$$

can be iterated. For numerical reasons, a re-orthogonalization of the Lanczos vectors \mathbf{p}_1 and \mathbf{w}_1 against their already calculated predecessor is absolutely necessary in the implementation of the iteration Eq. 4.39 in a computer program [114,115]. In the program that was written for this work, this takes place in a modified Gram-Schmidt algorithm which, e.g. for the right vectors, reads:

$$\text{FOR } v = 1 \text{ TO } (r-1) \text{ DO} \\ l_{wr}\mathbf{w}_r = l_{wr}\mathbf{w}_r - (l_{wr}\mathbf{w}_v^T\mathbf{w}_v)\mathbf{w}_v \quad (4.40)$$

The modified form of the Gram-Schmidt orthogonalization is numerically more efficient than its usual form for which all projections of the vector $l_{wr}\mathbf{w}_r$ onto their predecessors are subtracted simultaneously [116].

The PLS method was suggested for the first time by H. Wold for the solution of regression problems [117,118]. The equivalence of the applied algorithms (see e.g. [119]) to the numerically superior procedures of the bidiagonalization was noticed by the same group already in 1984 [120]. The algebraic details were first described later by Manne, however, and brought to the attention of the users in spectroscopy [113].

For the solution of the regression problem with the PLS algorithm, the following rank reduced inverse is defined:

$$\mathbf{A}_{R,PLS}^i = \mathbf{W}_R\mathbf{B}_R^{-1}\mathbf{P}_R^T \quad (4.41)$$

The index R is to be interpreted similarly as with the "PCR inverses" Eq. 4.30, however, the PLS factors cannot be individually selected from the user due to their connection in the neighboring diagonals of \mathbf{B} ; possible subsets *must* consist of the R first PLS factors. This limitation represents practically an advantage for the search for the best PLS estimator in the Q_{pred} sense. The calculation of the PLS solutions with Eq. 4.41 is simple and requires, e.g. for the use of Eq. 4.34,

$$\begin{aligned} \hat{\mathbf{b}}_{R,PLS} &= \mathbf{A}_{R,PLS}^i\mathbf{c} \\ &= (\mathbf{A}^T\mathbf{A})_{R,PLS}^i\mathbf{A}^T\mathbf{c} \\ &= \mathbf{W}_R(\mathbf{B}_R^T\mathbf{B}_R)^{-1}\mathbf{W}_R^T\mathbf{A}^T\mathbf{c} \end{aligned} \quad (4.42)$$

the inversion of a tridiagonal matrix.

The Lanczos bidiagonalization contains two algebraic characteristics which are important in connection with the definition of the PLS starting vector $\mathbf{w}_1 - \mathbf{A}^T\mathbf{c}$ the application in linear regressions. It can be shown namely that the best subset for the inversion must contain the first sequentially ordered PLS factors (cf. also [121]):

PLS Characteristic 1: The iterative bidiagonalization stops at a total of Ω PLS factors where Ω is the minimum number of (PCR) singular vectors that are required in order to linearly span the PLS starting vector \mathbf{w}_1 ; prediction-irrelevant variations \mathbf{v}_r in the spectra \mathbf{A} for which $\mathbf{v}_r^T\mathbf{w}_1 = 0$ is valid, do not occur in the PLS orthogonalization. Moreover, eigenvectors \mathbf{v}_r which span higher dimensional eigenspaces of $\mathbf{A}^T\mathbf{A}$ (multiple eigenvalues of $\mathbf{A}^T\mathbf{A}$) are rotated such that only a single vector \mathbf{v}_r yields a contribution to \mathbf{w}_1 [102:p. 326].

PLS Characteristic 2: The largest singular values of the iteratively arising bidiagonal matrix \mathbf{B}_R approximate the largest of the Ω prediction-relevant singular values of \mathbf{A} very quickly, i.e. an incomplete bidiagonalization represents the modes with largest variation almost as well as the incomplete SVD decomposition (with the largest singular values) [122,123:Ch. 13].

The second characteristic is the background for many applications of the Lanczos algorithm in numerical mathematics, while the first characteristic is considered disturbing.²² From a statistical standpoint, the combination of both algebraic characteristics is very desired, since with the special choice of the PLS starting vector \mathbf{w}_1 , a coordination of the effects of bias reduction and variance increase for the PLS factors occurs. The first characteristic guarantees that the systematic error of the parameter estimation $\hat{\mathbf{b}}_{R,PLS}$ disappears with the minimum possible number of PLS factors:

$$\begin{aligned} E[\hat{\mathbf{b}}_{R,PLS}] &= E[\mathbf{A}_{R,PLS}^i\mathbf{c}] \\ &= E[(\mathbf{A}^T\mathbf{A})_{R,PLS}^i\mathbf{A}^T\mathbf{c}] \\ &\rightarrow E[(\mathbf{A}^T\mathbf{A})^+\mathbf{A}^T\mathbf{c}] \\ &= E[\mathbf{A}^+\mathbf{c}] = \mathbf{b} \end{aligned} \quad (4.43)$$

where \mathbf{A}^+ is the (unbiased) Moore-Penrose inverse. Due to the second characteristic, the largest singular values of \mathbf{A} are first reproduced during the bias reduction so that only a small variance for the parameter estimation $\hat{\mathbf{b}}_{R,PLS}$ is generated (cf. Eq. 4.33).

Similarly, as with the PCR method, the SVD of the matrix \mathbf{A} is a numerically, more efficient version of the more visible eigenvalue decomposition $\mathbf{A}^T\mathbf{A}$; in this fashion, the PLS method can also be interpreted by the tridiagonalization of the matrix $\mathbf{A}^T\mathbf{A} = \mathbf{W}(\mathbf{B}^T\mathbf{B})\mathbf{W}^T$. This decomposition occurs through a Gram-Schmidt re-orthogonalization of the Ω linearly independent so-called Krylov vectors \mathbf{k}_r [102:Ch. 9]:

$$\mathbf{k}_r = (\mathbf{A}^T\mathbf{A})^{r-1}\mathbf{w}_1 \quad (r = 1, 2, \dots, \Omega) \quad (4.44)$$

The re-orthogonalization of the Krylov vectors

$$\begin{aligned} l_{w2}\mathbf{w}_2 &= (\mathbf{A}^T\mathbf{A})\mathbf{w}_1 - (\mathbf{w}_1^T\mathbf{A}^T\mathbf{A}\mathbf{w}_1)\mathbf{w}_1 \\ l_{w3}\mathbf{w}_3 &= (\mathbf{A}^T\mathbf{A})\mathbf{w}_2 - (\mathbf{w}_2^T\mathbf{A}^T\mathbf{A}\mathbf{w}_2)\mathbf{w}_2 - (\mathbf{w}_1^T\mathbf{A}^T\mathbf{A}\mathbf{w}_2)\mathbf{w}_1 \end{aligned} \quad (4.45)$$

²²The iteration Eq. 4.39 was first suggested as a preliminary step for the SVD diagonalization of large and sparsely filled matrices [124].

$$\begin{aligned}
l_{w_4} w_4 &= (ATA)w_3 - (w_3 TATAw_3)w_3 - (w_2 TATAw_3)w_2 \\
&\vdots \\
\end{aligned} \tag{4.46}$$

is a three-term recursion due to the symmetry of ATA, i.e. due to

$$\begin{aligned}
w_r T A w_{r+k} &= w_{r+k} T A T A w_r \\
&= w_{r+k} T \{ l_{w_{r+1}} w_{r+1} + (w_r T A T A w_r) w_r + (w_{r-1} T A T A w_{r-1}) w_{r-1} \} \\
&= 0 \text{ for } k \geq 2
\end{aligned} \tag{4.47}$$

the re-orthogonalization must be conducted only against both of the last predecessors (Lanczos tridiagonalization [125]). The PLS starting vector can be written with the singular value decomposition of the matrix A:

$$w_1 \sim A T c = V S U T c = \sum_{r=1}^{R_T} s_r (u_r T c) v_r \tag{4.48}$$

A comparison with Eq. 4.32 and Eq. 4.33 shows that with the definition of w_1 , variance effects (factor s_r) as well as bias effects (factor $u_r T c$) are weighted. For a fixed vector w_1 , the remaining PLS vectors are only dependent on the spectral data A. They arise under the consideration of small variance generation, as the iteration Eq. 4.45 visibly shows, since e.g. the vector w_2 through multiplication with ATA mainly points in the direction of the eigenvectors v_r with large eigenvalues s_r^2 (PLS Characteristic 2). However, this is valid only for the eigenvectors v_r that are, at the beginning, "excited" by w_1 : $v_r T w_1 = s_r (u_r T c) \neq 0$ (PLS Characteristic 1).

More modifications were suggested for the vectors w_r . Lorber et al. apply the Krylov series $k_r = \{(ATA)^\gamma\}^{r-1} w_1$ with $\gamma < 1$ in order to increase the influence of the small eigenvalues of ATA in comparison to PLS with $\gamma = 1$ [126]. Frank sets the smaller vector elements in the PLS vectors w_r to zero which corresponds to a regressor selection [127]. Through the additionally introduced degrees of freedom for the user, the time effort increases significantly in the search for the best estimator in the Q_{pred} sense, since from the one-dimensional problem of the determination of PLS factors, a higher dimensional one arises. Through the application of the aforementioned modifications to the data sets in this work, only statistically insignificant improvements in the Q_{pred} value are to be expected; for this reason, we worked exclusively with the original version of the PLS algorithm (Eq. 4.35).

The regression methods (LS, PCR, PLS, etc.) differentiate themselves from the standpoint of the statistical model Eq. 4.13 through the measures which are taken in the estimation of the sample covariance matrix $\hat{C}OV[a]$ for stabilizing the inversion, while the covariance vector $\hat{C}OV[a, c]$

is always estimated with the same procedure²³ (cf. Eq. 4.14 and Eq. 4.16):

$$\begin{aligned}
\hat{b} &= (A^T A)_R^i A^T c = \left((1/M) A^T A \right)_R^i \left((1/M) A^T c \right) \\
&\doteq \hat{C}OV[a]_R^i \hat{C}OV[a, c]
\end{aligned} \tag{4.49}$$

For example, for the LS solution, the exact inverse of $\hat{C}OV[a]$ is calculated such that this method fails for collinear regressors. Collinearities can either be of stochastic nature (noise in A) or they occur through the model generation (selection of regressors, etc.); the latter has the result that also the *true* covariance matrix $COV[a]$ is singular. The Wiener filter for the MSE optimal prediction also exists for this case and can, e.g. be determined with the Moore-Penrose inverses²⁴: $b_{\text{opt},W} = COV[a]^+ COV[a, c]$. The rank of the inverse matrix for the calculation of the Wiener filter can, however, be further reduced in that all eigenvectors of $COV[a]$, which stand perpendicular to the vector $COV[a, c]$, are removed from the calculation. The PLS method exactly follows this strategy of inversion with minimum rank through elimination of the "prediction-irrelevant" signal portions by the first aforementioned algebraic characteristic of the bidiagonalization and through the definition of the PLS starting vector $w_1 \propto \hat{C}OV[a, c]$. The second PLS characteristic induces the sensible series sequence with the occurrence of the PLS factors, since the large variance portions of $\hat{C}OV[a]$ are inverted first. This is important for the transfer from the ideal case with known statistics $COV[a]$ and $COV[a, c]$ to the real problem of a sample population with a finite number of calibration standards, since also in practice, "with PLS, the prediction relevant factors occur first" [21]. This important characteristic is based on the fact that the calibration standards represent a representative sample of the random vectors $[c, a^T]$ of the statistical model Eq. 4.13, i.e. a good approximation of $COV[a, c]$ and $COV[a]$ is allowed (the inverse of the poorly conditioned matrix $COV[a]$, on the contrary, cannot be reliably estimated [128]). In this work, the quality of the various PLS estimators was tested by the prediction of a number of "validation standards" that were not used in the calibration. Depending on the PLS rank, the average squared prediction error typically showed a smooth form with clear minimum (cf. Ch. 4.3) such that the efficient characteristics of the PLS method could be advantageously used in the search for the best Q_{pred} estimator.

In the following paragraphs, a rated comparison between the PLS and the PCR methods is conducted. One PLS advantage is the smaller computer effort of the bidiagonalization (finite algorithm) in comparison to the diagonalization of the regression matrix in PCR (infinite algorithm with convergence). For further consideration, the statistics of second order of the vector $[c, a^T]$ will be assumed to be known and the abbreviations $C \doteq COV[a]$ and $d \doteq COV[a, c]$ will be introduced. The Wiener filter $b_{\text{opt},W} = C^+ d$ yields, according to Eq. 4.15, the optimal MSE prediction error:

$$\begin{aligned}
MSE_{\text{opt}} &= E[(\hat{c}_{\text{opt}} - c)^2] \\
&= E[(a^T b_{\text{opt},W} - c)^2] = \sigma_{cc}^2 - d^T C^+ d
\end{aligned} \tag{4.50}$$

²³Due to the easier notation, it is assumed in Eq. 4.48 that the data A and c represent variations from the average values a_{av} and c_{ac} . For mean-centered data, $(ATA)/M \approx COV[a] + \mu_a \mu_a^T$ as well as $(ATc)/M \approx COV[a, c] + \mu_a \mu_c$ is valid and the Wiener filter reads

$$\hat{c}_{\text{opt},W} = a^T \{ COV[a] + \mu_a \mu_a^T \}^{-1} \{ COV[a, c] + \mu_a \mu_c \}$$

In practice, the data in the inverse regression model are either averaged or a constant regressor is inserted into the matrix A ("columns with ones") so that one can work with the form of the Wiener filter in Eq. 4.14.

²⁴The vector $COV[a, c]$ is located in the picture of the matrix $COV[a]$ so that the existence of a solution b of the equation $COV[a, c] = COV[a]b$ is guaranteed.

The rank reducing inverses of the covariance matrix $\text{COV}[\mathbf{a}]$ for both methods read:

$$\begin{aligned} \mathbf{C}_{R,\text{PLS}}^i &= \mathbf{V}_R \mathbf{S}_R^{-2} \mathbf{V}_R^T \\ &= \mathbf{V}_R (\mathbf{V}_R^T \mathbf{C} \mathbf{V}_R)^{-1} \mathbf{V}_R^T \end{aligned} \quad (4.51)$$

$$\begin{aligned} \mathbf{C}_{R,\text{PLS}}^i &= \mathbf{W}_R (\mathbf{B}_R^T \mathbf{B}_R)^{-1} \mathbf{W}_R^T \\ &= \mathbf{W}_R (\mathbf{W}_R^T \mathbf{C} \mathbf{W}_R)^{-1} \mathbf{W}_R^T \end{aligned} \quad (4.52)$$

The comparison takes place through substitution of Eq. 4.50 and Eq. 4.51 into the expression for the MSE error in Eq. 4.49 with the same inversion ranks R . If the practically-relevant case is assumed that the PCR inverses consist of the R first sequentially occurring modes and eigenvectors, the statement for the superiority of the PLS method can be more precisely expressed:

$$\begin{aligned} \text{MSE}_{\text{PLS}}(R) &= \sigma_{cc}^2 - \mathbf{d}^T \mathbf{W}_R (\mathbf{W}_R^T \mathbf{C} \mathbf{W}_R)^{-1} \mathbf{W}_R^T \mathbf{d} \\ &\leq \sigma_{cc}^2 - \mathbf{d}^T \mathbf{V}_R \mathbf{S}_R^{-2} \mathbf{V}_R^T \mathbf{d} = \text{MSE}_{\text{PCR}}(R) \quad (R = 1, 2, \dots, N) \end{aligned} \quad (4.53)$$

where equality only occurs with the identity $\mathbf{C}_{R,\text{PCR}}^i = \mathbf{C}_{R,\text{PLS}}^i$.

For the case $R = 1$, the inequality in Eq. 4.52 results immediately with

$$\frac{(\mathbf{d}^T \mathbf{v}_1)^2}{s_1^2} \leq \frac{(\mathbf{d}^T \mathbf{w}_1)^2}{\mathbf{w}_1^T \mathbf{C} \mathbf{w}_1} \quad (4.54)$$

due to the proportionality $\mathbf{w}_1 \sim \mathbf{d}$ and due to $s_1^2 = \mathbf{v}_1^T \mathbf{C} \mathbf{v}_1 \geq \mathbf{w}_1^T \mathbf{C} \mathbf{w}_1$; the latter arises from the definitions of the eigenvalues of a symmetric matrix according to the Courant-Fischer Minimax Principle (e.g. [102]). The proof for higher ranks is difficult so that the validity of Eq. 4.52 [129] was postulated using Monte Carlo simulations.

The inversion of the covariance matrix \mathbf{C} in the linear subspace of the R first PLS factors (and of the R first Krylov vectors, cf. Eq. 4.44) fulfills no absolute optimizing criterium regarding the minimization of the MSE error, i.e. there exists no optimal estimator class in the sense of a maximum MSE reduction "per inversion rank". The Wiener filter is optimal for each rank as one can easily see by the inversion with rank $R = 1$ inside the (one-dimensional) subspace $\mathbf{w}_{\text{opt}} = \mathbf{b}_{\text{opt},W} / \|\mathbf{b}_{\text{opt},W}\|$ that is spanned by the Wiener filter $\mathbf{b}_{\text{opt},W} = \mathbf{C}^+ \mathbf{d}$:

$$\begin{aligned} \text{MSE}_{\text{opt}}(R = 1) &= \sigma_{cc}^2 - \mathbf{d}^T \mathbf{w}_{\text{opt}} (\mathbf{w}_{\text{opt}}^T \mathbf{C} \mathbf{w}_{\text{opt}})^{-1} \mathbf{w}_{\text{opt}}^T \mathbf{d} \\ &= \sigma_{cc}^2 - \mathbf{d}^T \mathbf{C}^+ \mathbf{d} = \text{MSE}_{\text{opt}} \end{aligned} \quad (4.55)$$

In practice, $\mathbf{C} = \text{COV}[\mathbf{a}]$ and $\mathbf{d} = \text{COV}[\mathbf{a}, \mathbf{c}]$, are unknown and the Wiener filter must be estimated with a finite number of calibration standards. The inequality in Eq. 4.52 is also relevant in this case, since it is universally valid for cases in which a vector \mathbf{d} lies in the picture of a symmetric matrix \mathbf{C} . In the real case with a finite number of standards, this is true for random data sets \mathbf{A} and \mathbf{c} for the vector $\mathbf{A}^T \mathbf{c}$ and the matrix $\mathbf{A}^T \mathbf{A}$ so that equivalent statements to Eq. 4.52 are also valid in the inverse regression model Eq. 4.17. In this fashion, the sum of the squared error of the calibration fit reduces itself with the application of rank reducing inverses $\hat{\mathbf{b}}_R = \mathbf{A}_R^i \mathbf{c} = (\mathbf{A}^T \mathbf{A})_R^i \mathbf{A}^T \mathbf{c}$

$$\begin{aligned} \text{SSE}(R) &= (\mathbf{c} - \mathbf{A} \hat{\mathbf{b}}_R)^T (\mathbf{c} - \mathbf{A} \hat{\mathbf{b}}_R) \\ &= \mathbf{c}^T \mathbf{c} - \mathbf{c}^T \mathbf{A} (\mathbf{A}^T \mathbf{A})_R^i \mathbf{A}^T \mathbf{c} \end{aligned} \quad (4.56)$$

with increasing rank R for the PLS inverse that is faster than the corresponding PCR inverse. This is valid independent of whether data \mathbf{A} and \mathbf{c} are mean-centered or not. An appropriate statement can also be approximately made for the squared prediction error with new spectra $\hat{\mathbf{c}}_{\text{new}} = \mathbf{A}_{\text{new}} \hat{\mathbf{b}}_R$:

$$Q_{\text{pred}}(R) = (\mathbf{c}_{\text{new}} - \hat{\mathbf{c}}_{\text{new}})^T (\mathbf{c}_{\text{new}} - \hat{\mathbf{c}}_{\text{new}}) \quad (4.57)$$

$$\begin{aligned} &= \mathbf{c}_{\text{new}}^T \mathbf{c}_{\text{new}} - 2 \mathbf{c}_{\text{new}}^T \mathbf{A} (\mathbf{A}^T \mathbf{A})_R^i \mathbf{A}_{\text{new}}^T \mathbf{A}_{\text{new}} (\mathbf{A}^T \mathbf{A})_R^i \mathbf{A}^T \mathbf{c} \\ &\quad + \mathbf{c}_{\text{new}}^T \mathbf{A}_{\text{new}} (\mathbf{A}^T \mathbf{A})_R^i \mathbf{A}^T \mathbf{c} \end{aligned} \quad (4.58)$$

Since the calibration standards \mathbf{A}, \mathbf{c} as well as the prediction standards $\mathbf{A}_{\text{new}}, \mathbf{c}_{\text{new}}$ display a good representation of the random population of the vector $[\mathbf{a}^T, \mathbf{c}]$ in the basic statistical model, the following is approximately valid:

$$\begin{aligned} \text{COV}[\mathbf{a}] &\sim \frac{1}{M} \mathbf{A}^T \mathbf{A} = \frac{1}{M_{\text{new}}} \mathbf{A}_{\text{new}}^T \mathbf{A}_{\text{new}} \\ \text{COV}[\mathbf{a}, \mathbf{c}] &\sim \frac{1}{M} \mathbf{A}^T \mathbf{c} = \frac{1}{M_{\text{new}}} \mathbf{A}_{\text{new}}^T \mathbf{c}_{\text{new}} \end{aligned} \quad (4.59)$$

From Eq. 4.57, it follows:

$$Q_{\text{pred}}(R) = \mathbf{c}_{\text{new}}^T \mathbf{c}_{\text{new}} - \frac{M_{\text{new}}}{M} \mathbf{c}_{\text{new}}^T \mathbf{A} (\mathbf{A}^T \mathbf{A})_R^i \mathbf{A}^T \mathbf{c} \quad (4.60)$$

with which the superiority of the PLS method is not only for the calibration fit, rather also for the prediction quality with the new spectra (cf. Ch. 4.3).

4.3 Practical Model Generation and Examples

In this chapter, practical methods are described which were used in the construction and rating of the inverse regression in this work. In detail, the following will be discussed (1) the selection of the spectral regions for the calibration, (2) the recognition of outliers, and (3) the cross-validation for the robust estimation of the MSE prediction error. All calculations were conducted on an IBM-PC (386AT, 16MB RAM). The programs for this were written in the MATLAB software [130] which uses the numerical algorithms from the proven LINPACK [131] and EISPACK [132] Fortran program libraries in a comfortable interactive programming environment; the graphics were also written under MATLAB. For the data transfer from the FT spectrometer to the IBM-PC, JCAMP-DX files were generated from the IR spectra [133]. This ASCII format was specially defined for the exchange of spectral data and is the industry standard today. Next, the data were transferred to the PC with the public domain software KERMIT and were converted there with a Turbo Pascal program into the MATLAB binary format.

The examples in this chapter are taken from the glucose determination using ATR spectroscopy (see Ch. 5.1) in the mid IR spectral region, since here, the advances of spectroscopic analysis can be particularly well demonstrated. The first results for liquid samples were published already in 1989 for EDTA blood plasma [3] and heparinated whole blood [2].²⁵ Due to the large economic meaning of a reagentless automatic device for liquid blood analysis, improvement of the results

²⁵Heparin and Ethylendiamintetracetic acid (EDTA) were added to prevent coagulation of the blood.

from then with an average prediction error of approximately 20 mg/dl was a further main goal in the current work (Ch. 5) in addition to the non-invasive measurement. In the first study, the whole blood samples of 135 "average" patients without special medical conditions were examined. The measurements were conducted on a Perkin-Elmer 1750 spectrometer with a thermal DTGS detector and a micro-CIRCLE™ ATR cell in the Stuttgarter Katharinen Hospital (see [2], for experimental details). Fig. 4.1a shows an example of the extinction spectrum of blood with a spectral resolution of $\Delta\tilde{\nu} = 8 \text{ cm}^{-1}$. Due to the large absorption coefficient and the high concentration of water (> 90%) in blood, the spectrum of the water absorption with strong bands at 1640 cm^{-1} and below 1000 cm^{-1} dominates. In Fig. 4.1b, the extinction by the non-aqueous components is shown in comparison. The next stronger absorber after water in blood is protein whose signal determines the spectrum after subtraction of the water practically in the entire "biological fingerprint" spectral region represented and displays the prominent bands at 1650 cm^{-1} and 1540 cm^{-1} . The protein bands at 1650 cm^{-1} , which should actually yield the larger extinction signal, are weakened due to the strong water absorption at 1640 cm^{-1} through the "overcompensated" reference measurement.²⁶ The peak of the water absorption at 1640 cm^{-1} is also noticeable through the increase in the extinction noise in Fig. 4.1d. The increase in noise below about 900 cm^{-1} is caused by the absorption of water and the ATR crystal made of zinc selenide which is opaque for wavelengths larger than about $11 \mu\text{m}$. The glucose signal (Fig. 4.1c) is very small in comparison to the total absorption of the blood and is overlaid with the spectra of many other blood substrates such as e.g. various proteins, cholesterol, triglyceride, etc. with individually oscillating concentrations. The largest absorption signals of glucose in the region of about $1200\text{--}950 \text{ cm}^{-1}$ at the concentration of 145 mg/dL are hardly visible and lie only slightly above the noise.

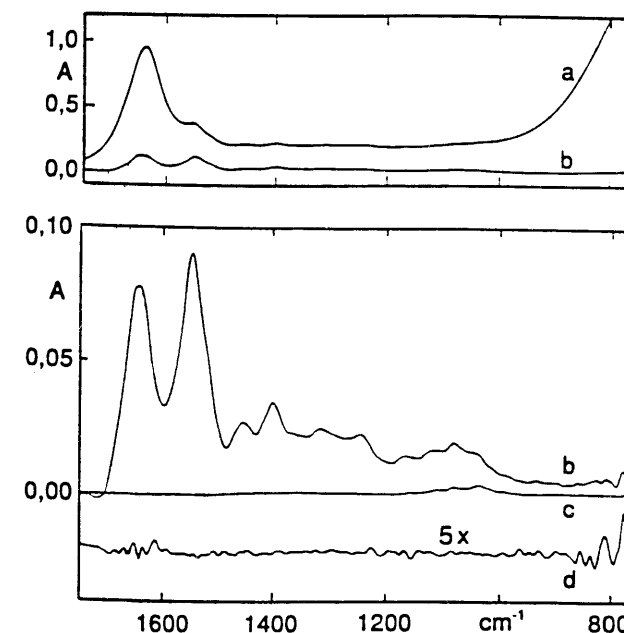


Fig. 4.1: (a) ATR extinction spectrum from whole blood in the mid IR (reference: "empty" ZnSe-crystal); (b) the same blood sample after subtraction of the water signal by the reference measurement with a 0.9% aqueous NaCl solution; (c) spectrum of

²⁶The water concentration of the reference measurement is somewhat larger than the water concentration in blood in which water is displaced by the protein.

glucose in an aqueous solution (concentrations in b and c: 145 mg/dL); (d) extinction noise from the difference of two reference spectra (with offset and enlargement).

1) Selection of the Spectral Region

The selection of the appropriate spectral region for the calibration is an important requirement for a good prediction model. Naturally, the decision depends mainly on the form of the extinction spectrum of the desired component medium, however, other points also influence it. Desired are the spectral regions with high information content (large signal entropy through large and sharp absorption bands) which are overlaid as little as possible by signals of other component media with oscillating concentrations. Moreover, there should be as few as possible disturbances from extinction noise (dependent on the background absorption of water) and from systematic errors (the susceptibility of baseline drifting increases in the region of sharp flanks of the single beam spectrum). For ideal measurement devices and an infinite number of calibration standards, the prediction quality of the model would monotonically increase by increasing the range of the spectral regions in case that through appropriate methods of multivariate statistics, the effect of the variance amplification through collinearity could be suppressed. Actually, one can, in practice, also achieve an improvement in the model quality through the application of spectral regions in which the desired medium is not absorbed, since the multivariate processing methods use quasi an "internal baseline correction". For extremely wide spectral regions, the prediction quality decreases again, however, since the actual signal variation is covered with spectral variations that do not correlate with the desired medium concentration. The selection of a "best" spectral region for a special experiment with a given measurement technology is an exhausting and calculation-intensive, iterative process in which in addition to the results for the optimized estimator in the Q_{pred} sense of the various spectral regions, also spectroscopic knowledge and technical considerations are required.

In addition to the aforementioned *a priori* information, a variable is also used for the selection of the wavenumber regions that can be determined from the measured data. With the mean-centered standards \mathbf{A}_{mc} and \mathbf{c}_{mc} , the least squares solution $\hat{\mathbf{s}}_0$ of the linear system of equations

$$\mathbf{A}_{\text{mc}} = \mathbf{c}_{\text{mc}} \mathbf{s}_0^T + \mathbf{E} \quad (4.61)$$

is used for the definition of the so-called *correlation spectrum* \mathbf{s} [134]:

$$\mathbf{s} \doteq c_{\text{av}} \hat{\mathbf{s}}_0 = c_{\text{av}} \frac{\mathbf{A}_{\text{mc}}^T \mathbf{c}_{\text{mc}}}{\mathbf{C}_{\text{mc}}^T \mathbf{c}_{\text{mc}}} \quad (4.62)$$

The correlation spectrum is quasi the portion of the spectral variation that can be linked to the desired component on average and represents a scaled estimation of $\text{COV}[\mathbf{a}, \mathbf{c}]$ (cf. Eq. 4.16). As one can easily show with the Lambert-Beer Law, Eq. 4.2, the correlation spectrum \mathbf{s} consists of a weighted sum of pure component spectra of all contents components whose concentrations correlate with the desired medium concentration, e.g. glucose [135]. Except for the average glucose spectrum (with the concentration c_{av}), further signals can therefore still appear in \mathbf{s} which, according to the cause for the correlation with glucose, can also be used for the prediction of new spectra. Fig. 4.2 shows an example of such an effect [2]:

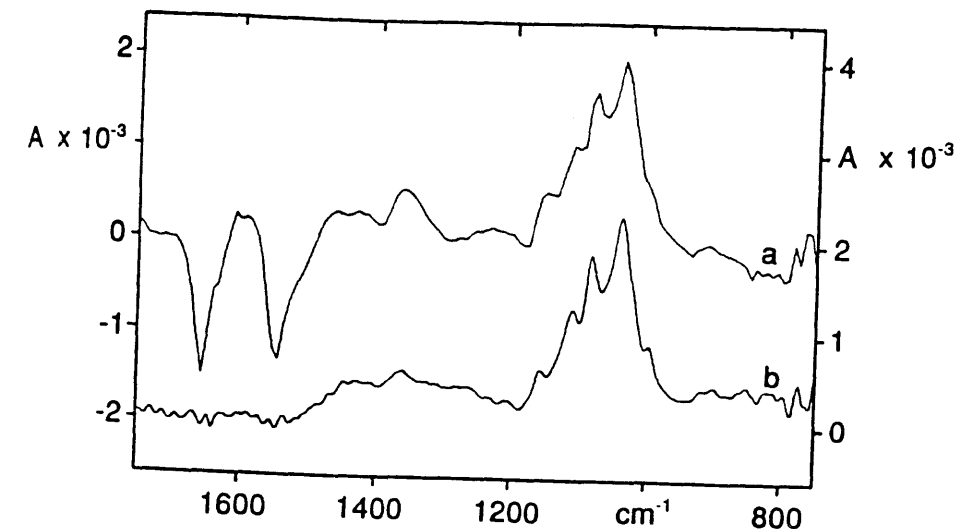


Fig. 4.2: Comparison of a correlation spectrum of glucose in whole blood (a; left coordinate axis) with the ATR absorption spectrum of an aqueous glucose solution (b; right coordinate axis); both spectra are scaled to the average glucose concentration 90 mg/dL of the 135 samples.

The lower curve of Fig. 4.2 shows the pure component spectrum of glucose in the aqueous solution for a physiologically normal concentration of 90 mg/dL. The characteristic 5-banded structure in the region of about 1200–950 cm^{-1} can be clearly seen which is reconstructed very well from the correlation spectrum of glucose (upper curve); the visible differences are based on the different point densities in the graphic representation ((a) 8 cm^{-1} , (b) 1 cm^{-1}). Furthermore, the correlation spectrum in the region around 1600 cm^{-1} also displays a negative correlation with protein and water. An actual "medical" correlation of the reference concentrations of glucose and total protein could be found neither for the Stuttgarter normal patients [3] nor for the diabetic population examined in this work (Ch. 5.2). In order not to influence the prediction of glucose through an apparent correlation, the region 1500–750 cm^{-1} was used for the calibration in whole blood in [2]. (The narrow region 1180–950 cm^{-1} yielded only slightly poorer results for the calibration in blood plasma [3].)

2) Recognition of Outliers

Measurements are termed as outliers that display obvious variations from the "average" behavior of the examined data set and, therefore, do not belong in the standard population for which a prediction model must be constructed in the statistical model, Eq. 4.13. The determination of a standard as an outlier is necessarily a subjective decision that results somewhat *a posteriori* on the basis of the measured sample standards [136]. Outliers can arise either through large measurement errors (e.g. incomplete filling of the cuvettes) or we are dealing with "true" outliers, i.e. with such blood samples that cannot be compared to the other samples for reasons of special medical characteristics.

The processes for identifying outliers are mainly based on the examination of the residuals of the calibration. The following discussion is valid for every regression method with rank reducing inverses, i.e. for the PLS and PCR methods. Therefore, the listing of the method in the index (such as, e.g. in $(ATA)_{R,PLS}^i$) is ignored in the following. The calibration residuals are calculated depending on the inversion rank R as

$$\mathbf{r}(R) = \mathbf{c} - \mathbf{A}\hat{\mathbf{b}}_R = (\mathbf{I} - \mathbf{H}_R)\mathbf{c} \quad \text{where: } \mathbf{H}_R \doteq \mathbf{A}(\mathbf{A}^T\mathbf{A})_R^i\mathbf{A}^T \quad (4.63)$$

The residuals \mathbf{r} are stochastic variables that are dependent on the error vector \mathbf{e} of the inverse regression model $\mathbf{c} = \mathbf{A}\mathbf{b} + \mathbf{e}$; due to $E[\mathbf{e}] = 0$ and $\text{COV}[\mathbf{e}] = \sigma^2\mathbf{I}$ (cf. Eq. 4.17) and the idempotency ($\mathbf{H}_R\mathbf{H}_R = \mathbf{H}_R$) of the matrix \mathbf{H}_R , it follows:

$$\text{COV}[\mathbf{r}(R)] = \sigma^2(\mathbf{I} - \mathbf{H}_R) \quad (4.64)$$

The elements of the residual vector $\mathbf{r}(R)$ in comparison to the error vector \mathbf{e} are correlated and display a variance whose size is dependent on the leverage value $h_{m,R}$ of the standard spectrum \mathbf{a}_m ($m = 1, 2, \dots, M$):

$$h_{m,R} = \mathbf{a}_m^T(\mathbf{A}^T\mathbf{A})_R^i\mathbf{a}_m \quad (4.65)$$

The values $h_{m,R}$ are diagonal elements of the idempotent \mathbf{H}_R with rank R so that it follows:

$$0 \leq h_{m,R} \leq 1 \quad (m = 1, 2, \dots, M) \quad (4.66)$$

$$\text{spur}(\mathbf{H}_R) = \sum_{m=1}^M h_{m,R} = R \quad (4.67)$$

For the mean-centered spectra \mathbf{A}_{mc} , the leverage values $h_{m,R}$ correspond to the Mahalanobis distances of the spectra \mathbf{a}_m to the average value of all M spectra measured in the linear subspace of the R orthogonal factors chosen for the inversion. The Mahalanobis distance is the relevant norm for measuring the separation of two random vectors and agrees with the Euclidian norm only in cases of uncorrelated vector elements with constant variance (further details in e.g. [94]). Calibration standards, whose IR spectra display a significantly large distance to the average spectra, apply a large influence with a large leverage value on the calibration. As a practical limiting value, which when surpassed requires a more extensive consideration of the spectrum, the doubled average value of the leverage value $h_{lim,R} = 2R/M$ (cf. Eq. 4.65) can be used [137].

The variance σ^2 of the error vector \mathbf{e} ($\text{COV}[\mathbf{e}] = \sigma^2\mathbf{I}$) is estimated²⁷ with

$$\hat{\sigma}(R)^2 = \frac{\mathbf{r}(R)^T\mathbf{r}(R)}{M-R} = \frac{\sum_{m=1}^M r_{m,R}^2}{M-R} \quad (4.68)$$

The $\hat{\sigma}$ statistic — also called the standard of the regression error — is for the rating of the MSE prediction quality of poorly conditioned regression systems [138].

²⁷If the mean-centered data \mathbf{A} and \mathbf{c} are used in the regression or if a constant term ("columns with ones") is added to the matrix \mathbf{A} , the number of "degrees of freedom for the regression" is increased to $R+1$ such that one uses the term $M-R-1$ in the denominator of Eq. 4.66. With this convention, it can be shown that $\hat{\sigma}^2$ in Eq. 4.66 represents an unbiased estimation of σ^2 for the LS estimator with maximum inversion rank $R = \text{rg}(\mathbf{A})$ [110:p. 84].

In order to better judge the absolute size of the calibration residuals, the studentized residuals

$$t_{m,R} \doteq \frac{r_{m,R}}{\hat{\sigma}\sqrt{1-h_{m,R}}} \quad (4.69)$$

are used which are scaled to unit variance. With normally distributed error vectors \mathbf{e} , the $t_{m,R}$ of a t -distribution results. For the larger calibration populations that were used in this work ($M > 100$), the standards could be seen as outliers with a residuum $t_{m,R} > 3$, and values $t_{m,R} > 2$ should excite attention [110:p. 253].

Large leverage values $h_{m,R}$ suggest that samples stand out of the IR spectra, while large residuals $t_{m,R}$ can also occur through errors in the clinical-chemical reference determination of the concentrations. A combined rating of both effects is achieved in the Cook distance scale

$$D_{m,R} \doteq \frac{t_{m,R}^2}{R} \frac{h_{m,R}}{1-h_{m,R}} \quad (4.70)$$

which statistically weights the changes in the full calibration result with the removal of the m th standard of the calibration. The value of $D_{m,R}$ corresponds quasi to the Mahalanobis norm of this change in the vector space of the result vector $\hat{\mathbf{b}}_R = \mathbf{A}_R^i\mathbf{c}$ and can be checked for significance with an F distribution with R and $M-R$ degrees of freedom [139]. A more practical method is the representation of all values $D_{m,R}$ ($m = 1, 2, \dots, M$) in the form of a cumulative distribution function: standards with outstandingly high values of $h_{m,R}$ and/or $t_{m,R}$ can be identified "at a glance" by the user.

In the statistical literature, a large number of further numerical and graphical procedures for the recognition of outliers are given (see [136] and references there). However, as Weisberg determined, the three statistics $h_{m,R}$, $t_{m,R}$, and $D_{m,R}$ yield the entire information that is required for the analysis of the influence of individual outliers [140]. For the large data sets of this work, the statement is valid also for the recognition of more outliers simultaneously (for procedures for small data sets, see e.g. [141]).

In this work, mainly the Cook distance scale was used for outlier recognition, since significant values of $D_{m,R}$ influence the full calibration result. The leverage values $h_{m,R}$ were used only in connection with the protocol notes of the spectroscopic experiments in which possible disturbances of the IR measurement were noted (e.g. filling of the detector dewar with liquid nitrogen). Such standards for which the studentized residuum $t_{m,R}$ was solely significant are only to be eliminated from the calibration with great care in order not to estimate the quality of the prediction model too optimistically. Important is that the classification of the standard as an outlier is dependent on the spectral region that was used for the calibration and on the number R of orthogonal factors for the inversion; the larger the rank R , the sooner a spectrum \mathbf{a}_m is disturbed by measurement errors inside the R subspace for the inversion. The number of standards that were classified as outliers is always given with the results of this work.

3) Cross-Validation of the Prediction Quality

For the cross-validation, the data set \mathbf{A}, \mathbf{c} is divided into two subsets that are statistically independent of each other $\mathbf{A}_1, \mathbf{c}_1$ with M_1 standards for the calibration and $\mathbf{A}_2, \mathbf{c}_2$ with M_2 standards for the validation. The prediction quality of a calibration $\hat{\mathbf{b}}_1 = \mathbf{c}_1$ with the first data set must

be checked with the validation set. The average squared prediction error is estimated with the so-called PRESS statistic (prediction error sum of squares):

$$\text{PRESS} = \frac{(\mathbf{c}_2 - \mathbf{A}_2 \hat{\mathbf{b}}_1)^T (\mathbf{c}_2 - \mathbf{A}_2 \hat{\mathbf{b}}_1)}{M_2} \quad (4.71)$$

The advantage of cross-validation is the independence of all assumptions about the statistical characteristics of the models through the simulation of the prediction quality under "real conditions" [142]. The disadvantage lies in the exhaustive measurement of a sufficiently high number of validation standards. PRESS estimates simultaneously the bias and the variance of the prediction error. According to a useful rule of thumb for "not altogether asymmetric distributions", about 30–100 standards are required for a satisfactory estimation of both error portions [143:p. 202]. In order to avoid the measurement of such a large number of additional standards, it is typical in such spectroscopic applications to remove a few small data sets one after each other from the calibration population and to use these for the validations. In the extreme case, an individual standard is removed and predicted with the regression result of the corresponding *reduced* model

$$\mathbf{c}_{(m)} = \mathbf{A}_{(m)} \mathbf{b} + \mathbf{e}_{(m)} \quad (m = 1, 2, \dots, M) \quad (4.72)$$

Here, the index (m) refers to the data set that was reduced by the m th standard. In this special procedure, the PRESS was calculated as

$$\text{PRESS}(R) = \frac{1}{M} \sum_{m=1}^M (c_m - \mathbf{a}_m^T \hat{\mathbf{b}}_{(m),R})^2 = \frac{1}{M} \sum_{m=1}^M r_{(m),R}^2 \quad (4.73)$$

where $r_{(m),R}$ is the so-called *independent prediction error* of the standard \mathbf{a}_m ; this arises in the prediction with the parameter vector $\hat{\mathbf{b}}_{(m),R}$ which remains for the inversion with rank R in the *reduced* model, Eq. 4.70. The application of Eq. 4.71 requires that the reduced models are similar to each other and to the complete model (with all M standards); in practice, this must be verified in order to remove an outlier from the cross-validation and from the full calibration. Naturally, more standards can also be simultaneously removed and predicted where the selection of the standards for the validation can occur randomly; in this so-called bootstrapping, each sample can be multiply used for the validation through which the "noise" of the PRESS statistic is reduced [144]. For the regressions in this work, over 100 standards were available such that a bootstrapping could be neglected. The strategy for cross-validation from Eq. 4.71 "Every standard individually every time" yielded good approximations of the true MSE prediction error and was applied regularly; in a few specially named cases, more standards were also simultaneously predicted ("Every standard one time in a group") in order to test the robustness of the regression models.

In the cross-validation, the effective use of the data set is purchased with large computer effort. Therefore, methods have been examined for quite some time now in order to computationally simplify a complete new calibration and removal of the standard [145]. The goal is not to newly conduct the orthogonalization (bidiagonalization with PCR, Lanczos bidiagonalization with PLS) for every matrix $\mathbf{A}_{(m)}$, rather to calculate the independent prediction error

$$\mathbf{r}_{(m),R} \doteq \mathbf{c}_m - \mathbf{a}_m^T (\mathbf{A}_{(m)}^T \mathbf{A}_{(m)})_R^i \mathbf{A}_{(m)}^T \mathbf{c}_{(m)} \quad (4.74)$$

through an "update" of the calibration results with the complete matrix \mathbf{A} . This approximately succeeds through application of the well-known Sherman–Morrison formula [102]

$$(\mathbf{X} + \mathbf{g}\mathbf{f}^T)^{-1} = \mathbf{X}^{-1} - \frac{\mathbf{X}^{-1}\mathbf{g}\mathbf{f}^T\mathbf{X}^{-1}}{1 + \mathbf{f}^T\mathbf{X}^{-1}\mathbf{g}} \quad (4.75)$$

where \mathbf{X} is a nonsingular (quadratic) matrix, \mathbf{g} and \mathbf{f} are vectors of proper dimension, and $1 + \mathbf{f}^T\mathbf{X}^{-1}\mathbf{g} \neq 0$ must be valid. If the formula Eq. 4.73 is applied to the symmetric matrix

$$\mathbf{A}_{(m)}^T \mathbf{A}_{(m)} = \mathbf{A}^T \mathbf{A} - \mathbf{a}_m \mathbf{a}_m^T \quad (4.76)$$

the requirement of nonsingularity in $\mathbf{A}^T \mathbf{A}$ is no longer necessary when instead of the exact inverses, the Moore–Penrose inverses are used (see Corollary 3.1.1 in [103]):

$$(\mathbf{A}_{(m)}^T \mathbf{A}_{(m)})^+ = (\mathbf{A}^T \mathbf{A})^+ + \frac{(\mathbf{A}^T \mathbf{A})^+ \mathbf{a}_m \mathbf{a}_m^T (\mathbf{A}^T \mathbf{A})^+}{1 - h_{m,+}} \quad (4.77)$$

$$\text{where: } h_{m,+} \doteq \mathbf{a}_m^T (\mathbf{A}^T \mathbf{A})^+ \mathbf{a}_m$$

An extension of Eq. 4.75 to rank reduced inverses $(\mathbf{A}_{(m)}^T \mathbf{A}_{(m)})_R^i$ with $R < R_T = \text{rg}(\mathbf{A}) \equiv \text{rg}(\mathbf{A}^T \mathbf{A})$ is not possible, since two corresponding mode subgroups of the orthogonal decompositions of $\mathbf{A}_{(m)}^T \mathbf{A}_{(m)}$ and $\mathbf{A}^T \mathbf{A}$ do not exactly span the same spectral subspace, although the differences are small for large representative data sets. If Eq. 4.75 is used with rank reduced inverses, these inverses are given quasi a "Moore–Penrose status", i.e. the portion of the data variation $(\mathbf{A}^T \mathbf{A})^+ = (\mathbf{A}^T \mathbf{A})_R^i + (\mathbf{A}^T \mathbf{A})_{R_T-R}^i$, which is not contained in the $(R_T - R)$ unselected PCR modes or PLS factors, is *implicitly* set to zero:

$$(\tilde{\mathbf{A}}_{(m)}^T \tilde{\mathbf{A}}_{(m)})_R^i = (\mathbf{A}^T \mathbf{A})_R^i + \frac{(\mathbf{A}^T \mathbf{A})_R^i \mathbf{a}_m \mathbf{a}_m^T (\mathbf{A}^T \mathbf{A})_R^i}{1 - h_{m,R}} \quad (4.78)$$

$$\text{where: } h_{m,R} \doteq \mathbf{a}_m^T (\mathbf{A}^T \mathbf{A})_R^i \mathbf{a}_m$$

Here, the tilde over $\tilde{\mathbf{A}}_{(m)}$ means the projection of the spectra (rows of $\mathbf{A}_{(m)}$) onto the linear subspace of the R orthogonal factors of the *complete* calibration matrix \mathbf{A} (with all M standards!) that were selected by the user. The eigenvectors of $(\tilde{\mathbf{A}}_{(m)}^T \tilde{\mathbf{A}}_{(m)})_R^i$ are rotated as compared to the eigenvectors of $(\mathbf{A}^T \mathbf{A})_R^i$, however, they span the same subspace. Therefore, the calculation of the inverse matrix actually desired $(\mathbf{A}_{(m)}^T \mathbf{A}_{(m)})_R^i$ takes place "only" in exactly the linear subspace in Eq. 4.76 that is commonly spanned by the eigenvectors of $(\mathbf{A}^T \mathbf{A})_R^i$ and $(\mathbf{A}_{(m)}^T \mathbf{A}_{(m)})_R^i$; for a rotation of both R -dimensional eigenspaces against each other in the N -dimensional spectral vector space, Eq. 4.76 yields the approximation $(\tilde{\mathbf{A}}_{(m)}^T \tilde{\mathbf{A}}_{(m)})_R^i$ instead of $(\mathbf{A}_{(m)}^T \mathbf{A}_{(m)})_R^i$. Especially, the eigenspace of $(\mathbf{A}_{(m)}^T \mathbf{A}_{(m)})_R^i$ which is orthogonal to that of $(\mathbf{A}^T \mathbf{A})_R^i$ is not inverted by Eq. 4.76. This is only possible through a complete new orthogonalization of $\mathbf{A}_{(m)}$. The quality of the approximation in Eq. 4.76 is dependent on the number of standards, the degree of collinearity of matrix \mathbf{A} , and from the orthogonalization method used, as a few examples for PLS and PCR will still show.

Through substitution of Eq. 4.76 into Eq. 4.72, the independent prediction error $r_{(m),R}$ approximately becomes the simple function of the calibration residuum $\mathbf{r}_{m,R}$:

$$\begin{aligned} \tilde{r}_{(m),R} &\doteq \mathbf{c}_m - \mathbf{a}_m^T (\tilde{\mathbf{A}}_{(m)}^T \tilde{\mathbf{A}}_{(m)})_R^i \mathbf{A}_{(m)}^T \mathbf{c}_{(m)} \\ &= \frac{\mathbf{r}_{m,R}}{1 - h_{m,R}} \end{aligned} \quad (4.79)$$

This formula represents an enormous simplification for the calculation of the cross-validation, since the orthogonalization of the spectral data must only be conducted one time for the complete data set. For the Moore–Penrose inversion with maximum rank $R = R_T$, the projection operator (the tilde) becomes meaningless; in this case, Eq. 4.77 yields exactly the desired result for the independent prediction error. The PRESS statistic was suggested by Allen in 1971 after he derived Eq. 4.77 for the LS solution with exact inverses [145]. For rank reduced inverses with $R < \text{rg}(\mathbf{A})$, Eq. 4.77 yields the so-called “leverage” approximation

$$\text{PRESS}_{\text{lev}}(R) = \frac{1}{M} \sum_{m=1}^M \left(\frac{\tau_{m,R}}{1 - h_{m,R}} \right)^2 \quad (4.80)$$

which best approximates the true PRESS value (Eq. 4.71) in the region of very low and very high inversion ranks: with low PCR and PLS ranks, large signal variations are inverted which are hardly influenced by the removal of an individual standard from the calibration, and for high inversion ranks, the projection in Eq. 4.77 increasingly loses meaning. After the orthogonalization, the leverage values $h_{m,R}$ can be kept practically without additional computer effort as the diagonal elements of the matrix

$$\begin{aligned} \mathbf{H}_R &= \mathbf{A}(\mathbf{A}^T \mathbf{A})_R^{-1} \mathbf{A}^T \\ &= \mathbf{U}_R \mathbf{U}_R^T \quad (\text{for PCR}) \\ &= \mathbf{P}_R \mathbf{P}_R^T \quad (\text{for PLS}) \end{aligned} \quad (4.81)$$

The $\text{PRESS}_{\text{lev}}$ statistic is also simple to calculate as the standard deviation $\hat{\sigma}$ of the regression (cf. Eq. 4.66). In comparison, however, $\text{PRESS}_{\text{lev}}$ weights the individual residuals $\tau_{m,R}$ differently and represents a much better estimation of the MSE prediction error.

As a result of the non-optimal measurement conditions in the Stuttgarter Katharinen Hospital, a total of eight standards had to be removed as outliers from the population examined [2]. The results of the glucose determination for the remaining 127 whole blood samples are shown in Fig. 4.3 [146] for the PLS method and for the PCR method with the selection strategy of the modes “from top down” in dependence on the inversion rank R . The solid lines in Fig. 4.3a show the $\text{PRESS}^{1/2}$ values for both methods as the important result. All regressions of this work were conducted with averaged data \mathbf{A}_{m_c} and \mathbf{c}_{m_c} such that the $\text{PRESS}^{1/2}$ curves begin at the “inversion rank” $R = 0$; this value arises through the prediction of the validation standards by the average value of the glucose concentration of the corresponding reduced data set, i.e. the IR spectra with $R = 0$ do not enter the prediction. In the patient population examined, there were only a few diabetics (90% of all values in the region < 200 mg/dl) such that the 127 glucose references displayed a physiologically normal mean value of $\bar{c}_{\text{pop}} = 90.4$ mg/dl and a standard deviation (biological oscillation width) of ca. $\hat{\sigma}_{\text{pop}} = 45$ mg/dl. The $\text{PRESS}^{1/2}$ statistic at $R = 0$ represents a slightly pessimistic estimation of $\hat{\sigma}_{\text{pop}}$.²⁸ The $\text{PRESS}^{1/2}$ values of the PLS method improve very quickly with increasing inversion

²⁸For example, the following is valid for the prediction of individual standards:

$$\text{PRESS}(R=0) = \frac{1}{M} \sum_{m=1}^M \left(c_m - \frac{M \bar{c}_{\text{pop}} - c_m}{M-1} \right)^2 = \frac{M}{(M-1)^2} \sum_{m=1}^M (c_m - \bar{c}_{\text{pop}})^2 = \frac{M}{M-1} \hat{\sigma}_{\text{pop}}^2$$

rank, and the best PLS estimator at $R_{\text{opt}} = 16$ yields an average squared prediction error of 19.8 mg/dl. For the PLS factors with $R > 16$, the variance increase overrides the effect of the bias decrease such that the total error increases again. The best PCR estimator produces a similar prediction error, however, more than double so many inversion ranks than with PLS are required. Moreover, the $\text{PRESS}^{1/2}$ curve of the PCR method is more “noisy” than that of PLS such that the determination of the best rank causes problems. As Fig. 4.3a shows, a somewhat lower PLS rank than $R = 16$ can be also selected for a nearly optimal prediction. Generally, the prediction error should be minimized with a number of factors that is as small as possible, since firstly, the degree of the overdetermination M/R of the regression increases and a larger statistical certainty of the calibration results is achieved, and secondly, the susceptibility to outliers sinks. The advantages of the PLS method are evident in Eq. 4.3a.

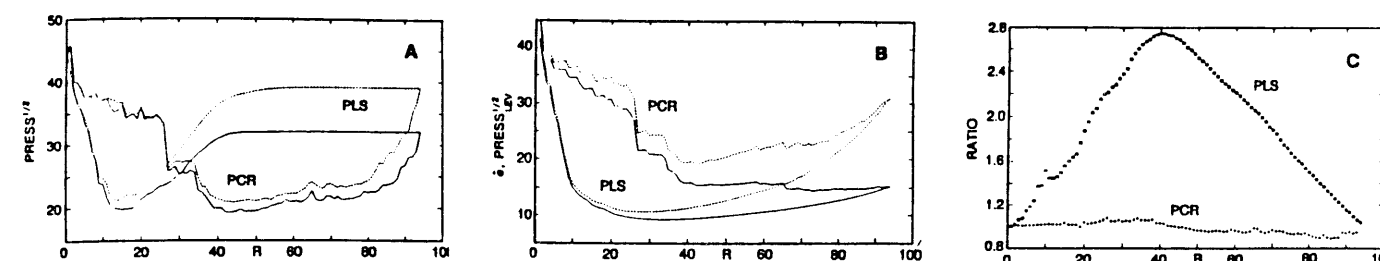


Fig. 4.3: Results of the PLS and PCR calibration of glucose in whole blood with 127 ATR whole blood spectra ($\bar{c}_{\text{pop}} = 90.4$ mg/dl) in the spectral region 1500–756/ $\Delta\bar{\nu} = 8$ cm^{-1} ($N = 94$). A: $\text{PRESS}^{1/2}$ values [mg/dl] for the prediction of the standards individually (—) and in groups of 10 (---); B: Standard deviation of the regression $\hat{\sigma}$ (—) and leverage approximation $\text{PRESS}_{\text{lev}}^{1/2}$ (---) in [mg/dl]; C: Ratio $\text{PRESS}^{1/2} / \text{PRESS}_{\text{lev}}^{1/2}$.

The average prediction error of the PLS estimator reaches a constant plateau for about $R > 40$, i.e. all information in the spectra that is correlated with glucose is “used” and the $\text{PRESS}^{1/2}$ value does not change up to the maximum rank $R_{\text{max}} = N = 94$; at this point, the PLS and the PCR curves re-unite themselves to form the LS result. Equivalent statements are also valid for the dashed curves in Fig. 4.3a for which ten standards were simultaneously removed from the calibration and independently predicted. The effect on the best $\text{PRESS}^{1/2}$ is approximately the same for both methods.

Fig. 4.3b shows the standard deviation for the regression and the leverage approximation of the $\text{PRESS}^{1/2}$ curves. The $\hat{\sigma}$ statistic cannot be used to estimate the independent prediction error, since generally, values that are too optimistic are shown for too large an inversion rank. In

order to be able to better judge the $PRESS_{lev}^{1/2}$ approximation, Fig. 4.3c shows the ratio to the exact $PRESS^{1/2}$ values. Since $PRESS_{lev}^{1/2}$ represents a good approximation for the PCR method, systematic variations in the form of a triangle arise for the PLS method. The form of this triangle can be determined with the results of the PLS calibration (with all M standards) [129]. The position of the triangle peak is located at the beginning of the $PRESS^{1/2}$ plateau (cf. Fig. 4.3a) at a rank R_{plat} , which, when surpassed, also does not change the quality of the PLS calibration fit: $SSE(R) = r(R)Tr(R) = \text{const.}$ for $R \geq R_{plat}$ (see [129] for details). The height of the triangle h_D has been empirically given:

$$h_D = \frac{M - R_{plat}}{M - R_{max}} \quad (4.82)$$

The relative error of the triangle-corrected $PRESS_{lev}^{1/2}$ values is smaller than about 10% for regressions with $M \geq 1.5R_{plat}$ [129]. Further examples of the behavior in Fig. 4.3c can be found in [146] where the procedure for underdetermined systems of equations with $M < N$ is also discussed.

The triangle-corrected $PRESS_{lev}^{1/2}$ statistic can be used advantageously in the iterative determination of the best spectral region for a PLS calibration, since in this calculation-intensive application, eventual approximation errors are outweighed by the savings in computer time. The optimized results introduced in Ch. 5 and Ch. 6 are all $PRESS^{1/2}$ curves that were calculated according exactly to Eq. 4.71.

5 Procedures for Liquid Blood

In this chapter, the possible technical procedures for a spectroscopic measurement of biotic liquid samples and the results achieved in the framework of this work will be described. The realization of an automatic laboratory device without the use of chemicals for routine analysis will be discussed. The results for liquid blood in the near IR are, furthermore, important for the estimation of feasibility for a non-invasive glucose measurement through the skin.

5.1 Problems of Biotic Liquid Samples

For some time now, IR spectroscopy has been used in clinical chemistry (see the recent overview in [147]). Important application examples are the monitoring of respiratory gases, e.g. in anesthesiology, and the quantitative analysis of kidney stones [148]. The main problem in the IR spectroscopic examination of biotic fluids is the large water content of the samples. In Fig. 5.1, the absorption coefficient of water is shown versus a broad optical spectral region (from [21]).

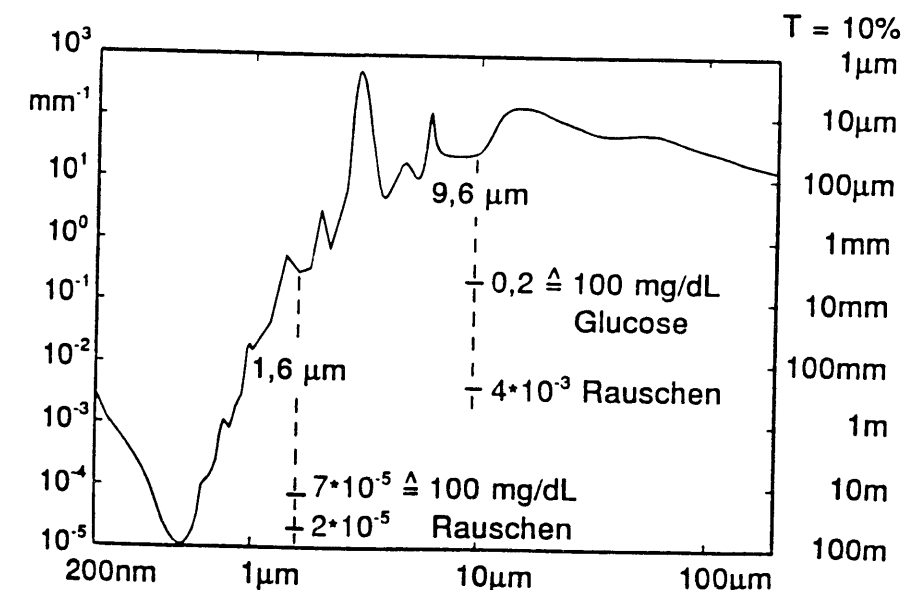


Fig. 5.1: Absorption coefficient of water (right ordinate: thickness of a water layer with transmission $T = 10\%$) as well as the order of magnitude of the largest glucose band at $\lambda = 1.6 \mu\text{m}$ and $\lambda = 9.6 \mu\text{m}$ and the noise achieved in this work (cf. Fig. 5.9 and Fig. 5.15).

The minimum of the water absorption occurs in the visible range at about 500 nm. At the transition into the IR spectral region, the water absorption increases sharply. Glucose signals are located in the mid IR mainly in the region of $1200\text{--}950 \text{ cm}^{-1}$ ($8.3\text{--}10.5 \mu\text{m}$) and in the near IR in the region of $6600\text{--}6000 \text{ cm}^{-1}$ ($1.51\text{--}1.67 \mu\text{m}$). For optimizing the S/N ratio of the extinction, the sample layer thickness in a transmission experiment must be chosen so that around 20–30% of the radiation power goes through the sample and falls onto the detector (cf. Fig. 3.10 and the corresponding text). As suggested by Fig. 5.1, thicknesses on the order of magnitude of 1 mm

must be used for an optimal measurement of the glucose signals in the near IR ($1.6 \mu\text{m}$), while for measurements in the mid IR ($9.6 \mu\text{m}$), cuvettes with thicknesses in the region of $10 \mu\text{m}$ are required. With decreasing thickness, the difficulties in the filling and cleaning of the measurement cuvettes increases, and problems occur for thicknesses in the μm region through interferences (see e.g. [149,89]). The measurement of biotic liquid samples in transmission is problematic in the mid IR and is not appropriate for the routine operation of an automatic analysis device with high sample volume rates.

In addition to transmission, various other measurement techniques are known in IR spectroscopy for liquid samples. Fig. 5.2 gives an overview. In the transfection procedure, the sample liquid is brought onto a mirrored background and quasi measured in "doubled" transmission. Here, it is assumed that the Fresnel reflection from the sample surface area is negligible. For small thicknesses, the same problems occur with cleaning and reproducible filling as with the transmission measurement such that this procedure is also not appropriate for liquid blood analysis. In the procedure of diffuse reflection (Fig. 5.2b), the reproducibility of the filling is less critical, since the radiation that is detected is diffusely reflected through scattering from inhomogeneities in the sample; in the quantitative description of this effect, the absorption coefficient of the sample as well as the sample specific parameters of the scattering are necessary (details in Ch. 6). The measurement technique of diffuse reflection is not technically challenging and is used routinely for on-line measurements, e.g. for process monitoring in the food industry [150]. However, the procedure is not appropriate for liquid blood analysis in the mid IR, since practically no diffuse return radiation from the sample takes place due to the high water absorption. At this point, it should be mentioned that one-way cuvettes could also be used for the routine operation of a future automatic laboratory device which are properly disposed of after use. Here, small plates with a rough, diffusely reflecting surface area are imaginable as a user-friendly and inexpensive variation (e.g. sandpaper steamed with gold with an average kernel size in the μm region). A sufficiently reproducible filling would be possible using adhesion or simply by placing a drop of the sample onto the surface area and washing off the excess. This measurement represents quasi a combination of procedures (a) and (b) in Fig. 5.2 in the form of a "diffuse transfection".

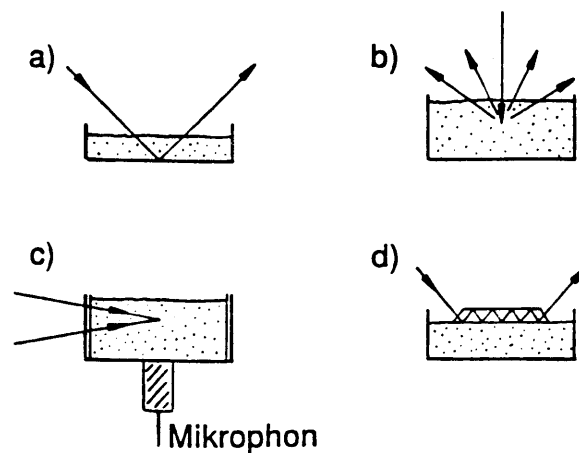


Fig. 5.2: Measurement technique for liquid samples: transfection (a), diffuse reflection (b), photo-acoustics (c), and attenuated total reflection (d).

In photo-acoustic spectroscopy (Fig. 5.2c), the heating and thermal expansion of the sample at the location of radiation absorption is used. Through a temporal modulation of the radiated IR power, a pressure wave occurs in the sample which can be detected by a microphone. The amplitude of the pressure wave is dependent on the optical absorption coefficient as well as further macroscopic parameters of the sample (e.g. heat capacity, thermal expansion coefficient, speed of sound). The entire measurement cuvette must be optimized for a special application purpose through adjustment of the mechanical wave resistances. In order to reduce the effort of the measurement, air-tight sealable cuvettes are used for which the mechanical wave in the sample excites a volume of gas that lies over it into oscillation which can be detected with a microphone. A disadvantage of the gas-microphone cells is the low sensitivity in comparison to cells with piezoelectric sensors in contact with the sample. The exact quantitative description of the measurement effect is complicated so that usually, simple one-dimensional models are used ([151], see also [152] and the literature cited there).

Photo-acoustic spectra of human blood have been published for the visible spectral region [153]. The advantage of this measurement technology is a general insensitivity to diffuse scattering in the sample, which e.g. can provide for enormous problems in a transmission measurement. In the mid IR, a saturation of the photo-acoustic effect is predicted by the theory due to the large water absorption, i.e. the measured signal should display no dependence on the absorption coefficient of the sample [151: p. 106]. However, a measurement with a pulsed CO_2 laser was reported recently (pulse length $\sim 1 \mu\text{s}$; energy in the sample $< 10 \mu\text{J}$) in which a correlation of the photo-acoustic signal in the region of the maximum glucose bands between $9.564 \mu\text{m}$ and $9.694 \mu\text{m}$ (8 laser lines) with the glucose concentration of a whole blood sample could be verified which, through dotation, was available at three different concentrations (217, 278, 406 mg/dL) [154]. A transmission cuvette with a 10 mm thickness and zinc selenide windows was used as the measurement cell into which the laser was focused. A piezoelectric sensor was placed on the bottom of the cuvette about 8 mm under the laser focus. A possible explanation for the measurement effect is given as the fact that the photo-acoustic signal in cases of optically "thicker" samples is not proportional to the absorbed radiation power [W], rather to the absorbed radiation density [W/m^3]. The measurement results for the whole blood sample of a second patient showed that a person-independent calibration was not possible inside the narrow frequency region over which the laser was tuned (ca. $1046\text{--}1032 \text{ cm}^{-1}$). Photo-acoustic spectroscopy of aqueous solutions in the mid IR is still in the stadium of fundamental research today. The experimental effort of the measurements is not insignificant. In this work, photo-acoustics were, therefore, not examined further.

The procedure of Attenuated Total Reflection (ATR) shown in Fig. 5.2d is especially appropriate for the examination of liquid samples with small thicknesses. Here, the IR radiation is fed through a crystal with high index of refraction ("light guider") whose total reflecting surface area is in contact with the sample. ATR measurements can be described well with a simple physical model [155]. The effective layer thickness is determined mostly by the indices of refraction of the crystal and sample as well as by the reflection angle and the number of total reflections. This guarantees various technical possibilities for the realization of thicknesses in the region around $10 \mu\text{m}$. For measurements in aqueous solutions, a larger range of accessories has been commercially available for years which can be directly used in the sample chamber of FT spectrometers. Problems with interferences do not occur in the ATR measurements. The ATR method has the largest chances for use in the spectroscopic routine analysis of blood in the mid IR and was also used in this work.

A second problem in the measurement of biotic liquid samples, is the bio-compatibility of the materials used. Difficulties occur with the depositions on all surface areas that come in contact with the sample. Especially critical are the protein adsorptions on the ATR crystal, since, as a result, systematic changes in the measurement conditions can arise (e.g. [156,157]). In older studies for the determination of glucose in whole blood as well as blood plasma, the ZnSe crystal had to be removed after 30–40 sample measurements and mechanically cleaned (polished with CeO₂ powder) [2,3]. Such a procedure is not practical in routine analysis; additionally, the reproducibility of the measurement after re-inserting the crystal can be degraded by changes in the optical alignment of the crystal [158]. For improvement of the prediction certainty, the suppression of protein adsorption through the introduction of an appropriate cleaning cycle was, therefore, a further goal of the ATR experiments of this work.

For a non-invasive measurement through the skin, the IR radiation must go through at least the 10–15 μm thick outer keratinized, calloused skin layer (cf. Ch. 6.1). Here, possibilities are only available in the visible and near IR region. For examining the information content of the NIR spectra of liquid blood, the region of the oscillation overtone signals of glucose around 1.6 μm were used in this work. The measurements were conducted in transmission for a layer thickness of 1 mm.

5.2 Data Set for the Liquid Blood Analysis

The data set examined in this work consisted of EDTA blood plasma samples from 126 different patients at the Diabetes Research Institute, Duesseldorf. The samples were collected over a time frame of about 6 weeks from stationary and ambulant patients (diabetics as well as those suspected to have diabetes). The application of blood plasma instead of whole blood was justified by the results of earlier studies [2,3] in which an extensive identity of the spectra in the mid IR was determined. The automatic analysis devices used in Duesseldorf require blood plasma for the reference determination of the blood substrates in the framework of the routine analysis. Blood plasma is the usually clear liquid which remains after removal of the cellular blood contents (red and white blood cells and blood platelets) through centrifuging. In plasma, the average concentrations are somewhat increased in comparison to whole blood, for glucose e.g. around ca. 12–13% [6]. A part of the plasma samples was used immediately after the centrifuging for the reference analysis, the rest were frozen and stored about 3 months (NIR) and 5 months (MIR) at -35°C before the spectroscopic experiments. From each sample, there was a total of around 8 ml of plasma available in many sample tubes so that “fresh” samples could always be thawed for the measurements.

In the realization of novel automatic analysis devices, the simultaneous determination of a larger number of components is very desirable for economic reasons. Therefore, in addition to glucose (reference method: Hexokinase/G6P-DH), the concentrations of a few more medically important blood substrates were determined (reference methods in parentheses): total protein (Biuret), total cholesterol (CHOD-PAP), triglyceride (GPO-PAP), urea (Urease/GLDH), and uric acid (Uricase-PAP). The glucose references were determined with an Eppendorf ACP 5040 device; for the remaining substrates, a Boehringer Mannheim/Hitachi 704 analyzer was used. In order to increase the precision and to avoid outliers, all reference concentrations were determined three times

and averaged. Table 5.1 gives an overview of the arising concentration regions and the population averages as well as the biological variances:²⁹

Table 5.1: Concentration regions $c_{\min} - c_{\max}$ as well as average values \bar{c}_{pop} and standard deviations $\hat{\sigma}_{\text{pop}}$ for the population of the 126 blood plasma (protein in [g/l], otherwise [mg/dl]).

	Glucose	Total Protein	Total Cholesterol	Triglyceride	Urea	Uric Acid
$c_{\min} - c_{\max}$	36–482	59–83	125–329	47–640	14–69	2.1–9.8
\bar{c}_{pop}	207.5	70.5	219.0	163.1	36.8	5.2
$\hat{\sigma}_{\text{pop}}$	90.4	4.4	44.0	98.6	10.0	1.4

As Fig. 5.3 shows, the glucose concentrations of the diabetic populations follow a normal distribution, in good approximation, whose average value $\bar{c}_{\text{pop}} = 207.5$ mg/dl lies at about twice that of the physiologically normal value. The standard deviation $\hat{\sigma}_{\text{pop}} = 90.5$ mg/dl is also doubled in comparison to the glucose dynamics of the population of “average” patients (cf. Fig. 4.3a). The distribution functions of the other blood substrates examined do not stand out for the diabetic population, i.e. the average values lie in the physiologically normal region. Except for the triglycerides, all reference concentrations are, in good approximation, normally distributed (the Kolmogoroff-Smirnow Test does not stand out for a significance number of about 20% [143:p. 234ff]). The triglycerides (blood fats) are, through a grouping of higher values, distributed asymmetrically around the mean value similar to the population of “average” patients in [3]. A further interesting point is the correlation between the concentrations of the blood substrates examined. The matrix of coefficients is given in Table 5.2 for the plasma population examined.

²⁹In the following, the unbiased estimations for the variances are solely used, e.g.

$$\hat{\sigma}_{\text{pop}}^2 = \frac{1}{M-1} \sum_{m=1}^M (c_m - \bar{c}_{\text{pop}})^2$$

“with the degree of freedom correction” in the denominator.

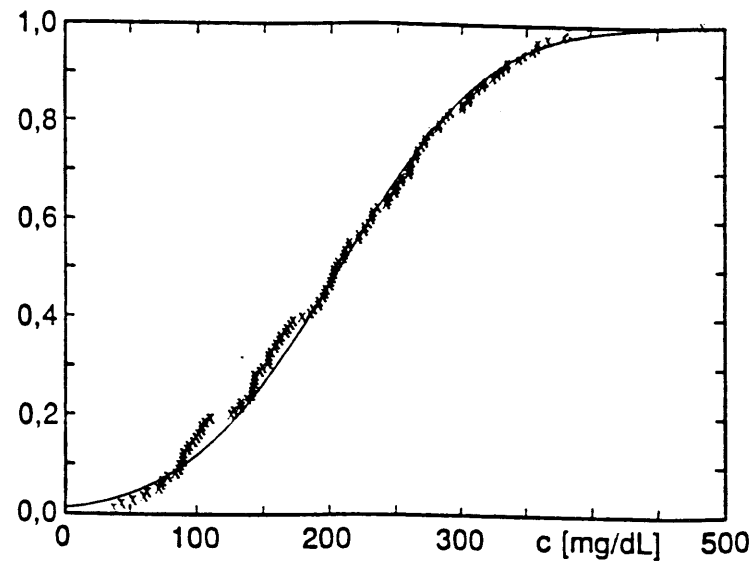


Fig. 5.3: Cumulative distribution function of the glucose reference values of the 126 blood plasma (solid line: normal distribution with parameters $\mu = \bar{c}_{\text{pop}}$ and $\sigma = \hat{\sigma}_{\text{pop}}$).

Table 5.2: Correlation matrix of the substrate concentrations for the populations of the 126 blood plasma.

	Glucose	Total Protein	Total Cholesterol	Triglyceride	Urea	Uric Acid
Glucose	1.000	0.124	0.267	0.329	0.288	-0.015
Total Protein	0.124	1.000	0.148	0.052	0.127	0.139
Total Chol.	0.267	0.148	1.000	0.469	0.139	0.120
Triglyceride	0.329	0.052	0.469	1.000	0.167	0.369
Urea	0.288	0.127	0.139	0.167	1.000	0.394
Uric Acid	-0.015	0.139	0.120	0.369	0.394	1.000

The statistical significance of the correlation coefficients can be verified with a test according to R. A. Fisher (Biometrika 10, 1915, 507). The hypothesis $r_{\text{true}} = 0$ is tested against the alternative $r_{\text{true}} \neq 0$, where a normal distribution of the concentrations is assumed (cf. [143:p. 316]). The values entered in bold-faced type in Table 5.2 are with a significance level of $\leq 0.5\%$ different from zero.³⁰ In the diabetic population examined, there exists a positive correlation between glucose and cholesterol, triglycerides, and urea. However, it is uncertain whether a correlation of the quickly changing glucose with the other substrates examined was present for an individual patient whose concentrations only change over a very large time period. In order to quantitatively estimate the possible correlations in Table 5.2 on the prediction of glucose, the glucose concentration of 126 plasma samples was regressed against the concentration of the remaining substrates with the PLS method. The $\text{PRESS}^{1/2}$ results of the cross-validation (Eq. 4.69) are given in Table 5.3.

³⁰In case $r_{\text{true}} = 0$ is valid and a normal distribution is present, a value with $|r| \geq 0.175$ could be calculated only in ca. 5 cases from 1000 populations with 126 samples.

Table 5.3: $\text{PRESS}^{1/2}$ prediction error [mg/dl] of glucose in the regression against the reference concentrations of the remaining five substrates (upper row) and from cholesterol, triglycerides, and urea (lower row).

PLS Rank	0	1	2	3	4	5
$\text{PRESS}^{1/2}$	90.8	86.1	85.8	84.4	83.6	82.3
$\text{PRESS}^{1/2}$	90.8	86.1	85.8	84.4		

As the results in Table 5.3 show, a prediction of glucose with the help of the remaining substrate concentrations alone is not possible. This means that a successful glucose calibration of the IR spectra is not possible through a regression against the extinction spectra of other correlated components, rather must be based on spectroscopic glucose signals.

In order to check the precision and the correctness of the clinical-chemical reference methods, blood serums with certified concentration values were measured in the analysis device in the framework of the routine analysis at periodic intervals. Here, various test serums were used with differing compositions in order to test the certainty of larger medically interesting concentration regions. For the rating of the various reference methods, the control results from the months April and May 1992 from the Duesseldorfer Diabetes Institute were available. For glucose, the control data are summarized in Table 5.4 (for remaining substrates, see Appendix C):

Table 5.4: For the certainty of the glucose reference method (c_{true} certified concentration of the test serum; n number, \bar{c}_S average, and $\hat{\sigma}_S$ standard deviation of the control measurement; concentrations in [mg/dl]).

	c_{true}	n	\bar{c}_S	$\hat{\sigma}_S$	$\hat{\sigma}_S/\bar{c}_S$	$\bar{c}_S - c_{\text{true}}$
low	42.2	58	36.7	2.0	5.4%	-5.5
middle	123	58	116.9	5.0	4.3%	-6.1
high	241	58	233.1	10.0	4.3%	-7.9

The prediction certainty of the spectroscopic calibration ($\text{PRESS}^{1/2}$ statistic) can generally not be better than the random error of the reference method that is averaged over the calibration population. As Table 5.4 shows, the precision of the reference measurement is dependent on the glucose concentration and displays a so-called *trust coefficient* $VK = \hat{\sigma}_S/\bar{c}_S$ with a nearly constant value around 5%. This relationship, which often occurs in the analysis methods with chemical reactions, is made visible in Fig. 5.4. A model for the description of the precision in dependence on the true concentration can be comprised of both an additive and a multiplicative error:

$$\sigma_{\text{Ref}}(c) = a + bc \quad (5.1)$$

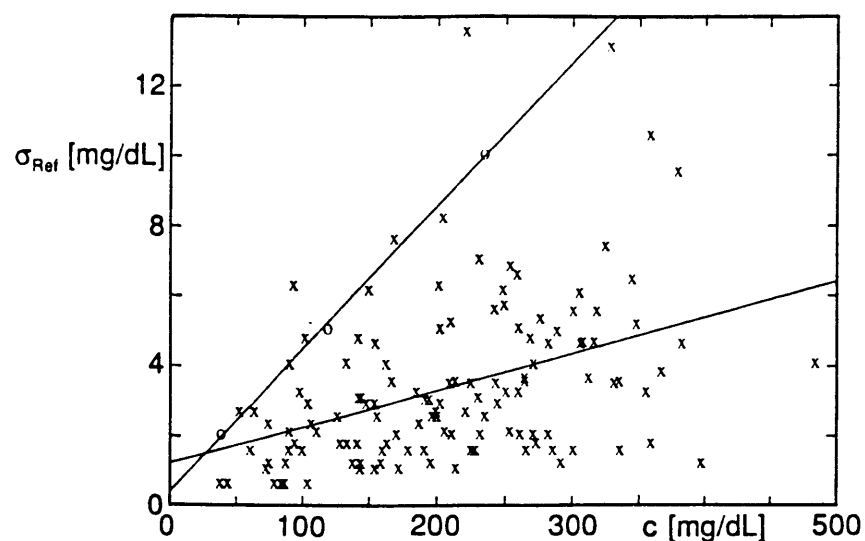


Fig. 5.4: Standard deviation of the glucose reference determinations of the three (o) test sera ($n = 58$) and the 126 plasma ($n = 3$) versus the determination averages (see text).

Both of the compensation lines drawn in Fig. 5.4 represent the models Eq. 5.1 estimated with the least-squares method for the standard deviation of "day-to-day" (upper line for the three test sera) and the standard deviation "in series" (lower line for the plasma). The variance in the measurement of the test sera (1 measurement/day) combines all daily laboratory random error sources that arise and is therefore larger than the variance of the triple determinations of the plasma "in series" which include only error sources with time constants up to about 1 min. The results of the estimation of both precisions are $\hat{\sigma}_{T-T}(c) = 0.40 + 0.041c$ and $\hat{\sigma}_{ser}(c) = 1.21 + 0.010c$ such that $\hat{\sigma}_{T-T} > \hat{\sigma}_{ser}$ is valid in the medically relevant concentration region of glucose ($c > 30$ mg/dl). The validity of the model Eq. 5.1 for the description of the precision $\hat{\sigma}_{T-T}$ of "day-to-day" is clear ($r^2 = 0.999$, cf. Fig. 5.4). Due to the large noise in the estimation of the standard deviations "in series", the approximation quality by the LS compensation line is poorer here, however, the t -statistic of the estimated coefficient $\hat{b}_{ser} = 0.010$ with a value of $t_b = 4.92$ clearly displays a $b_{ser} > 0$ (significance $\ll 1\%$).

In order to display the precision of the reference methods, the variances from Eq. 5.1 are averaged over the concentrations c_m ($m = 1, 2, \dots, M$) of the calibration population:

$$\hat{\sigma}_{av} = \sqrt{\frac{1}{126} \sum_{m=1}^{126} (\hat{a} + \hat{b}c_m)^2} \quad (5.2)$$

Since the 126 blood plasma samples were collected over a time period of ca. 6 weeks, they display an average error in the reference analysis from "day-to-day": $\hat{\sigma}_{av,T-T} = 9.6$ mg/dl. This is comprised of the uncorrelated portions of the error with larger time constants (hours) and the determination error "in series": $\hat{\sigma}_{av,ser} = 3.5$ mg/dl. Through the triple measurement of the plasma, only the

variance of the error "in series" is reduced such that the effective average precision of the reference values

$$\hat{\sigma}_{av,Ref} = \sqrt{\hat{\sigma}_{av,T-T}^2 - \frac{2}{3}\hat{\sigma}_{av,ser}^2} \quad (5.3)$$

for glucose with $\hat{\sigma}_{av,ref} = 9.2$ mg/dl is only slightly improved through the multiple determination.

The systematic error (bias) $\bar{c}_S - c_{true}$ of the glucose references is approximately constant over the entire concentration region (cf. Table 5.4). The PRESS^{1/2} statistic of the spectroscopic prediction is not influenced by a constant bias, since through the application of mean-centered data in the regression, solely *deviations* from the (false) average value of the reference concentrations are predicted. An influence on the average spectroscopic prediction error is only possible by a concentration-dependent bias error of the reference method, where the PRESS^{1/2} statistic according to the sign of the bias is either improved or worsened. An estimation of the bias error averaged over the plasma population (analogous to the aforementioned procedure in Eq. 5.1 and Eq. 5.2) yielded that this is negligible for all substrates, except for cholesterol, in comparison to the average random error in the reference determinations ($\overline{bias}^2 < 0.05\sigma_{av,ref}^2$). In Table 5.5, the average precisions of the reference methods determined with Eq. 5.1 and Eq. 5.3 are summarized.

Table 5.5: Overview of the reference methods and their average determination errors (protein in [g/l], otherwise [mg/dl]; see text for details).

	\hat{a}_{T-T}	\hat{b}_{T-T} X100	$\hat{\sigma}_{av,T-T}$	\hat{a}_{ser}	\hat{b}_{ser} X100	$\hat{\sigma}_{av,ser}$	$\hat{\sigma}_{av,ref}$
Glucose	0.40	4.09	9.62	1.21	1.04	3.50	9.19
Total Protein	0.63	—	0.63	0.44	—	0.44	0.51
Total Chol.	0.84	0.80	2.60	0.83	0.75	2.51	1.61
Triglyceride	1.00	0.49	1.87	0.68	0.58	1.72	1.24
Urea	0.16	4.43	1.84	0.14	0.81	0.45	1.80
Uric Acid	0.00	4.14	0.23	0.02	0.25	0.03	0.22

For protein, the LS fit $\sigma = a + bc$ yielded neither for the "day-to-day" test sera nor for the precision "in series" a statistically significant slope coefficient \hat{b} different from zero so that instead of Eq. 5.1, the model $\sigma_{ref} = a$ was used. This exception is made understandable by the small biological variation of the protein concentration (cf. Table 5.1).

In addition to the six substrates mentioned, the reference values for creatinin and total bilirubin were available. The concentrations of both of these substrates are, however, so small ($\bar{c}_{pop,crea} = 0.72$ mg/dl; $\bar{c}_{pop,bili} = 0.55$ mg/dl) that through the calibration of the IR spectra, no significant improvement could be achieved in comparison to the error in the "prediction with the average value" ($\sigma_{pop,crea} = 0.15$ mg/dl; $\hat{\sigma}_{pop,bili} = 0.23$ mg/dl). Therefore, creatinin and bilirubin will not be discussed further.

5.3 ATR Measurements in the Mid IR

5.3.1 Experimental Details

In the selection of the ATR measurement cuvettes, two criteria are important: the filling volume should be as small as possible in order to be able to analyze small amounts of blood, and the entire sample apparatus must be pressure sealed in order to avoid hygienic problems during cuvette filling and cleaning. Both requirements are fulfilled by the micro-CIRCLE™ cells (Spectra Tech, Stamford, CT, USA) [159].

In the micro version, a cylindrical zinc selenide (ZnSe) crystal with a diameter of $1/8'' = 3.175$ mm and a length of about 33 mm is used. ZnSe transmits in the spectral region from about 0.5–20 μm and displays in the mid IR a refraction index of 2.40 (at 10.6 μm) [160]. The sealing of these cells by O-rings made from chemically inert Teflon is advantageous. The sample volume of the micro cells is given as 25 μl with which the separation between the crystal surface area and the wall of the sample space can be determined to be ca. 90 μm . By drilling the cell with a diameter of $\phi = 3.50$ mm, this separation was approximately doubled in order to avoid potential problems during filling and cleaning. The volume of the cell used then was ca. 50 μl . The ATR crystal displays a 45° conical point at both ends. The focusing of the IR radiation takes place through Cassegrain-similar mirror pairs with surface mirrors whose form arises through rotation of the off-axis segments of two ellipsoid mirrors [161]. Through application of such "axicon" optics [162,163], *all* light beams meet below an angle of about 45° to the optical axis in the focus so that the bordering area air-crystal is impinged nearly perpendicularly and vignetting losses through the small mirrors can be completely avoided. A further advantage is the homogeneous radiation strength [W/m^2] in the axicon focus.

As suggested in Fig. 5.5, the beam slightly enters into the optically thinner medium with each total reflection which e.g. is also noticeable from the beam translation (Goos-Haehnchen effect). The amplitude of the electric field decreases exponentially when entering the thinner medium and reaches the $1/e$ th value of the initial field strength at a penetration depth d_p [155:p. 22]

$$d_p = \frac{\lambda}{2\pi n_1 \sqrt{\sin^2 \theta - \left(\frac{n_2}{n_1}\right)^2}} \quad (5.4)$$

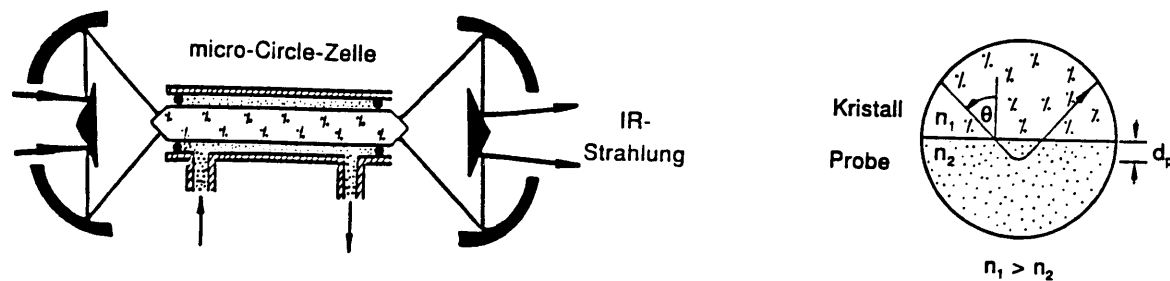


Fig. 5.5: A micro-CIRCLE™ cell from Spectra-Tech.

The penetration depth is given as a multiple of the wavelength used and is dependent on both refraction indices and the angle θ for which the total reflection takes place; the field distribution in the crystal does not enter into the penetration depth. With Eq. 5.4, an unlimited growth of the penetration depth is assumed when reaching the limiting angle of total reflection $\theta_{gr} = \sin^{-1}(n_2/n_1)$. However, this effect is not useful for the generation of large penetration depths, since the Fresnel reflectivity sinks very quickly when nearing θ_{gr} . For a realistic description, the complex refraction index of the absorbing sample $n_2(\lambda) = n_2(\lambda) - ik(\lambda)$ must be considered where $k(\lambda) = \lambda\alpha(\lambda)/4\pi$ is directly proportional to the absorption coefficient $\alpha(\lambda)$ (Eq. 3.1). The penetration depth d_p is determined in this case by forming the real portions in Eq. 5.4.³¹ The relationships for the ATR measurement of an aqueous solution in the region of the maximum glucose signal at 1037 cm^{-1} (9.64 μm) are shown in Fig. 5.6.

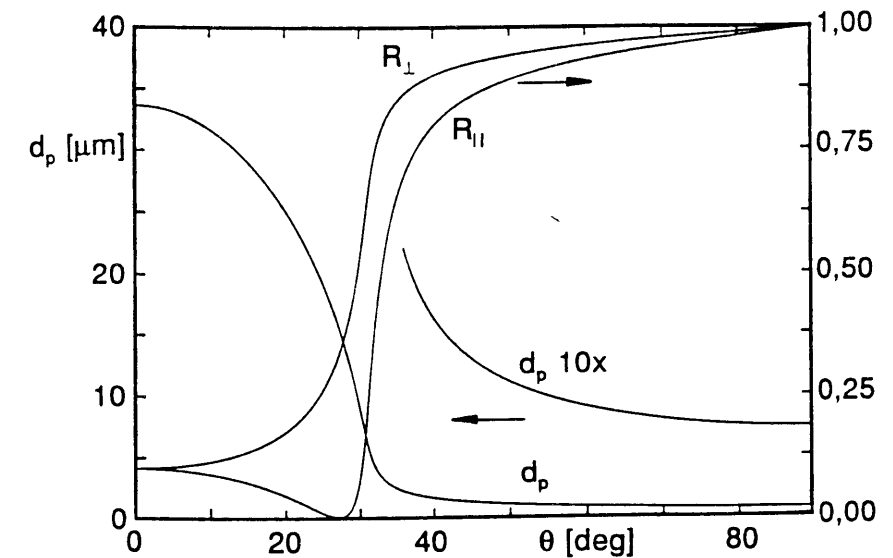


Fig. 5.6: Penetration depth d_p and Fresnel reflectivities $R_{||}$ and R_{\perp} on the bordering area ZnSe \rightarrow water at $\lambda = 9.6 \mu\text{m}$ in dependence on the reflection angle ($n_1 = 2.41$ [164]; $n_2 = 1.24 - i0.0454$ [21]).

Although the penetration depths can be theoretically increased by operating below the critical angle, practically no radiation energy, however, reaches the detector. The efficiency of the ATR crystal as a light guide (the radiation in FT-IR spectrometers is approximately unpolarized, i.e. $R_{\text{eff}} = 1/2(R_{||} + R_{\perp})$) would, through multiple reflections in the crystal, decrease significantly more quickly for an *individual* total reflection as shown in Fig. 5.6.

The CIRCLE™ cells display a penetration depth in water of 0.6 μm for wavelengths around 10 μm (cf. Fig. 5.6 for $\theta = 45^\circ$; since d_p describes the attenuation of the *electric* field, the value for the radiation power should be halved). The effective thickness of the ATR cuvette is proportional to d_p [155] and was determined to be 13.1 μm by a comparison with a transmission measurement at 1037 cm^{-1} [2]; a total of about 7.5 total reflections occur on the crystal surface area in contact with the sample (see [165] for further details).

³¹ $d_p = 1/\text{Re}[1/d_p]$ where d_p is the complex value from Eq. 5.4.

An older suggestion for a non-invasive glucose determination using ATR spectroscopy of the lip [166] is unrealistic due to the small penetration depth into the tissue. The lip is also covered by a keratinized calloused layer which in the region of the moist inner lips, dissolves into a mucous skin layer (cf. Ch. 6.1). The premise that the glucose concentration in the interstitial liquid of the upper epithel cell layers of the mucous skin layer is correlated with the blood glucose concentration [167] could not be confirmed by experiments. For this, a special skin-ATR accessory (Specac, Orpington, England) was available which e.g. is routinely used for the examination of cosmetics. As with the CIRCLE™ cells, a ZnSe crystal with a 45° total reflection is used; however, this one has a rectangular cross-sectional area and can be inserted into the spectrometer such that a 50×10 mm large crystal surface area connects with the cover of the sample chamber and is reachable from above. After an oral ingestion of 100 g of glucose, ca. 120 spectra of the inner "clapped down" underlip were taken from various test persons (three diabetics, two non-diabetics) over a time period of about 4–5 h. In intervals of 15–20 min, blood was additionally sampled from the finger and the glucose concentration was determined with the usual reference method (glucose–hexokinase). The blood glucose values at the times of the lip measurements were interpolated with a spline approximation afterwards (cf. Fig. 6.13 and the corresponding text). A measurement of the glucose concentration in the saliva is also not appropriate for the determination of blood glucose, since no significant correlation of the concentration in both liquids occurs (see [168] and the references cited there). Stationary values of the glucose concentration in the saliva occur underneath strong individual oscillations and lie in the region of 0.1–0.7 mg/dl which is clearly below the resting values in blood [168]. The ATR measurement series was conducted at the beginning with "moist" inner lips (normal state) and also later with lips that were dried before each measurement. For the "dry" lips, no useful prediction models could be calibrated. With the "moist" lip series, occasionally PRESS^{1/2} prediction errors were calculated with the PLS algorithm that were clearly below the standard deviation of the glucose reference values (at inversion rank $R = 0$). The calibrations of different measurement series, however, did not allow themselves to be transferred (also not for an individual person from day A to day B) so that apparent correlations must be assumed as the cause for these results. These arise through trends in the measurement conditions that randomly run temporally parallel to the true glucose concentration, e.g. also pressure on the lip, lip moisture, etc. Through the drying of the lip before each measurement, these type of effects were apparently suppressed.

For the liquid blood measurements, the plasma samples were thawed over a time period of at least 1 h at room temperature and homogenized afterwards. For filling and cleaning of the measurement cell in the spectrometer, a cuvette filling station was built which allowed a reproducible handling of the samples under consideration of the hygiene guidelines (see Fig. 5.7). The sample was pulled into a glass hypodermic needle with a Luer–Lock connection and was injected into the measurement cell through a steel capillary tube (outer- ϕ 1/16"). The dead volume of the capillary up to the measurement cell was about 160 μ l. After the measurement, the cuvette could be cleaned using a hose pump (Pharmacia LKB, Freiburg, BRD: Typ Microperpex 2132–002) with three different cleaning liquids and could be dried with nitrogen gas; for switching, miniature valves (Hamilton, Darmstadt: Typ HVP) were used.

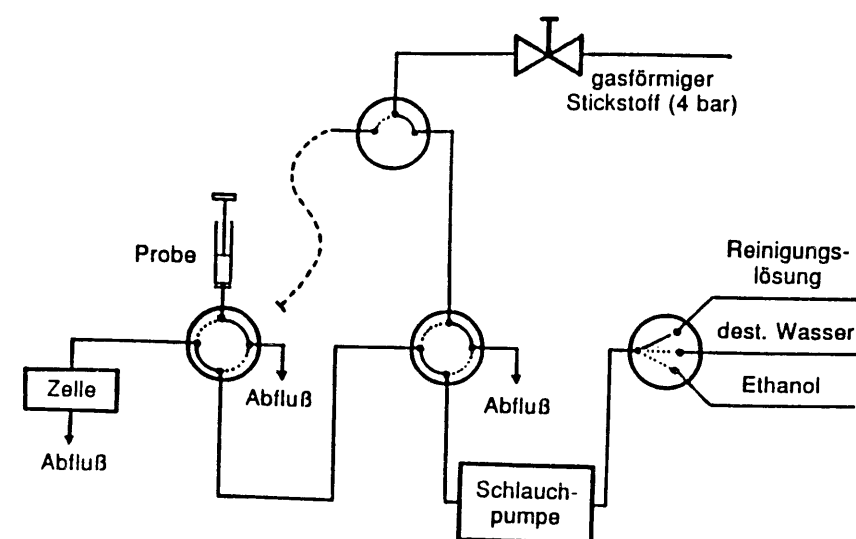


Fig. 5.7: Schematic representation of the cuvette filling station.

For the measurement of sample and reference, ca. 0.5 mL of plasma and tri-distilled water were injected into the CIRCLE™ cells. These were equipped with a commercial accessory for thermal stabilization of the sample volume (Spectra-Tech Heating/Cooling Jacket) on which a thermostat (Messgerate-Werk Lauda, Lauda-Koenigshofen, BRD: Typ KS 6) with water circulation was connected. All measurements were conducted at 37°C sample temperature. For this, a ca. 57×33×10 mm large copper disk was screwed onto the "heating jacket" of the cell which carried a Pt-100 measurement resistor (Juchheim, Fulda, BRD: Typ PK 1.4830.1) in a properly sized hole whose temperature could be measured with a precision of 0.01°C (Lauda: Digital-Thermometer Typ R 42). The oscillations in the cuvette temperature were smaller than ca. $\pm 0.02^\circ\text{C}$ over the entire measurement series. The thermal stabilization of the sample to a constant temperature is required, since the large background extinction bands of water drift with oscillations in the temperature along the wave number axis. Around the absorption bands at 1640 cm^{-1} , an approximately 100 cm^{-1} wide peak with an amplitude of ca. $+7 \cdot 10^{-3}\text{ AU}/^\circ\text{C}$ occurs in the calculation of the extinction $E = -\log_{10}(\text{water}(T + \Delta T)/\text{water}(T))$. In the region of the maximum glucose signals $1200\text{--}950\text{ cm}^{-1}$, a relatively flat systematic error arises through temperature drifting which essentially consists of a constant baseline offset on the order of magnitude of $+1.2 \cdot 10^{-3}\text{ AU}/^\circ\text{C}$. Through the exhaustive thermal stabilization, no influence on the glucose calibration in the mid IR through temperature effects arises (cf. Ch. 5.4 for the less advantageous situation in the near IR).

Distilled water, ethanol, and a 1% aqueous solution of Extran (AP 41 enzymatic) from the firm Merck (Darmstadt) were used as the cleaning fluids, each of which was pumped through the CIRCLE™ cell at about 5.3 ml/min. An overview of the temporal sequence of the measurement is given in Table 5.6.

Table 5.6: Temporal sequence during filling and cleaning of the CIRCLE™ cell.

<u>Reference:</u>	inject water (ca. 0.5 mL)
	0.5 min equilibration of the cell temperature
	2.0 min IR measurement
	1.5 min cleaning with ethanol
	3.5 min drying with nitrogen (4 bar)
<u>Sample:</u>	inject plasma (ca. 0.5 mL)
	0.5 min equilibration of the cell temperature
	2.0 min IR measurement
	1.5 min cleaning with 1% Extran solution
	1.5 min cleaning with water
	1.5 min cleaning with ethanol
	3.5 min cleaning with nitrogen (4 bar)

The cleaning of the cell to remove plasma deposits is achieved through the Extran solution. Afterwards, it is rinsed with water. In the last step, ethanol is pumped through the cell, since additionally, fast drying is possible when cleaning due to the low boiling point of 78.3°C.

All times in Table 5.6 were determined using kinetic measurements for which the ethanol drying is represented in Fig. 5.8 as an example. After about 3 min, the large ethanol bands at 1085 cm⁻¹ and 1047 cm⁻¹ (cross-sensitivity to glucose) go below the noise. The drying of the water-filled CIRCLE™ cells would have taken about 15 min at the same conditions. The measurement of the 126 plasma samples could be conducted within one week with the procedure given in Table 5.6. The cuvette filling station was operated manually with a stopwatch. A total of 30 different grasps of the hand were required for one measurement. In comparison to older studies [2,3], a periodic, mechanical polishing of the ATR crystal with the aforementioned cleaning cycle was not necessary.

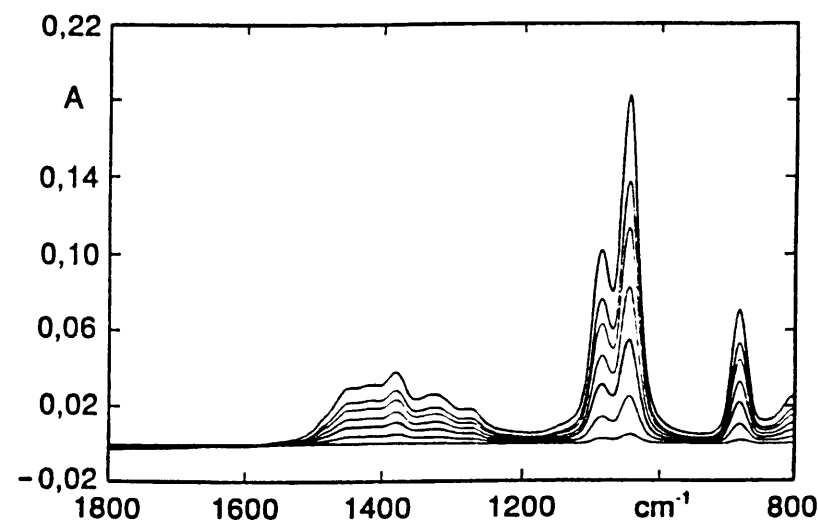


Fig. 5.8: Drying of the ethanol-filled micro-CIRCLE™ cells (see text for details); shown are seven average values, each from 150 spectra, that were measured during the time periods (1) 0–20 sec, (2) 20–40 sec, ..., (7) 120–140 sec after switching on the nitrogen (reference: dry ATR crystal).

In the mid IR, the Bruker IFS-66 spectrometer was equipped with a globar at the radiation source, a KBr beam splitter, and a MCT detector (Infrared Associates, Suffolk, UK, $\square = 1 \times 1$ mm). The mirror velocity was chosen to be $c_M = 1.90$ cm/s which gave a measurement time of ca. 2 min per single beam spectrum (including FFT calculation) when averaging over 500 interferogram scans and using a spectral resolution of $\Delta\tilde{\nu} = 4$ cm⁻¹ (Eq. 3.14). The spectra were taken in the region 4000–600 cm⁻¹ ($\equiv 15.2$ –2.3 kHz) so that the interferograms were sampled at every third zero crossing of the HeNe laser signal (sampling rate ≈ 10533 cm⁻¹ $\equiv 40$ kHz). After “zero filling”, an FFT calculation with 8192 points was conducted from which the spectra were available with a “digital resolution” of $\Delta\tilde{\nu}_{\text{dig}} = 1.286$ cm⁻¹. The interferograms were apodized with the Blackman-Harris 3-term window function and after the Fourier transformation, were made symmetric with the Mertz phase correction where the nominal resolution of the two-sided interferograms for the phase calculation was $\Delta\tilde{\nu}_{\text{sym}} = 9.258$ cm⁻¹.

5.3.2 Results

In Fig. 5.9, the spectroscopic data basis for the quantitative blood substrate analysis in the mid IR is summarized. In comparison to the first study [2,3], an approximately ten fold reduction of the noise in the extinction region was achieved (cf. Fig. 4.1) through the optimization of the spectroscopic measurement conditions regardless of the factor of 2 larger resolution $\Delta\tilde{\nu} = 4$ cm⁻¹ for comparable collection times. The characteristic five-band structure of glucose in the region of 1200–950 cm⁻¹ can be clearly seen in the correlation spectrum also due to the high average concentration of $\bar{c}_{\text{pop}} = 207.5$ mg/dl, while the negative apparent correlation around 1600 cm⁻¹ of the older study (cf. Fig. 4.2) has disappeared. In the region of the C-H stretching oscillation ca. 3000–2800 cm⁻¹, a double band can be noticed in the correlation spectrum of glucose which arises for all blood substrates examined, however, due to the smaller chemical specificity of the of the C-H bond.

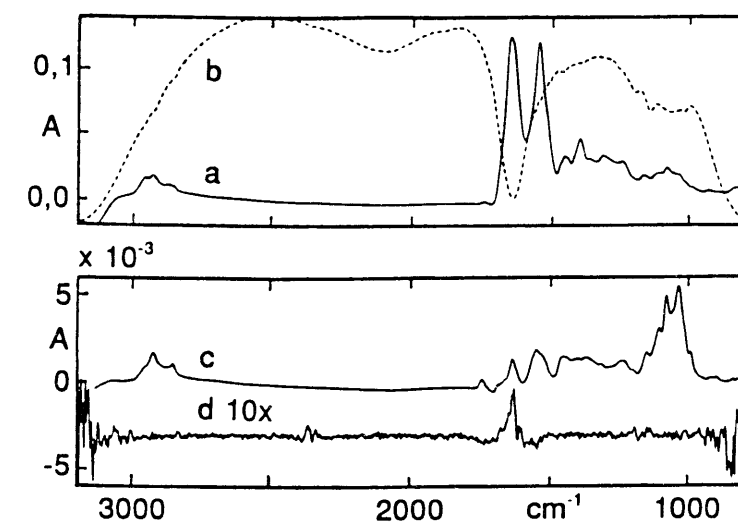


Fig. 5.9: (a) Average value of the ATR extinction spectra of the 126 blood plasma; (b) single beam spectrum of the water reference (random units); (c) correlation spectrum of glucose ($\bar{c}_{\text{pop}} = 207.5$ mg/dl); (d) extinction noise from two water references (with offset and enlargement).

All calculations were conducted with "raw" extinction spectra, i.e. no data pre-processing in the form of filtering, band normalization, baseline correction, or similar approach was used. Optimal calibration results were achieved for glucose in the narrow spectral region 1200–950 cm^{-1} of the maximum signal amplitudes. As a result of the higher Cook distance scale, two spectra were removed from the population as outliers; the studentized residuum of one of these spectra displayed an extremely high value at 4.45. For the remaining 124 standards, an inverse regression model was generated and solved by the PLS method. The results for the prediction error are represented in the following figures. In Fig. 5.10, the $\text{PRESS}^{1/2}$ statistics for two different spectral "resolutions of the calibration" $\Delta\tilde{\nu}_{\text{cal}} = 3\Delta\tilde{\nu}_{\text{dig}} \approx 3.9 \text{ cm}^{-1}$ and $\Delta\tilde{\nu}_{\text{cal}} = 6\Delta\tilde{\nu}_{\text{dig}} \approx 7.7 \text{ cm}^{-1}$ are shown with $N = 65$ and $N = 33$ data points in the interval 1200–950 cm^{-1} . From the small differences, it follows that through the measurement with spectral resolutions better than about $\Delta\tilde{\nu} = 8 \text{ cm}^{-1}$ in the fingerprint spectral region, no additional information for the glucose prediction can be gained. The specificity for glucose of the chosen spectral region is displayed in the fast reduction of the prediction error with increasing PLS rank. The optimal MSE prediction error for glucose is estimated at $R_{\text{opt}} = 9$ and $\Delta\tilde{\nu}_{\text{cal}} = 7.7 \text{ cm}^{-1}$ to be $\text{PRESS}^{1/2} = 10.4 \text{ mg/dl}$ and is approximately twice as good as the result of the earlier study ($\text{PRESS}^{1/2} = 19.8 \text{ mg/dl}$ at $R_{\text{opt}} = 16$, cf. Fig. 4.3). As a result of the improved S/N ratio and the reduced systematic error in the spectra, the calibration standards contain smaller stochastic variance portions in comparison to the first study so that only a small increase in the $\text{PRESS}^{1/2}$ values for inversion ranks $R > R_{\text{opt}}$ arise. Through the removal of ten standards simultaneously from the calibration and the calculation of the $\text{PRESS}^{1/2}$ statistic "in groups of ten", only very small changes occur which can hardly be considered true in Fig. 5.10; this is a further hint to the robustness of the calibration in the spectral region 1200–950 cm^{-1} . The certainty of the glucose prediction is impressively documented in Fig. 5.11 in which the independent predictions (in the sense of Eq. 4.70) of the PLS estimator with rank $R_{\text{opt}} = 9$ in the model are shown with the resolution $\Delta\tilde{\nu}_{\text{cal}} = 7.7 \text{ cm}^{-1}$. For the majority of the 124 standards, the glucose concentration is predicted with a relative error of better than $\pm 10\%$ (related to the reference value). Five spectra displayed relative errors in the region of $\pm 10 - 15\%$, and one spectrum (reference value 51 mg/dl) was predicted ca. 25% too high. As Fig. 5.11 shows, the estimation of blood glucose is practically unbiased over the entire concentration region examined, i.e. a systematic deviation from the ideal 45° line does not occur. This was to be expected due to the small increase in the $\text{PRESS}^{1/2}$ statistic for inversion ranks $R > R_{\text{opt}}$ (cf. Fig. 5.10), since quasi the entire systematic prediction error can be eliminated before the MSE error increases again through inversion of the prediction-irrelevant variance portions.

In Fig. 5.12, the solutions of the PLS calibration are shown for various inversion ranks with which the prediction of the glucose concentration is conducted by scalar multiplication of the mean-centered extinction spectra (cf. Eq. 4.14).

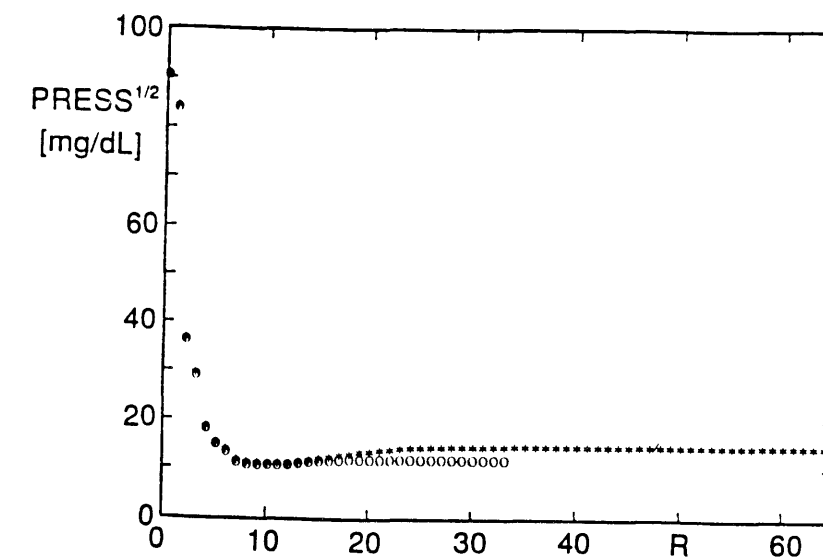


Fig. 5.10: $\text{PRESS}^{1/2}$ statistic for glucose in dependence on the PLS rank; spectral region 1200–950 cm^{-1} with (\star) $\Delta\tilde{\nu}_{\text{cal}} = 3.9 \text{ cm}^{-1}$ ($N = 65$) and (\circ) $\Delta\tilde{\nu}_{\text{cal}} = 7.7 \text{ cm}^{-1}$ ($N = 33$).

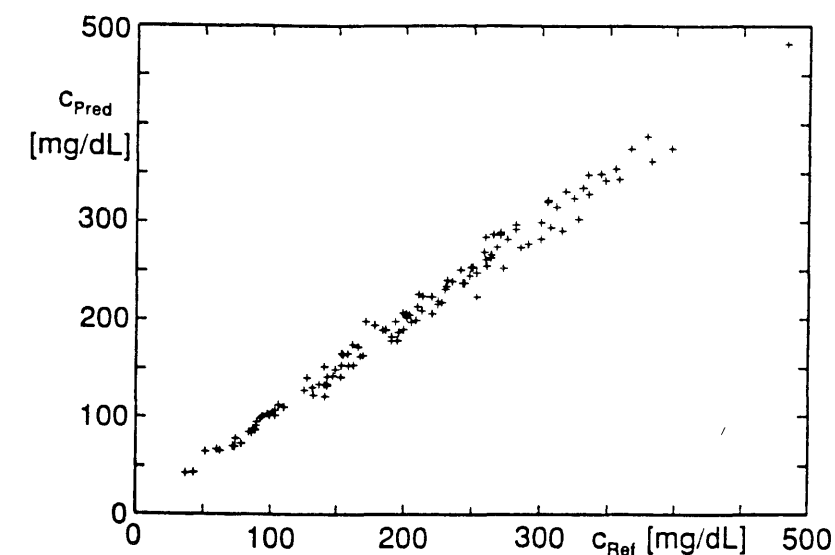


Fig. 5.11: Independent glucose predictions of the MSE-optimized PLS model with the ATR spectroscopic measurement procedure versus the clinical-chemical reference values.

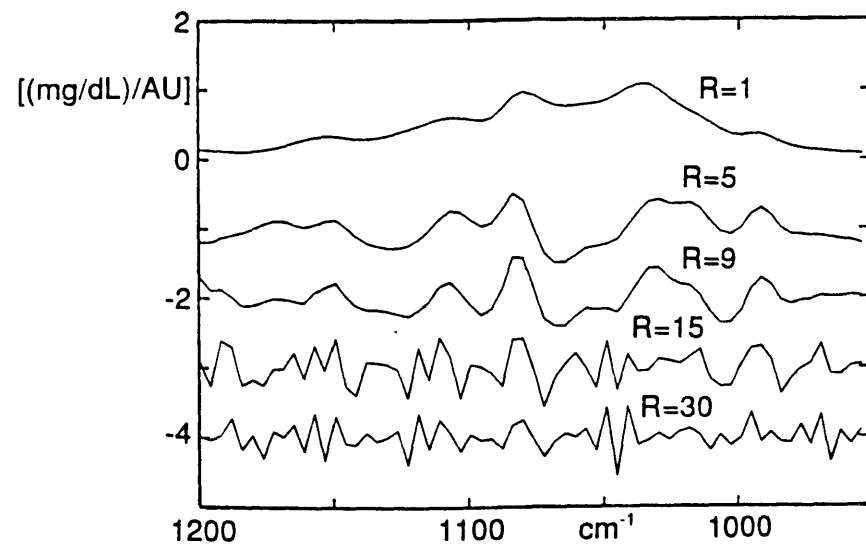


Fig. 5.12: Solution vectors of the PLS glucose calibration with $\Delta\bar{\nu}_{\text{Cal}} = 3.9 \text{ cm}^{-1}$ for various inversion ranks (offset and normalization: $b_1/313$; $b_5/30705 - 1$; $b_9/54549 - 2$; $b_{15}/148051 - 3$; $b_{30}/362790 - 4$).

The PLS estimator with rank $R = 1$ in Fig. 5.12 represents a scaled version of the glucose correlation spectrum (cf. Ch. 4.2.2) that displays only positive values in the wave number region $1200\text{--}950 \text{ cm}^{-1}$ and approximates the five-band structure of glucose. The PLS estimators with higher ranks display positive and negative values whose absolute size increases significantly with increasing rank (see normalization factors in Fig. 5.12). The optimal PLS estimator with $R_{\text{opt}} = 9$ accents, in comparison to the correlation spectrum with $R = 1$, not only both of the largest glucose bands at 1081 cm^{-1} and 1037 cm^{-1} , rather also the three neighboring bands at 1154 , 1107 , and 993 cm^{-1} as well as the diverse band shoulders. With further increasing of the inversion rank, the estimators become “noisy”, and structures in the regions without glucose information also appear, e.g. below ca. 975 cm^{-1} . For inversion ranks in the $\text{PRESS}^{1/2}$ “plateau” (Fig. 5.10) the PLS solutions no longer change, i.e. the LS solution vector for the maximum rank $R = 65$ runs approximately identical to the displayed curve for $R = 30$. For the calibration with the point separation $\Delta\bar{\nu}_{\text{Cal}} = 7.7 \text{ cm}^{-1}$, all statements mentioned are equivalently valid. The solution vectors differ up to rank $R = 9$ only through the higher resolution of the shapes in Fig. 5.12; for $R = 15$ and $R = 30$, the solutions are more noisy with $\Delta\bar{\nu}_{\text{Cal}} = 3.9 \text{ cm}^{-1}$ than with $\Delta\bar{\nu}_{\text{Cal}} = 7.7 \text{ cm}^{-1}$ which can also be observed in the shape of the $\text{PRESS}^{1/2}$ statistic (Fig. 5.10).

The prediction quality of the IR spectra can be influenced through the occurrence of “atypical” components in the blood that are not well represented by the standards used in the calibration. An example for this type of medical outlier with significant change in the IR spectroscopic signals are patients after intravenous injection of so-called plasma expanders (see Fig. 3 in [2]). Further potential disturbers can be medications and can occur in blood with concentrations in the thousandths range, e.g. acetylsalicylic acid (painkiller). The cross-sensitivity of a spectroscopic prediction to materials that do not appear in the calibration population is generally strongly dependent on the

inversion rank of the calibration. This dependence is not monotonic and “noisy” such that large differences occur for neighboring ranks. The systematic error in the glucose prediction through alcohol in the blood was estimated e.g. through scalar multiplication of the PLS solution vector with the extinction spectra of an aqueous ethanol solution: the maximum value of the disturbance occurred at $R = 3$ and contained ca. $+84 \text{ (mg/dl)/thousandth blood alcohol}$; the minimum value (≈ 0) was (randomly) achieved at $R_{\text{opt}} = 9$, and for $R = 8$, a value of ca. $32 \text{ (mg/dl)/thousandths}$ was determined. The cross-sensitivities of the glucose predictions must be further examined, also in order to also adjust the algorithms for outlier recognition especially for practically important medical interferences in future routine automatic devices.

In the following, it was attempted to divide the optimized average prediction error $\text{PRESS}_{\text{opt}}^{1/2}$ of the spectroscopic analysis method into parts by the error of the clinical-chemical reference method, the “physical” error in the spectroscopic measurement (noise and instabilities of the spectrometer as well as irreproducibilities of the sample handling), and the “biological” error through the individual variation in the IR spectra, where the latter occurs from the overlaying of extinction signals of many blood components with oscillating concentration and represents a lower limit for the certainty of the spectroscopic measurement. For the uncorrelated error sources, the following will be defined:

$$\text{PRESS}_{\text{opt}}^{1/2} \doteq \sqrt{\sigma_{\text{ref}}^2 + \sigma_{\text{Spec}}^2 + \sigma_{\text{Bio}}^2} \quad (5.5)$$

The average error in the glucose reference determination is estimated in Table 5.5 to be $\hat{\sigma}_{\text{ref}} = 9.2 \text{ mg/dl}$. The “physical” error part can be estimated by scalar multiplication of the PLS solution vector (Fig. 5.12, $R_{\text{opt}} = 9$) with a number of spectra that realistically reconstruct the spectrometer instabilities as well as the further variance influences on the sample measurement. For this, extinction spectra were calculated from each of two sequential water references that were sampled in a measurement series at an interval of ca. 18 min. A total of 108 spectra were available for the test of the baseline stability, since 17 pairs could not be used due to the larger time intervals. The baseline drifting in the spectral region of $1200\text{--}950 \text{ cm}^{-1}$ typically displays a smooth monotonically decreasing/increasing form with constant offsets on the order of magnitude of $\pm 15 \text{ mAU}$ (prediction error for glucose -2.6 mg/dl per 10 mAU offset) where the differences between the values at the interval limits reached to about $\pm 10 \text{ mAU}$ (maximum slope at 950 cm^{-1} about $\pm 0.1 \text{ mAU/cm}^{-1}$). The 108 drift spectra of the simulation produced prediction errors with a Gauss-similar distribution in the region up to ca. $\pm 10 \text{ mg/dl}$ and a standard deviation of $\hat{\sigma}_{\text{Spec}} = 4.4 \text{ mg/dl}$; the average value was statistically insignificantly different from zero at 0.23 mg/dl such that a bias term for the “physical error” need not be considered as with the error of the reference method (cf. Ch. 5.2). The same is also valid for the $\text{PRESS}_{\text{opt}}^{1/2}$ statistic due to the practically unbiased predictions and, hence, also for the method-inherent “biological” error whose standard deviation can be estimated with Eq. 5.5 to be $\hat{\sigma}_{\text{Bio}} = 1.9 \text{ mg/dl}$.

According to the guidelines of the Bundesärztekammer valid in the Federal Republic of Germany [169], the required precision and correctness of an analysis method for clinical acceptance was verified by periodic measurements of standard samples of constant composition (mostly sera with lower, medium, and higher substrate concentrations, cf. Ch. 5.2). The specially prescribed measurements and examinations of cross-sensitivities for proof of clinical acceptance were not conducted in the framework of this work and must be conducted in future studies before a commercialization of the new IR spectroscopic methods occurs. The medical requirements prescribe relative error limits, e.g. for glucose a variation coefficient $VK \leq 5\%$. (Due to the dangers associated with hypoglycemia

(Ch. 2), the exact determination of lower concentrations is particularly important for glucose.) For an estimation of the clinical acceptance of a spectroscopic analysis method, the "trust coefficient of the prediction" $VK_{\text{pred}} = \text{PRESS}_{\text{opt}}^{1/2} / \bar{c}_{\text{pop}}$ can be used which describes the average relative certainty in the prediction of the standard calibration population. This also contains error portions as a result of the *biological* variations between different individuals and, therefore, represents a pessimistic estimation of clinical acceptance. However, an important difference from the current chemical reference methods must be observed in the rating of the certainty of the spectroscopic analysis methods. These display a standard error which increases linearly with the true concentration (Eq. 5.1) which compensates for the requirement of a relative error limit. The precision of the spectroscopic methods, in comparison, does not increase automatically for smaller concentrations, rather reaches an optimal value at the average value \bar{c}_{pop} of the calibration population. An advantage of the spectroscopic analysis methods as compared to the conventional procedures is the possibility to divide the entire physiological concentration region into a few sections and to predict with various regression models, and especially, results could approach the requirement of a relative error limit through calibration with selected standards in lower concentration regions. Such a procedure also offers advantages regarding an improved outlier recognition, however, the effort for the calibration increases significantly.

The essential conclusions from the error estimation for the glucose prediction are: (1) The region of clinical acceptance is achieved with $VK_{\text{pred}} = 5.0\%$. (2) The information content of the IR spectra in the glucose specific frequency region $1200\text{--}950\text{ cm}^{-1}$ is so high that theoretically uncertainties up to about $\sigma_{\text{bio}} = 2\text{ mg/dl}$ are achievable. (3) For improving the certainty of IR spectroscopic glucose analysis methods in the future, the error in the clinical-chemical reference method should be primarily reduced.

The optimized calibration results for all substrates examined are summarized and discussed in the following sections (see Table 5.7 as well as Appendix D for further figures). The division of the prediction error into the various error variances according to Eq. 5.5 should display the potential for possible future improvements and should simplify the estimation of the method certainty regarding clinical acceptance. The variation coefficients named in the discussion for clinical acceptance have all been taken from [170].

Total Protein: Due to the dominance of the protein extinction over the other non-soluble blood components, the selection of an appropriate spectral region for the calibration is not critical. The wide frequency region of $1700\text{--}1351\text{ cm}^{-1}$ encompasses both of the prominent protein bands at 1650 cm^{-1} and 1540 cm^{-1} . The $\text{PRESS}^{1/2}$ statistic decreases at the beginning very sharply and, at PLS rank $R = 3$, already reaches approximately the optimal result of $\text{PRESS}^{1/2} = 1.21\text{ g/L}$ at $R_{\text{opt}} = 16$. In Table 5.7, the results are listed, therefore, for the optimal rank $R_{\text{opt}} = 16$ as well as for $R = 3$. No standards were classified as outliers. A limitation of the spectral region to $1599\text{--}1351/7.7\text{ cm}^{-1}$ ($N = 33$) without inclusion of the water absorption at 1640 cm^{-1} yielded no essential change in the prediction quality ($\text{PRESS}^{1/2} = 1.44\text{ g/l}$ at $R = 3$ and $\text{PRESS}^{1/2} = 1.29\text{ g/l}$ at $R_{\text{opt}} = 12$); the same is valid for an increase in the spectral resolution to $\Delta\tilde{\nu}_{\text{cal}} = 3.9\text{ cm}^{-1}$. The error estimation for the prediction with both of the different regression models shows how the physical error $\hat{\sigma}_{\text{spec}}$ increases with increasing inversion rank and how the inherent method error $\hat{\sigma}_{\text{bio}}$ sinks. Due to the high concentration of total protein in the blood and the relatively small biological

dynamics of this parameter, a prediction quality is possible with clinical acceptance ($VK \leq 3\%$) in the physiological concentration region without problems.

Total Cholesterol represents an exception to all of the substrates examined, since the best spectral region here was not found in the information rich fingerprint region of ca. $1750\text{--}750\text{ cm}^{-1}$, rather in the region C-H stretching vibration below 3000 cm^{-1} (see Fig. 5.9). In this frequency region, the higher spectral resolution $\Delta\tilde{\nu} = 4\text{ cm}^{-1}$ brings an advantage in the sampling of the typical C-H absorption bands. The calibration with $\Delta\tilde{\nu}_{\text{cal}} = 7.7\text{ cm}^{-1}$ ($\text{PRESS}^{1/2} = 10.0\text{ mg/dl}$ at $R_{\text{opt}} = 8$) is, therefore, poorer than the result given in Table 5.7 for $\Delta\tilde{\nu}_{\text{cal}} = 3.9\text{ cm}^{-1}$. One standard was removed as an outlier due to an outstanding Cook distance, another one due to an extreme *t*-residuum.

The calibration result for cholesterol is surprising, since (nearly) all organic molecules display C-H atom groups, and the signals are, therefore, chemically very unspecific. Although regression models can also be generated for other substrates in the spectral region $3001\text{--}2800/3.9\text{ cm}^{-1}$, these are poorer than in the fingerprint region ($\text{PRESS}^{1/2}$ results: glucose 27.2 mg/dl ($R_{\text{opt}} = 7$); protein 1.52 g/L ($R_{\text{opt}} = 7$); triglyceride 25.1 mg/dl ($R_{\text{opt}} = 7$); no prediction information for urea and uric acid). The sole application of the C-H spectral region for the prediction presents the danger that one of the aforementioned "medical" interference media (medications, etc.) may display a C-H signal, which correlates with the C-H absorption of cholesterol such that no outlier recognition is possible. Therefore, a regression model was alternatively constructed that uses the C-H stretching vibration region as well as the optimized spectral region of the fingerprint region (see Table 5.7). The $\text{PRESS}^{1/2}$ result of this calibration is only slightly better than for the model in the C-H area alone where the optimal PLS inversion rank increases enormously. The result of the calibration only in the fingerprint region is $\text{PRESS}^{-1/2} = 11.3\text{ mg/dl}$ at $R_{\text{opt}} = 13$; for cholesterol, this value can be increased by the application of higher spectral resolution $\Delta\tilde{\nu}_{\text{cal}} = 3.9\text{ cm}^{-1}$ up to $\text{PRESS}^{1/2} = 9.9\text{ mg/dl}$ ($R_{\text{opt}} = 21$).

For error estimation, it is important to observe that the reference method for cholesterol displays a concentration-dependent bias (cf. Appendix C) that is not negligible in comparison to the average random error σ_{ref} . Since the form of this bias error (high concentrations are determined too high, low ones determined too low) compensates the systematic error of the spectroscopic prediction (bias always in the direction of the population average), a more realistic estimation for the error portion through the reference method is $\sigma_{\text{ref}}^2 + \overline{\text{bias}}^2 \approx 2.4\text{ mg/dl}$. However, this correction has no influence on the conclusions from the error estimations; the region of clinical acceptance ($VK \leq 6\%$) is achieved with the spectroscopic measurement procedure where the essential contribution to the prediction error is by the "physical" error of the measurement.

Table 5.7: Optimized results of the PLS calibrations of 126 blood plasma for the ATR measurement procedure with the micro-CIRCLE™ cell (M is the number of the standards, N is the number of the spectral data points in the regression; R_{opt} is the optimal PLS inversion rank; see text for the remaining variables; results for protein [g/l], otherwise [mg/dl]).

	$\tilde{\nu}_{max} - \tilde{\nu}_{min}/\Delta\tilde{\nu}_{cal}$	M/N	R_{opt}	$\hat{\sigma}_{ref}$	$\hat{\sigma}_{spec}$	$\hat{\sigma}_{bio}$	$PRESS^{1/2}$	VK_{pred}
Glucose	1200-950/7.7	124/33	9	9.2	4.4	1.9	10.4	5.0%
Total Protein	1700-1351/7.7	126/46	16	.51	.98	.50	1.21	1.7%
			3	.51	.61	1.2	1.42	2.0%
Total Chol.	3001-2800/3.9	124/53	8	1.6	7.1	4.3	8.4	3.9%
	3001-2800/3.9	124/119	20	1.6	6.3	4.8	8.1	3.7%
	1800-1701/7.7 1500-1099/7.7							
Triglyceride	1800-1701/7.7	125/66	13	1.2	6.4	8.0	10.3	6.3%
	1500-1099/7.7							
Urea	1801-1130/7.7	124/88	20	1.8	2.2	.71	2.9	8.0%
Uric Acid	1800-1701/7.7	125/72	19	.22	.91	.31	.99	19.0%
	1599-1151/7.7							

Triglyceride: Through its chemical composition, the IR signals of this blood substrate are similar to those of cholesterol such that the same fingerprint spectral region delivers optimized results. The application of a higher spectral resolution $\Delta\tilde{\nu}_{cal} = 3.9 \text{ cm}^{-1}$ yielded only insignificant changes of the $PRESS^{1/2}$ result. The same is valid for a calibration in the spectral region from 1801-1099/7.7 cm^{-1} including the water bands at 1640 cm^{-1} , however, the optimal rank of $R_{opt} = 15$ increases here and the $PRESS^{1/2}$ values initially reduce more slowly ($R < 15$). A plasma sample with the extremely high reference concentration of 640 mg/dl was removed as an outlier from the calibration (outstanding Cook distance). Due to the relatively weak and specific extinction signals, the spectroscopic determination of triglyceride is difficult (signals in the correlation spectrum for $\bar{c}_{pop} = 163 \text{ mg/dl}$ about three times smaller than for cholesterol with $\bar{c}_{pop} = 219 \text{ mg/dl}$). Regardless of the use of a wide spectral region, the error estimation displays the inherent method error $\hat{\sigma}_{bio} = 8.0 \text{ mg/dl}$ as the largest portion of the total prediction error. The region of clinical acceptance ($VK \leq 7\%$) is achieved with the results of this work.

For **urea**, the physiological concentrations clearly lie below the values for the aforementioned substrates (Table 5.1). The IR signals are correspondingly small such that for an optimized calibration, the entire fingerprint spectral region must be used. However, the region of clinical acceptance ($VK \leq 8\%$) is still achieved for urea. Due to large Cook distances, two standards were classified as outliers. The exclusion of the region 1700-1602 cm^{-1} (water bands) from the calibration leads, with $PRESS^{-1/2} = 3.2 \text{ mg/dl}$, to a slight degradation of the prediction certainty without having to change the optimal rank $R_{opt} = 20$. Noteworthy is that for urea, improvements in the $PRESS^{1/2}$ values of around 5% are possible through use of higher spectral resolutions $\Delta\tilde{\nu}_{cal} = 3.9 \text{ cm}^{-1}$.

With **uric acid**, the optimized spectral region excludes the region around the water bands at 1640 cm^{-1} that are especially susceptible to spectrometer drifts. Due to the low concentration ($\bar{c}_{pop} = 5.2 \text{ mg/dl}$) of uric acid in blood, the IR signals are slightly overlaid with uncorrelated variances in the spectra. Calibration with $\Delta\tilde{\nu}_{cal} = 3.9 \text{ cm}^{-1}$ yielded no changes to the results. Uric

acid is a medical parameter that clearly sets the limits for possibilities of an IR spectroscopic blood analysis. Clinically acceptable results ($VK \leq 6\%$) are not possible with today's technology. The size of the inherent method error $\hat{\sigma}_{bio} = 0.31 \text{ mg/dl}$ shows that the chances for an IR spectroscopic analysis of uric acid in blood must be estimated as small; the same statement is valid for substrates with even smaller concentrations, e.g. for creatinin and bilirubin.

The reduction of the problem of the protein adsorption on the ATR crystal with the help of the aforementioned cleaning cycle (Table 5.6) is made clear in Fig. 5.13. Here, the extinction spectra of the "empty" measurement cuvettes are shown for the morning of the second measurement day (a), for the evening of the fourth measurement day (b), and for the morning of the fifth measurement day (c). The stored single beam spectrum of the crystal was used as the reference before the beginning of the measurement campaign. Since the spectrometer at the time of the measurement was not optimally cleaned, the extinction spectra are overlaid with negative absorption bands of atmospheric moisture (rotation-fine structure of the bending oscillation at 1640 cm^{-1}); the absorption bands of protein at the ATR crystal can also be seen in Fig. 5.13. During the 5-day measurement series, the crystal was cleaned overnight with the 1% Extran solution which was pumped through the cell at a reduced flow rate of about 0.5 ml/min. As Fig. 5.13 shows, a protein layer builds up in the course of a measurement day with ca. 25 plasma samples (b) which, through the nightly cleaning, was removed except for a "basis layer" (a,c). The thickness of this basis layer can be estimated with the absorption coefficient of protein ($\alpha_{Prot} \approx 190 \text{ [mm}^{-1}]$ at 1540 cm^{-1} , cf. Fig. 5.9) and the number of ATR reflections at the crystal surface area contacting the sample ($n \approx 7.5$ [165]) to ca. 4 nm. We are dealing with a layer which, at first contact with the crystal, becomes attached to its surface area. The molecular layers (thickness in the evening ca. 7 nm) that are formed on top of this can be reproducibly removed through the Extran solution. The daily growing of the protein layer from sample to sample, which could be avoided through a further optimization of the cleaning cycle, is the possible cause for the fact that during the estimation of the "physical" prediction error for protein with help of the simulated drift spectra (water reference versus the following water reference), a negative average value was calculated. For the rank $R_{opt} = 16$, the average value of the 108 prediction errors lay at $\bar{c}_{spec} = -0.21 \text{ g/l}$ (-.3% of the population average value for the protein concentration) which stands out due to $\hat{\sigma}_{spec}/\sqrt{108} = 0.09 \text{ g/l}$ (Table 5.7).

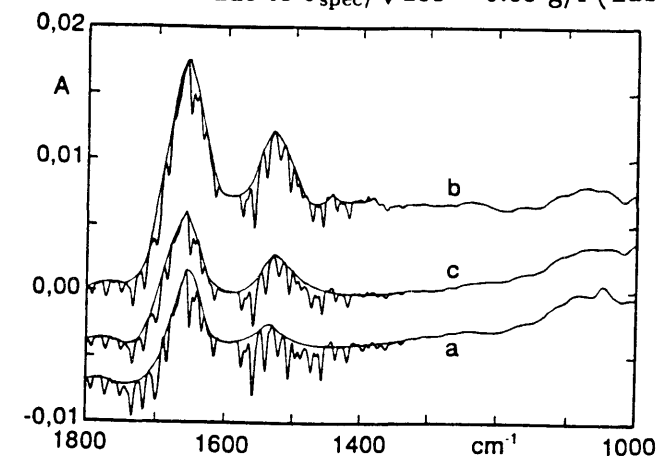


Fig. 5.13: Extinction spectra of the protein layers on the ZnSe crystal of the micro-CIRCLE™ cell (with offset; see text for details).

Mastering the protein adsorption is an essential requirement for the use of the ATR measurement technique in the routine analysis of biotic liquid samples. Although the procedure that was used for the cleaning of the crystal is surely still not optimal and completely reproducible measurement conditions from sample to sample could still not be generated, the essential conclusion is proven that ATR measurements are possible over longer periods of time without regular *mechanical* cleaning of the crystal. With the results of this work, the realizability of a reagentless automatic analysis device for glucose, total protein, total cholesterol, triglyceride, and urea is shown.

5.4 Transmission Measurement in the Near IR

5.4.1 Experimental Details

For the NIR liquid blood experiments, a self-constructed transmission cuvette with quartz glass windows (made from 3 mm thick Infracil) and thickness 1 mm (Teflon spacer) were used. The volume of the cell was ca. 30 μl and 190 μml including the steel capillary at the connection to the cuvette filling station described in Ch. 5.3. For the measurement of the reference spectra, tri-distilled water was used. The cuvette temperature was 27°C. Due to the poor size *relationship* of the blood substrate extinction signals to the background absorption of water in the near IR, a precise thermostating of the sample for suppressing the temperature dependent water band drift is definitely required. For this, a 1.23 kg copper ring ($\phi_i = 57$ mm, $\phi_a = 98$ mm, $\square = 20.5 \times 30$ mm) was made and placed over the steel housing of the measurement cuvette in order to damp oscillations in the cell temperature. This was measured with a Pt-100 measurement resistor with a resolution of 0.01°C and was held constant with a water circulation thermostat during the entire 4-day measurement series to about $\pm 0.02^\circ\text{C}$ (description of the apparatus in Ch. 5.3). The temperature differences between two sequentially occurring measurements of sample and reference were smaller than 0.01°C.

The volume flow rate of the cleaning liquids through the NIR cuvette was about 9.5 ml/min. A further difference to the measurements (conducted later) with the micro-CIRCLE™ ATR cell was the application of 1% water RBS solution (Carl Roth GmbH, Karlsruhe: RBS Neutral) instead of Extran (cf. Ch. 5.3) for cleaning the cuvette of protein depositions. RBS, however, was proven to be less appropriate for the reduction of protein adsorption such that the cuvette windows displayed a "milky" layer at the end of the measurement series with the 126 plasma samples. Generally, the problem of protein adsorption in the NIR transmission procedure is essentially less critical than with the ATR procedure due to the large thickness of 1 mm. Therefore, the determination of the length of time of the individual steps in Table 5.8 took place not through kinetic measurements, rather through a visual control of the measurement cuvette. The only exception was the determination of the temperature settling time after insertion of the sample. An adjustment of the sample temperature to the measurement temperature of 27°C, which was purposely chosen somewhat lower, already occurs at the input through the steel capillary tube (a further change of the measurement temperature toward the room temperature would have required a strong cooling effect of the thermostat and the control for holding the temperature constant would have been made difficult). For the transmission experiments, the homogenization of the samples and a filling free of air bubbles are, moreover, especially important.

Table 5.8: Temporal series of events during the filling and cleaning of the transmission cuvette.

<u>Reference:</u>	inject water (ca. 0.5 ml)
	1.5 min equilibration of the cell temperature
	1.5 min IR measurement
	0.5 min cleaning with ethanol
	2.5 min drying with nitrogen (4 bar)
<u>Sample:</u>	inject plasma (ca. 0.5 ml)
	1.5 min equilibration of the cell temperature
	1.5 min IR measurement
	0.5 min cleaning with RBS solution
	0.5 min cleaning with water
	0.5 min cleaning with ethanol
	2.5 min drying with nitrogen (4 bar)

For the NIR measurements, the Bruker IFS-66 spectrometer was equipped with a tungsten/halogen glow lamp (12V, 50W) as the radiation source, a CaF_2 beam splitter, and an InSb detector (Infrared Associates, Suffolk, UK $\phi = 4$ mm). The spectral region of 14000–4000 cm^{-1} was measured with a resolution of $\Delta\tilde{\nu} = 32$ cm^{-1} such that the interferograms were digitized with the maximum available sampling rate by the HeNe laser reference signal of ca. 31600 cm^{-1} . The symmetric deflection of the mirror around the ZPD position for the Mertz phase correction resulted with a resolution of $\Delta\tilde{\nu}_{\text{sym}} = 123.4$ cm^{-1} . The interferograms were apodized and were extended to 2048 points by "zero filling" for the FFT transformation so that the spectra were available with a "digital resolution" of $\Delta\tilde{\nu}_{\text{dig}} = 15.43$ cm^{-1} . The mirror velocity was chosen as $c_M = 1.90$ cm/s with which the frequency region of the measurement became 15.2–53.2 kHz at a sampling rate of 120 kHz. The measurement time for averaging 1500 interferogram scans was ca. 1.5 min per single beam spectrum (including FFT calculations).

In Fig 5.14a, the extinction signal of blood plasma in the near IR is shown. The negative band around 7000 cm^{-1} occurs through the water overcompensation in the reference measurement. In the special regions of 5400–4750 cm^{-1} and below about 4200 cm^{-1} , the background absorption of water is so large that a quantitative analysis of the extinction is no longer possible (Fig. 5.14d). The main information for the glucose prediction is found in both of the water transmission windows of ca. 6800–5400 cm^{-1} and 4750–4200 cm^{-1} , while in the "water free" area above ca. 7200 cm^{-1} , only very weak overtones and combination bands of glucose occur at a thickness layer of 1 mm (cf. Fig. 3.6). Fig. 5.14b shows the extinction spectrum of a milky (turbid) plasma sample with a pathologically increased blood fat concentration that is cloudy in the visible spectral region (sample tubes with $\phi = 10$ mm not transparent). The diffuse scattering in milky samples increases for shorter wavelengths where a linear increase of the extinction in wave number $\tilde{\nu}$ takes place in good approximation in the NIR transmission procedure. From the 126 plasma samples, two were strongly milky and were removed as outliers from all NIR calibrations. Through this, the population average ($M = 124$) for the triglycerides was reduced to $\bar{c}_{\text{pop}} = 158.1$ mg/dl, while the average values of the remaining substrates (Table 5.1) remained nearly unchanged.

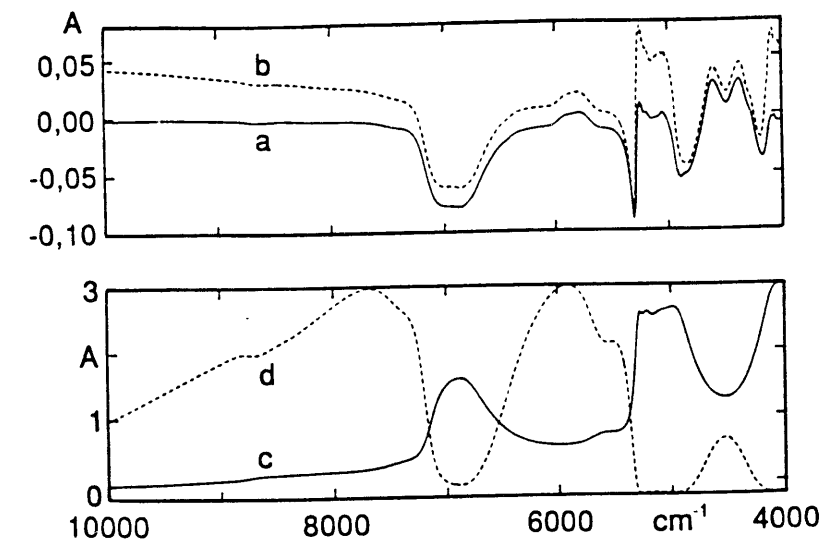


Fig. 5.14: FT-NIR spectra in transmission with thickness 1 mm: (a) average of the extinction spectra of the 126 blood plasma; (b) spectrum of a milky (turbid) sample; (c) extinction of water with empty cuvette as reference; (d) single beam spectrum of water (in random units).

In Fig. 5.15, the poor situation for the glucose calibration in the NIR is displayed. The strongest NIR bands at ca. 6350 cm^{-1} and 4400 cm^{-1} (Fig. 5.15a) generate extinctions on the order of magnitude of $1 \cdot 10^{-6}\text{ AU}/(\text{mg}/\text{dl})$ such that the signals for a physiologically normal value of $100\text{ mg}/\text{dl}$ are comparable to the noise of the extinction (c). In the correlation spectrum of glucose (b), the signals are only slightly noticeable as band shoulders. Both of the strong correlation bands in the water window $4750\text{--}4200\text{ cm}^{-1}$ occur through the positive correlation of glucose to the other blood substrates, mainly protein and cholesterol (cf. Table 5.2). The extremely poorly conditioned measurement problem of glucose determination in the NIR is well documented in Fig. 5.15.

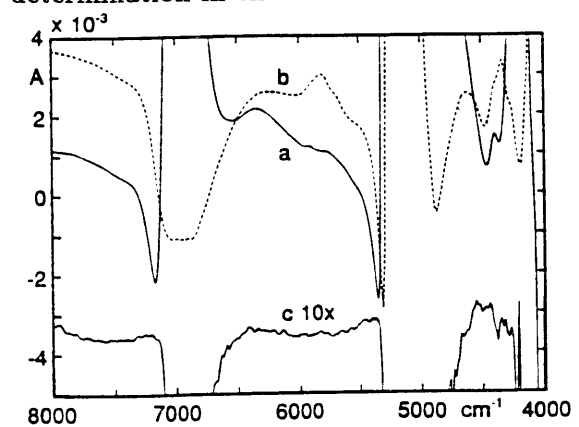


Fig. 5.15: FT-NIR spectra in transmission with thickness layer 1 mm: (a) extinction of $800\text{ mg}/\text{dl}$ glucose in an aqueous solution; (b) correlation spectrum of glucose for the 124 blood plasma ($\bar{c}_{\text{pop}} = 206.4\text{ mg}/\text{dl}$); (c) extinction noise from two water references (with offset and enlargement).

5.4.2 Results

All NIR calibrations were calculated with raw extinction spectra, i.e. the standards were not subjected to baseline correction, band normalization, scaled water subtraction, or similar techniques before the regression. Through these forms of data pre-processing, an improvement of the $\text{PRESS}^{1/2}$ statistics could not be achieved. The prediction quality of the PLS regression models was strongly dependent on the choice of spectral regions for the calibration. For a first determination, the NIR absorption spectra of crystalline pure components (Fig. 3.6), and to a small degree, the correlation spectra were also used. The integral limits were iteratively optimized using the $\text{PRESS}^{1/2}$ statistic. The best results were achieved for spectral regions outside of the strong water absorption bands for which the S/N ratio and the stability of the spectroscopic measurement are severely limited. All regressions were calculated with a point separation $\Delta\tilde{\nu}_{\text{cal}} = 2\Delta\tilde{\nu}_{\text{dig}} = 30.9 \text{ cm}^{-1}$ which compares favorably with the spectral resolution of the measurement $\Delta\tilde{\nu} = 32 \text{ cm}^{-1}$. The optimal results for glucose were obtained through use of the entire width of both water transmission windows with the spectral regions $6788\text{--}5461 \text{ cm}^{-1}$ and $4736\text{--}4212$ ($N = 62$ data points) where the determination of the interval limits was critical. Except for both of the aforementioned strongly milky samples, no further standards were classified as outliers.

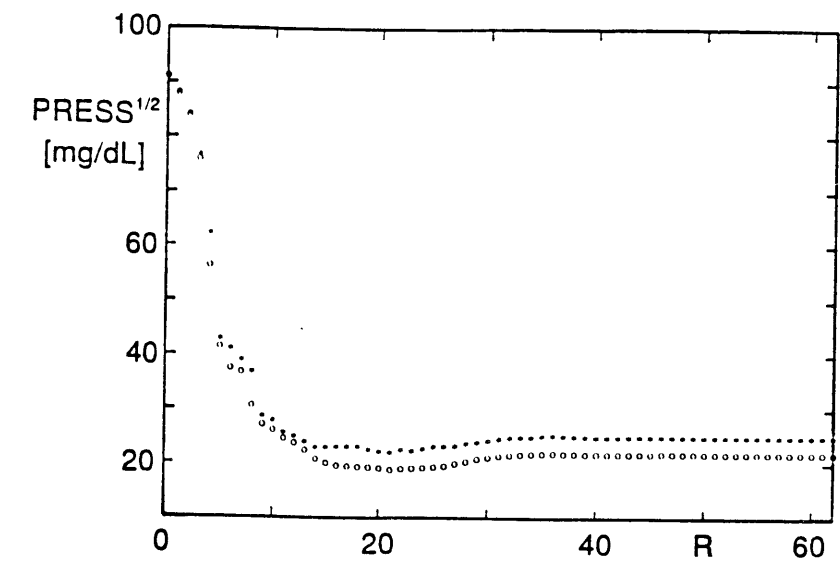


Fig. 5.16: $\text{PRESS}^{1/2}$ statistic of the glucose prediction in dependence on the PLS rank in the optimized spectral region (see text) with prediction of the standards (\circ) individually and (\star) in groups of 25 simultaneously.

As Fig. 5.16 shows, although the situation is poorer in comparison to the mid IR, a statistically stable NIR calculation is possible through selection of an appropriate spectral region. The minimum prediction error of $\text{PRESS}^{1/2} = 18.8 \text{ mg/dl}$ at $R_{\text{opt}} = 21$ increases only relatively little for higher inversion ranks up to ca. 22.0 mg/dl for the LS solution with $R_{\text{max}} = 62$. A similar statement is valid for the cross-validation with removal of 25 (1×24) standards simultaneously from the calibration. The form of the $\text{PRESS}^{1/2}$ curve changes comparably small through this relatively strong intervention into the regression model with 124 standards. In Fig. 5.17, the optimized glucose predictions for $R_{\text{opt}} = 21$ and cross-validation with individual standards are displayed. The prediction showed no recognizable bias; in the analysis of turbid-scattering samples, however, such an effect might be expected with the NIR transmission procedure as the prediction of both of the aforementioned lipamischen outliers with 305 ($c_{\text{ref}} = 250$) mg/dl and 358 ($c_{\text{ref}} = 304$) mg/dl suggests.

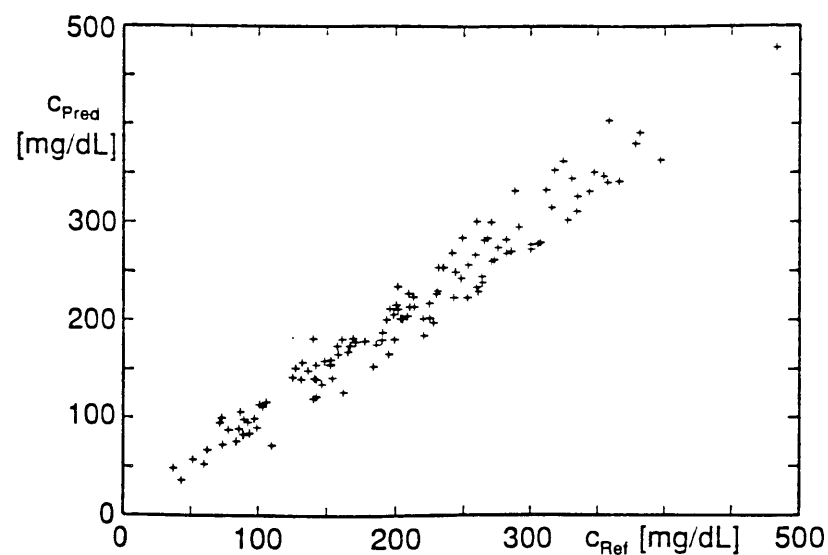


Fig. 5.17: Independent glucose predictions of the MSE optimized PLS model with the NIR transmission procedure versus the clinical-chemical reference values.

The interpretation of the PLS solution vectors in Fig. 5.18 is difficult due to the small specificity of the NIR extinctions and the relatively high optimal rank $R_{opt} = 21$, however, the glucose bands around 6350 cm^{-1} and 4400 cm^{-1} are recognizable. The application of only one water window to the glucose calibration generates prediction errors on the order of magnitude of $PRESS^{1/2} \approx 25\text{ mg/dl}$ ($6788\text{--}5461\text{ cm}^{-1}$) and $PRESS^{1/2} \approx 35\text{ mg/dl}$ ($4736\text{--}4212\text{ cm}^{-1}$) for slightly reduced optimal inversion ranks.³² In order to examine the information contents for the weak glucose overtone bands above ca. 7200 cm^{-1} , the extinction spectra were subjected to a baseline correction for compensation of the diffuse scattering. For this, in spectral region of $12000\text{--}8000\text{ cm}^{-1}$, an LS compensation line was approximated from the spectrum (extrapolated) and subtracted in the entire spectral region. A calibration of the "scattering-corrected" standards in the region $8501\text{--}7822\text{ cm}^{-1}$ yielded only insufficient prediction qualities with $PRESS^{1/2} \approx 65\text{ mg/dl}$ at $R_{opt} = 8$. Introductory attempts at a broadband calibration including the water bands at 7000 cm^{-1} also display no glucose correlation (best "prediction" with $R = 0$).

³²The PLS solution vectors of these regressions do not run parallel to the curves in Fig. 5.14 (cf. Eq. 4.45) for $R > 1$.

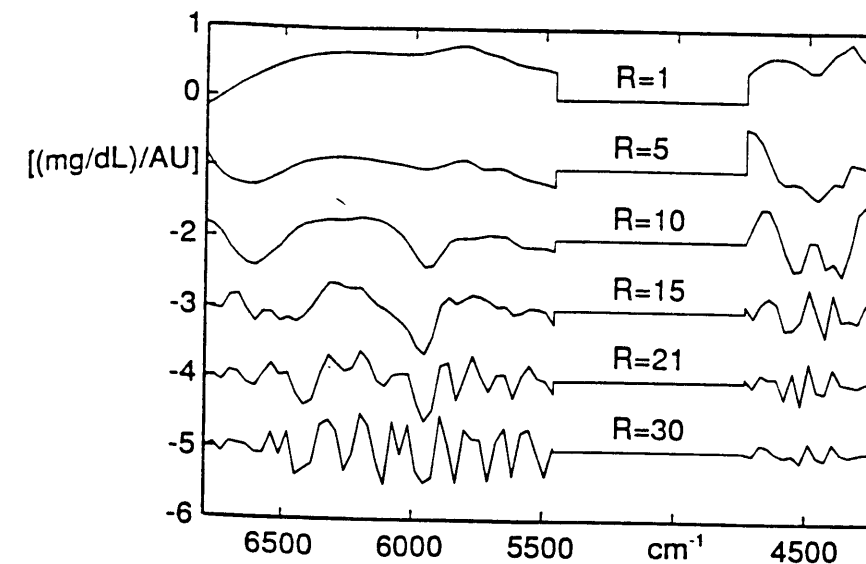


Fig. 5.18: PLS solution vectors of the glucose calibration in the region $6788\text{--}5461\text{ cm}^{-1}$ and $4736\text{--}4212\text{ cm}^{-1}$ with $\Delta\tilde{\nu}_{Cal} = 30.9\text{ cm}^{-1}$ for various inversion ranks (offset and normalization: $b_1/203$; $b_5/53949\text{--}1$; $b_{10}/92496\text{--}2$; $b_{15}/313282\text{--}3$; $b_{21}/674138\text{--}4$; $b_{30}/999385\text{--}5$).

For an estimation of the prediction error through noise and drift of the spectrometer as well as irreproducibilities in the sample handling, extinction spectra were calculated from each of two sequentially occurring water references (separation about 13 min) analogous to the procedure in the mid IR and were scalar multiplied with the optimal PLS solution vector. As a result of the larger temporal separations between the measurements, 26 pairs had to be removed from the simulation such that in the NIR, a total population of 99 baseline test spectra were available. These displayed, in the spectral region $10000\text{--}7200\text{ cm}^{-1}$ and $6600\text{--}5300\text{ cm}^{-1}$ as well as $4750\text{--}4200\text{ cm}^{-1}$, typically very flat forms with variations $< 1\text{ mAU}$ from the horizontal. The "physical" prediction errors were approximately normally distributed for all blood substrates examined with an average value that was only insignificantly different from zero so that the application of Eq. 5.5 for estimation of the inherent method error $\hat{\sigma}_{bio}$ is also justified in the near IR. With the optimal PLS solution vector of the glucose regression, the errors are scattered up to ca. $\pm 25\text{ mg/dl}$ with a standard deviation of $\hat{\sigma}_{spec} = 11.9\text{ mg/dl}$ with which the lower limit for the certainty of the NIR spectroscopic method can be estimated with $\hat{\sigma}_{bio} = 11.3\text{ mg/dl}$ which corresponds approximately to the $PRESS^{1/2}$ result of the ATR measurement procedure in the mid IR. A contribution to the "physical" error of the NIR measurement occurs through the temperature dependent drift of the water absorption band. To examine this effect, different spectra of water were measured with larger temperature differences.

The height of the dispersion-similar distinction bands displayed in Fig. 5.19 is linear for temperature differences up to about $\pm 15^\circ\text{C}$. Through scalar multiplication with the PLS solution vector ($R_{opt} = 21$), the prediction error of glucose can be estimated through temperature effects to about $-1.5\text{ (mg/dl)}/0.01^\circ\text{C}$ (maximum disturbance at PLS rank $R = 7$ with ca. $-2.2\text{ (mg/dl)}/0.01^\circ\text{C}$). By thermostating the cuvette to about $\pm 0.01^\circ\text{C}$, the portion of the temperature error on the entire "physical" error through noise and spectrometer instabilities is small.

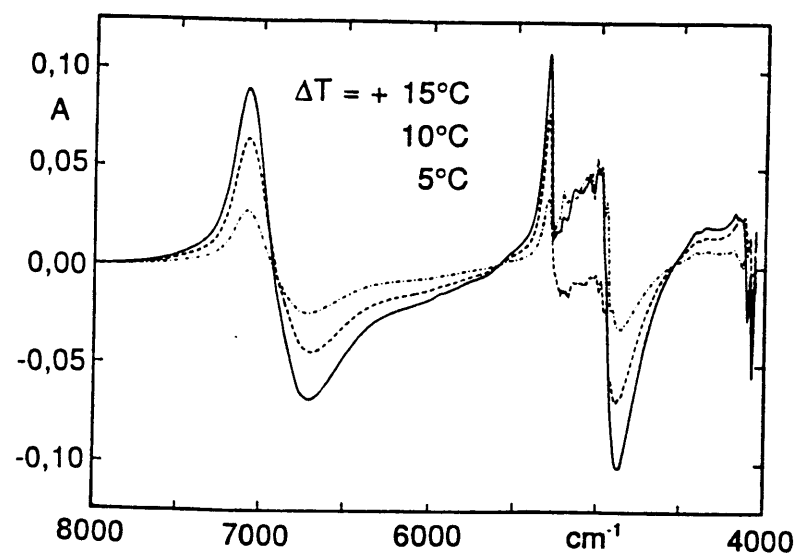


Fig. 5.19: Difference extinctions of water at various temperatures (thickness 1 mm; reference temperature 25°C).

Through the result of the glucose analysis of liquid blood sample with NIR spectra, the realization of a non-invasive pocket device for self-monitoring of blood sugar has neared. This results firstly, from the sufficiently large penetration depth of the NIR radiation into the skin (Ch. 6.2) and secondly, from the multiple technical possibilities for the construction of small NIR compact spectrometers; e.g. uncooled diode arrayed detectors for use in dispersive devices without mechanically moving components are commercially available up to ca. 1.7 μm . For the self-monitoring of blood sugar, the requirements on the analysis certainty are smaller than for the clinical use, and moreover, individual calibrations offer a further possibility for increasing the precision for an individual user. The results of the optimized calibrations of all blood substrates examined in the near IR are summarized in Table 5.9 (see Appendix D for further figures). The estimation of the prediction error through the clinical-chemical reference method $\hat{\sigma}_{\text{ref}}$, the spectroscopic measurement $\hat{\sigma}_{\text{spec}}$, and the biological variation of the IR spectra $\hat{\sigma}_{\text{bio}}$ (cf. Ch. 5.3) makes an exacter rating of the spectroscopic analysis methods and their potential improvement possibilities possible.

Table 5.8: Optimized results of the PLS calibrations of 124 blood plasma for the NIR transmission procedure (M is the number of standards, N the number of spectral data points in the regressions with $\Delta\tilde{\nu}_{\text{cal}} = 30.9 \text{ cm}^{-1}$; R_{opt} is the optimal PLS inversion rank; see text for the remaining variables; protein in [g/l], otherwise [mg/dl]).

	$\tilde{\nu}_{\text{max}} - \tilde{\nu}_{\text{min}}$	M/N	R_{opt}	$\hat{\sigma}_{\text{ref}}$	$\hat{\sigma}_{\text{spec}}$	$\hat{\sigma}_{\text{bio}}$	$\text{PRESS}^{1/2}$	VK_{pred}
Glucose	6788–5461 4736–4212	124/62	21	9.2	11.9	11.3	18.8	9.1%
Total Protein	6001–5508	122/17	7	.51	.44	.71	.98	1.4%
Total Chol.	6001–5508 4520–4212	123/28	21	1.6	6.4	5.1	8.3	3.8%
Triglyceride	6001–5508 4520–4212	124/28	20	1.2	9.3	10.0	13.7	8.7%
Urea	4736–4304	124/15	10	1.8	4.7	4.6	6.9	18.8%

Total Protein is also the strongest absorber in blood in the near IR after water. An NIR-spectroscopic analysis of blood sera in “diffuse transfection” (see Ch. 5.1) with an effective thickness of around 0.6 mm and five optical (interference) bandpass filters in the region 1680–2270 nm has been reported [171], where the average prediction error of the tabulated values there is 1.77 g/l. As Table 5.9 shows, the prediction quality can be clearly improved by a multivariate data analysis expressed in that the $\text{PRESS}^{1/2}$ curve hardly increases after reaching the optimal value of 0.98 g/l at $R_{\text{opt}} = 7$ for higher inversion ranks ($\text{PRESS}^{1/2} = 1.00 \text{ g/l}$ for $R = 17$). Two plasma samples were removed from the calibration due to outstanding Cook distances. An expansion of the spectral region into the water windows below 4700 cm^{-1} did not improve the result in Table 5.9, although a calibration solely in the region of $4736\text{--}4304 \text{ cm}^{-1}$ ($N = 15$) yielded an optimal prediction of $\text{PRESS}^{1/2} = 1.25 \text{ g/l}$. Due to its relatively high concentration, protein is strongly negatively correlated with the water content of the plasma such that the calibration against the water bands in the spectral region $7205\text{--}6711 \text{ cm}^{-1}$ ($N = 17$) leads to the representative result $\text{PRESS}^{1/2} = 2.09 \text{ g/l}$ ($R_{\text{opt}} = 7$), while for the remaining blood substrates, the regions with strong water absorptions must be strictly left out of the calibration. The prediction results of both of the strongly milky plasma with the optimal PLS solution from Table 5.9 suggests a possible systematic error of the protein prediction for turbid samples with 71.5 ($c_{\text{ref}} = 72.3$) g/l and 65.2 ($c_{\text{ref}} = 67.0$) g/l. In comparison to the ATR method in the mid IR, the NIR transmission procedure displays an even better $\text{PRESS}^{1/2}$ statistic, and regarding the error estimation, the same conclusions are valid; the NIR-spectroscopic determination of total protein is possible with clinically acceptable certainty ($VK \leq 3\%$) without problems.

Total Cholesterol has already been analyzed as well with simple spectrometers and NIR reflection methods in blood serum [172,173]. Lodder et al. estimate the *theoretically* achievable MSE prediction error for their method to be ca. 12.6 mg/dl where a classification of the sera should result in three different “biological clusters” (triglycerides could not be successfully calibrated in the work mentioned). Peuchant et al. report correlation coefficients of $r = 0.965$ and $r = 0.982$ for two different reference methods for the cholesterol prediction of blood sera spectra of 60 hospital

patients. The optimized result of the broadband calibration with FT-NIR spectra (Ch. 5.9) is with $\text{PRESS}^{1/2} = 8.3 \text{ mg/dl}$ nearly identical to the result of the analysis in the mid IR, where this is also valid for the composition of the prediction error in the error estimation. One plasma had to be removed from the calibration due to an outstanding t -residuum. The correlation coefficient between the independent predictions (in the sense of Eq. 4.70) and the clinical-chemical references was $r = 0.982$. Both of the milky standards were predicted with 204.8 ($c_{\text{ref}} = 216.7$) mg/dl and 230.6 ($c_{\text{ref}} = 232.3$) mg/dl. In the error estimation in Table 5.9, it should be noted that the error through the bias-containing reference method can be more realistically approximated with 2.4 mg/dl (cf. Ch. 5.3). The region of clinical acceptance ($VK \leq 6\%$) is achieved for cholesterol.

For the triglyceride, the calibration results were optimized due to the chemical similarity in the same spectral region as for cholesterol. The larger difficulties for the prediction of the triglycerides as a result of smaller extinction signals cause increased error parts $\hat{\sigma}_{\text{spec}}$ and $\hat{\sigma}_{\text{bio}}$ where the optimal result $\text{PRESS}^{1/2} = 13.7 \text{ mg/dl}$ is worsened in comparison to the ATR method in the mid IR. For the triglycerides, no standards were classified as outliers. A systematic influence of the prediction through turbid samples appears probable with the results for both milky plasma of 349.1 ($c_{\text{ref}} = 310.3$) mg/dl and 653.5 ($c_{\text{ref}} = 640.3$) mg/dl. The calibration in the spectral region of the upper water window $6001\text{--}5508 \text{ cm}^{-1}$ ($N = 17$) yielded alone a $\text{PRESS}^{1/2} = 16.3 \text{ mg/dl}$ at $R_{\text{opt}} = 10$. The region of clinical acceptance ($VK \leq 7\%$) is approximately achieved.

Urea could be successfully calibrated in the region of the water window below 4750 cm^{-1} where, however, the optimized prediction result $\text{PRESS}^{1/2} = 6.9 \text{ mg/dl}$ is clearly poorer than that in the mid IR (2.9 mg/dl). Urea is the blood substrate in Table 5.9 with the smallest concentration and signifies the current limits of the NIR spectroscopic analysis method. The optimal predictions for urea already display a clear bias in the direction of the average value of $\bar{c}_{\text{pop}} = 37 \text{ mg/dl}$. The high value for $\hat{\sigma}_{\text{bio}} = 4.7 \text{ mg/dl}$ suggests only small chances for realization of a future application in the clinical-chemical routine analysis.

For uric acid, the spectroscopic calibration in the near IR could not yield significant improvement in comparison to the result for the prediction with the population average value (at "inversion rank" $R = 0$). A tabulated summary of the calibration results for liquid blood plasma in the near and mid IR with discussion can be found in the concluding Ch. 7 of this work.

6 Noninvasive Measurement Procedure

6.1 The Skin

The skin is the largest organ of the human body with ca. 15% of the total weight. It displays a high mechanical stability and hinders the penetration of chemicals, bacteria, and sunlight into the body [174]. Further important tasks of the skin are the regulation of body temperature and body content salt. In a coarse treatment of it, the skin can be divided into three tissue layers: the *epidermis* (overskin), the *dermis* (leather skin), and the *subcutaneous fatty tissue*. The latter serves for heat isolation as well as absorption of mechanical shocks and displays according to experience an individually strongly oscillating thickness. The structure of the upper skin layers is sketched in Fig. 6.1 (from [175]):

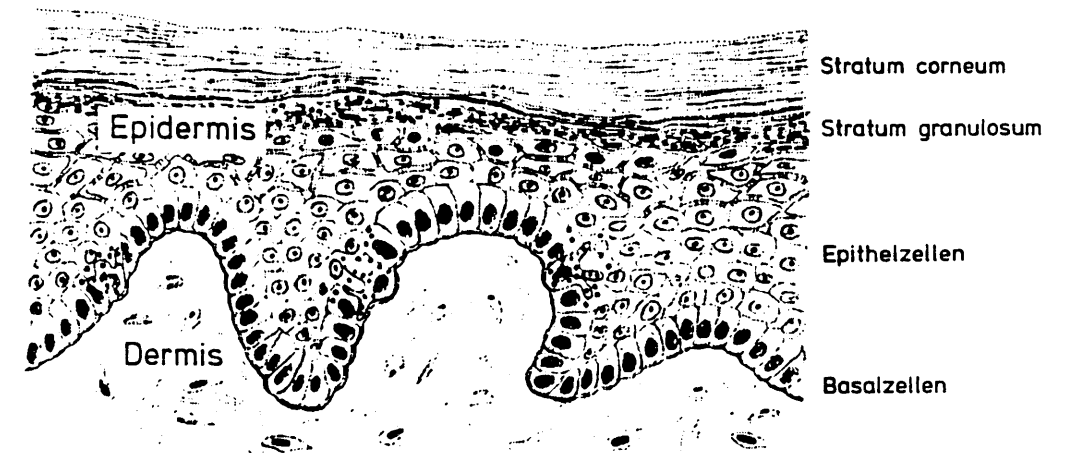


Figure 6.1: Schematic cross-section of the epidermis.

The thickness of the epidermis is notably constant over the entire body surface area and has a value around $60\text{--}100 \mu\text{m}$ [174]. The main task of the epidermis is the constant new construction of its upper layer, the ca. $10\text{--}15 \mu\text{m}$ thick *stratum corneum*. This consists of lamellarly thickly packed dead cells that are continually mechanically rubbed off. Through cell division in the basal layer, the construction of epithelial cells results which, on their way to the outside, take on a lamellar form, connect themselves to each other, dehydrate, and die off (through "calloused skin" generation, the stratum corneum can achieve thicknesses up to 0.6 mm [174]). The water content of stratum corneum *in vivo* is with ca. 70 wt.% smaller than in the lower skin layers [176]. The epidermis does not contain any blood passages such that the providing of energy to the living cells is maintained solely through diffusion of nutrients into the *interstitial fluid* of the spaces between the cells. The dermis which consists of 98% collagen fibers is connected to the underside of the epidermis and contains a thick network of blood capillaries. For the providing of nutrients, this passageway network is strongly overdimensioned. It is additionally required for the transport of body heat by convection from the skin surface area where up to 10% of the total blood volume of the body

is concentrated in the skin [175]. The thickness of the dermis whose collagen fibers display an enormous stability to strain varies over the surface area of the body in the region of ca. 1–4 mm [174].

In medicine, one differentiates between three different "spaces" from which the body is built: (1) The cellular space (the cell inside), (2) the intracellular or interstitial space between cells as well as (3) the volume of space with the arteries, capillaries, and veins. The venous glucose concentration can temporarily lie up to ca. 30% below the arterial, whereby the stationary values are identical. The medically relevant parameter is the glucose concentration in the capillaries which, for quite some time, has been determined through puncture, e.g. of the fingertip or the earlobe. For the non-invasive spectroscopic determination of glucose, it is not necessary that the IR measurement radiation is focused onto a larger blood passageway. The small glucose molecule in comparison to many other organic molecules is water soluble and diffuses along a concentration gradient for providing nutrients through the interstitial space to the living cell. Glucose is already contained immediately below the stratum corneum in the body. After entrance into the cell, the glucose is burned so that the concentration in the cellular space is very small. Since the epidermis consists on the order of about 90 vol-% cellular and 10 vol-% interstitial space, an appropriate reduction of the glucose signal in comparison to blood must be assumed in the examination of epidermal tissue. Also, there are no trustworthy data available about the time delay due to diffusion and the eventual stationary differences between the glucose concentrations in the capillaries and in the interstitial space of the epidermis. For the tissue fluid of the lower skin layers, experimental delay time constants of ca. 5 min to the capillary blood and stationary identity were determined [13,14].

In order to increase the chances of success of a non-invasive measurement technique, a penetration depth of the IR radiation into the tissue of at least ca. 150 μm was, therefore, desired in this work in order to also reach the most upper layer of the dermis which is densely comprised of many passageways (so-called venous plexus at a depth of ca. 125 μm [177]). For many reasons, the region of the inner lip can be seen as an appropriate skin region on the surface area of the body for a non-invasive glucose measurement using transcutaneous diffuse deflection. As opposed to the stratum corneum, the inner lip possesses a mucous skin layer of equal thickness³³ which, in comparison to the stratum corneum, does not build a compact layer and is transparent (resorption of medication into the mucous skin layers of the mouth) for diffusion processes so that the glucose also diffuses into the upper skin layers. Furthermore, the constant temperature relationships on the inner side of the lips are advantageous where a possible translation of the position of the absorption bands of the tissue water is avoided. The most important reason is the exceptionally good blood circulation of the lip tissue.

Biological tissue is, due to its cellular construction and numerous further "biological" variabilities, not optically homogeneous. During the propagation of optical radiation in the skin, therefore, the diffuse scattering in the tissue plays a decisive role next to absorption. For descriptive purposes, the radiation transport equation is used [179] which is equivalent to the Boltzmann equation from the transport theory of electrically neutral particles [180] and, for monochromatic radiation, reads:

$$\mathbf{s} \cdot \nabla L(\mathbf{r}, \mathbf{s}) \doteq \frac{d}{ds} L(\mathbf{r}, \mathbf{s}) = -(\mu_a + \mu_s)L(\mathbf{r}, \mathbf{s}) + \mu_s \int_{4\pi} p(\mathbf{s}, \mathbf{s}') L(\mathbf{r}, \mathbf{s}') d\Omega' \quad (6.1)$$

³³Prof. Dr. med. H. Otto (Pathological Institute, Dortmund) graciously made many tissue cuts for these examinations available.

Here, $L(\mathbf{r}, \mathbf{s})$ is the beam density [$\text{W m}^{-2} \text{sr}^{-1}$] at the location \mathbf{r} and in the direction of the unit vector \mathbf{s} in the tissue, i.e. $L(\mathbf{r}, \mathbf{s}) d\Omega$ is the radiation power that, inside of the space angle $d\Omega$ around the direction \mathbf{s} , impinges a unit area at \mathbf{r} that is perpendicular to \mathbf{s} ; μ_a is the absorption coefficient [mm^{-1}], μ_s is the scattering coefficient [mm^{-1}] of the tissue, and $p(\mathbf{s}, \mathbf{s}')$ is the so-called phase function which gives the probability that a photon is deflected through an individual scattering event from an old direction \mathbf{s}' into the new direction \mathbf{s} . The first term on the right side of Eq. 6.1 describes the loss in $L(\mathbf{r}, \mathbf{s})$ for propagation in the direction \mathbf{s} through absorption and diffuse scattering.³⁴ The second term describes the gain in $L(\mathbf{r}, \mathbf{s})$ through that radiation that is scattered from all other directions \mathbf{s}' in the direction \mathbf{s} ; here, one integrates over the entire space angle 4π , where the weighting function $p(\mathbf{s}, \mathbf{s}')$ is normalized as the probability density:

$$\int_{4\pi} p(\mathbf{s}, \mathbf{s}') d\Omega' = 1 \quad (6.2)$$

The transport equation, Eq. 6.1, sets up the energy equilibrium for radiation of a particular wavelength for a differentially small volume at the location \mathbf{r} . Here, it is required that the average separation between two scattering events is so large that no influence results amongst themselves; moreover, inelastic scattering as well as fluorescence and polarization effects are neglected. A description of the propagation of the electromagnetic waves under consideration for all defractions and interferences is possible with the help of the Maxwell equations, however, analytic solutions in turbid media are only available for simple models [181]. The heuristic corollary, Eq. 6.1, is visibly and mathematically simpler and the applicability to biological tissue in the visible and near IR spectral region has been shown [182,183]. The diffuse scattering of optical radiation in biological tissue takes place mostly through stochastic refraction/reflection on objects that are larger than the wavelengths used [184]; the diameter of an epithel cell, e.g. is about 6–7 μm . For this type of diffuse scattering, a strong forward direction of the phase function, i.e. a relatively small direction deflection "per scattering event", is characteristic. In practice, electromagnetic theory is used only for frequencies up to ca. 300 GHz for describing the radiation propagation in tissue, since then the wavelengths are significantly larger than the cellular structures, and diffuse scattering can be neglected [185,186].

Exact analytical solutions of the transport equation, Eq. 6.1, are known only in special cases [187]. The simplest is the case of dominant absorption, $\mu_a \gg \mu_s$, for which Eq. 6.1 becomes the Lambert-Bouguer Law (Eq. 3.1) and is the case, e.g. in the mid IR for biological tissue. In the reverse case, $\mu_s \gg \mu_a$, Eq. 6.1 can be approximately substituted by the diffusion equation [188] which is analytically solvable for simple geometric boundary conditions. Due to the aforementioned forward characteristic of the phase function and the relatively small penetration depth of NIR radiation into the skin, the diffusion approximation is not valid in the near IR, rather Eq. 6.1 must be solved with a numerical procedure [182]. From the various numerical methods for the solving of the Boltzmann transport equation [187], the following Monte Carlo simulation procedure used is most appropriate, since it can be flexibly adjusted and processed to the experimental boundary conditions concerning the geometry of the radiation source, tissue, and detector.

³⁴According to the usual notation, the reduction coefficients μ_a and μ_s are based on natural logarithms.

6.2 Monte Carlo Simulation of the Optical Characteristics of Skin in the Near IR

The radiation from outside directed onto the skin is exponentially damped with $\exp(-(\mu_a + \mu_s)l)$ in the tissue, i.e. absorbed and scattered away from the original direction. In the Monte Carlo simulation, the radiation is described as a discrete flow of photons. In the computer, a random path is simulated for each photon through the tissue, and the macroscopic optical characteristics are determined by averaging over a larger number of photon "histories" (see e.g. [189] and the references cited there). A schematic representation of the conditions during penetration of an NIR photon into the skin is given in Fig. 6.2. As shown in the following, the penetration depths of radiation of the long wave near IR into the skin are small such that smaller body parts like e.g. the earlobe, cannot be completely penetrated by the radiation. In Fig. 6.2A, therefore, the practically important case of a photon is shown which, after multiple scattering in the skin, is diffusely reflected. The separation l [mm] between two scattering events is a statistical variable in the Monte Carlo simulation which results in the given exponential distribution with average value $1/\mu_s$ in Fig. 6.2B. Along its random path through the skin, the photon loses energy with $\exp(-\mu_a l)$. With exception of the cross-wise striated fiber tissue of the skeletal muscle, biological tissue is isotropic [190], i.e. the phase function is only dependent on the direction change $\cos(\theta) = s^T s'$ (see Fig. 6.2C). This corresponds to a factorization $p(s, s') = 1/(2\pi) p_\theta(\cos(\theta))$, where the factor $1/(2\pi)$ yields the equally formed azimuthal distribution of the new photon direction s about the old direction s' . The most important parameter for describing the direction characteristic of the scattering is the mean value of the distribution function $p_\theta(\cos(\theta))$, the so-called *anisotropy factor*:

$$g \doteq \int_{-1}^1 p_\theta(\cos(\theta)) \cdot \cos(\theta) \cdot d(\cos(\theta)) \quad (6.3)$$

For the anisotropy factor, $-1 \leq g \leq 1$ is valid where the extreme values correspond to an extreme forwardly ($g = 1$) or backwardly ($g = -1$) directed Dirac function. The complete phase function for biological tissue can be described with the parameter g in good approximation [191–193] with a Henyey–Greenstein function [194]:

$$p_\theta(\cos(\theta)) = \frac{1}{2} \frac{1 - g^2}{\sqrt{(1 + g^2 - 2g \cos(\theta))^3}} \quad (6.4)$$

In Fig. 6.2C, the function Eq. 6.4 is shown for the realistic value $g = 0.7$; as the figure shows, the probability for a "direction reversal" ($|\theta| \geq 90^\circ$) by an individual scattering event in the tissue is extremely small. For $g = 0$, the scattering is isotropic with uniform distribution over the entire space angle 4π (corresponds to a circle around zero in Fig. 6.2C).

During entrance of the radiation into the skin, Fresnel reflection losses as a result of the non-matching refraction indices can occur. The refraction index of various biological tissue has been experimentally determined to be 1.38–1.41 at 633 nm (in comparison to $n = 1.33$ for water [21]). Wilson et al. suggest for 633 nm the equation $n \approx 1.53 - 0.2W$ in dependence on the water content W [g/g] of the tissue [177] which is consistent with the results from [195]. The refraction index of water falls off very flatly at the transition from visible to the near IR and at $\lambda = 1.57 \mu\text{m}$ is $n = 1.32$ [21]. In this work, $n = 1.37$ was assumed for skin at $1.57 \mu\text{m}$ which corresponds to the realistic water content of $W = 0.75$ for the upper most skin layers (see Ch. 6.1). At other

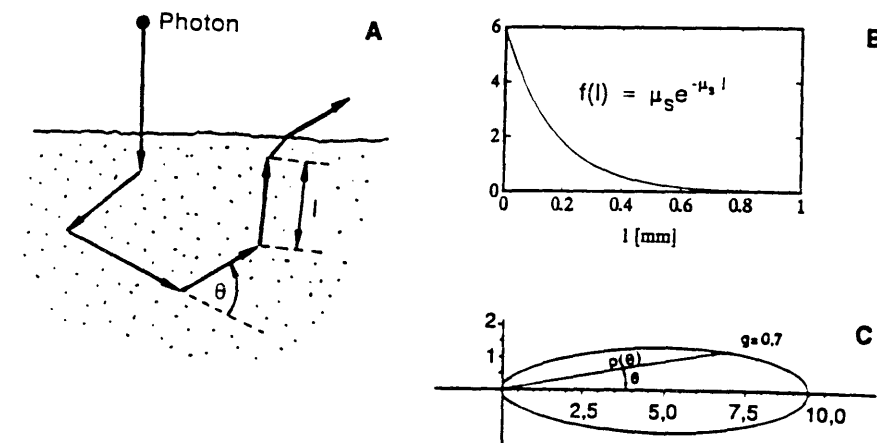


Figure 6.2: (A) Diffuse reflection of a photon in the skin; (B) Probability density of the pathlength l between two scattering events for $\mu_s = 6 \text{ mm}^{-1}$; (C) An example of a phase function in biological tissue (Henyey–Greenstein function with $g = 0.7$ in polar coordinates, see text for details).

wavelengths than $\lambda = 1.57 \mu\text{m}$, the value of $n = 1.37$ was slightly modified corresponding to the water dispersion (see Table 6.1). In the Monte Carlo calculations, the skin surface area was simulated as an ideally, smooth, even bordering surface for which Snell's refraction law and the Fresnel formulas for unpolarized radiation could be applied. This procedure is justified by the results of Bruls et al. who examined the influence of surface area roughness of the stratum corneum in the UV spectral region [196]. After scattering on the surface area, ca. 75% of the radiation power displays an angle deflection $< 7.5^\circ$ to the "Snell preferred direction" at $\lambda = 254 \text{ nm}$ so that the diffuse surface area scattering of the skin can be neglected for the longer wavelengths of the near IR.

Currently, the largest problem for a precise Monte Carlo simulation of skin is the lack of publications with experimentally determined parameters μ_a , μ_s , and g . This lies in the fact that the majority of medical applications use photo-thermal effects with intense laser sources for specifically heating a (sick) tissue volume so that the optical parameters of the skin were mostly examined at the wavelengths of the technically important lasers (mainly HeNe laser at 633 nm, in the NIR, Nd:YAG lasers at $1.06 \mu\text{m}$ or more seldom $1.32 \mu\text{m}$, cf. [183]). On the other hand, the direct measurement of the optical parameters is experimentally difficult, since here, very thin tissue layer, ($d \ll 1/\mu_s$) must be examined. For this reason, the desired values are indirectly determined from three common measurements independent of each other which can be used to back out the parameters μ_a , μ_s , and g . For this, the diffuse (total) transmission and the diffuse reflection as well as the direct (unscattered) transmission are mostly used [183]. Reliable methods for solving this complicated inverse problem, however, have been only recently available [182], and at the present time, there exists solely one individual publication in which the optical parameters μ_a , μ_s , and g were determined in this fashion over a broader spectral region including the near IR. Parsa et al.

examined rat livers in the spectral region of 350–2200 nm [197] (see Fig. 6.3) in their work. The results from Parsa et al. can be used in the Monte Carlo simulation of human skin for an estimation of the desired coefficients and their dependence on wavelength. As Fig. 6.3A shows, the absorption is dominated in the long wave near IR by both water bands at 1420 nm (7042 cm^{-1}) and 1940 nm (5155 cm^{-1}). The so-called “therapeutic transmission window” connects to the visible region of ca. 1300–600 nm in which at lower tissue absorption, the largest penetration depths into the skin can be achieved [198]. Below 600 nm, specific chromophores like hemoglobin, melanin, and further pigments absorb [199]. In the UV spectral region, the stratum corneum is already not transparent through the strong absorption of proteins and nucleic acids as has been known for quite some time [200]. The scattering coefficient μ_s is almost larger than μ_a in the entire spectral region of Fig. 6.3B and tends to decrease with increasing wavelength. The correlation of the peaks in the spectra of μ_a and μ_s in Fig. 6.3 is obviously an artifact of the approximation for solving the inverse problem in [197]; especially, the band of μ_s around 1940 nm cannot be clearly explained. The comparison of the absorption coefficient μ_a of the rat livers with the values for the water absorption from [21] yields some insight into the eventual systematic errors in the spectral region: While both values for the absorption peak at 1420 nm are identical $\mu_a \approx 27\text{ cm}^{-1}$ within the certainty of reading the diagram, the value $\mu_a \approx 73\text{ cm}^{-1}$ at 1940 nm (Fig. 6.3A) clearly shows too large of a variation to water with $\mu_a = 120\text{ cm}^{-1}$.

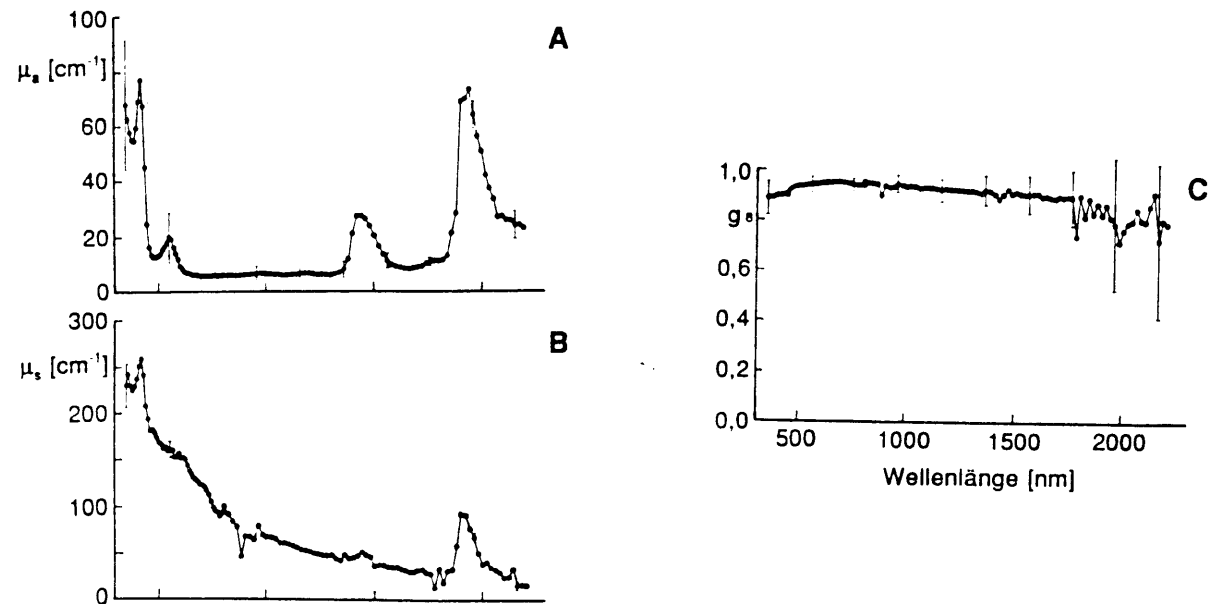


Figure 6.3: A absorption coefficient, B scattering coefficient, and C anisotropy factor of rat livers *in vitro*; shown are the average values from 11 samples from 6 rats in intervals of 200 nm. The error bars (\pm standard deviation $\hat{\sigma}$) are given by the biological variation (from [197]).

The important results from Fig. 6.3 are: (1) Above ca. 1400 nm, the absorption of biological tissue is nearly identical to water absorption. (2) In the therapeutic window 1300–600 nm, the tissue absorption is mostly constant. (3) The phase function of the scattering is strongly forward directed in the visible and the near IR with an approximately constant anisotropy factor. (4) The scattering coefficient μ_s decreases proportionally with $\lambda^{-1.4}$.

A further useful instrument for determining the optical parameters in skin *in vivo* are the so-called simulation transformations of the transport equation. One can analytically show that for the beam densities $L(\mathbf{r}, \mathbf{s})$ and $L'(\mathbf{r}, \mathbf{s})$ [$\text{W mm}^{-2}\text{ sr}^{-1}$] in two turbid bodies with identical geometric boundary conditions, the following is valid [201]:

$$L_N(\mathbf{r}, \mathbf{s}) = \sum_{n=0}^N \sum_{m=-n}^n a_{mn}(\mathbf{r}) Y_n^m(\theta, \varphi) = \sum_{n=0}^N \sum_{m=-n}^n a'_{mn}(\mathbf{r}) Y_n^m(\theta, \varphi) = L'_N(\mathbf{r}, \mathbf{s}) \quad (6.5)$$

$$\text{for: } \begin{aligned} 1) & \mu_a = \mu'_a \text{ and (6.5a)} \\ 2) & \mu_s(1 - p_n) = \mu'_s(1 - p'_n) \text{ for } n = 1, 2, \dots, N \text{ (6.5b)} \end{aligned}$$

with the phase functions:

$$\begin{aligned} p_\theta(\cos(\theta)) &= \sum_{n=0}^{\infty} \sqrt{\frac{2n+1}{2}} p_n P_n(\cos(\theta)) \\ p'_\theta(\cos(\theta)) &= \sum_{n=0}^{\infty} \sqrt{\frac{2n+1}{2}} p'_n P_n(\cos(\theta)) \end{aligned}$$

Here, the Y_n^m are the spherical functions in \mathbf{R}^3 , the P_n are the Legendre polynomials and the a_{mn} , a'_{mn} , p_n , and p'_n are the coefficients of the orthogonal series expansion [202]. The similarity relationship (Eq. 6.5) states that the beam densities $L(\mathbf{r}, \mathbf{s})$ and $L'(\mathbf{r}, \mathbf{s})$ in two different turbid media “are identical up to an N th order” for the case that $\mu_a = \mu'_a$ and the Legendre moments of both phase functions fulfill Eq. 6.5b. The Legendre moment of first order $p_1 \equiv g$ is identical to the anisotropy factor.³⁵ Of practical importance is the case of the ideal diffuse radiation flow with small $a_{mn} = 0$ for $m > 1$. For this case, constancy of the so-called “reduced scattering coefficient” $\mu_s(1 - g)$ is solely required in Eq. 6.5b. Since the reflected radiation from the skin is ideally diffuse in good approximation, the similarity transform of first order can be used. Wilson et al. even come to the conclusion through experiments and from numerous Monte Carlo simulations that the diffuse reflection of *each* homogeneous, semi-infinite medium is a *unique* function of $\mu_s(1 - g)/\mu_a$ and increases monotonically with this relationship (see Fig. 4 in [177]). This observation corresponds with the results of the known Kubelka–Munk theory which describes the transport of ideal diffuse radiation ([203], see e.g. also [204]). If two of the three parameters μ_a , μ_s , and g are known, then the similarity relationship can be used to determine the third parameter with the help of the diffuse reflection of the medium.

Monte Carlo simulations of the skin were conducted in the region of both NIR water transmission windows at the wavelengths with the maximum extinction signals of glucose, $\lambda = 1.57\text{ }\mu\text{m}$ (6350 cm^{-1}) and $\lambda = 2.27\text{ }\mu\text{m}$ (4400 cm^{-1}); for comparison, the therapeutic window at $\lambda = 1.25\text{ }\mu\text{m}$ (8000 cm^{-1}) was additionally examined. Due to the lack of the experimental data, μ_a , μ_s , and g were assumed to be constant in position in the Monte Carlo calculations of this work, i.e. the skin was simulated without a layered structure. This assumed simplification, which is often found in the literature, is additionally justified in the case of the intended diffuse reflection experiment, since the layered structure of the skin in the region of the inner lips is less prominent. Up to now, the optical parameters of the human skin were determined solely for the wavelength of the HeNe laser.

³⁵For the Henyey–Greenstein phase function (Eq. 6.4), the following is, furthermore, valid: $p_n = g^n$ ($n = 0, 1, \dots$) [201].

Jacques et al. determined *in vitro* for the dermis at 633 nm: $\mu_a = 0.27 \text{ mm}^{-1}$, $\mu_s = 18.7 \text{ mm}^{-1}$ and $g = 0.81$ [192]. The value $g = 0.81$ of the anisotropy factor, which is smaller for skin than for the very homogeneous tissue of the liver,³⁶ was used for the simulation in the near IR. An overview over the optical parameters used is given in Table 6.1. At $\lambda = 1.57 \mu\text{m}$ and $\lambda = 2.27 \mu\text{m}$, the absorption coefficients μ_a of water were taken from the figures in [21]; at $\lambda = 1.25 \mu\text{m}$, the value for skin from [192] at $\lambda = 633 \text{ nm}$ was used due to the constancy of μ_a in the therapeutic window (Fig. 6.3A). In comparison to rat liver, the skin absorbs only about half as strongly at 633 nm, while the absorption at $1.57 \mu\text{m}$ and $2.27 \mu\text{m}$ is nearly identical (Fig. 6.3A). The scattering coefficients μ_s of the skin are larger than the corresponding values for the more homogeneous rat liver for all wavelengths in Table 6.1. The value of $\mu_s = 5.0 \text{ mm}^{-1}$ at $\lambda = 1.57 \mu\text{m}$ was determined iteratively by adjustment of the Monte Carlo results of the diffuse reflection of the skin to the published values. There exists two publications about the diffuse reflection of human skin in the spectral region of the near IR. Jacques et al. examined in 1955 the underarm *in vivo* with an Ulbricht sphere [205]. No reliable reflection standards were available at that time in the near IR such that the absolute height of the reflection spectrum shown there ($R_{\text{diff}} = 12\%$ at $1.57 \mu\text{m}$) is uncertain. In this work, the value $R_{\text{diff}} \approx 5\%$ for $\lambda = 1.57 \mu\text{m}$ was used as the intended value, which was determined shortly afterwards by Hardy et al. by a complete goniometric measurement for skin *in vitro* [206]. Reliable values for both of the other wavelengths cannot be found in the Hardy work due to the small thickness of the skin samples (max. 1.6 mm) and the disturbance by background radiation. Noteworthy is that the values of μ_s at $1.57 \mu\text{m}$ and 633 nm (from [192]) follow the relationship $\mu_s - \lambda^{-1.4}$ in good approximation which was also found for rat liver (Fig. 6.3B). Therefore, the values of μ_s at $2.27 \mu\text{m}$ and $1.25 \mu\text{m}$ in Table 6.1 were interpolated and extrapolated with this relationship. Furthermore, the good agreement of our Monte Carlo results with the scattering parameters $\mu_s = 5.0 \text{ mm}^{-1}$ and $g = 0.8$ at $1.57 \mu\text{m}$ to the (up to now only) goniometric measurements of diffuse transmission of thin skin samples (0.43 mm) in [206] is worth mentioning.

Table 6.2: The optical parameters for the Monte Carlo simulation of the skin

λ [μm]	$\tilde{\nu}$ [cm^{-1}]	μ_a [mm^{-1}]	μ_s [mm^{-1}]	g	n
1.25	8000	0.3	7.0	0.8	1.37
1.57	6350	0.9	5.0	0.8	1.37
2.27	4400	1.8	3.0	0.8	1.34

The values in Table 6.1 are the best possible estimates at the present time for the optical parameters of the skin in the near IR spectral region. Statements about the error bars and biological variations are not possible due to the lack of experimental data, however, the certainty of the values is sufficient in order to make semi-quantitative statements about the realization possibilities of a non-invasive measurement procedure for blood glucose in the framework of a Monte Carlo simulation.

³⁶For comparison: the optical parameters of rat liver at $\lambda = 633 \text{ nm}$ are: $\mu_a = 0.65 \text{ mm}^{-1}$, $\mu_s = 14.37 \text{ mm}^{-1}$ and $g = 0.95$ (see Table 1 in [197]).

In the simulation, a photon beam with a point-shaped diameter was directed perpendicularly onto a piece of skin with semi-infinite expansion. Photons were generated until a total of 10,000 photons were diffusely reflected. Their data were averaged in order to determine the macroscopic optical tissue characteristics, where the energy of the photons upon exit from the hand was used as the waiting factor. The "history" of each photon was simulated until the photon energy in the tissue through absorption and Fresnel exit from the skin sank to the $5 \cdot 10^{-4}$ th portion of the initial energy (it was verified for the calculations that the results for this simulation were not influenced by this limiting value). The Monte Carlo simulation was programmed in MATLAB [130]. The calculation times on an IBM-PC (386AT, 33 MHz) varied between 4–10 hours. For a complete description of comparable program codes, see [207] and [208].

An important result of the Monte Carlo simulations is that in the region of the glucose overtone bands at $\lambda = 1.57 \mu\text{m}$, no sufficient transmission signals for a non-invasive measurement can be obtained. For planar, parallel tissue layers with thicknesses of 1 mm, 2 mm, and 3 mm, diffuse (total) transmissions of about 10%, 1%, and 0.1% were calculated. The average pathlength of the transmitted radiation power in the tissue is ca. 1.4 times the tissue thickness. Since the thinnest body parts such as earlobes, skin folds, etc. already display thicknesses of at least 3 mm, a transmission measurement only with wavelengths in the region of the therapeutic window of ca. 1300–600 nm can be considered. In the following, the results are shown in detail for the diffuse reflection of NIR radiation in the skin. Here, the following variables were stored from each diffusely reflecting photon in addition to the remaining energy upon exit from the skin:

1. The radial separation r [mm] of the exit position to the original coordinate position (= entrance position).
2. The angle θ to the skin normal of the photon exit direction.
3. The maximum achieved penetration depth z_{max} [mm] during the residence in the skin.
4. The total pathlength L [mm] traveled in the tissue.

For the size of the diffuse reflection, it is, furthermore, important whether the refraction indices (n_1 skin, n_2 medium above the skin) are adjusted to the bordering area. Monte Carlo simulations were calculated for perfect adjustment ($n_1 = n_2$) and for diffuse reflection in air ($n_2 = 1.0$). The diffuse reflectivities R_{diff} and the averages of the four, aforementioned variables with the photon exit energy as the waiting factor are summarized in Table 6.2. The corresponding cumulative distribution functions are shown in Fig. 6.4 and Fig. 6.5. Fresnel reflections during entrance into the tissue are not contained in the values of R_{diff} and must be added to R_{diff} for determining the total reflectivity of the skin, $R_{\text{tot}} = R_{\text{diff}} + R_{\text{Fres}}$ for unmatched boundary conditions. The most important results of the Monte Carlo simulation pertain to the penetration depth and the pathlength in the tissue of radiation at $\lambda = 1.57 \mu\text{m}$. As Table 6.2 shows, penetration depths into the skin are achieved with the measurement procedure of diffuse reflection at $1.57 \mu\text{m}$ that lie at double the required minimum depth of $150 \mu\text{m}$ (cf. Ch. 6.1). The measurement of blood capillaries in the upper dermis is possible. Simultaneously, the skin yields an optimal average pathlength in the tissue of ca. $L = 1 \text{ mm}$ through its optical characteristics at $1.57 \mu\text{m}$; this thickness was also selected in the NIR transmission measurement of liquid blood plasma for optimizing the S/N ratio for the extinction spectra (Ch. 5.4). The average pathlength L is essentially determined from the scattering

characteristics and the background absorption of the tissue, and these summed parameters display only a small individual variation. Therefore, in the diffuse reflection measurement of the lip in the near IR, the assumption of a constant, i.e. from the test person and his/her momentary blood composition, independent "thickness" of the tissue is justified. As Table 6.2 further shows, the value of R_{diff} can be doubled by matching the refraction indices. This large advantage is superior to the relatively small disadvantage of a reduced average penetration depth, since radiation traveling flatly underneath the skin surface area is no longer hindered by Fresnel total reflection upon exit.

Table 6.3: Results of the Monte Carlo simulation of diffuse reflection of skin (for optical parameters, see Table 6.1; for further details, see text).

		r [mm]	θ [deg]	z_{max} [mm]	L [mm]	R_{diff} [%]
$\lambda = 1.25 \mu\text{m}$ $\tilde{\nu} = 8000 \text{ cm}^{-1}$	$n_1 = n_2$	0.34	44.9	0.50	1.99	27.2
	$n_2 = 1.0$	0.38	44.5	0.54	2.48	16.4
$\lambda = 1.57 \mu\text{m}$ $\tilde{\nu} = 6350 \text{ cm}^{-1}$	$n_1 = n_2$	0.27	47.1	0.31	1.06	8.7
	$n_2 = 1.0$	0.27	44.7	0.37	1.25	4.1
$\lambda = 2.27 \mu\text{m}$ $\tilde{\nu} = 4400 \text{ cm}^{-1}$	$n_1 = n_2$	0.21	50.3	0.19	0.60	2.5
	$n_2 = 1.0$	0.18	45.6	0.23	0.64	1.1

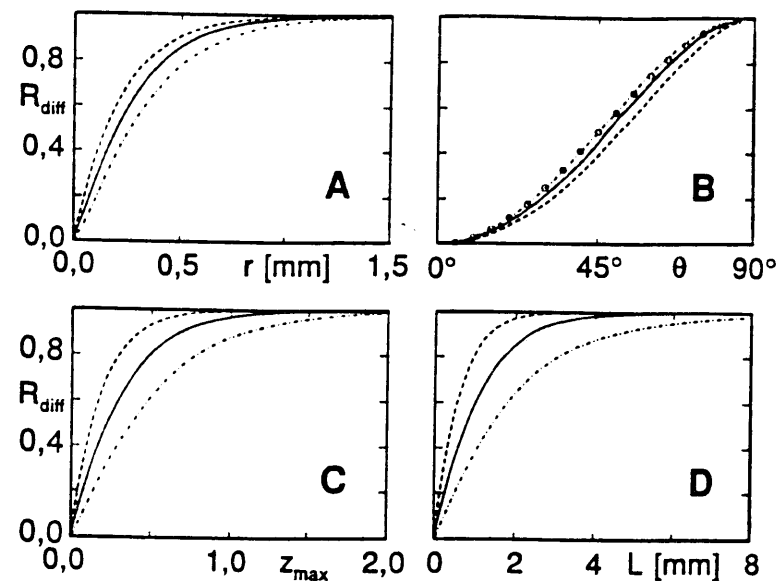


Figure 6.4: Cumulative distribution function of the diffusely reflecting radiation power for perfectly matched refraction indices $n_1 = n_2$ (for remaining titles, see Fig. 6.5).

The diameter of the diffusely reflecting skin spot around the entrance position of the Monte Carlo photons into the skin can be given independent of the wavelengths roughly as ca. $\phi = 1 \text{ mm}$ (cf. Fig. 6.4A and Fig. 6.5A). Fig. 6.4B shows that the radiation at the wavelengths of $\lambda = 1.57 \mu\text{m}$ and $\lambda = 2.27 \mu\text{m}$ for matched boundary conditions $n_1 = n_2$ exit on average somewhat flatter from

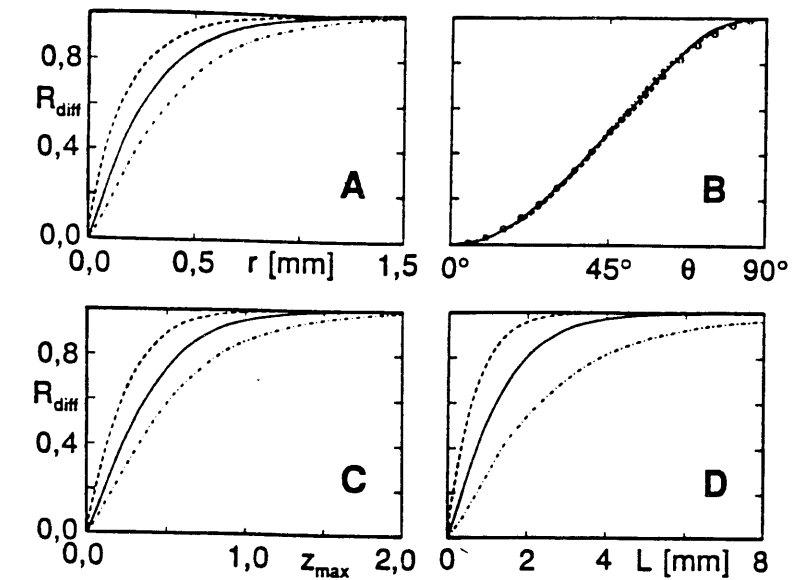


Figure 6.5: Cumulative distribution function of the diffusely reflecting radiation power in air ($n_2 = 1.0$) at $\lambda = 1.57 \mu\text{m}$ (—), $\lambda = 2.27 \mu\text{m}$ (- - -) and $\lambda = 1.25 \mu\text{m}$ (- · - ·) versus: (A) the radial separation r of the exit position, (B) the angle θ to the skin normal of the exit direction (points "o" mark the ideal Lambert radiator), (C) the maximum achieved penetration depth z_{max} [mm], and (D) the total pathlength L traveled in the tissue.

the skin than for an ideal Lambert radiator. The reflection in air ($n_2 = 1.0$) does not show this behavior and is practically ideally diffuse (Fig. 6.5B). The cumulative distribution in Fig. 6.4C shows that ca. 20% of the diffusely reflecting radiation power at $1.57 \mu\text{m}$ achieves a depth of $\geq 0.5 \text{ mm}$ in the tissue.

The "automatic" thickness optimization described above by the optical characteristics of the skin at $\lambda = 1.57 \mu\text{m}$ functions in the diffuse reflection procedure also for the wavelengths $\lambda = 2.27 \mu\text{m}$ and (approximately) for $\lambda = 1.25 \mu\text{m}$. At $2.27 \mu\text{m}$, the penetration depth still lies above the required $150 \mu\text{m}$ such that blood capillaries can also be measured here. The largest penetration depth into the skin is achieved for $\lambda = 1.25 \mu\text{m}$ as expected.

In the region of the therapeutic window from 1300–600 nm, a diffuse transmission measurement, e.g. through the finger, is also imaginable. A size estimation of the glucose overtone signals using the NIR spectrum of the chemically similar glycerines $\text{C}_3\text{H}_8\text{O}_3$ shows, however, that the absorption signals at $\lambda \leq 1.25 \mu\text{m}$ are at least an order of magnitude smaller than at $\lambda = 1.57 \mu\text{m}$ [209]. Through the larger thickness of the radiated finger tissue, the signal reduction can partly be compensated, however, a thickness matching for optimizing the S/N ratio at $1.25 \mu\text{m}$ is not possible, since the tissue absorption at transition to the visible region reduces less strongly than the glucose signal (cf. Table 6.1). A further disadvantage of the transmission procedure occurs through the increased biological variability in the finger region. Since the spectral region around $1.6 \mu\text{m}$ for the glucose analysis of liquid blood samples could already be successfully used (Ch. 5), the procedure of diffuse reflection in the long wave NIR was chosen for the non-invasive blood glucose measurement.

6.3 Development of the Measurement Accessory

The region of the inner lip is seen as the appropriate position on the body surface area for a non-invasive, transcutaneous glucose measurement using diffuse reflection. For the quantitative analysis, an absolute measurement of the diffuse reflection, e.g. with an integrating hollow sphere according to Ulbricht ([210], see e.g. [211–213]) is not required. The reflection spectra can be measured relative to a reflection standard where a high reproducibility of the measurement is necessary. The requirements on the optical accessory for measurement of the diffuse reflection of the lip are:

1. Possibility for an *in situ* analysis of small spots ($\phi = 1 \text{ mm}$) on larger samples.
2. High optical “throughput” for the purpose of optimizing the S/N ratio of the spectra.
3. Suppression of and insensitivity to Fresnel reflection on the skin surface area.
4. Reproducibility of the measurement regarding the positioning of the lip and the reflection standards.
5. Minimum measure on patient friendliness.

Teflon-similar plastics are available as reflection standards in the visible and the near IR which diffusely reflect ideally in good approximation up to about $\lambda = 2.5 \mu\text{m}$ (so-called SPECTRALON™ [214]). Further advantages over the standards normally used in the mid IR, such as e.g. alkali-halogenide powders or gold-coated sandpaper, are mechanical formability, robustness against environmental influences (especially moisture), and problemless cleaning. A basic problem in the examination of absorption characteristics using diffuse reflection is the mirrored reflected radiation from the sample surface area. This radiation power lies on the skin on the order of magnitude of the diffusely reflecting portion *into* the skin (cf. Table 6.2) and is dependent through the Fresnel equations on the *complex* refraction index $n - ik$ of the tissue, where the spectral form of the Fresnel reflection degree is essentially determined from the real part n . Due to the relationship of n and k through a Hilbert transformation (e.g. [215:p. 214]), the Fresnel reflection degree in the region of an absorption band looks similar to its first derivative (“dispersion form”); only in the region of very strong absorption bands does the absorption index k dominate the Fresnel reflection and allows these to increase to values near 100% (“remaining beam bands”). For the skin in the near IR, $k \ll n$ (at $\lambda = 2.27 \mu\text{m}$, maximum $k = 2.4 \cdot 10^{-4}n$, cf. Table 6.1) is valid such that the Fresnel reflection practically contains no information about the absorption index of the tissue. Moreover, for the non-invasive glucose measurement, the information about the radiation absorption in larger tissue depths is required. The difference between the diffuse reflection and the Fresnel reflection lies primarily in the physical occurrence of both power portions and only secondarily in the direction characteristic of the radiation; for rough surface areas, an undirected and even diffuse, Fresnel return radiation can also occur. However, the Fresnel reflection displays most often a preferred direction which is defined by the macroscopic surface area normal of the sample.³⁷

³⁷In the following, the diffusely reflected radiation portion through (multiple) scattering *in the skin* is implied with “diffuse reflection”.

In contrary to the optical accessories for the measurement of the absolute reflection degree, the accessories for relative measurement offer the possibility to exclude the preferred direction of the Fresnel reflection. Furthermore, they are universally more light intensive than the aforementioned Ulbricht spheres. A schematic overview of the available accessories that are also described in the literature for measurement of the relative reflection degree is shown in Fig. 6.6. In Fig. 6.6A, an example of a commercially available accessory is shown which can be used in the sample compartment of the FT spectrometer (cf. Fig. 3.8). With these accessories, only small samples up to 1 cm^3 can be examined. For radiating the sample and the collection of the diffuse reflection portion, a maximum of 50% of the halfspace above the sample is available due to symmetry characteristics, however, for blocking out the preferred Fresnel direction, a smaller space angle is used (e.g. [216]). For the use of ideal diffusely reflecting samples, typically around 10% of the radiation power is passed on to the detector.

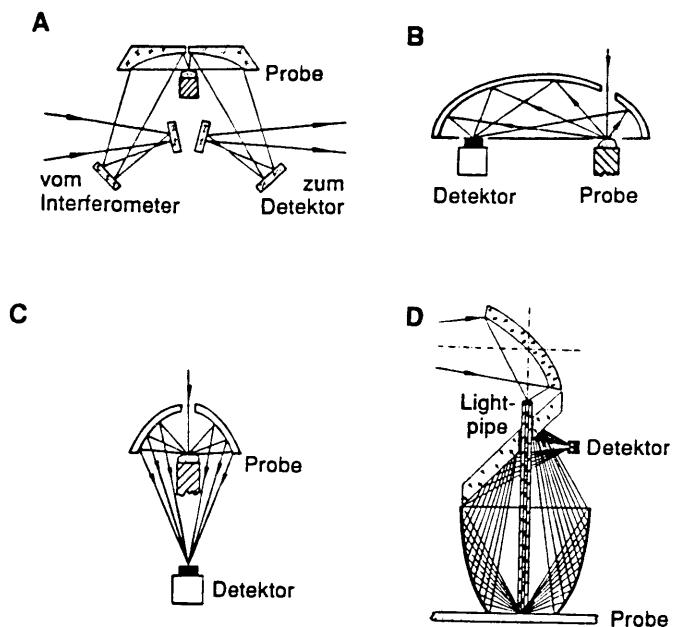


Figure 6.6: Accessories for the diffuse reflection measurement: (A) Use in the spectrometer sample compartment; (B)–(D) Various suggestions with rotational ellipsoid mirrors.

In Fig. 6.6B–C, diverse accessories with mirrors from rotation ellipsoid segments and separate detectors are shown. The eldest suggestion (Fig. 6.6B) came from Kortum and Delfs [217] and represents a further development of the Coblenz half-sphere [218] with improved optical imaging characteristics [219]. The significant disadvantage of this setup is the large opening angle of 180° of the radiation meeting the detector, since most of the commercially available IR detectors are supplied over a field of vision of only 60° (half opening angle $\beta = 30^\circ$). With nitrogen-cooled semiconductor detectors, the field of vision is limited by a cooled aperture that is located immediately before the detector element. Through this, the portion of additive photon noise is reduced by the background radiation in the spectrometer (mostly at 300°K) (Ch. 3.3.4) and the sensitivity against scattered light is reduced. Detectors with a field of vision $2\beta = 60^\circ$ are an industry standard, since the Fresnel losses through the detector window in this angle region also lie nearly constant at the lower value for perpendicular impingement.

The setup in Fig. 6.6C of Dunn et al. ([220], see also [221,222]) offers the possibility of matching to the limited field of vision to commercial detectors with which only small samples, however, can be examined. This disadvantage disappears with the setup according to Korte [223] for which (randomly) large samples can be allowed (Fig. 6.6D). Moreover, as Korte determined, the diffusely radiating sample spot at the optical image onto the detector is less strongly enlarged by the upwardly directed ellipsoid than with the accessory in Fig. 6.6C so that smaller detector areas are required to sample the radiation. The spatial separation of radiation source and detector through the sample additionally requires optical components like e.g. the 45° planar mirror with an opening in Fig. 6.6D. A design of this accessory with a so-called light pipe for illuminating the sample (quartz capillaries laid with gold on the inside as "light guides" in the IR) is described in [224,225]; as a result of the high losses of these radiation optics, the "transmission degree" of the accessory for use with gold-coated sandpaper as the reflection standard in the mid IR is only about 1% in comparison to the empty sample compartment of the attached FT-IR spectrometer.

For suppression of the Fresnel reflection, it is advantageous to illuminate the sample perpendicularly with a converging radiation bundle (half opening angle α_0 about the macroscopic skin normal) so that the mirrored, reflected radiation portion falls back preferably into the space angle of the illumination $\Omega_0 = 2\pi(1 - \cos\alpha_0)$ sr. (A Monte Carlo simulation of skin upon impingement by a point-shaped photon beam below $\alpha_0 = 30^\circ$ to the skin normal showed no significant change in the results to the perpendicular case in Table 6.2, and the reflected photons displayed no preferred direction.) If a circularly formed focus of size πr_0^2 [mm²] is generated on the skin, the optical throughput value of the illuminated beam bundle can be given in good approximation as $G_0 = \pi^2 r_0^2 \sin^2 \alpha_0$ [mm²sr] (see Appendix A: Eq. A.7). The principal problem during construction of the measurement accessory lies in the fact that the law of the invariance of the optical throughput value of sequentially occurring radiation cones is not valid for the process of diffuse reflection.³⁸ Here, the radiation in the entire halfspace above is distributed over the sample, where simultaneously the diffusely radiating spot is increased to $\pi(r_0 + r_d)^2$ [mm²] (r_d describes the "spreading" of the radiated skin spot through photon wandering in the tissue). The optical throughput value according to diffuse reflection $G_{\text{diff}} = \pi^2(r_0 + r_d)^2 \sin^2 \alpha_{\text{diff}}$ with $\alpha_{\text{diff}} = 90^\circ$ is essentially larger than the value G_0 of the radiating bundle before, which is matched in an optimally designed spectrometer with $G_0 = G_{\text{det}}$ to the throughput value of the IR detector $G_{\text{det}} = \pi^2 r_{\text{det}}^2 \sin^2 \beta$. An imaging of G_{diff} to G_{det} without losses is (also through enlargement of the detector area) not possible, since for collection of the diffusely reflecting radiation, only the ring-shaped space angle $\Omega_C = 2\pi - \Omega_0$ sr is available with an optical throughput value $G_C = (1 - \sin^2 \alpha_0)G_{\text{diff}}$. The technical problems in the construction of an accessory for the measurement of the diffuse reflection can be divided as follows:

1. The first problem entails the division of the space angle over the sample into two portions for the illumination (Ω_0) and the collection (Ω_C) of the diffusely reflected radiation. Through enlargement of the opening angle $2\alpha_0$ for the illumination, the radiation strength [W mm⁻²] onto the skin is increased, however, at the cost of a reduced collection efficiency for the diffusely reflected radiation.

³⁸Invariance of the optical throughput value occurs only for validity of the Fermat Principal (minimum optical path difference between two points on a light beam); this is valid for all mirrored and refracted components, however, not for diffuse scattering (see e.g. Appendices in [226]).

2. The second problem is the imaging of the ring-shaped space angle $\Omega_C = 2\pi \cos \alpha_0$ sr onto the detector with a standard field of vision $2\beta = 60^\circ$.
3. Finally, the components of the radiation optics inside of the cone with opening angle $2\alpha_0$ must be located above the sample, where losses through vignetting should be minimized.

The criteria for determining the optimal opening angle for the radiation cone $2\alpha_0$ have been examined in the mid IR by Hirschfeld [227] and Korte [223] for the accessories shown in Fig. 6.6C and Fig. 6.6D. Since in the mid IR, the additive detector noise dominates, and this increases with the square root of the detector area for semiconductor detectors (Ch. 3.3.4), a combination of collection efficiency and size of the generated beam focus on the detector was used as the criterium. From both authors, the optimal angle for Lambert-radiating samples is given as $\alpha_0 = 40^\circ$. For the non-invasive glucose measurement in the near IR, the S/N ratio of the spectra is determined from the photon noise of the signal power meeting the detector so that an enlargement of the detector area must not be rated negatively. Theoretically, 100% of the diffusely reflected power in the space angle Ω_C could be accounted for with a sufficiently large detector without disadvantage, however, in the spectral region around 1.6 μm , the technically optimal indium-antimonide (InSb) detectors are only commercially available in diameters up to 5 mm. With the mean density of the NIR source (tungsten/halogen glowlamps with about $L_0 = 0.17 \text{ W mm}^{-2}\text{sr}^{-1}$ in the sample compartment of the Bruker IFS-66) and the lower reflection degree of the skin, it follows that an InSb semiconductor detector will be operated in the linear region in the planned experiment as a result of the limited collected power. The practical optimality criterium is, therefore, a high radiation strength [W mm⁻²] in the detector plane in order to concentrate as much reflective power as possible onto the available detector area.

For optimization of the (half) opening angle of the illumination α_0 , the realistic assumptions are made that (1) the power $P_0 = L_0 \pi^2 r_0^2 \sin^2 \alpha_0$ [W] from the spectrometer is focused with a beam density L_0 onto the skin independent of position and direction, (2) the skin ideally, diffusely reflects the R_{diff} th portion of the radiation (see Table 6.2), and (3) for collection optics according to Fig. 6.6D, the effective transversal enlargement resulting during the optical imaging of the skin spot onto the detector $V_{\text{eff}} = r_{\text{det}}/(\tau_0 + r_d)$ is approximately independent of α_0 : $V_{\text{eff}}(\alpha_0; \beta(\alpha_0)) \approx \text{const}(\alpha_0)$ (cf. footnote p. 131; for fulfillment of $\beta = 30^\circ$, the geometric parameters of the optics must be matched in the next step to the optimal value of α_0 [223]). Hence, the optimality criterium for maximizing the radiation strengths E_{det} in the detector plane reads:

$$E_{\text{det}}(\alpha_0) = \frac{L_0 \pi^2 r_0^2 \sin^2(\alpha_0) R_{\text{diff}}}{\pi^2 (r_0 + r_d)^2} \frac{\pi(1 - \sin^2(\alpha_0))}{V_{\text{eff}}^2} = \frac{\pi L_0 R_{\text{diff}}}{V_{\text{eff}}^2} \frac{r_0^2}{(r_0 + r_d)^2} \sin^2(\alpha_0) \cos^2(\alpha_0) \stackrel{!}{=} \max \left[\frac{\text{W}}{\text{mm}^2} \right] \quad (6.6)$$

In the first line of Eq. 6.6, the first term describes the beam density [W mm⁻² sr⁻¹] of the diffusely reflecting skin spot. The numerator of the second term gives the efficiency of the radiation collection, since the special characteristics of the collection optics are subsummed in the factor V_{eff} . If the photon wandering in the tissue is neglected ($r_d \approx 0$), the criterium in Eq. 6.6 for $\alpha_0 = 45^\circ$ can be optimized, i.e. the halfspace above the sample is divided into the same optical throughput values for illumination and radiation collection. Due to the results from Ch. 6.2, however, ca.

$r_d = 0.5$ mm must be used for skin in the calculations (see Fig. 6.4 and Fig. 6.5). Through $r_0 = P_0^{1/2}/(L_0^{1/2}\pi \sin \alpha_0)$, the influence of this effect on the optimal value of α_0 is dependent on the entire radiation power P_0 directed onto the skin which, for FT-IR spectrometers, is controlled using field apertures of different diameters ϕ_{bl} (cf. "AC" in Fig. 3.8). During initial experiments, it was determined that with the available beam density L_0 and the low reflection degree R_{diff} of the skin, field apertures with at least about $\phi_{bl} = 2r_{bl} = 3$ mm must be used for the measurement with InSb detectors. With the $f/4.5$ optics of the Bruker IFS-66 spectrometer (half opening angle $\alpha_{IFS} = 6.4^\circ$), it follows:

$$r_0 = r_{bl} \frac{\sin \alpha_{IFS}}{\sin \alpha_0} \quad (6.7)$$

In Fig. 6.7, the form of the criterium Eq. 6.6 after substitution of Eq. 6.7 is shown for various values of r_d and r_{bl} . The determination of the angle α_0 for illumination is relatively uncritical, and optimal values are achieved in the region of around $\alpha_0 = 30^\circ$.

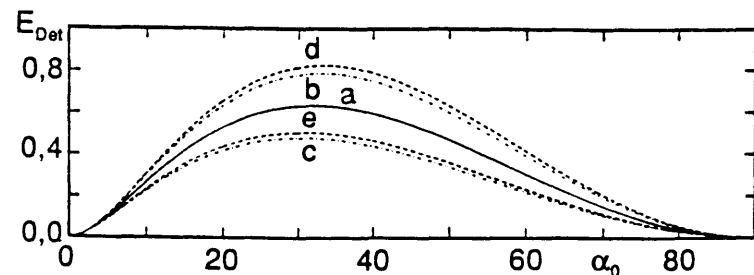


Figure 6.7: Dependence of the (normalized) radiation strength in the detector plane on the half opening angle α_0 of the radiation cone onto the skin (for details, see text; a: $r_d = 0.5$ mm, $r_{bl} = 1.5$ mm; b: $r_d = 0.5$ mm, $r_{bl} = 1.8$ mm; c: $r_d = 0.5$ mm, $r_{bl} = 1.2$ mm; d: $r_d = 0.4$ mm, $r_{bl} = 1.5$ mm; e: $r_d = 0.6$ mm, $r_{bl} = 1.5$ mm).

Further problems pertain to the optical imaging of the diffusely reflecting radiation in the space angle $\Omega_C = 2\pi \cos \alpha_0$ sr onto an IR detector with a 60° field of vision and the addition of radiation optics without vignetting losses. For this, two observations: first, in the IR spectral region, mirrors are more appropriate than lenses as optical components, since the common glass types like, e.g. BK7 glass strongly absorb for wavelengths above $\lambda = 2 \mu\text{m}$. Second, the selection of commercially available components, with the exception of spherical mirrors, is extremely limited such that the constructive tasks must be solved under consideration of the availability of the elements and the price of individual manufacturing. The realized measurement accessory is shown in Fig. 6.8 and Fig. 6.9 [228] and is based on the Korte set up (Fig. 6.6D) which was further developed and optimized for the special application purpose of skin measurement. Using diverse mirrors, the

collimated beam from the Michelson interferometer of the attached FT-IR spectrometer is focused onto the flat area of a half spherical immersion lens (L1) against which the lip is pressed. The half opening angle of the beam bundle for illumination is $\alpha_0 = 35.3^\circ$. Simultaneously, the lip is in the focus of an ellipsoid mirror M1 which collects the diffusely reflected radiation in the angle region $\alpha_0 \leq \alpha \leq 90^\circ$ and images it onto an IR detector. The collection efficiency for ideally diffuse samples is $\eta = (1 - \sin^2 \alpha_0) = 0.67$.

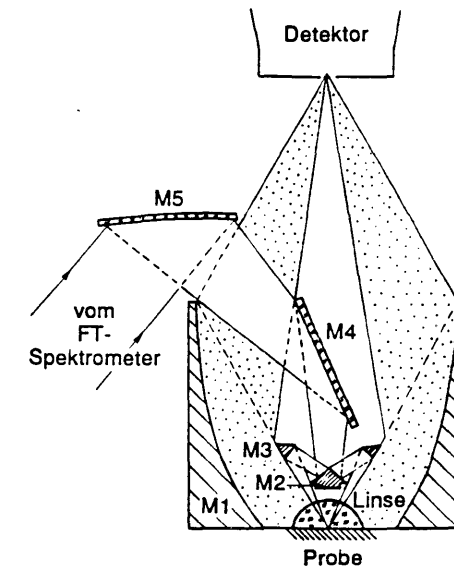


Figure 6.8: Schematic representation of the accessory for the measurement of diffuse reflection of the lip (M1 rotation ellipsoid; M2/M3 Cassegrain-similar objective; M4 planar mirror; M5 off-axis paraboloid; L1 immersion lens).

The quality of the optical image on the detector is not optimal, since the Abbe sine condition [229] is not filled by an ellipsoid (perfect image of both foci into each other, however, coma error at the image of finitely expanded areas). As a result, the radius of the beam focus on the detector is larger than the value for an ideal, i.e. aplanatic image (cf. Fig. 6.10). An additional enlargement occurs through the unused space angle in the center of the field of vision in the IR detector which can, however, be held quite small by the ellipsoid collection mirror (Fig. 6.8). As Welford and Winston determined, the optimal radiation strength E_{det} [W mm^{-2}] can be better approximated with a so-called "non-imaging concentrator" [226]. With this, the "boundary condition" disappears such that at the image of the reflecting bundle with $G_C = \pi^2(r_0 + r_d)^2(1 - \sin^2 \alpha_0)$ onto the collection bundle with $G_{det} = \pi^2 r_{det}^2 \sin^2 \beta$, two beams, which arose from the same position on the skin area, $\pi(r_0 + r_d)^2$, must impinge the detector area πr_{det}^2 at the same position as well. In the \mathbf{R}^3 , sub-optimal non-imaging concentrators can be realized through rotation of curves of second order (parabolas and ellipses) about an optical axis that is tilted to the symmetry axis of the corresponding areas of second order [226]. The manufacturing costs for such bodies are, however, larger than for the ellipsoid in Fig. 6.8 which was completed as an individual piece and gold inlaid on the inside (Hanseatische Präzisions- und Orbittechnik GmbH, Bremen, BRD). An additional manufacturing related advantage for the ellipsoid occurs, since exactly one ellipsoid with axis ratio 1:2 is defined by the selection of the angle $\alpha_0 = 30^\circ$ and $\beta = 30^\circ$ (detector field of vision) which

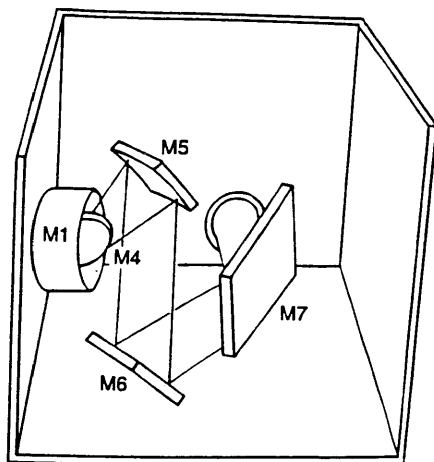


Figure 6.9: Schematic representation of the transfer optics to the connection of the accessory onto the Bruker IFS-66 spectrometer (M1 rotation ellipsoid; M5 off-axis paraboloid; M4, M6, M7 planar mirror).

ends in the "equator plane" (see Fig. 4 in [223]). In a compromise between manufacturing costs and space requirements for the detector housing and radiation optics, the main axes of the ellipsoid were chosen to be $2a = 100$ mm and $2b = 200$ mm such that the separation between the equator and the focal planes (see Fig. 6.8) along the optical axis is 86.6 mm.³⁹

The imaging characteristics of the ellipsoid were examined with a Monte Carlo simulation. The model calculation is based on 5000 photons which exit from a circular, ideally diffuse radiation source with radius $r_S (= r_0 + r_d)$ into the ellipsoid (without immersion lens) and from this, are reflected onto the detector without losses. Fig. 6.10 yields information about the transversal enlargement in the optical image of the diffusely radiating sample spot onto the detector. The ideal value for the optical enlargement under consideration of the unused space angle with opening angle $2\beta_{\text{tot}} = 16.4^\circ$ in the center of the field of vision of the detector (Fig. 6.8) would be $V = 1.7$ for an aplanatic image through the ellipsoid mirror,⁴⁰ and the corresponding distribution of radiation power is shown in Fig. 6.10. Around 50% of the radiation is optimally focused mostly independent of the absolute size r_S of the radiation spot from ellipsoids; about 20% of the power, however, is distributed over a relatively large position region. An effective enlargement factor $V_{\text{eff}} = 2$ can be given for the ellipsoid for which ca. 75% of the radiation power is accounted.

³⁹This manufacturing procedure was also conducted for the ellipsoid mirrors used, however, the possibility for radiation collection in the angle region $30^\circ \leq \alpha \leq 35.3^\circ$ was not used; according to the basic principal of [223] and with the definition of the effective enlargement over the 75% quantile of the radial beam power distribution in the detector plane, a numerical approximation can be used for the ellipsoid $V_{\text{eff}}(\alpha_0) \approx 1.68 + 3.47 \cdot 10^{-4} (\alpha_0/\text{deg})^2$.

$$V = \sqrt{\frac{1 - \sin^2 \alpha_0}{\sin^2 \beta - \sin^2 \beta_{\text{tot}}}} \approx 1.7 \quad \text{with} \quad \alpha_0 = 35.3^\circ, \beta = 30^\circ \text{ and } \beta_{\text{tot}} = 8.2^\circ$$

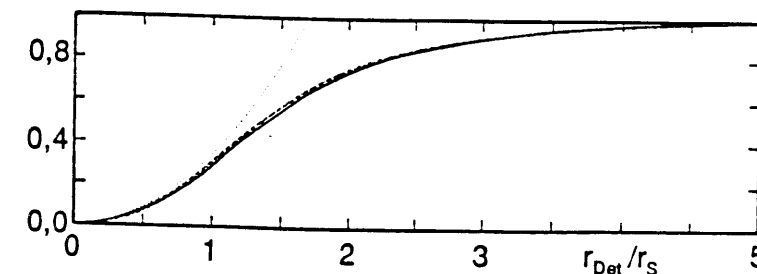


Figure 6.10: Cumulative distribution of the radiation power imaged onto the detector in the focal plane of the ellipsoid mirror versus the radial separation r_{det} to the center point of the detector (radius r_S of the diffuse radiation spot: '—' $r_S = 0.5$ mm, '- -' $r_S = 2.5$ mm, '· ·' $r_S = 5$ mm, '- ·' ideal curve for aplanatic imaging).

Essential improvements could be achieved over the accessory with quartz capillaries [224] through optimized radiation optics. The collimated IR beam leaves the Bruker IFS-66 spectrometer through the exit "X3" (Fig. 3.8) and after deflection onto the planar mirrors M7 and M6 (Porschke, Hoechst/Odw., BRD: V1.800 (M7) and V1.801 (M6); Coating: Gold + MgF_2), increasingly perpendicularly reaches the 90° off-axis paraboloid mirror M5 (Bruker, Karlsruhe, BRD: focal length of the generating parabolas 76.2 mm, i.e. effective focal length at the 90° off-axis image $f = 152.4$ mm; aperture number $f/\# = 3.810$). The mirror M5 is identical to the parabolooids which collimate the IR radiation in the IFS-66 spectrometer into the Michelson interferometer and generate a 1:1 image of the iris "AC" in the IFS-66 spectrometer (with $f/\# = 4.5$) about 19 mm outside of the focal plane of the ellipsoid M1. The planar mirror M4 (Porschke, Hoechst/Odv., BRD: MF-24-C (thickness 3 mm), Coating: Alu + SiO) positioned at an angle 22.5° to the ellipsoid axis deflects the radiation, however, for further focusing onto the Cassegrain-similar objective M2/M3 which was made in the fine mechanics workshop of the Institute for Spectrochemistry and Applied Spectroscopy from a substitute mirror pair for the CIRCLETM-ATR cell (SPECTRA-TECH, Warrington, UK) (cf. Fig. 5.5 and discussion). An advantage of the conical optics of M2/M3 for the special application in Fig. 6.8 lies in the fact that through translation of the "spectrometer focus" generated from the parabolooids M5 along the ellipsoid axis of opening angle α_0 , the radiation can be aligned without having to change the distance of M2/M3 to the focal plane of the ellipsoid.⁴¹ In order to use this characteristic, the mirrors M5 and M6 can travel together on a translation table with a micrometer screw along the optical axis M4/M5 and M6/M7 so that the illumination of M3 with $\alpha_0 = 35.3^\circ$ is precisely adjustable. As mentioned in Ch. 5.3.1, the objective M2/M3 is free

⁴¹This characteristic is used with commercial ATR accessories by selective construction of the CIRCLETM cell with a "micro" or "macrocrystal" [230].

from vignetting through the conical optics, i.e. 100% of the incoming power meets the sample in the angle region $\alpha_{\text{tot}} \leq \alpha \leq \alpha_0$ with $\alpha_{\text{tot}} = 23.6^\circ$; at the image, the "spectrometer focus" is reduced by about $V = 3.7$ by the objective M2/M3.⁴²

The half spherically shaped immersion lens L1 (Porschke, Hoechst/Odw., BRD: $r_{L1} = 10.0$ mm) of CaF_2 crystal ($n_{L1} = 1.426$ at $\lambda = 1.64 \mu\text{m}$ [164]) induces a further reduction of the diameter of the beam focus on the skin around $n_{L1}^{-1} \approx 0.7$ [231:p. 233]. The influence of lens L1 on the collection of diffusely reflected radiation was examined in a Monte Carlo simulation in which the Fresnel losses on the bordering areas were considered. The absorption losses in the CaF_2 are negligible [164]. The results for a circular, ideally diffuse skin spot with radius $r_S (= r_0 + r_d)$ are: (1) Up to the spot size $r_S \leq 0.5r_{L1}$, the diffuse transmission of the lens is constant ($T = 97\%$) and the direction distribution of the radiation after passing through the lens remains nearly ideally diffuse. (2) The optical image with enlargement n_{L1} through the immersion lens also functions satisfactorily for a Lambert radiator (with opening angle 180°): For $r_S \leq 0.3r_{L1}$, less than 10% of the transmitted radiation power through the immersion lens from points with $r > n_{L1}r_S$ appears to be emitted when considering the diffuse skin spot. As a result of its size ($r_{L1} = 10$ mm), the immersion lens has approximately ideal optical imaging characteristics in the application of non-invasive glucose measurement with about $r_S \leq 0.15r_{L1}$, and the immersion effect (reduction of the beam focus) is compensated for by the returning image of the diffusely reflecting spot onto the detector. The important advantages of immersion lens L1 for the transcutaneous diffuse reflection measurement are: (1) Through the nearly complete matching of the refraction indices of CaF_2 and skin, the diffuse reflection degree of the tissue is increased significantly (cf. Table 6.2). (2) With L1, a flat sample area is achieved for a successful suppression of the Fresnel reflection. (3) Through L1, a reproducible lip measurement is possible.

Fig. 6.11 shows the developed accessory in more detail. A front plate, which is made of brass and sealed with a teflon strip against the ellipsoid body, holds the immersion lens L1 and the objective M2/M3. During the measurement, the front plate is thermostated with water circulation. For improving the heat transfer and for hygienic reasons, L1 is screwed into the front plate in a holding assembly made of copper conducting bronze that is coated with gold. A SPECTRALONTM cylinder (details, see Ch. 6.4) is used as the diffuse reflection standard that is pressed rotation-free against the bottom of the immersion lens by a spring. For this, the holding rails of the reflection standards are set upon both of the press fit pegs and are held in place with butterfly nuts. A quick exchange of the reflection standards is possible by unscrewing a nut.

The housing of the accessory is screwed onto the cast iron baseplate of the Bruker IFS-66 spectrometer and has the dimensions $40 \times 33 \times 38$ cm ($B \times W \times H$ for a view onto L1). On the backside, a controllable nitrogen inlet (Rotameter Typ 901120.1901) is located so that the atmosphere of the accessory can be purged separately from the spectrometer. The filling of the InSb detector with liquid nitrogen is possible through an opening in the housing lid. Except for the ellipsoid mirror L1 and the objective M2/M3, all mirrors are kinematically set on bearings with three degrees of freedom for the alignment. Additional degrees of freedom for the alignment pertain

$$V = \frac{\sqrt{\sin^2 \alpha_0 - \sin^2 \alpha_{\text{tot}}}}{\sin \alpha_{\text{IFS}}} \approx 3.7 \quad \text{with} \quad \alpha_0 = 35.3^\circ, \alpha_{\text{tot}} = 23.6^\circ \text{ and } \alpha_{\text{IFS}} = 6.4^\circ$$

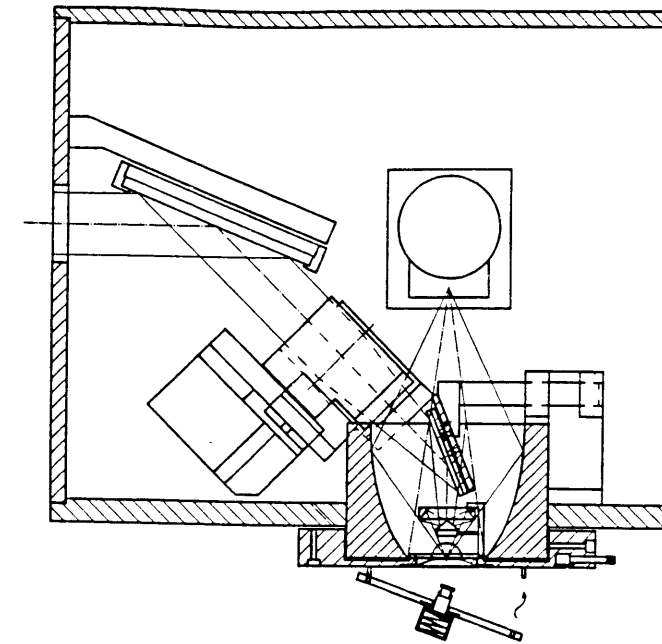


Figure 6.11: Horizontal cut through the measurement accessory.

to the height of the paraboloid M5 and the axial position of the mirror M2/M3 and the lens L1 relative to the fixed ellipsoid M1. The alignment takes place with a HeNe laser that is centered onto the ellipsoid after removal of the front plate.

Vignetting losses occur in the accessory through the tripod for holding the objective M2/M3 on the brass front plate ($V_1 = 9.3\%$) through which three threaded rods ("spider legs") for fixing M2 ($V_2 = 7.2\%$) into place and through the arm for mounting M4 ($V_3 = 2.3\%$), since M4 itself does not contribute to the vignetting by polishing to an appropriate elliptical form (Optical Workshop Leopold Lampen, Ennigerloh, BRD). Under the assumption of the perfectly matched refraction indices of skin and CaF_2 , only the Fresnel losses on the curved surface area of the immersion lens L1 ($V_{L1} \approx 6.2\%$) must be considered. With the collection efficiency of the ellipsoid $\eta = 0.67$ and all losses mentioned above, the optical efficiency of the accessory ("transmission degree" for the measurement of ideally diffusely reflecting samples with $R_{\text{diff}} = 1$) is $\eta_{\text{eff}} = 0.52$. This value is achieved with the InSb detector ($\phi = 4$ mm) used for diffuse radiation spot up to a size of about $\phi = 2$ mm and lies about 1 1/2 orders of magnitude above the efficiencies of comparable accessories.

Essential improvements in the described accessory are only possible through application of radiation sources with higher beam density. Technologically optimal are diode lasers which are already available in the near IR with wavelengths up to ca. $\lambda = 1800$ nm [232]. For radiating with lasers, practically the entire halfspace above the sample can be used for radiation collection, since complicated radiation optics are not necessary. To what degree increases of the radiation strength [W mm^{-2}] on the skin are possible is difficult to estimate according to the current state of security guidelines for laser use. The *guideline* for the maximum allowed radiation of the skin (or of the eye) with laser radiation is presently given as 1 mW mm^{-2} for $\lambda \geq 1.4 \mu\text{m}$ [233]. The radiation strengths in the described measurement accessory lie on the order of magnitude of 10 mW mm^{-2} , and thermal loadings on the sensitive lips could not be noticed in any case.

6.4 Diffuse Reflection Measurement of the Lip

All measurements for the non-invasive blood glucose determination were conducted with the diffuse reflection unit developed in this work (Ch. 6.3) in which a portion of the inner lip was pressed against the immersion lens. At the Institute for Spectrochemistry and Applied Spectroscopy, two single person experiments were conducted, since at the Diabetes Institute in Duesseldorf, a larger population with 133 different patients could be measured. The Bruker IFS-66 spectrometer was equipped for the measurements with an InSb detector (Infrared Associates, Suffolk, UK, $\phi = 4$ mm), CaF_2 beam splitter, and a tungsten/halogen glowlamp as the NIR radiation source. The spectra were taken in the spectral region $\tilde{\nu} = 14000 - 2000 \text{ cm}^{-1}$ with a nominal resolution of $\Delta\tilde{\nu} = 32 \text{ cm}^{-1}$ so that the interferograms were sampled with the doubled HeNe laser frequency (ca. 31600 cm^{-1}) for a mirror velocity $c_M = 1.90 \text{ cm/s}$. This corresponds to a sampling rate of exactly 120 KHz and a signal bandwidth of about 7.6–53.2 KHz. For the FFT calculation, the interferograms were extended by “zero filling” to 2048 points so that the spectroscopic resolution $\Delta\tilde{\nu} \approx 2\Delta\tilde{\nu}_{\text{dig}}$ can be approximated well with the “digital resolution” of $\Delta\tilde{\nu}_{\text{dig}} = 15.43 \text{ cm}^{-1}$. For the Mertz phase correction, the interferograms were sampled with a resolution of $\Delta\tilde{\nu}_{\text{sym}} = 123.4 \text{ cm}^{-1}$ symmetrically about the ZPD position. During the measurement time of ca. 70 s for a single beam spectrum, 1200 interferogram scans were averaged, apodized with the Blackman–Harris 3-term function, FFT transformed, and phase corrected.

The temperature of the front plate of the reflection accessory with the immersion lens (see Fig. 6.11) was held constant at $37^\circ\text{C} \pm 0.02^\circ\text{C}$ during the measurements by a water circulation thermostat (accessory cf. Ch. 5.3) and monitored with a PT-100 foil temperature probe (Juchheim, Fulda, BRD: Typ PF 1.2150.1) glued to the front plate. For a measurement of the single beam reference spectra $S_{\text{ref}}(\tilde{\nu})$, SPECTRALON™ cylinders with varying reflectivities as the diffuse reflection standards were pressed against the immersion lens of the accessory (cf. Fig. 6.11). The “extinction”, $E_d(\tilde{\nu}) = -\log_{10}(R_d(\tilde{\nu}))$, was calculated through the reflectivity $R_d(\tilde{\nu}) = S_{\text{Lip}}(\tilde{\nu})/S_{\text{ref}}(\tilde{\nu})$ into which small changes of the absorption coefficient of the tissue enter linearly (as long as the average pathlength of the reflected radiation in the tissue is constant). Fig. 6.12 gives an impression of the diffuse reflectivity of the body surface area in the near IR.

As the reference, a cylinder ($\phi = 10\text{mm}$, $h = 10 \text{ mm}$) from the SPECTRALON™ standard white material was used for the spectra in Fig. 6.12 (Labsphere SRM-99L-100C) which display a nearly ideally diffuse Lambert characteristic in the spectral region $0.25\text{--}2.5 \mu\text{m}$ according to the manufacturer; the reflectivity achieves the value $R_d > 0.98$ in the region of ca. $\lambda = 0.4 - 1.6 \mu\text{m}$ and slowly decreases in the long wave IR ($R_d = 0.976, 0.957, 0.944$ at $\lambda = 1.8, 2.0, 2.2 \mu\text{m}$ [214]). The absolute measurement errors through the reflection standard are smaller than the individual oscillations in the skin spectra in Fig. 6.12, which example measurements for an individual test person show. A comparison of the reflection spectrum of the lip with the values determined in the Monte Carlo simulation for the diffuse reflection (Table 6.2 with $n_1 = n_2$) shows good agreement with which the optical parameters of the skin used in the simulation (Ch. 6.2) are confirmed. In the reflection spectrum of the tongue (Fig. 6.12b), which, due to its larger surface area, represents quasi a biological model for lips in poor contact with the immersion lens, a clear increase in the Fresnel reflection can be determined. The extinction spectrum $E_d(\tilde{\nu})$ of the lip is similar to the extinction of a 1 mm thick water layer (Fig. 5.14C) additionally with a baseline increasing toward the longer wave IR that describes the portion of radiation power which remains in the tissue and does not

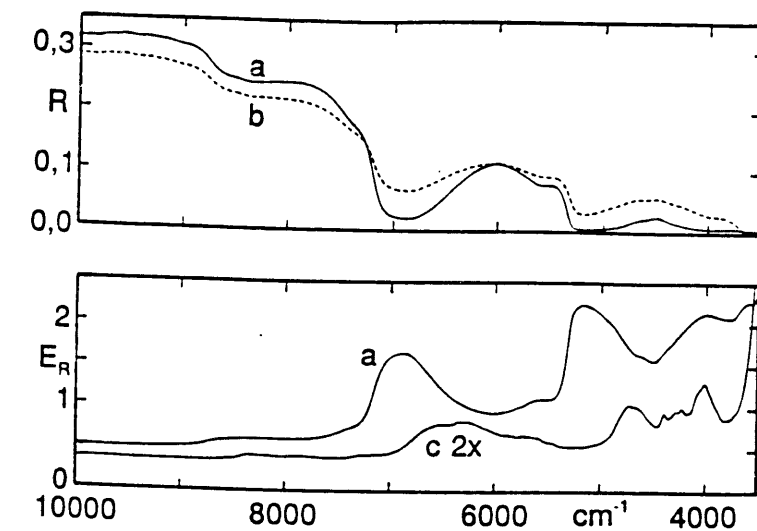


Figure 6.12: Diffuse reflectivity R_d and extinction E_d of (a) the inner lip, (b) tip of the tongue, and (c) of crystalline glucose.

return to the surface area. As a result of the wavelength dependence of the average pathlength of the reflected radiation in the tissue, the water absorption is damped at ca. $\tilde{\nu} = 5000 \text{ cm}^{-1}$ relative to the value at 7000 cm^{-1} . For completeness, the diffuse reflection spectrum of water-free, crystalline glucose (Fluka Feinchemikalien, Neu-Ulm, BRD) is shown in Fig. 6.12c. This spectrum was taken by shaking up a 8 mm thick sample layer in front of the immersion lens. Overtone and combination bands of glucose are visible above 4000 cm^{-1} , around 6000 cm^{-1} , and further along the curve at ca. 8400 cm^{-1} .

6.4.1 Single Person Experiment with Oral Glucose Tolerance Test

A first test series for the non-invasive determination of glucose was conducted with the so-called oral glucose tolerance test. For this, a normalized sugar syrup (400 m/L Dextro O.G.-T., Boehringer, Mannheim, BRD) that contains a mixture of mono- and oligosaccharides which corresponds to an amount of 100 g water-free glucose after enzymatic breakdown in the digestive tract was drunk by a test person with Typ 1 diabetes. The standardized test for the diagnosis of a diabetic inflection prescribes a monitoring of the blood glucose level (3–6 measurements) in a time frame of up to 3 hours after intake of the syrup. Two examples of self-sampled blood glucose profiles are shown in Fig. 6.13.

In intervals of about 20 min, capillary blood was taken from the finger of the test persons and the glucose concentration was determined (simple measurements with the glucose-hexokinase method at the Diabetes Institute, Duesseldorf). The reference values at the times of the blood samples (crosses in Fig. 6.13) were used as the data points for an approximation of the glucose profile with a cubic spline function [234,235:p. 59ff]. Normally, three lip spectra between two blood samples were measured, and the lines in Fig. 6.13 connect the reference values approximated in

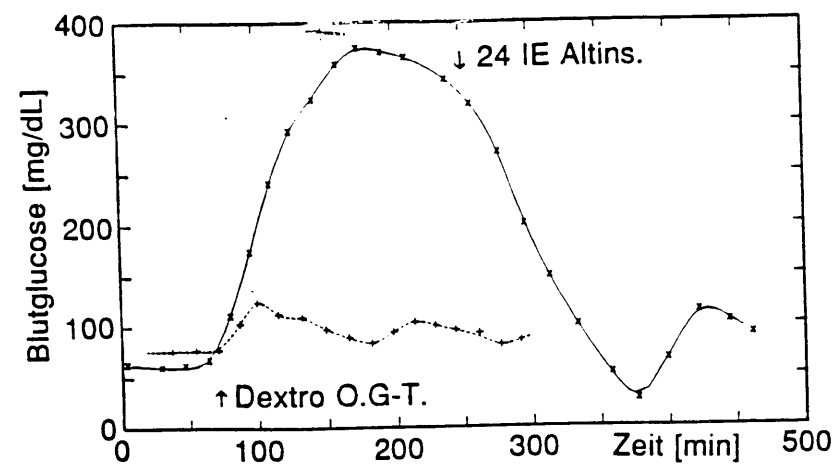


Figure 6.13: Blood glucose curves in the oral glucose tolerance test for a Type 1 diabetic (—) and a healthy test person (- - -).

the above fashion to the times of the lip measurements. The blood glucose profiles were begun in the mornings; both examples in Fig. 6.13 initially display a relatively constant glucose level. After drinking of the sugar syrup, dramatic changes are seen in both curves: in comparison to the healthy test person, the blood sugar of the diabetic increases to much higher values. After achieving a slightly decreasing upper plateau due to the flooding of glucose through the kidneys, the test person applied a larger amount of so-called ALT-insulin (see Fig. 6.13⁴³) undelayed such that hypoglycemia with the ensuing counterreaction took place (Ch. 2). For the examination of the information content of the lip spectra, the large dynamics of the glucose profile of the diabetic are advantageous, since distributions of the reference glucose values with standard deviations of typically of $\sigma_{\text{pop}} > 160$ mg/dl can be realized. As a result, prediction errors above the desired order of magnitude of about 20 mg/dl can be statistically differentiated from errors in the "prediction with the average value".⁴⁴

The certainty of the reference values in the experiment with the oral glucose tolerance test is limited. In addition to the uncertainty of the clinical-chemical reference method at the points, errors arise through the spline approximation, especially through the finite certainty (in the best case, ± 0.5 min) of the times of the blood sampling and the lip measurement during protocol recording. These errors are dependent on the form of the glucose profile and are maximum in regions with larger slope. Therefore, a realistic estimation of the average error of the reference method is hardly possible, however, the value lies maximally at about double the determination error at the data points.

The big problem in single person experiments lies in the danger that regressions of the IR spectra against the reference values of the glucose concentrations are influenced by the so-called apparent

⁴³1 IE (international unit) insulin = 0.04167 mg of a mixture of 52% beef and 48% pork insulin [236].

⁴⁴cf. commentary to Fig. 4.14: "inversion with rank $R = 0$ ".

correlations. Trends in the measurement conditions are meant which arbitrarily correlate with the temporal curve of the true glucose concentration, e.g. changes of the interferometer alignment with the room temperature can falsely show an increased information content of the IR spectra (cf. note for this in Ch. 5.3.1). A very important point in the generation of statistical calibration models (Ch. 4.2) is the independence of the calibration standards (IR spectrum including glucose reference value) among each other. The best possible safety measure against apparent correlations lies in the arbitrary selection of the measurement data ("randomization") which e.g. was guaranteed in the Duesseldorfer Diabetes Institute by random selection of the test subjects in the patient measurements. In the generation of a single person calibration with oral glucose tolerance test, the calibration standards taken in short temporal separation are correlated among each other. In this case, true spectroscopic correlations of the IR signals with the glucose concentration cannot be differentiated from eventual apparent correlations due to random trends in the measurement conditions. A further safety measure against apparent correlations can practically be achieved, however, in that in the temporal curve of the blood glucose profile, multiple increases and decreases are run.

For this, a total of 133 lip spectra were measured on two sequentially occurring days in which two blood glucose profiles over about 8 hours were monitored. The time curves are similar to those in Fig. 6.13, however, the insulin injection was dosed so that no hypoglycemia took place during reduction, i.e. the curves begin and end in the normal region of glucose concentration around 100 mg/dl. In order to increase the safety against apparent correlations in the framework of the possibilities, the sugar syrup was consumed in two portions such that during the blood glucose increase, a nearly 1 hour plateau was run between both. During the first few days, a bottle of Dextro O.G.-T. was used, and a maximum blood sugar value of ca. 420 mg/dl was achieved. In the course of the second day, a total of two bottles of syrup were consumed by test subjects so that the maximum value could be increased up to around 600 mg/dl. As a result, the glucose reference values of the lip spectra displayed a nearly equal distribution in the region 34–603 mg/dl with an average value $\bar{c}_{\text{pop}} = 301$ mg/dl and a standard deviation of $\sigma_{\text{pop}} = 167$ mg/dl.

For the diffuse reflection standard, a cylinder of SPECTRALON™ grey standard (Labsphere SRS-10-020, $\phi = 20$ mm, $h = 10$ mm) was manufactured whose diffuse reflectivity was given as 10%. (The grey standards were manufactured by adding coal particulates to the plastic of the white standards [214].) A comparison with the white standard showed that the reflectivity of the grey standard in the spectral region 8000–4000 cm^{-1} lay at about 13% on average. The S/N ratio of the measurements is documented in Fig. 6.14:

In addition to both single beam spectra for sample and reference, the extinction noise from each of two lip and reference measurements is also shown in Fig. 6.14. With these, conclusions can be made about the S/N ratios of both single beam spectra and about the noise in the extinction spectra $E_d(\bar{\nu})$ of the lip.⁴⁵ In the region of the strongest glucose overtone bands around 6300 cm^{-1} , the latter achieved values on the order of magnitude $n_A = 4 \cdot 10^{-5}$ AU which corresponds to the maximum band of absorption for a glucose concentration of 50 mg/dl in an aqueous solution with thickness

$$n_A(\bar{\nu}) = \sqrt{\frac{n_{A,\text{lip}}^2(\bar{\nu}) + n_{A,\text{ref}}^2(\bar{\nu})}{2}}, \text{ cf. Eq. 3.32.}$$

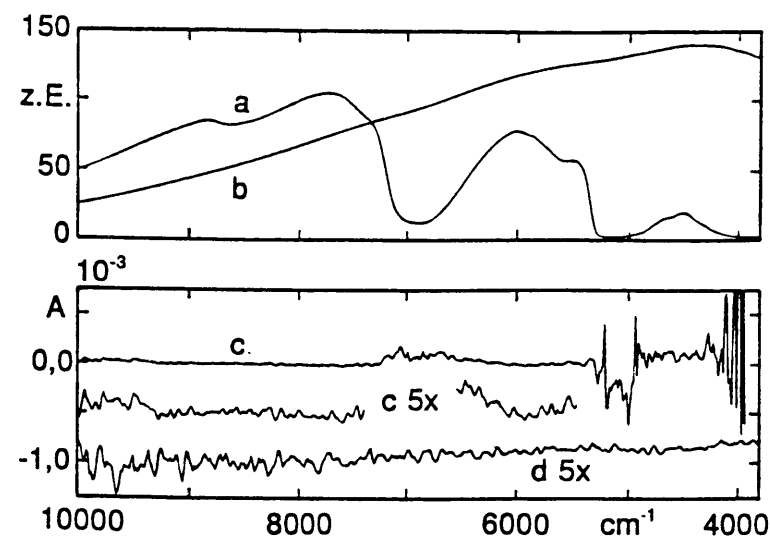


Figure 6.14: A single beam spectrum of the diffuse reflection of (a) the lip and of (b) the grey standard ($R_d \approx 13\%$) in arbitrary units; extinction noise from (c) two lip measurements $n_{A,\text{lip}}$ and from (d) two references $n_{A,\text{ref}}$ ($R_d \approx 13\%$).

1 mm. If the possibly up to ten times thinning of the glucose concentration in the spectroscoped tissue volume is calculated as a result of the smaller portion of the interstitial volume in the upper layers of the skin (Ch. 6.1), it becomes clear that the non-invasive measurement approaches the upper limit of that technically possible today and of that appropriate for the patient (measurement time ca. 1 min). The application of optimized multivariate procedures for the quantitative signal analysis is, for the non-invasive glucose determination using IR spectroscopy, a *conditio sine qua non*. For this, inverse, i.e. statistical, calibration models (Ch. 4.1) were generated and solved with the PLS estimation procedure according to the criterium of the minimum quadratic prediction error (Ch. 4.2.2), where the described methods for model optimization and cross-validation of the prediction quality were applied (Ch. 4.3). As a result of an outstanding Cook distance, one lip spectrum was classified as an outlier.

The results seen in Fig. 6.15 are noteworthy for two reasons. First, the prediction quality of the diffuse reflection spectra of the skin are optimized by selection of a very broad spectral region (see Fig. 6.15) which includes the water absorption bands at 7000 cm^{-1} . In the quantitative processing of transmission spectra for liquid blood plasma, the water bands around 7000 cm^{-1} and 5000 cm^{-1} had to be strictly excluded from the calibration in order to be able to generate sensible prediction models (Ch. 5.4). This apparent contradiction occurs through the chemical and spectroscopic differences between the "free water" in plasma and the "bonded water" in tissue. In the latter, the water molecule is in a changed energetic state through the building of hydrogen bonds mainly to the proteins, apparently reducing the susceptibility of the corresponding absorption bands to wavelength translation as a result of temperature oscillations, etc. (cf. Fig. 6.14c and Fig. 5.15c). In the literature, the special behavior of water in biological tissue is still undescribed; a note that the peak "free" water bands at $2.94\text{ }\mu\text{m}$ shift in tissue to $3.05\text{ }\mu\text{m}$ can be found in [237].

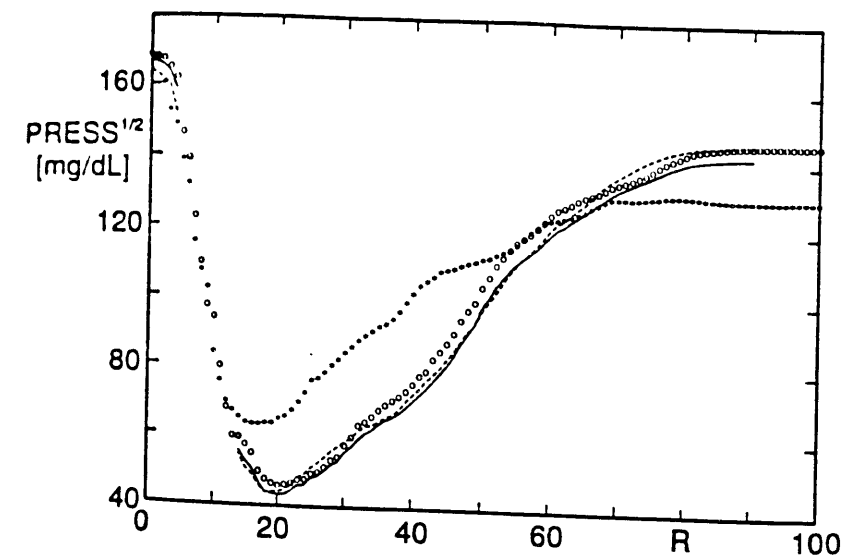


Figure 6.15: $\text{PRESS}^{1/2}$ statistic of the average prediction error for glucose versus the PLS inversion rank for the non-invasive single person calibration after the oral glucose tolerance test; results for regression against the (*) extinction spectra $E_d(\tilde{\nu})$ as well as the (o) logarithmic single beam spectra $-\log_{10}(S_{\text{lip}}(\tilde{\nu}))$ with (—) $T = 10\text{ min}$ and (- - -) $T = 20\text{ min}$ lowpass filtering of the glucose reference profile; 132 reflection spectra of the lip in the spectral region $8994\text{--}5477/\Delta\tilde{\nu}_{\text{Cal}} = 30.8\text{ cm}^{-1}$ ($N = 115$).

The second important note to Fig. 6.15 pertains to the type of the spectra used for the glucose calibration. The optimal MSE prediction error for blood glucose for the calibration with the extinction spectra $E_d(\tilde{\nu}) = -\log_{10}(S_{\text{lip}}(\tilde{\nu})/S_{\text{ref}}(\tilde{\nu}))$ is $\text{PRESS}^{1/2} = 62.9\text{ mg/dl}$ at $R_{\text{opt}} = 16$. It is important to mention that the prediction quality of the "linearized" single beam spectra $-\log_{10}(S_{\text{lip}}(\tilde{\nu}))$ of the lip according to the Lambert-Beer law with $\text{PRESS}^{1/2} = 45.6\text{ mg/dl}$ ($R_{\text{opt}} = 20$) is better, although the amplitude of the single beam spectra during the measurement series oscillated relatively strongly such that the glucose correlations in the IR spectra of signal variances were disturbed by spectrometer drifts (see Ch. 3.3.3). During the first measurement day, a trend due to the increasing freezing of the remaining moisture in the dewar housing of the detector was overlaid onto the "stochastic" oscillations through variations in the application pressure of the lips (during the ca. 70 s measurement, typically, 2-4%) so that the exit power of the NIR radiation source had to be multiply re-adjusted using the power supply. Data pre-processing in the form of filtering, normalization, baseline correction, or similar techniques was not used, since no improvement in the MSE prediction quality could be achieved. The advantage of the calibration with single beam spectra with extinctions is the approx. $\sqrt{2}$ times reduced noise (cf. Fig. 6.14); an additional advantage for the single channel spectra occurred during the experiment with the oral glucose tolerance test in that the immersion lens and the diffuse reflection standard were not (as in the following experiments) cleaned of dust with compressed air before each reference measurement so that a few spectra $S_{\text{ref}}(\tilde{\nu})$ were disturbed by dust particles.

In Fig. 6.15, the results of the regression of single channel spectra versus two lowpass filtered glucose reference time curves can also be found. For this, the compensation spline functions (cf. Fig. 6.13) were equidistantly sampled with 1 min^{-1} after approximation of the blood sugar values at the data points and were digitally filtered in software.⁴⁶ Due to the constant level of the glucose values at the beginning of the profiles, no problems occurred through unknown initial values. With the lowpass filtering of the reference values, the time delay through the diffusion of glucose from the capillaries into the upper skin layers is simulated. As Fig. 6.15 shows, these lie on the order of magnitude $T = 10 \text{ min}$ ($\text{PRESS}^{1/2} = 43.0 \text{ mg/dl}$ at $R_{\text{opt}} = 20$), since the prediction results for larger response times of the lowpass filter tend to become poorer again ($\text{PRESS}^{1/2} = 43.7 \text{ mg/dl}$ at $R_{\text{opt}} = 19$ and $T = 20 \text{ min}$). Fig. 6.16 gives an impression of the quality of the non-invasive blood glucose determination using diffuse reflection measurement of the inner lip where the results of the cross-validation for the optimized PLS model with single channel spectra are shown:

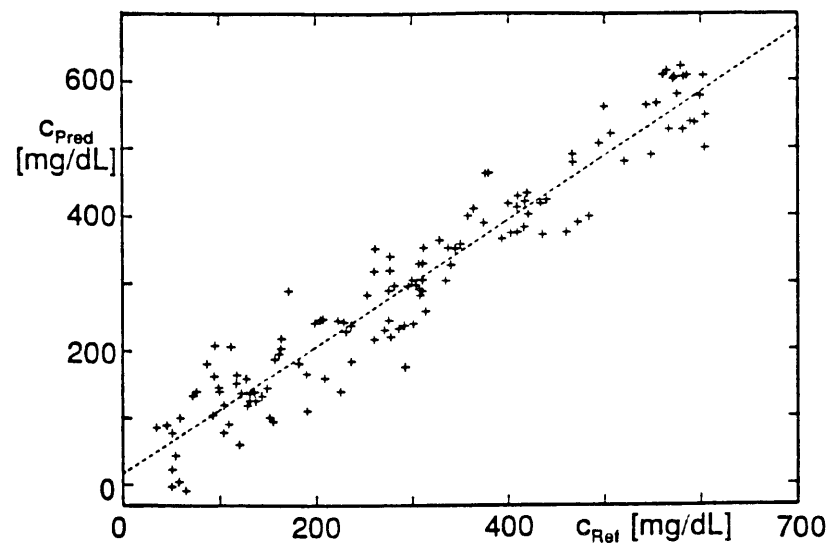


Figure 6.16: Independent glucose predictions of the MSE optimal PLS model during the non-invasive single person experiment with oral glucose tolerance test versus the non-lowpass filtered reference values with LS compensation lines.

For the clinical use and the application in monitoring of blood sugar (Ch. 2), the determination certainty in Fig. 6.16 is not sufficient. Here, improvements of the $\text{PRESS}^{1/2}$ values of about 2–2.5 times are necessary. An LS compensation line through the independent predictions in Fig. 6.16 is $\hat{c}_{\text{pred}} = 17.0 + 0.945c_{\text{ref}}$ (correlation coefficient: $r^2 = 0.924$) and displays a noticeable bias in the direction of the population average value $\bar{c}_{\text{pop}} = 301 \text{ mg/dl}$ of the glucose concentration in contrary to the calibration results for the liquid blood samples (Ch. 5).

In the calibration of the single channel spectra of the lip, it is noteworthy that a regression against the “raw” spectra $S_{\text{lip}}(\tilde{\nu})$ in comparison to $-\log_{10}(S_{\text{lip}}(\tilde{\nu}))$ yields only slightly poorer results (e.g. instead of $\text{PRESS}_{\text{opt}}^{1/2} = 45.6 \text{ mg/dl}$ in Fig. 6.15 a reduction in quality to $\text{PRESS}_{\text{opt}}^{1/2} =$

⁴⁶Butterworth lowpass first order: $y(n) = (1 - e^{-(1/T)})x(n) + e^{-(1/T)}y(n-1)$ where T is the time constant of the filter as a multiple of the sampling interval.

48.5 mg/dl for identical R_{opt}). As a result of the extremely small size of the glucose signals, the generation of the correct *linear* calibration model according to the Lambert–Beer law, i.e. in the desired concentrations, yields only small advantages. The processing of single channel spectra in the narrow wave number regions $6788\text{--}5461/\Delta\tilde{\nu} = 30.8 \text{ cm}^{-1}$ ($N = 44$) and $4736\text{--}4212/\Delta\tilde{\nu} = 30.8 \text{ cm}^{-1}$ ($N = 18$), which were optimal over the transmission spectra of the liquid plasma for the glucose prediction, still yields a $\text{PRESS}^{1/2} \approx 58 \text{ mg/dl}$ ($R_{\text{opt}} = 18$), since the sole application of the region above 4000 cm^{-1} allows only low prediction quality ($\text{PRESS}^{1/2} \approx 93 \text{ mg/dl}$ at $R_{\text{opt}} = 13$). This was to be expected as a result of the clearly increasing noise through the small diffuse reflectivity R_{diff} of the skin in this spectral region (cf. Fig. 6.14 and Table 6.2).

6.4.2 Experiment with Larger Patient Population

The Bruker IFS-66 spectrometer including accessory was transported to the Duesselder Diabetes Research Institute for the diffuse reflection measurement of the lip. During a time period of two weeks, lip spectra from a total of 133 different persons were sampled there. The measurements were conducted throughout the day on randomly selected stationary and ambulant patients for which the statistical independence of the calibration standards is guaranteed. Six patients were doubly and one patient triply measured such that a total of 144 measurements, the majority from diabetics, were available. These were divided into 73 male and 68 female patients as well as 45 smokers and 96 nonsmokers. Before entering the measurement room, capillary blood was taken out of the finger of the test subjects as well as venous blood from the arm such that in addition to the capillary glucose concentration, the venous glucose and the concentrations of total protein, total cholesterol, and triglycerides could also be clinically-chemically determined. Additionally, the age of the patients as well as the time of the last meal were added to the protocol. For comparison with the diabetic population of the liquid blood plasma (Ch. 5.2), the clinical-chemical reference values are summarized in Table 6.3. The patient population of the non-invasive measurement series displays a similar distribution for the blood substrate concentrations as the population of the liquid blood samples. After removal of two extremely high triglyceride values (4360 and 1150 mg/dl from two older male smokers), this is valid also for the triglycerides (then: $\bar{c}_{\text{pop}} = 158.9 \text{ mg/dl}$, $\hat{\sigma}_{\text{pop}} = 98.4 \text{ mg/dl}$). The most obvious difference pertains to the reduced glucose dynamics of the non-invasive study with about $\hat{\sigma}_{\text{pop}} = 76 \text{ mg/dl}$ as compared to ca. $\hat{\sigma}_{\text{pop}} = 90 \text{ mg/dl}$ in the liquid blood study. Apparently, this can be attributed to a larger portion of stationary handled patients whose blood sugar level during the hospital visit was especially well monitored and normalized.⁴⁷ The blood substrate concentrations were determined at the Duesselder Diabetes Research Institute by simple measurements with the clinical-chemical methods mentioned in Ch. 5.2.

For the spectroscopic reference material, a SPECTRALON™ cylinder ($\phi = 10 \text{ mm}$, $h = 10 \text{ mm}$) of 5% grey standard (Labsphere USRS-05-010) was used in Duesseldorf, since on average over many persons, a better matching of the radiation power meeting the detector during the measurement of the lip and the reference was achieved. The original reflectivity of the grey standard was multiply ($6\times$) achieved during the course of the measurement series by polishing the upper surface area of the cylinder with an appropriate sandpaper in a specially constructed tool. Many

⁴⁷An “average” patient population without selection of diabetics displays about $\hat{\sigma}_{\text{pop}} = 45 \text{ mg/dl}$ (cf. Fig. 4.3); this corresponds approximately to the variation in the blood glucose profile of a healthy person in the oral glucose tolerance test.

Table 6.4: Concentration region $c_{\min} - c_{\max}$ as well as average values \bar{c}_{pop} and standard deviations $\hat{\sigma}_{\text{pop}}$ of the population of 141 lip measurements (133 different patients; age in [years]; protein in [g/l], otherwise [mg/dl]).

	Age	venous Glucose	Capillary Glucose	Total Protein	Total Cholesterol	Triglyceride
$c_{\min} - c_{\max}$	13-79	37-401	35-417	52-86	112-330	39-1360
\bar{c}_{pop}	44.9	148.7	154.2	69.2	210.8	174.5
$\hat{\sigma}_{\text{pop}}$	16.5	75.3	76.7	5.4	47.6	163.2

lip spectra were sampled from each test subject after the blood sampling, where most often, the following series of measurements was maintained: (1) reference, (2-3) two lips, (4) reference, and (5) lip. This sequence should increase the chance of at least one successful lip measurement near in time to a reference measurement and simultaneously minimize the time effort per patient. Between the blood sampling and the last lip measurement, depending on the "ability to learn" of the test subject, between 15 and 45 min passed such that the quality of the reference values for the glucose concentration is limited. The pairing of the single channel spectra of the lip and the reflection standard for the calculation of the extinctions took place individually under consideration of the time intervals and further special circumstances in each case.⁴⁸ Before each lip and reference measurement, the immersion lens was washed off with a Kleenex tissue soaked in ethanol and dried and removed of dust with nitrogen gas from a compressed air pistol. For disinfection during the exchange of patients, a cottonball soaked with the disinfectant Spitacid was pressed for 2 min against the bottom of the immersion lens and the bordering metal of the lens holding assembly and additionally, a new plastic foil with opening for the lens was glued over the frontplate of the accessory in order to completely prevent bodily contact with contaminated surface areas. From a total of 390 lip spectra, 9 had to be removed from the regression as outliers. Three spectra were already classified during a visual check as unsuccessful and six further ones displayed high Cook distances from which all three spectra were from a younger woman (apparently through lipstick). The test subjects were instructed before the measurement to wash out the mouth and eventually remove makeup from the lips.

The conditions for the spectroscopic measurement in the Duesseldorfer clinic were comparably unfavorable. A closed off room for the IR spectrometer was indeed available, however, as a result of the patient traffic and the communication with the medical personnel, a constant air exchange with the waiting room located in front of the measurement room took place whereby the windows were regularly opened. Through this, the air moisture and temperature at the measurement station were subjected to significant oscillations (for long-term measurements with the Bruker IFS-66 spectrometer, the manufacturer recommends oscillations of max. $\pm 1^\circ\text{C}$); also, the temperature of the baseplate of the reflection accessory with the immersion lens could only be controlled to ca. $37^\circ\text{C} \pm 0.05^\circ\text{C}$. A further problem pertained to the purging of the spectrometer and the reflection accessory with nitrogen which was delivered in 50 l pressure bottles (200 bar). In order to maintain a constant round-the-hour purge, only about 450 l/h days and only about 150 l/h nights of nitrogen

⁴⁸Normally, with the pairs (see text further above): (2)/(1), (3)/(4), and (5)/(4).

could be taken from the bottles (as opposed to the 600 l/h recommended by Bruker). As a result of the unfavorable environmental conditions, the prediction quality of the single beam spectra of the lip measured in Duesseldorf was not satisfactory and the optimized results of the calibration shown in Fig. 6.17 were achieved with the extinction spectra $E_d(\bar{\nu})$.

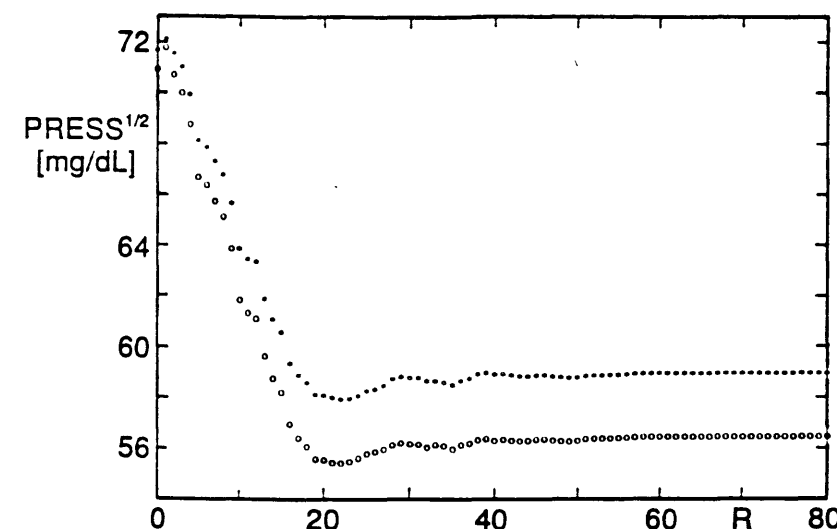


Figure 6.17: $\text{PRESS}^{1/2}$ statistic of the average prediction error for the (o) venous and the (*) capillary blood glucose versus the PLS inversion rank for the non-invasive measurement procedure; 381 extinction spectra from 133 patients in the spectral region $8994-7421/\Delta\bar{\nu} = 30.8 \text{ cm}^{-1}$ and $7004-5924/\Delta\bar{\nu} = 30.8 \text{ cm}^{-1}$ ($N = 88$).

The optimal MSE prediction error for the Duesseldorfer extinction spectra is $\text{PRESS}_{\text{opt}}^{1/2} = 55.4 \text{ mg/dl}$ (venous glucose) and $\text{PRESS}_{\text{opt}}^{1/2} = 57.9 \text{ mg/dl}$ (capillary glucose). The better result for the prediction of the venous blood glucose values is a further indication that the glucose in the upper skin layers of the lip sampled in the diffuse reflection experiment is a few minutes behind the capillary blood glucose. In comparison to the single person experiment with oral glucose tolerance test (Fig. 6.15), the prediction of capillary blood glucose with extinction spectra is slightly improved as a result of the larger care taken during the spectroscopic reference measurement with the diffuse reflection standard (cleaning with compressed air), and in contrary to the single person calibration, the $\text{PRESS}^{1/2}$ statistic in Fig. 6.17 no longer increases steeply after running through the MSE optimal PLS inversion rank which indicates a larger statistical robustness of the calibration.

The optimized spectral region for the calibration of the patient population (see Fig. 6.17) shows two changes in comparison to the single person experiment (see Fig. 6.15). Due to the problems in the spectrometer from purging with nitrogen from compressed gas bottles, firstly, the frequency region of ca. $7400-7000 \text{ cm}^{-1}$ which is disturbed by atmospheric water bands had to be removed from the calibration (the finely structured bands of the gaseous water are displaced to higher frequencies in comparison to the broad absorption bands of condensed water at 7000 cm^{-1}). The second change pertains to the lower limit of 5924 cm^{-1} of the spectral region for the regression, while for the single person experiment, 5477 cm^{-1} was selected. The reason here was the sporadic

occurrence of absorption band structure slightly below 6000 cm^{-1} . As Fig. 6.18a shows, this irreproducible double band occurred more often with women than with men and achieved peak heights up to about 0.07 AU in isolated cases. As the comparison to the reflection spectra (b) and (c) in Fig. 6.18 shows, which were measured by placing a ca. 4 mm thick layer of beef tartar onto the immersion lens, the double band occurs below 6000 cm^{-1} through an increased fat percentage in the spectroscoped tissue volume. For a few patients, e.g. also the test person in both single person experiments, outstanding absorption bands of fat could never be observed (i.e. the peak height was always smaller than ca. $5 \cdot 10^{-3}$ AU).

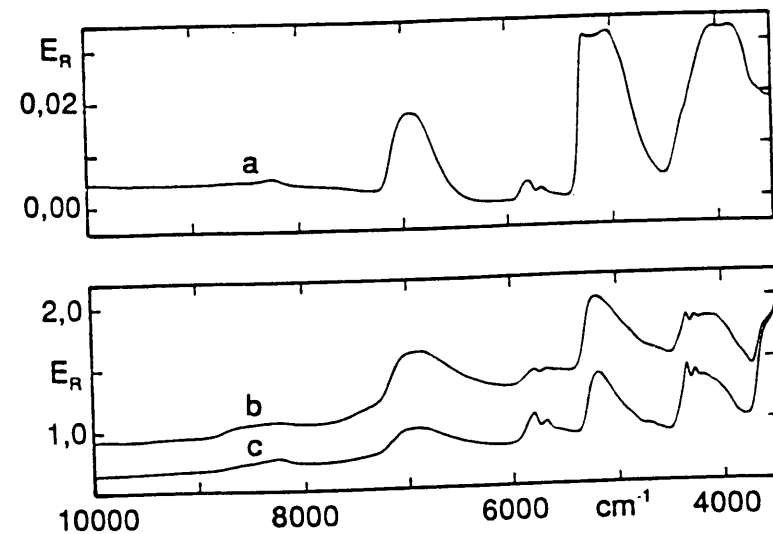


Figure 6.18: (a) Difference of the average spectra of all 182 “female” (+) and all 199 “male” (-) lip extinctions; diffuse reflection spectrum from (b) unsorted beef tartar and from (c) beef tartar with increased fat percentage (Reference: SPECTRALON™ white standard).

An extension of the spectral region for the calibration to frequencies above 9000 cm^{-1} yields only insignificant improvement of the prediction quality: e.g. a $\text{PRESS}^{1/2} = 57.4\text{ mg/dl}$ is calculated for regression in the regions $11000\text{--}7421/\Delta\tilde{\nu} = 61.6\text{ cm}^{-1}$ ($N = 59$) and $7004\text{--}5924/\Delta\tilde{\nu} = 30.8\text{ cm}^{-1}$ ($N = 36$) and $R_{\text{opt}} = 20$ (as compared to $\text{PRESS}^{1/2} = 57.9\text{ mg/dl}$ for $R_{\text{opt}} = 22$ in Fig. 6.17). Obviously, the information content of the diffuse reflection spectra in the spectral region above 9000 cm^{-1} is small due to the increased noise (cf. Fig. 6.14) and the pathlengths of the radiation which are too short in this spectral region in tissue. The test ran unsuccessfully for using the measurement procedure of diffuse reflection for the non-invasive determination of total protein, total cholesterol, and triglycerides. The molecules of these materials are much larger than that of freely diffusing glucose such that the concentrations in the upper skin layers do not correlate with the blood concentrations.

6.4.3 Single Person Experiment with Random Blood Glucose Levels

The quality of the Duesselderfer patient spectra was not optimal regarding the reproducibility of lip positioning, application pressure, etc. and as a result of the limited stability of the FT spectrometer due to the measurement conditions in the hospital. As a result, a further single person experiment with the same test person as in the oral glucose tolerance test (Ch. 6.4.1) was conducted in which the reference values of blood glucose were randomly selected as a safety measure against apparent correlations. Over a time period of two weeks (nine measurement days), lip spectra were sampled three times daily. In order to guarantee the largest possible dynamics of the blood glucose reference values ($\hat{\sigma}_{\text{pop}}$), the diabetic was instructed to control meals and insulin dosing during these days such that mornings, afternoons (shortly before eating), and evenings, a constant level of the blood glucose concentration was attained (see Table 6.4).

Table 6.5: Selected blood glucose levels from a random number generator in the second single person experiment (see text).

	mornings	afternoons	evenings		mornings	afternoons	evenings
1. day	low	middle	high	6. day	high	middle	low
2. day	middle	high	low	7. day	low	high	middle
3. day	middle	low	high	8. day	high	middle	low
4. day	high	middle	low	9. day	low	high	middle
5. day	high	low	middle				

A “high” in Table 6.4 means that the test subject should have achieved a blood sugar level $> 400\text{ mg/dl}$, for “low”, the desired level was $< 150\text{ mg/dl}$ and for “middle”, an arbitrary between value was allowed. During the levels, eight lip measurements and three capillary blood samples from the finger were normally taken in ca. 35–40 min, where the following sequence was given: (1) lip spectrum, (2) blood sample, (3–5) three lip spectra, (6) blood sample, (7–9) three lip spectra, (10) blood sample, and (11) lip spectrum. The glucose content of the blood samples was determined at the Duesselderfer Diabetes Research Institute with the hexokinase method, and the average values of double measurements formed the data points for the reconstruction of the temporal curve of the blood sugar level during the 27 levels by an approximation with cubic compensation splines [234]. The variation of the blood glucose during a level was maximally ca. 80 mg/dl and typically $< 40\text{ mg/dl}$ such that the aforementioned sequence of measurements with short temporal extrapolation of the glucose concentration was not problematic. At the end, 219 calibration standards were available for the regression, where the glucose references in the region 34–590 mg/dl were scattered approximately uniformly (average $\bar{c}_{\text{pop}} = 268.6\text{ mg/dl}$, standard deviation $\hat{\sigma}_{\text{pop}} = 161.8\text{ mg/dl}$).

For the spectroscopic reference measurement immediately before each measurement, a cylinder made from the SPECTRALON™ white standard (Labsphere SRM-99L-100C, $\phi = 10\text{ mm}$, $h = 10\text{ mm}$) was used with a centrally drilled hole ($\phi = 7\text{ mm}$, $t = 2\text{ mm}$). This reflection standard with diffuse return radiation $R_d \approx 8\%$ is robust against surface area changes through dust or mechanical loading in comparison to a standard lying on the inversion lens made of gray

SPECTRALON™. The immersion lens was cleaned before each lip and reference measurement with a Kleenex tissue soaked in ethanol and removed of dust with compressed air. Two lip spectra, which were also suspect during a visual examination, were removed from the regression as outliers due to high leverage values (cf. Eq. 4.63) and a further one due to a large Cook distance.

The MSE optimal prediction results were achieved for the same spectral region of the calibration as in the single person experiment with oral glucose tolerance test (Ch. 6.4.1). In contrary to this (Fig. 6.15), the $PRESS^{1/2}$ statistic no longer steeply increases in Fig. 6.19 after achieving a minimum value for higher inversion ranks as a result of the random selection of glucose reference values, where the higher quality of the calibration data is underlined. The optimized result for the extinction spectra ($PRESS^{1/2} = 55.9$ mg/dl at $R_{opt} = 22$) is practically identical to the prediction quality for the venous blood glucose in the patient population from the Diabetes Research Institute. The results for the "linearized" single beam spectra $-\log_{10}(S_{lip}(\tilde{\nu}))$ are better for the single person experiment with glucose levels ($PRESS^{1/2} = 51.9$ mg/dl at $R_{opt} = 24$) than with extinctions regardless of the relatively long measurement time of two weeks, however, in comparison to the shorter experiment with oral glucose tolerance test (measurement time 2 days, cf. Ch. 6.4.1), the results are poorer. (The calibration with the "raw" single beam spectra $S_{lip}(\tilde{\nu})$ yields practically identical results: $PRESS^{1/2} = 52.2$ mg/dl at $R_{opt} = 22$.) The causal relationship of the glucose prediction with the spectroscopic signals can be confirmed by examination of the PLS solution vectors, i.e. the estimations for the Wiener filter, for different inversion ranks. In Fig. 6.20, the PLS solution vectors of both single person experiments with glucose tolerance test and random ("randomized") glucose reference values are compared.

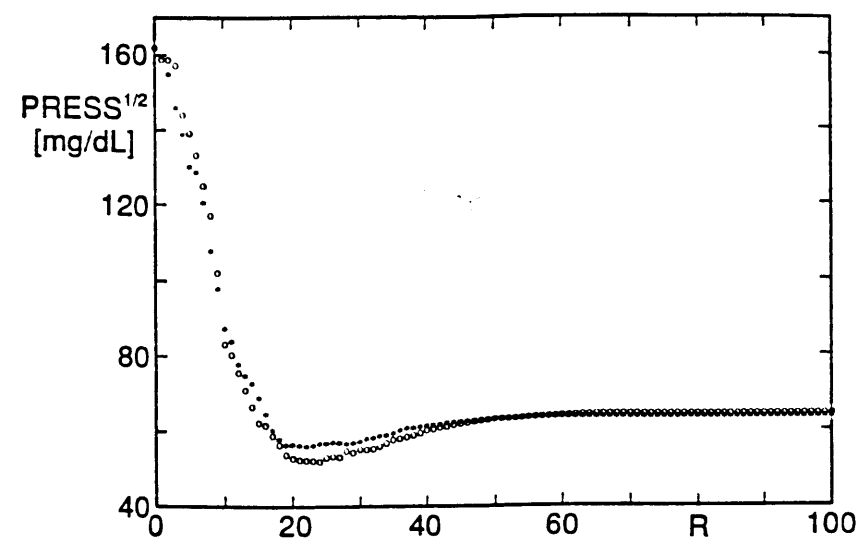


Figure 6.19: $PRESS^{1/2}$ statistic of the average prediction error for glucose versus the PLS inversion rank for the optimized, non-invasive single person calibration with randomly selected glucose levels; results for regression against the (\star) extinction spectra $E_d(\tilde{\nu})$ as well as the (\circ) logarithmic single beam spectra; 216 reflection spectra of the lip in the spectral region $8994-5477/\Delta\tilde{\nu}_{Cal} = 30.8$ cm^{-1} ($N = 115$).

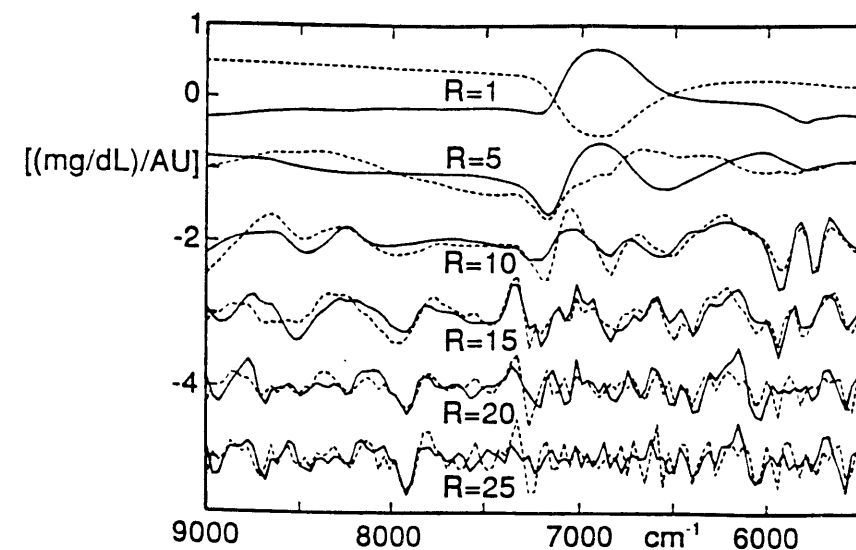


Figure 6.20: PLS solution vectors of the non-invasive glucose calibration with the logarithmic single beam spectra $-\log_{10}(S(\tilde{\nu}))$ for the single person experiments with (---) oral glucose tolerance test (b_o) and (—) random glucose levels (b_r) (offset and normalization: $b_{o1}/26.8 - 0$, $b_{r1}/3.8 - 3$, $b_{o5}/12534 - 1$, $b_{r5}/6302 - 1$, $b_{o10}/112434 - 2$, $b_{r10}/179280 - 2$, $b_{o15}/513564 - 3$, $b_{r15}/411975 - 3$, $b_{o20}/1550174 - 4$, $b_{r20}/1138705 - 4$, $b_{o25}/1808298 - 5$, $b_{r25}/2067855 - 5$).

In Fig. 6.20, the large similarity between the PLS solution vector for both single person experiments becomes obvious at higher inversion ranks. Near the optimal inversion rank, the coefficients are positive in the region of the glucose bands above 6000 cm^{-1} (see Fig. 6.20 at $R = 15$ and $R = 20$). Obvious apparent correlations cannot be recognized in the experiment with the oral glucose tolerance test in Fig. 6.20. The order of magnitude of the structures of the prediction estimator is consistent with the estimators of blood plasma (cf. Fig. 5.18).

For an estimation of the "physical" prediction error through the noise and the instability of the FT spectrometer, extinction spectra from each of two sequentially occurring reference spectra of the diffuse reflection standards were calculated analogous to the procedure for the determination in liquid blood plasma (Ch. 5) and were scalar multiplied with the optimal PLS solution vector for the lip extinctions ($R_{opt} = 22$). From the 218 baseline test spectra, 34 were removed from the simulation, from these, 26 due to the large time intervals between the blood glucose levels. The 184 simulation spectra showed maximum deviations from the ideal null line up to above $\pm 2 \cdot 10^{-3}$ AU over a broad spectral range of the glucose calibration of ca. $9000-5500$ cm^{-1} ; the "physical" prediction errors scattered in the region up to ± 60 mg/dl with an average value insignificantly different from zero and standard deviation $\hat{\sigma}_{spec} = 25.0$ mg/dl. This result is confirmed by the difference in the $PRESS^{1/2}$ values of the optimal prediction model in Fig. 6.19, since the lip extinctions in comparison to the single beam spectra display double the "physical" error variance. The prediction quality of the non-invasive measurement procedure is limited by the "biological" irreproducibility of the lip measurement, i.e. through the variation of the lip positioning and the application pressure. With Eq. 5.5 and the realistic estimation of the error through the clinical-chemical reference

determination $\hat{\sigma}_{\text{ref}} \approx 15$ mg/dl the "biological" error in the experiment with random glucose levels can be estimated to be around $\hat{\sigma}_{\text{bio}} = 48$ mg/dl as the dominating error part.

The possibility of a non-invasive blood glucose determination using diffuse reflection spectroscopy of the inner lip in the near IR is shown by the experiments of this work. For future improvements, primarily the reproducibility of the measurements must be increased. A suggestion for this is the use of a glass fiber bundle on the lip. Through this, a spectroscopic signal over a larger skin surface area can be averaged and the influence of the lip positioning can be decreased; the variation of the application pressure could, e.g. through use of a pressure sensor, be eliminated. Further improvements pertain to the increase of the S/N ratio for reduction of the current measurement time of about 1 min in order to simplify the future use in self-monitoring of blood sugar. Advances for the quality of the spectrometric measurement are expected through the use of necessary technologies for miniaturization, especially diode laser spectroscopy.

7 Summary and Outlook

The molecule-specific absorption of electromagnetic radiation in the infrared (IR) spectral region offers realization chances for novel automatic analysis devices for the determination of blood glucose ("blood sugar") concentrations. Important development goals are the reagentless determination of blood glucose in biotic liquid samples like blood, plasma, etc. as well as the non-invasive measurement through the skin. Since glucose is contained in blood only in small concentrations (ca. 1 wt.-%) and the main component water strongly absorbs in the IR spectral region, the quantitative analysis of IR spectra is difficult: the glucose signal displays a low S/N ratio and is overlaid by a significantly larger, biologically variable background spectrum. In this work, (1) the multivariate procedures for the quantitative signal processing were optimized, (2) the possibilities of IR spectroscopy for analysis of biotic liquid samples were examined, and (3) a non-invasive measurement procedure for glucose was developed and tested. For this, numerous measurements were conducted with a Fourier transform spectrometer and patient populations at the Duesseldorfer Diabetes Research Institute in which the necessary clinical-chemical reference analyses were also undertaken for the calibration.

Multivariate Signal Processing: Due to the small size of the glucose signal as well as the complexity and biological variability of the blood composition, physical calibration models are inappropriate. Alternatively, a statistical corollary must be selected in which the correlation of the IR spectra with the glucose concentration is processed over broad spectral regions ("multivariate"). Here, a representative number of calibration standards were measured and a so-called inverse regression model was generated which represents a poorly conditioned linear system of equations for the application case of blood analysis. The optimal *linear* estimator of glucose concentration in the sense of the mean squared prediction error (MSE), the Wiener filter [91] is also the *globally* best MSE estimator for validity of the Lambert-Beer law. For approximation of the Wiener filter on the basis of a finite number of calibration standards, the PCR and the PLS procedures are preferably used currently with which the inverse regression model can be iteratively ("user-controlled") solved. The algebraic similarity of both procedures was given, the numerical problems were discussed, and the superiority of the PLS procedure for the approximation of the MSE optimal solution could be verified. For determining information-rich spectral regions and for estimating the MSE prediction qualities, the methods were described with which an optimization of the calibration model is possible with practical computer effort.

Procedures for Liquid Blood: For the calibrations, a population of 126 EDTA blood plasma from different patients was available. In the mid IR spectral region (ca. $\lambda = 2.5 - 25 \mu\text{m}$), the measurement procedure was used with attenuated total reflectance (ATR); through optimization of the S/N ratios and the multivariate signal processing, the results of the first study [2,3] could be significantly improved. Moreover, through appropriate cleaning steps, the protein adsorption on the ATR crystal could be reproducibly suppressed for which a significant obstacle for the application of the ATR procedure disappears in routine analysis. For preparing the non-invasive measurements through the skin, furthermore, a transmission measurement of blood plasma in the near IR at a thickness of 1 mm was conducted. The quantitative determination of blood glucose in the near IR spectral region (NIR), which could be shown for the first time in this work is more difficult than in the mid IR as a result of the relative increased size of the background spectrum of water to glucose absorption (for 100 mg/dl glucose, the relationship is about 4200 at $\lambda = 1.6 \mu\text{m}$ compared

to about 150 at $\lambda = 9.6 \mu\text{m}$) and of the smaller information content of the broadbanded, structureless NIR spectra. In addition to glucose, further medically important substrates were examined, since the economic advantages of a reagentless automatic analysis device increased through the simultaneous determination of many parameters. The region of clinical acceptance was achieved for all substrates examined except for uric acid. In a variance analysis, the potential for future improvements was shown. The small concentration of uric acid in blood signifies the current limit for an IR spectroscopic analysis of complex biotic liquids.

Table 7.6: Overview of the average determination errors for the IR spectroscopic analysis for different substrates in blood plasma (\bar{c}_{pop} is the concentration average for the 126 samples (protein in [g/l], otherwise [mg/dl]); VK_{pred} is the mean squared prediction error related to \bar{c}_{pop} ; VK is the maximum allowed variation coefficient for clinical acceptance [170]).

	\bar{c}_{pop}	$VK_{\text{pred}}[\%]$		$VK [\%]$
		ATR-Verfahren in mid IR	Transmission in near IR	
Glucose	207.5	5.0	9.1	5
Total Protein	70.5	1.7	1.4	3
Total Cholesterol	219.0	3.7	3.8	6
Triglyceride	163.1	6.3	8.7	7
Urea	36.8	8.0	18.8	8
Uric Acid	5.2	19.0	—	6

Non-invasive Measurement Procedure: Due to the high water content of biological tissue with correspondingly strong absorption in the mid IR, a transcutaneous measurement of blood glucose is only possible in the near IR. The radiation distribution in skin, which is determined through absorption and diffuse scattering in the optically inhomogeneous tissue, was examined with a Monte Carlo simulation. Transmission measurements through thinner body parts such as earlobes and fingers are possible in the spectral region ca. $\lambda = 600 - 1300 \text{ nm}$, however, the difficulties that arise here through the required high reproducibility of the measurement are difficult to estimate. In the longer wave near IR spectral region, which was also used for the experiments with blood plasma, the procedure of diffuse reflection offers advantages. In the region of glucose absorption around $1.6 \mu\text{m}$, the average penetration depth of diffusely reflecting radiation from the skin lies at 0.3–0.4 mm and reaches blood capillaries; simultaneously the S/N ratio of extinction signals is optimized by the mean pathlength of the radiation in the tissue of about 1 mm. In this work, the measurement procedure of diffuse reflection of the inner lip was examined whose advantages among others are the small biological variations “from patient to patient” and the good circulation of the lip tissue. For this, a special optical measurement accessory with optimized efficiency was developed for the transmission of the radiation power from the radiation source through the diffusely reflecting skin to the detector; as compared to existing accessories, the efficiency could be improved about 1-1/2 orders of magnitude. In addition to single person experiments, a calibration with 133 patients of the Duesseldorfer Diabetes Research Institute was tested with the following results:

1. A correlation of the diffuse reflection spectra of the lip with the blood glucose concentration can be clearly proven.
2. The glucose concentration in the upper skin layers collected by the measurement is about 10 min behind the glucose in capillary blood.
3. The extinction spectrum of the “bonded water” in the tissue is less influenced by temperature oscillations than the spectrum of free water in blood plasma.
4. The prediction quality is not limited by the S/N ratio, rather through the irreproducibility of the lip measurement as a result of the variation in the lip positioning and application pressure.
5. For a measurement time of 1 min, the prediction error of the method is ca. 45–50 mg/dl, i.e. approximately double that of the medically tolerable error limit. For sole limitation by the S/N ratio, the prediction error would lie at about 25 mg/dl.

A big advantage of optical spectroscopy in the near IR spectral region is the multitude of possibilities for realization of a cost-effective and robust pocket spectrometer for the self-monitoring of blood glucose by patients at home. For this, uncooled semiconductor detectors as well as compact lenses and fiber optics can be used. For miniaturization, laser spectroscopy with diode lasers available up to ca. $\lambda = 1.8 \mu\text{m}$ offers the largest chances. For commercial use of the non-invasive blood sugar measurement, the analysis certainty must be increased for which primarily the reproducibility of the measurement must be improved. A possibility for this are sensors with fiber optic bundles which, however, due to their relatively small light throughput values and the required high S/N ratio of the measurement for this special application purpose, must be optimized. Another important point for the commercialization is the product liability such that cross-sensitivities of the measurement through interferences from, e.g. highly concentrated medicines should be carefully estimated. On the path toward a non-invasive glucose sensor, the current initial development of reagentless automatic analysis devices is an important step for the routine analysis of biotic liquid samples in the clinical-chemical laboratory.

Appendix A: Effective Optical Throughput

The *geometric throughput* G_o between two arbitrarily formed surface areas F_1 and F_2 (transmitter and receiver) is defined as [238]

$$G_o \doteq \int_{F_1} \int_{F_2^*} \frac{dF_1 \cos \alpha_1 dF_2 \cos \alpha_2}{r_{12}^2} \quad [\text{m}^2 \text{sr}] \quad (\text{A.1})$$

where r_{12} is the separation between the area elements dF_1 and dF_2 , and α_1 and α_2 are the angles between the connecting lines $\overline{dF_1 dF_2}$ and the area normals. The integration is to be carried out for each transmitter element dF_1 over the area dF_2^* to which dF_1 transmits radiation. For the treatment of dF_1 , each radiated area element dF_2 appears inside the space angle

$$d\Omega_2 = \frac{dF_2 \cos \alpha_2}{r_{12}^2} \quad [\text{sr}] \quad (\text{A.2})$$

With this, G_o can also be written as:

$$G_o = \int_{F_1} \int_{\Omega_2} dF_1 \cos \alpha_1 d\Omega_2 \quad [\text{m}^2 \text{sr}] \quad (\text{A.3})$$

A beam source, whose exit power over the area elements dF_1 and the "effectively used" space angle elements $\cos \alpha_1 d\Omega_2$ ($\Omega_2 \leq 2\pi$) is evenly distributed, is called a Lambert radiator [226:p. 151ff]. If absorption losses in the medium between the areas F_1 and F_2 can be ignored, a Lambert radiator emits a beam density L_M [$\text{W m}^{-2} \text{sr}^{-1}$] in this medium independent of position and direction and generates the power at the exit of an optical accessory with throughput G_o :

$$P_{\text{out}} = G_o L_M \quad [\text{W}] \quad (\text{A.4})$$

If a medium is located between both areas F_1 and F_2 with refraction index $n > 1$, the *optical throughput* G becomes

$$G \doteq n^2 G_o \quad (\text{A.5})$$

since the exiting radiation of the source due to the Snell refraction index law is distributed over a small n^2 -times space angle, i.e. in comparison to the beam density L in air ($n = 1$), L_M increases in the space angle Ω_2 to $L_M = n^2 L$ ($P_{\text{out}} = LG$). The optical throughput of an arbitrary beam bundle is invariant against mirroring and optical refraction so that for all beam cones inside of the optical device, $G = \text{const.}$ is valid; an important exception from this is diffuse scattering [239]. The mechanical components, which determine the integration limits F_1 and Ω_2 in Eq. A.3, are called field stops or apertures. Losses from non-ideal optical components, e.g. through absorption and reflection as well as losses through chopper wheels, beam splitters, etc. are described by transmission degrees or efficiency factors τ which normally are dependent on the radiation frequency $\tilde{\nu}$. The *effective optical throughput* G_{eff} is the product of the optical throughput G with all occurring efficiency factors:

$$G_{\text{eff}}(\tilde{\nu}) \doteq \tau(\tilde{\nu})G \quad (\text{A.6})$$

In practice, the geometric throughput G_o can be determined with approximation formulas [240]. In optical devices, the areas F_1 of the beam source and its between images are most often small in

comparison to the separation to the next optical element such that

$$\begin{aligned} G_o &\approx F_1 \int_{\Omega_2} \cos \alpha_1 d\Omega_2 \\ &= F_1 \pi \sin^2 \alpha_{1,\text{max}} \end{aligned} \quad (\text{A.7})$$

where α_1 is the angle between the normals of the (approximately) flat area F_1 and the beams into the space angle element $d\Omega_2$. For paraxial radiation cones, the cos-factor can also be neglected such that the throughput G_o between source F_1 and aperture F_2 can be approximated to be

$$G_o \approx F_1 \Omega_2 \approx \frac{F_1 F_2}{r^2} \quad (\text{A.8})$$

where r is the separation along the optical access which perpendicularly impinges the (approximately) flat areas F_1 and F_2 . The actual throughput of an optical device can be comfortably estimated with Eqs. A.7-8 as the minimum of the throughputs of its radiation cones that are ordered in series.

Appendix B: Definitions for Random Vectors

The cumulative distribution function of an N -dimensional random vector $\mathbf{e}^T = [e_1, e_2, \dots, e_N]$ is defined as the event probability:

$$F_E(\mathbf{e}) \doteq \text{probability density}\{E_1 \leq e_1 \text{ and } E_2 \leq e_2 \text{ and } \dots \text{ and } E_N \leq e_N\} \quad (\text{B.1})$$

The probability density function follows as:

$$f_E(\mathbf{e}) \doteq \frac{\partial^N}{\partial e_1 \partial e_2 \dots \partial e_N} F_E(e_1, e_2, \dots, e_N) \quad (\text{B.2})$$

The expected value of an arbitrary function $g(\mathbf{e}) : \mathbf{R}^N \rightarrow \mathbf{R}^M$ is defined as:

$$E[g(\mathbf{e})] = \int_{-\infty}^{\infty} \int_{-\infty}^{\infty} \dots \int_{-\infty}^{\infty} g(\mathbf{e}) f_E(e_1, e_2, \dots, e_N) de_1 de_2 \dots de_N \quad (\text{B.3})$$

where the N integrations are to be conducted for all M dimensions. In the case of an N -variate normal distribution, the probability density function is a function of the first two statistical moments $E[\mathbf{e}]$ and $\text{COV}[\mathbf{e}] = E[(\mathbf{e} - E[\mathbf{e}])(\mathbf{e} - E[\mathbf{e}])^T]$ and reads:

$$f_E(\mathbf{e}) = \frac{\exp\left(-\frac{1}{2}(\mathbf{e} - E[\mathbf{e}])^T \text{COV}[\mathbf{e}]^{-1} (\mathbf{e} - E[\mathbf{e}])\right)}{\sqrt{(2\pi)^N \det(\text{COV}[\mathbf{e}])}} \quad (\text{B.4})$$

For further details, see e.g. [70].

Appendix C: Certainty of the Clinical-Chemical Reference Method

Table C.1: Analysis results of different control sera at the Duesseldorfer Diabetes Research Institute over a time period of two months (c_{true} certified concentration of the test serum; n number, \bar{c}_S mean value, and $\hat{\sigma}_S$ standard deviation of the control measurement; concentrations for protein in [g/l], otherwise [mg/dl]; for glucose, see Table 5.4).

	c_{true}	n	\bar{c}_S	$\hat{\sigma}_S$	$\hat{\sigma}_S/\bar{c}_S$	$\bar{c}_S - c_{\text{true}}$
Total Protein						
low	46	39	45.2	0.56	1.2%	-0.82
middle	51	39	50.4	0.64	1.3%	-0.56
high	91	39	88.9	0.69	0.8%	-2.05
Total Cholesterol						
low	106	39	112.2	2.1	1.9%	6.2
middle	124	39	130.9	1.4	1.1%	6.9
high	250	39	262.5	3.0	1.1%	12.5
Triglyceride						
low	97	39	97.1	1.0	1.1%	0.1
middle	115	39	117.2	2.1	1.8%	2.2
high	254	39	254.2	2.2	0.9%	0.2
Urea						
low	14.2	38	16.3	0.9	5.7%	2.1
middle	55.7	38	56.4	2.6	4.5%	0.7
high	158	38	157.2	7.1	4.5%	0.8
Uric Acid						
low	3.5	18	3.9	0.17	4.3%	0.37
middle	5.1	18	5.5	0.22	4.0%	0.41
high	11.0	18	11.5	0.48	4.2%	0.54

Appendix D: Results of the Spectroscopic Analysis of Further Substrates in Blood Plasma

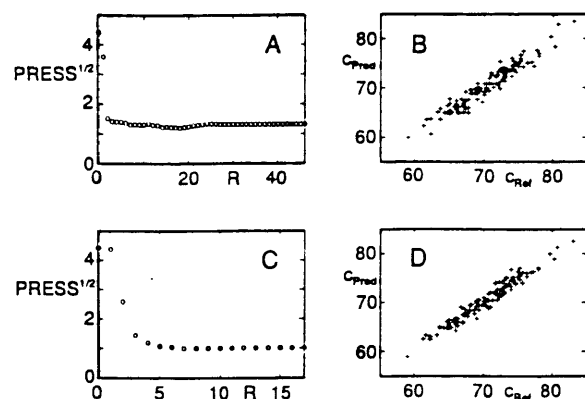


Fig. D.1: Prediction results of the ATR procedure (A,B) in the mid IR ($1700-1351/\Delta\tilde{\nu} = 7.7 \text{ cm}^{-1}$) and the transmission procedure (C,D) in the near IR ($6001-5508/\Delta\tilde{\nu} = 30.9 \text{ cm}^{-1}$) with the PLS calibration: $\text{PRESS}^{1/2}$ statistic (A,C) [g/l] in dependence on the PLS rank as well as optimal independent predictions (cf. Eq. 4.70) versus the clinically-chemically determined reference concentrations in [g/l] (B: $R_{\text{opt}} = 16$; D: $R_{\text{opt}} = 7$; for further details, see Table 5.7 and Table 5.9).

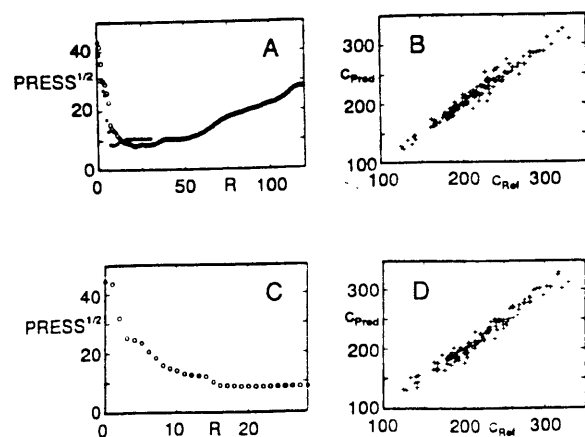


Fig. D.2: Prediction results of the ATR procedure (A,B) in the mid IR ("o": $3001-2800/\Delta\tilde{\nu} = 3.9$, $1800-1701/\Delta\tilde{\nu} = 7.7$, $1500-1099/\Delta\tilde{\nu} = 7.7 \text{ cm}^{-1}$; "x": $3001-2800/\Delta\tilde{\nu} = 3.9 \text{ cm}^{-1}$) and the transmission procedure (C,D) in near IR ($6001-5508/\Delta\tilde{\nu} = 30.9$, $4520-4212/\Delta\tilde{\nu} = 30.9 \text{ cm}^{-1}$) with the PLS calibration: $\text{PRESS}^{1/2}$ statistic (A,C) [mg/dl] in dependence on the PLS rank as well as optimal independent predictions (cf. Eq. 4.70) versus the clinically-chemically determined reference concentrations in [mg/dl] (B: $R_{\text{opt}} = 20$; D: $R_{\text{opt}} = 21$).

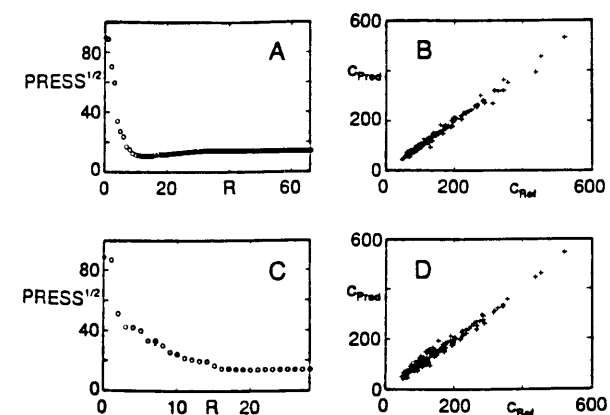


Fig. D.3: Prediction results of the ATR procedure (A,B) in the mid IR ($1800-1701/\Delta\tilde{\nu} = 7.7$, $1500-1099/\Delta\tilde{\nu} = 7.7 \text{ cm}^{-1}$) and the transmission procedure (C,D) in near IR ($6001-5508/\Delta\tilde{\nu} = 30.9$, $4520-4212/\Delta\tilde{\nu} = 30.9 \text{ cm}^{-1}$) with the PLS calibration: $\text{PRESS}^{1/2}$ statistic (A,C) [mg/dl] in dependence on the PLS rank as well as optimal independent predictions (cf. Eq. 4.70) versus the clinically-chemically determined reference concentrations in [mg/dl] (B: $R_{\text{opt}} = 13$; D: $R_{\text{opt}} = 20$).

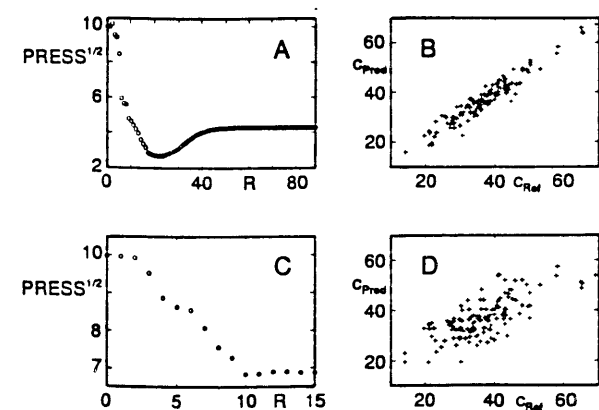


Fig. D.4: Prediction results of the ATR procedure (A,B) in the mid IR ($1800-1130/\Delta\tilde{\nu} = 7.7 \text{ cm}^{-1}$) and the transmission procedure (C,D) in near IR ($4736-4304/\Delta\tilde{\nu} = 30.9 \text{ cm}^{-1}$) with the PLS calibration: $\text{PRESS}^{1/2}$ statistic (A,C) [mg/dl] in dependence on the PLS rank as well as optimal independent predictions (cf. Eq. 4.70) versus the clinically-chemically determined reference concentrations in [mg/dl] (B: $R_{\text{opt}} = 20$; D: $R_{\text{opt}} = 10$).

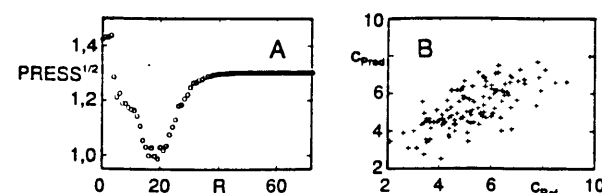


Fig. D.5: Prediction results of the ATR procedure (A,B) in the mid IR ($1800-1701/\Delta\tilde{\nu} = 7.7$, $1599-1151/\Delta\tilde{\nu} = 7.7 \text{ cm}^{-1}$) with the PLS calibration: $\text{PRESS}^{1/2}$ statistic (A) [mg/dl] in dependence on the PLS rank as well as optimal independent predictions (cf. Eq. 4.70) versus the clinically-chemically determined reference concentrations in [mg/dl] (B: $R_{\text{opt}} = 19$).

9 Bibliography

1. D. Stamm, H. Wisser, *Blutanalytik*, in *Analytiker-Taschenbuch*, Bd.3, R. Bock, W. Fresenius, H. Gunzler, W. Huber, G. Tolg (Hrg.), Springer, Berlin, 87-119, 1983.
2. H. M. Heise, R. Marbach, G. Janatsch, J. D. Kruse-Jarres, *Multivariate Determination of Glucose in Whole Blood by Attenuated Total Reflection Infrared Spectroscopy*, *Anal. Chem.* **61**, 2009-2015, 1989.
3. G. Janatsch, J. D. Kruse-Jarres, R. Marbach, H. M. Heise, *Multivariate Calibration for Assays in Clinical Chemistry Using Attenuated Total Reflection Infrared Spectra of Human Blood Plasma*, *Anal. Chem.* **61**, 2016-2023, 1989.
4. H. J. Kroenke, *Diabetes: Krankheitsbild, Therapie, Kontrollen, Schwangerschaft, Sport, Urlaub, Alltagsprobleme*, Falken-Verlag, Niedernhausen/Ts., 1989.
5. G. Reach, G. S. Wilson, *Can Continuous Glucose Monitoring Be Used for the Treatment of Diabetes?*, *Anal. Chem.* **64**, 381A-386A, 1992.
6. J. M. Burrin, C. P. Price, *Measurement of Blood Glucose*, *Ann. Clin. Biochem.* **22**, 327-342, 1985.
7. J. Biermann, B. Toohey, *The Diabetic's Book: All Your Questions Answered*, Jeremy P. Tarcher Inc., Los Angeles, 1990.
8. T. Koschinsky, K. Dannehl, F. A. Gries, *New Approach to Technical and Clinical Evaluation of Devices for Self-Monitoring of Blood Glucose*, *Diabetes Care* **11**, 619-29, 1988.
9. M. E. Fisher, K. L. Teo, *Optimal Insulin Infusion Resulting from a Mathematical Model of Blood Glucose Dynamics*, *IEEE Trans. Biomed. Eng.* **36**, 479-486, 1989.
10. E. F. Pfeiffer, W. Kerner, *Implantable Glucose Sensors-The State of the Art*, Thieme Medical Publishers, New York, 1988.
11. J. D. Kruse-Jarres, *Physicochemical Determinations of Glucose in vivo*, *J. Clin. Chem. Clin. Biochem.* **26**, 201-208, 1988.
12. F. W. Scheller, F. Schubert, B. Neumann, D. Pfeiffer, R. Hintsche, I. Dransfeld, U. Wollenberger, R. Renneberg, A. Warsicke, G. Johansson, M. Skoog, X. Yang, V. Bogdanovskaya, A. Buckmann, S. Zaitsev, *Second generation biosensors*, *Biosensors* **6**, 245-253, 1991.
13. U. Fischer, R. Ertle, P. Abel, K. Rebrin, E. Brunstein, H. Hahn von Dorsche, E. J. Freyse, *Assessment of Subcutaneous Glucose Concentration: Validation of the Wick Technique as a Reference for Implanted Electrochemical Sensors in Normal and Diabetic Dogs*, *Diabetologia* **30**, 940-945, 1987.
14. P. A. Jansson, J. Fowelin, U. Smith, P. Loennroth, *Characterization by Microdialysis of Inter-cellular Glucose Level in Subcutaneous Tissue in Humans*, *Am. J. Physiol.* **255** (Endocrinol. Metab. **18**), E218-E220, 1988.

15. H. Brauner, G. Mueller, *Glucosebestimmung-Stand und Perspektiven*, Biomed. Techn. **25**, 26-32, 1980.
16. B. Bauer, T. A. Floyd, *Monitoring of Glucose in Biological Fluids by Fourier-Transform Infrared Spectroscopy With a Cylindrical Internal Reflection Cell*, Anal. Chim. Acta **197**, 295-301, 1987.
17. Y. Mendelson, B. C. Lin, R. A. Peura, A. C. Clermont, *Carbon Dioxide Laser Based Multiple ATR Technique for Measuring Glucose in Aqueous Solutions*, Appl. Opt. **27**, 5077-5081, 1988.
18. Y. Mendelson, A. C. Clermont, R. A. Peura, B. C. Lin, *Blood Glucose Measurement by Multiple Attenuated Total Reflection and Infrared Absorption Spectroscopy*, IEEE Trans. Biomed. Eng. **37**, 458-465, 1990.
19. K. J. Ward, D. M. Haaland, M. R. Robinson, R. P. Eaton, *Quantitative Infrared Spectroscopy of Glucose in Blood Using Partial Least-Squares Analyses*, 7th International Conference of Fourier Transform Infrared Spectroscopy, D. G. Cameron (ed.), Proc. SPIE **1145**, 607-608, 1989.
20. J. Lambrecht, *Routinemethoden der Glucose-Bestimmung im Lichte der FDA Referenzmethode*, GIT Labor-Medizin **6**, 38-43, 1983.
21. G. M. Hale, M. R. Querry, *Optical Constants of Water in the 200 nm to 200 μ m Wavelength Region*, Appl. Opt. **12**, 555-563, 1973.
22. M. A. Arnold, G. W. Small, *Determination of Physiological Levels of Glucose in an Aqueous Matrix with Digitally Filtered Fourier Transform Near-Infrared Spectra*, Anal. Chem. **62**, 1457-1464, 1990.
23. D. M. Haaland, *Multivariate Calibration Applied to the Quantitative Analysis of Infrared Spectra*, 8th International Conference on Fourier Transform Spectroscopy, H. M. Heise, E. H. Korte, H. W. Siesler (eds.), Proc. SPIE **1575**, 87-95, 1992.
24. P. Rolfe (ed.), *Non-Invasive Physiological Measurements*, Academic Press, London, Vol. 1, 1979; *ibid.* Vol. 2, 1983.
25. M. Cope, D. T. Delpy, *System for Long-Term Measurement of Cerebral Blood and Tissue Oxygenation on Newborn Infants by Near Infrared Transillumination*, Med. & Biol. Eng. & Comput. **26**, 289-294, 1988.
26. H. M. Heise, R. Marbach, Th. Koschinsky, F. A. Gries, *Multivariate Determination of Blood Substrates in Human Plasma by FT-NIR Spectroscopy*, 8th International Conference on Fourier Transform Spectroscopy, H. M. Heise, E. H. Korte, H. W. Siesler (eds.), Proc. SPIE **1575**, 507-508, 1992.
27. A. Mueller, *Verfahren und Vorrichtung zur quantitativen Bestimmung optisch aktiver Substanzen*, Europaisches Patent EP 0 030 610 B1 (Patent Date: May 3, 1986).

28. C. Daehne, *Spectrophotometric Apparatus for the Non-Invasive Determination of Glucose in Body Tissues*, Europaisches Patent EP 0 160 768 B1 (Patent Date: March 5, 1989).
29. R. D. Rosenthal, L. N. Paynter, L. H. Mackie, *Non-Invasive Measurement of Blood Glucose*, U.S. Patent No. 5,086,229 (Date of Patent: Feb. 4, 1992).
30. R. D. Rosenthal, *Research into Non-Invasive Measurement of Blood Glucose Using Near-Infrared Technology*, Paper No. 2 of the 24th Annual Oak Ridge Conference on Advanced Analytical Concepts for the Clinical Laboratory, San Diego, California, April 9-10, 1992.
31. R. Robinson, P. Eaton, D. Haaland, G. Koeppe, E. Thomas, *Noninvasive Glucose Determination by Near-Infrared Spectroscopy*, Paper No. 38 of 52nd Annual Meeting ADA, San Antonio, Texas, June 20-23, 1992.
32. H. Guenzler, H. Boeck, *IR-Spektroskopie: Eine Einfuehrung*, Verlag Chemie, Weinheim, 2'te Auflage, 1983.
33. A. N. Davies, *Datenbanken fuer die Spektroskopie*, Nachr. Chem. Tech. Lab. **37** (Sonderheft), 263-270, 1989.
34. J. E. Stewart, *Infrared Spectroscopy: Experimental Methods and Techniques*, Marcel Dekker, Inc., New York, 1970.
35. T. Hirschfeld, *Quantitative FT-IR: A Detailed Look at the Problems Involved*, Chap. 6 in *Fourier Transform Infrared Spectroscopy—Applications to Chemical Systems*, J. R. Ferraro, L. J. Basile (eds.), Academic Press, New York, 1979.
36. R. J. Anderson, P. R. Griffiths, *Errors in Absorbance Measurements in Infrared Fourier Transform Spectrometry because of Limited Instrument Resolution*, Anal. Chem. **47**, 2339-2347, 1975.
37. R. Borsdorf, M. Scholz, *Spektroskopische Methoden in der organischen Chemie*, 2nd Ed., Vieweg & Sohn, Braunschweig, 1968.
38. G. Kemmner, *Infrarot-Spektroskopie: Grundlagen, Anwendung, Methoden*, Franckh'sche Verlagsbuchhandlung, Stuttgart, 1969.
39. B. Schrader, *Infrarot- und Ramanspektrometrie*, in *Ullmanns Encyklopaedie er technischen Chemie*, Ch. 5, H. Kelker (ed.), 4th Ed., Verlag Chemie, Weinheim, 1980.
40. M. Hesse, H. Meier, B. Zeeh, *Spektroskopische Methoden in der organischen Chemie*, 2nd Ed., Georg Thieme Verlag, Stuttgart, 1984.
41. R. Demuth, F. Kober, *Grundlagen der Spektroskopie*, Diesterweg-Salle, Frankfurt, 1977.
42. P. Jacquinet, *The Luminosity of Spectrometers With Prisms, Gratings, or Fabry-Perot Etalons*, J. Opt. Soc. Am. **44**, 761-765, 1954.
43. P. R. Griffiths, J. A. de Haseth, *Fourier Transform Infrared Spectrometry*, John Wiley & Sons, New York, 1986.

44. A. A. Michelson, *Phil. Mag.* **31**, 338, 1891; A. A. Michelson, *Phil. Mag.* **34**, 280, 1892.
45. J. W. Goodman, *Statistical Optics*, John Wiley & Sons, New York, 1985.
46. J. Chamberlain, *The Principles of Interferometric Spectroscopy*, John Wiley & Sons, New York, 1979.
47. W. H. Steel, *Interferometry*, 2nd Ed., Cambridge University Press, Cambridge, 1983.
48. A. B. Carlson, *Communication Systems: An Introduction to Signals and Noise in Electrical Communication*, 3rd Ed., McGraw-Hill, New York, 1986.
49. R. H. Norton, R. Beer, *New Apodizing Functions for Fourier Spectrometry*, *J. Opt. Soc. Am.* **66**, 259-264, 1976; *erratum: J. Opt. Soc. Am.* **67**, 419, 1977.
50. J. K. Kauppinen, D. J. Joffatt, D. G. Cameron, H. H. Mantsch, *Noise in Fourier Self-Deconvolution*, *Appl. Opt.* **20**, 1866-1879, 1981.
51. E. Hecht, *Optics*, Addison-Wesley, Reading, MA, 2nd Ed., 1987.
52. P. R. Griffiths, H. J. Sloane, R. W. Hannah, *Interferometers vs. Monochromators: Separating the Optical and Digital Advantages*, *Appl. Spectrosc.* **31**, 485-495, 1977.
53. P. B. Fellgett, Ph.D. Thesis, University of Cambridge, 1951.
54. J. W. Cooley, J. W. Tukey, *An Algorithm for the Machine Calculation of Complex Fourier Series*, *Math. Comput.* **19**, 297-301, 1965.
55. Gekauft von Bruker Analytic Meßtechnik GmbH, Wikingerstr. 13, D-7500 Karlsruhe 21.
56. D. R. Mattson, *Sensitivity of a Fourier Transform Infrared Spectrometer*, *Appl. Spectrosc.* **32**, 335-338, 1978.
57. E. G. Coddling, G. Horlick, *Apodization and Phase Information in Fourier Transform Spectroscopy*, *Appl. Spectrosc.* **27**, 85-92, 1973.
58. W. H. Steel, *Interferometers without Collimation for Fourier Spectroscopy*, *J. Opt. Soc. Am.* **54**, 151-156, 1964.
59. D. B. Chase, *Nonlinear Detector Response in FT-IR*, *Appl. Spectrosc.* **38**, 491-494, 1984.
60. D. B. Chase, *Phase Correction in FT-IR*, *Appl. Spectrosc.* **36**, 240-244, 1982.
61. M. L. Forman, W. H. Steel, G. A. Vanasse, *Correction of Asymmetric Interferograms Obtained in Fourier Spectroscopy*, *J. Opt. Soc. Am.* **56**, 59-63, 1966.
62. L. Mertz, *Transformations in Optics*, John Wiley & Sons, New York, 1965.
63. L. Mertz, *Auxiliary Computation for Fourier Spectrometry*, *Infrared Phys.* **7**, 17-23, 1967.
64. R. B. Sanderson, E. E. Bell, *Multiplicative Correction of Phase Errors in Fourier Spectroscopy*, *Appl. Opt.* **12**, 266-270, 1973.

65. R. O. Carter III, N. E. Lindsay, D. Beduhn, *A Solution to Baseline Uncertainty Due to MCT Detector Nonlinearity in FT-IR*, *Appl. Spectrosc.* **44**, 1147-1151, 1990.
66. R. A. Hoult, R. P. Ragusa, *Detector Preamplifier for Use with a MCT Detector*, U.S. Patent No. 4682022, 1987.
67. A. Baghdadi, W. K. Gladden, D. R. Flach, *Nonlinear Effects of Digitizer Errors in FT-IR Spectroscopy*, *Appl. Spectrosc.* **40**, 617-628, 1986.
68. T. Hirschfeld, *Digitization Noise in Fourier Transform Infrared Spectroscopy and Gain Ranging*, *Appl. Spectrosc.* **33**, 525-527, 1979.
69. E. L. Dereniak, D. G. Crowe, *Optical Radiation Detectors*, John Wiley & Sons, New York, 1984.
70. A. Papoulis, *Probability, Random Variables and Stochastic Processes*, 2nd Ed., McGraw-Hill, Singapore, 1984.
71. A. van der Ziel, *Noise*, Prentice-Hall, Englewood Cliffs, NJ, 1954.
72. H. W. Ott, *Noise Reduction Techniques in Electronic Systems*, John Wiley & Sons, New York, 1976.
73. C. T. Foskett, *Noise and Finite Register Effects in Infrared Fourier Transform Spectroscopy*, *Appl. Spectrosc.* **30**, 531-539, 1976.
74. G. M. Alber, A. G. Marshall, *Effect of Sampling Rate on Fourier Transform Spectra: Oversampling is Overrated*, *Appl. Spectrosc.* **44**, 1111-1116, 1990.
75. R. O. Carter III, *The Determination of S/N in an FT-IR Experiment and the Optimization of a Broad-Band HgCdTe Detector*, *Appl. Spectrosc.* **40**, 272-273, 1986.
76. T. Hirschfeld, *Ideal FT-IR Spectrometers and the Efficiency of Real Instruments*, *Appl. Spectrosc.* **40**, 1239-1240, 1986.
77. R. A. Smith, T. E. Jones, R. P. Chasmar, *The Detection and Measurement of Infrared Radiation*, 2nd Ed., Oxford University Press, London and New York, 1968.
78. A. S. Zachor, *Drive Nonlinearities: Their Effects in Fourier Spectroscopy*, *Appl. Opt.* **16**, 1412-1424, 1977.
79. A. S. Zachor, S. M. Aaronson, *Delay Compensation: Its Effect in Reducing Sampling Errors in Fourier Spectroscopy*, *Appl. Opt.* **18**, 68-75, 1979.
80. H. O. Tittel, D. Wissmann, *Diagnostic of Noise at an Interferometer by Fourier Transformation of Disturbances*, 8th International Conference on Fourier Transform Spectroscopy, H. M. Heise, E. H. Korte, H. W. Siesler (eds.), *Proc. SPIE* **1575**, 244-245, 1992.
81. D. R. Brillinger, *Time Series Data Analysis and Theory*, Holt, Rinehart and Winston, Inc., New York, 1975.

82. S. L. Meyer, *Data Analysis for Scientists and Engineers*, John Wiley & Sons, New York, 1975.
83. D. Gingras, *Modeling and Parametric Estimation in Infrared Interferometric Spectrometry*, Dissertation Ruhr-Universität Bochum, published as Fortschr.-Ber. VDI Reihe 10, Nr. 104, VDI-Verlag, Dusseldorf, 1989.
84. F. J. Harris, *On the Use of Windows for the Harmonic Analysis with the DFT*, Proc. IEEE **66**, 51-83, 1978.
85. H. Weitkamp, R. Barth, *Einfuehrung in die quantitative Infrarot-Spektrophotometrie*, Georg Thieme Verlag, Stuttgart, 1976.
86. H. Martens, T. Naes, *Multivariate Calibration*, John Wiley & Sons, Chichester, 1989.
87. J. Bibby, H. Toutenbourg, *Prediction and Improved Estimation in Linear Models*, John Wiley & Sons, New York and Academy-Verlag, Berlin, 1977.
88. G. Trenkler, *Biased Estimators in the Linear Regression Model*, Hain, Königstein, 1981.
89. M. R. Nyden, G. P. Forney, K. Chittur, *Spectroscopic Quantitative Analysis of Strongly Interacting Systems: Human Plasma Protein Mixture*, Appl. Spectrosc. **42**, 588-594, 1988.
90. J. D. Kruse-Jarres, G. Janatsch, *Towards Non-Invasive Clinical Chemistry—IR-Spectroscopy of Glucose in Whole Blood*, unveröffentlicher Bericht of the Institute for Clinical Chemistry, Katharinen Hospital, Stuttgart, 1987.
91. S. J. Orfanidis, *Optimum Signal Processing*, McGraw-Hill, New York, 2nd Ed., 1990.
92. G. W. Stewart, *Collinearity and Least Squares Regression*, Statistical Science **2**, 68-100, 1987.
93. G. Strang, *Linear Algebra and Its Applications*, Academic Press, New York, 1976.
94. S. Weisberg, *Applied Linear Regression*, John Wiley & Sons, New York, 1980.
95. R. R. Hocking, *Developments in Linear Regression Methodology: 1959-1982*, Technometrics **25**, 219-249, 1983 (see auch anschließende Diskussionsbeiträge).
96. D. W. Marquardt, *Generalized Inverses, Ridge Regression, Biased Linear Estimation, and Nonlinear Estimation*, Technometrics **12**, 591-612, 1970.
97. C. M. Theobald, *Generalization of Mean Square Error Applied to Ridge Regression*, J. R. Statist. Soc. **B36**, 103-106, 1974.
98. R. W. Helms, *The Average Estimated Variance Criterion for the Selection of Variables Problem in General Linear Models*, Technometrics **16**, 261-273, 1974.
99. A. S. Young, *The BiVar Criterion for Selecting Regressors*, Technometrics **24**, 181-189, 1982.
100. A. P. Dempster, M. Schatzoff, N. Wermuth, *A Simulation Study of Alternatives to Ordinary Least Squares*, J. Amer. Statist. Assoc. **72**, 77-91, 1977 (see auch anschließende Diskussionsbeiträge).

101. J. Mandel, *Use of the SVD in Regression Analysis*, Am. Stat. **36**, 15-24, 1982.
102. G. H. Golub, C. F. van Loan, *Matrix Computations*, John Hopkins University Press, Baltimore, 1983.
103. S. L. Campbell, C. D. Meyer, *Generalized Inverses of Linear Transformations*, Pitman, London, 1979.
104. P. C. Gillette, J. L. Koenig, *Noise Reduction via Factor Analysis in FT-IR Spectra*, Appl. Spectrosc. **36**, 535-539, 1982.
105. S. L. Marple Jr., *Digital Spectral Analysis With Applications*, Prentice-Hall, Englewood Cliffs, NJ, 1987.
106. P. M. Fredericks, J. B. Lee, P. R. Osborne, D.A.J. Swinkels, *Materials Characterization Using Factor-Analysis of FT-IR Spectra. Part 2: Mathematical and Statistical Considerations*, Appl. Spectrosc. **39**, 311-316, 1985.
107. E. R. Malinowski, *Theory of the Distribution of Error Eigenvalues Resulting from Principal Component Analysis with Applications to Spectroscopic Data*, J. Chemometrics **1**, 22-40, 1987.
108. R. C. Hill, T. B. Fomby, S. R. Johnson, *Component Selection Norms for Principal Component Regression*, Commun. Statist.-Theor. Method **A6**, 309-334, 1977.
109. T. Naes, H. Martens, *Principal Component Regression in NIR Analysis: Viewpoints, Background Details and Selection of Components*, J. Chemometrics **2**, 155-167, 1988.
110. R. F. Gunst, R. L. Mason, *Regression Analysis and Its Application: A Data-Oriented Approach*, Marcel Dekker, New York, 1980.
111. F. Mosteller, J. W. Tukey, *Data Analysis and Regression: A Second Course in Statistics*, Addison-Wesley, Reading, MA, 1977.
112. I. T. Jolliffe, *A Note on the Use of Principal Components in Regression*, J. Roy. Statist. Soc. C (Appl. Statist.) **31**, 300-303, 1982.
113. R. Manne, *Analysis of Two Partial Least-Squares Algorithms for Multivariate Calibration*, Chem. Int. Lab. Sys. **2**, 187-197, 1987.
114. C. C. Paige, *Bidiagonalization of Matrices and Solution of Linear Equations*, SIAM J. Numer. Anal. **11**, 197-209, 1974.
115. C. C. Paige, M. A. Saunders, *A Bidiagonalization Algorithm for Sparse Linear Equations and Least Squares Problems*, ACM Trans. Math. Software **8**, 43-71, 1982 (see Algorithmus "LSQR").
116. A. Bjorck, *Solving Linear Least-Squares Problems by Gram-Schmidt Orthogonalization*, BIT **7**, 1-21, 1967.
117. H. Wold, *Soft Modelling by Latent Variables; the Non-Linear Iterative Partial Least Squares Approach*, in *Perspectives in Probability and Statistics, Papers in Honour of M. S. Bartlett*, J. Gani (ed.), Academic Press, London, 1975.

118. H. Wold, *Soft Modelling: The Basic Design and Some Extensions*, in *Systems Under Indirect Observation*, vol. 2, K.G. Joreskog, H. Wold (eds.), North-Holland, Amsterdam, 1-54, 1982.
119. H. Martens, T. Naes, *Multivariate Calibration by Data Compression*, in *Near Infrared Technology in Agricultural and Food Industries*, K. Norries, P. C. Williams (eds.), American Cereal Association, St. Paul, MN, 57-87, 1987.
120. S. Wold, A. Ruhe, H. Wold, W. J. Dunn, *The Collinearity Problem in Linear Regression: The Partial Least-Squares (PLS) Approach to Generalized Inverses*, SIAM J. Sci. Stat. Comput. **5**, 735-743, 1984.
121. T. Naes, H. Martens, *Comparison of Prediction Methods for Multicollinear Data*, Commun. Statist. Simula. Computa. **14**, 545-576, 1985.
122. Y. Saad, *On the Rates of Convergence of the Lanczos and Block Lanczos Methods*, SIAM J. Numer. Anal. **17**, 687-706, 1980.
123. B. N. Parlett, *The Symmetric Eigenvalue Problem*, Prentice-Hall, Englewood Cliffs, 1980.
124. G. H. Golub, W. Kahan, *Calculating the Singular Values and Pseudo-Inverse of a Matrix*, SIAM J. Numer. Anal. **B2**, 205-224, 1965.
125. C. Lanczos, *An Iteration Method for the Solution of the Eigenvalue Problem of Linear Differential and Integral Operators*, J. Res. Nat. Bur. Stand. **45**, 255-282, 1950.
126. A. Lorber, L. E. Wangen, B. R. Kowalski, *A Theoretical Foundation for the PLS Algorithm*, J. Chemometrics **1**, 19-31, 1987.
127. I. E. Frank, *Intermediate Least-Squares Regression Method*, Chem. Int. Lab. Sys. **1**, 233-242, 1987.
128. Y. Zhang, *The Exact Distribution of the Moore-Penrose Inverse of X with a Density*, 6th Int. Symposium on Multivariate Analysis, Pittsburgh, July 1983, in *Multivariate Analysis-VI*, P.R. Krishnaiah (ed.), Elsevier Science Publishers, 633-635, 1985.
129. R. Marbach, H. M. Heise, *Calibration Modeling by Partial Least-Squares and Principal Component Regression and its Optimization Using Improved Leverage Correction for Prediction Testing*, Chem. Int. Lab. Sys. **9**, 45-63, 1990.
130. 386-MATLAB, Vers. 3.5d (The Math Works Inc., South Natick, MA, USA).
131. J. J. Dongarra, C. B. Moler, J. R. Bunch, G. W. Stewart, *LINPACK User's Guide*, SIAM, Philadelphia, 1979.
132. B. T. Smith, J. M. Boyle, J. J. Dongarra, B. S. Garbow, Y. Ikebe, V. C. Klema, C. B. Moler, *Matrix Eigensystem Routines—EISPACK Guide*, Lecture Notes in Computer Science, Bd. 6, 2nd Ed., Springer-Verlag, 1976; see also: B. S. Garbow, J. M. Boyle, J. J. Dongarra, C. B. Moler, *Matrix Eigensystem Routines—EISPACK Guide Extension*, Lecture Notes in Computer Science, Bd. 51, Springer-Verlag, 1977.

133. R. S. McDonald, P. A. Wilks, Jr., JCAMP-DX: A Standard Form for Exchange of Infrared Spectra in Computer Readable Form, Appl. Spectrosc. **42**, 151-162, 1988.
134. D. E. Honigs, G. M. Hieftje, T. Hirschfeld, *A New Method for Obtaining Individual Component Spectra from Those of Complex Mixtures*, Appl. Spectrosc. **38**, 317-322, 1984.
135. J. Uozumi, T. Asakura, *Estimation Errors of Component Spectra Estimated by Means of the Concentration-Spectrum Correlation: Part I*, Appl. Spectrosc. **43**, 74-80, 1989.
136. R. J. Beckman, R. D. Cook, *Outlier...s*, Technometrics **25**, 119-149, 1983 (see also nachfolgende Diskussionsbeiträge).
137. D. C. Hoaglin, R. Welch, *The Hat Matrix in Regression and ANOVA*, Am. Stat. **32**, 17-22, 1978.
138. R. Marbach, H. M. Heise, *Comparison of Multivariate Calibration with PCR and PLS for Glucose Using Infrared Spectra of Human Whole Blood*, 7th International Conference on Fourier Transform Infrared Spectroscopy, D. G. Cameron (ed.), Proc. SPIE **1145**, 437-438, 1989.
139. R. D. Cook, S. Weisberg, *Characterizations of an Empirical Influence Function for Detecting Influential Cases in Regression*, Technometrics **22**, 495-508, 1980.
140. S. Weisberg, *Diskussionsbeitrag to R. R. Hocking, Developments in Linear Regression Methodology: 1959-1982*, Technometrics **25**, 240-244, 1983.
141. M. G. Marasinghe, *A Multistage Procedure for Detecting Several Outliers in Linear Regression*, Technometrics **27**, 395-399, 1985.
142. M. Stone, *Cross-Validatory Choice and Assessment of Statistical Predictions*, J. Roy. Statist. Soc. **B36**, 111-147, 1974.
143. E. Kreyszig, *Statistische Methoden und ihre Anwendungen*, 6th Ed., Vandenhoeck & Ruprecht, Göttingen, 1977.
144. B. Efron, G. Gong, *A Leisurely Look at the Bootstrap, the Jackknife, and Cross-Validation*, Am. Stat. **37**, 36-48, 1983.
145. D. M. Allen, *The Prediction Sum of Squares as a Criterion for Selecting Prediction Variables*, Technical Report 23, Department of Statistics, University of Kentucky, 1971; see also: R. R. Hocking, *Criteria for Selection of a Subset Regression: Which One Should Be Used?*, Technometrics **14**, 967-970, 1972.
146. R. Marbach, H. M. Heise, *On the Efficiency of Algorithms for Multivariate Linear Calibration Used in Analytical Spectroscopy*, Trends Anal. Chem. **11**, 270-275, 1992.
147. H. M. Heise, *Infrarot-Spektroskopie und ihre potentiellen Moeglichkeiten in der Klinischen Chemie*, Lab. med. **15**, 470-476, 1991.
148. A. Hesse, G. Sanders, *Infrarotspektren-Atlas zur Harnsteinanalyse*, George Thieme Verlag, Stuttgart, 1988.

149. L. T. Rozelle, L. J. Hallgren, J. E. Bransford, R. B. Koch, *The Identification of Major Infrared Absorbing Components of Human Urine*, Appl. Spectrosc. **19**, 120-124, 1965.
150. B. G. Osborne, T. Feam, *Near Infrared Spectroscopy in Food Analysis*, John Wiley & Sons, New York, 1986.
151. A. Rosencwaig, *Photoacoustics and Photoacoustic Spectroscopy*, Chemical Analysis Series Vol. 57, John Wiley & Sons, New York, 1980.
152. T. Ahmed, A. Biswas, J. W. Monzyk, G. Yang, K. W. Johnson, *Photoacoustic Signal Enhancement*, Appl. Phys. **B43**, 53-56, 1987.
153. H. Schmidt-Kloiber, H. Tschetsch, *Die photoakustische Spektroskopie—ein geeignetes Hilfsmittel zur Analyse biologischer Proben*, Biomed. Techn. **31**, 169-174, 1986.
154. G. B. Christison, H. A. MacKenzie, *A Laser Photoacoustic Determination of Physiological Glucose Concentrations in Human Whole Blood*, Med. & Biol. Eng. & Comput. 1992 (in Druck).
155. N. J. Harrick, *Internal Reflection Spectroscopy*, Interscience Publishers (division of John Wiley & Sons), New York, 1967.
156. K. K. Chittur, D. J. Fink, R. I. Leininger, T. B. Hutson, *Fourier Transform Infrared Spectroscopy/Attenuated Total Reflection Studies of Protein Adsorption in Flowing Systems: Approaches for Bulk Correction and Compositional Analysis of Adsorbed and Bulk Proteins in Mixtures*, J. Colloid Interface Sci. **111**, 419-433, 1986.
157. R. Kellner, G. Goetzing, *FTIR-ATR Spectroscopic Analysis of the Protein Adsorption on Polymer Blood Contact Surfaces*, Mikrochim. Acta II, 61-74, 1984.
158. W. M. Doyle, *Absorbance Linearity and Repeatability in Cylindrical Internal Reflectance FT-IR Spectroscopy of Liquids*, Appl. Spectrosc. **44**, 50-59, 1990.
159. E. G. Bartick, R. G. Messerschmidt, *Cylindrical Internal Reflection for FTIR Liquid Sampling*, Am. Lab. **16**, 56-61, 1984.
160. J. H. Moore, C. C. Davis, M. A. Coplan, *Building Scientific Apparatus: A Practical Guide to Design and Construction*, 2nd Ed., Addison-Wesley, Redwood City, 1989.
161. D. W. Sting, *Multiple Internal Reflection Cell Optical System for Use in Infrared Spectrophotometry of Liquids and Fluidized Samples*, U.S. Patent No. 4595833, 1986.
162. J. H. McLeod, *The Axicon: A New Type of Optical Element*, J. Opt. Soc. Am. **44**, 592-597, 1954.
163. J. H. McLeod, *Axicons and Their Uses*, J. Opt. Soc. Am. **50**, 166-169, 1960.
164. W. L. Wolfe, *Optical Materials*, in *The Infrared Handbook—revised edition*, W. L. Wolfe, G. J. Zissis (ed.), The Infrared Information Analysis (IRIA) Center, Ann Arbor, MI, USA, 1989.

165. R. P. Sperline, S. Muralidharan, H. Freiser, *New Quantitative Technique for Attenuated Total Reflection (ATR) Spectrophotometry; Calibration of the "CIRCLE" ATR Device in the Infrared*, Appl. Spectrosc. **40**, 1019-1022, 1986.
166. N. Kaiser, *Geraet zur Bestimmung des Gehaltes von Stoffwechselprodukten im Blut*, Offenlegungsschrift Nr. 2606991 des deutschen Patentamtes 1977; see also: N. Kaiser, *Unblutige Blutanalyse*, Spektrum der Wissenschaft, Heft-Nr. 1, S. 77, 1978.
167. N. Kaiser, personal message.
168. A. Borg, D. Birkhed, *Secretion of Glucose in Human Parotid Saliva after Carbohydrate Intake*, Scand. J. Dent. Res. **96**, 551-556, 1988.
169. *Richtlinien der Bundesaerztekammer zur Qualitätssicherung im medizinischen Laboratorium*, Dt. Aerzteblatt **85**, C449-C464, 1988.
170. R. Heidrich, H.-D. Helb, *Qualitätsicherung mit Labor-EDV*, GIT Labor-Medizin **10**, 387-399, 1991.
171. A. W. van Toorenenbergen, B. G. Blijenberg, B. Leijnse, *Measurement of Total Serum Protein by Near-Infrared Reflectance Spectroscopy*, J. Clin. Chem. Clin. Biochem. **26**, 209-211, 1988.
172. E. Peuchant, C. Salles, R. Jensen, *Determination of Serum Cholesterol by Near-Infrared Reflectance Spectrometry*, Anal. Chem. **59**, 1816-1819, 1987.
173. R. A. Lodder, G. M. Hieftje, W. Moorehead, S. P. Robertson, P. Rand, *Assessment of the Feasibility of Determination of Cholesterol and Other Blood Constituents by Near-Infrared Reflectance Analysis*, Talanta **36**, 193-198, 1989.
174. R. Rushmer, K.J.K. Buettner, J. M. Short, G. F. Odland, *The Skin*, Science **154**, 343-348, 1966.
175. J. A. Parrish, *The Scope of Photomedicine*, in *The Science of Photomedicine*, J. D. Regan, J. A. Parrish (eds.), Plenum Press, New York, 1982.
176. I. Simon, A. G. Emslie, C. M. Apt, I. H. Blank, R. R. Anderson, *Determination in vivo of Water Concentration Profile in Human Stratum Corneum by a Photoacoustic Method*, in *Bioengineering and the Skin*, R. Marks, P. A. Payne (eds.), MTP Press, Lancaster, 1981.
177. B. C. Wilson, S. L. Jacques, *Optical Reflectance and Transmittance of Tissues: Principles and Applications*, IEEE J. Quantum Electron. **26**, 2186-2199, 1990.
178. A. M. Kligman, *The Biology of the Stratum Corneum*, in *The Epidermis*, W. Montagna, W. C. Lobitz Jr. (eds.), Academic Press, New York, 1964.
179. S. Chandrasekhar, *Radiative Transfer*, Dover, New York, 1960.
180. B. Davison, *Neutron Transport Theory*, Clarendon, Oxford, 1957.
181. A. Ishimaru, *Diffusion of Light in Turbid Material*, Appl. Opt. **28**, 2210-2215, 1989.

182. M.J.C. van Gemert, S. L. Jaques, H.J.C.M. Sterenborg, W. M. Star, *Skin Optics*, IEEE Trans. Biomed. Eng. **36**, 1146-1154, 1989.
183. W. F. Cheong, S. A. Prahl, A. J. Welch, *A Review of the Optical Properties of Biological Tissues*, IEEE J. Quantum Electron. **26**, 2166-2185, 1990.
184. M. R. Amfield, J. Tulip, M.S. McPhee, *Optical Propagation in Tissue with Anisotropic Scattering*, IEEE Trans. Biomed. Eng. **35**, 372-381, 1988; *erratum* in IEEE Trans. Biomed. Eng. **36**, 572, 1989.
185. C. C. Johnson, A. W. Guy, *Nonionizing Electromagnetic Wave Effects in Biological Materials and Systems*, Proc. IEEE **60**, 692-718, 1972.
186. H. P. Schwan, *Interaction of Microwave and Radio Frequency Radiation with Biological Systems*, IEEE Trans. Microwave Theory Tech. **19**, 146-152, 1971.
187. A. E. Profio, *Light Transport in Tissue*, Appl. Opt. **28**, 2216-2222, 1989.
188. A. Ishimaru, *Wave Propagation and Scattering in Random Media*, vol. 1, Academic Press, New York, 1978.
189. S. T. Flock, M. S. Patterson, B. C. Wilson, D. R. Wyman, *Monte Carlo Modeling of Light Propagation in Highly Scattering Tissues-I: Model Predictions and Comparison with Diffusion Theory*, IEEE Trans. Biomed. Eng. **36**, 1162-1168, 1989.
190. D. R. Wyman, M. S. Patterson, B. C. Wilson, *Similarity Relations for the Interaction Parameters in Radiation Transport*, Appl. Opt. **28**, 5243-5249, 1989.
191. S. T. Flock, B. C. Wilson, M. S. Patterson, *Total Attenuation Coefficients and Scattering Phase Functions of Tissues and Phantom Materials at 633 nm*, Med. Phys. **14**, 835-841, 1987.
192. S. L. Jacques, C. A. Alter, S. A. Prahl, *Angular Dependence of HeNe Laser Light Scattering by Human Dermis*, Lasers Life Sci. **1**, 309-333, 1987.
193. R. Marchesini, A. Bertoni, S. Andreola, E. Melloni, A. E. Sichirollo, *Extinction and Absorption Coefficients and Scattering Phase Functions of Human Tissues in vitro*, Appl. Opt. **28**, 2318-2324, 1989.
194. L. G. Henyey, J. L. Greenstein, *Diffuse Radiation in the Galaxy*, Astrophys. J. **93**, 70-83, 1941.
195. F. P. Bolin, L. E. Preuss, R. C. Taylor, R. J. Ference, *Refractive Index of Some Mammalian Tissues Using a Fiber Optic Cladding Method*, Appl. Opt. **28**, 2297-2303, 1989.
196. W.A.G. Bruls, J. C. van der Leun, *Forward Scattering of Human Epidermal Layers*, Photochem. Photobiol. **40**, 231-242, 1984.
197. P. Parsa, S. L. Jacques, N. S. Nishioka, *Optical Properties of Rat Liver Between 350 and 2200 nm*, Appl. Opt. **28**, 2325-2330, 1989.

198. J. A. Parrish, *New Concepts in Therapeutic Photomedicine: Photochemistry, Optical Targeting and the Therapeutic Window*, J. Invest. Dermatol. **77**, 45-50, 1981.
199. J. L. Bulnois, *Photophysical Processes in Recent Medical Laser Developments: A Review*, Lasers Med. Sci. **1**, 47-66, 1986.
200. A. Bachem, C. I. Reed, *The Penetration of Light Through Human Skin*, Am. J. Physiol. **97**, 86-91, 1931.
201. D. R. Wyman, M. S. Patterson, B. C. Wilson, *Similarity Relations for Anisotropic Scattering in Monte Carlo Simulations of Deeply Penetrating Neutral Particles*, J. Comput. Phys. **81**, 137-150, 1989.
202. I. N. Bronstein, K. A. Semendjajew, *Taschenbuch der Mathematik*, 20th Ed., Eds. von G. Grosche and V. Ziegler, Verlag Harri Deutsch, Thun, 1981.
203. P. Kubelka, F. Munk, *Ein Beitrag zur Optik der Farbanstriche*, Z. techn. Phys. **12**, 593, 1931.
204. G. Kortuem, *Reflection Spectroscopy*, Springer, Berlin, 1969.
205. J. A. Jacquez, J. Huss, W. McKeehan, J. M. Dimitroff, H. F. Kuppenheim, *Spectral Reflectance of Human Skin in the Region 0.7-2.6 μm* , J. Appl. Physiol. **8**, 297-299, 1955.
206. J. D. Hardy, H. T. Hammel, D. Murgatroyd, *Spectral Transmittance and Reflectance of Excised Human Skin*, J. Appl. Physiol. **9**, 257-264, 1956.
207. R. R. Meier, J.-S. Lee, D. E. Anderson, *Atmospheric Scattering of Middle UV Radiation from an Internal Source*, Appl. Opt. **17**, 3216-3225, 1978.
208. R.A.J. Groenhuis, H. A. Ferwerda, J. J. ten Bosch, *Scattering and Absorption of Turbid Materials Determined from Reflection Measurements. 1: Theory*, Appl. Opt. **22**, 2456-2462, 1983.
209. *The Atlas of Near Infrared Spectra*, published by Sadtler Research Laboratories, Philadelphia, PA, USA, 1981.
210. R. Ulbricht, *Die Bestimmung der mittleren räumlichen Lichtintensität durch nur eine Messung*, Elektrotechn. Z. **29**, 595, 1900.
211. W. Richter, *Fourier Transform Reflectance Spectrometry between 8000 cm^{-1} (1.25 μm) and 800 cm^{-1} (12.5 μm) Using an Integrating Sphere*, Appl. Spectrosc. **37**, 32-38, 1983.
212. D. Sheffer, U. P. Oppenheim, D. Clement, A. D. Devir, *Absolute Reflectometer for the 0.8-2.5 μm Region*, Appl. Opt. **26**, 583-586, 1987.
213. D. Sheffer, U. P. Oppenheim, A. D. Devir, *Absolute Reflectometer for the Mid Infrared Region*, Appl. Opt. **29**, 129-132, 1990.
214. siehe Katalog der Fa. Labsphere, North Sutton, NH, USA, in Deutschland vertreten durch: LOT-ORIEL GmbH, Im Tiefen See 58, D-6100 Darmstadt.

215. G. W. Chantry, *Long-Wave Optics: The Science and Technology of Infrared and Near-millimetre Waves—Volume 1: Principles*, Academic Press, London, 1984.
216. siehe Katalog der Fa. Harrick-Scientific, Ossining, NY, USA, in Deutschland vertreten durch: Stama GmbH, Schillerstr. 10, D-6102 Pfungstadt.
217. G. Kortuem, H. Delfs, *Reflexionsspektrometrische Messungen im infraroten Spektralgebiet*, Spectrochim. Acta 20, 405–413, 1964.
218. W. W. Coblenz, *The Diffuse Reflecting Power of Various Substances*, Natl. Bur. Stand. Bull. 9, 283, 1913.
219. W. M. Brandenburg, *Focusing Properties of Hemispherical and Ellipsoidal Mirror Reflectometers*, J. Opt. Soc. Am. 54, 1235–1237, 1964.
220. S. T. Dunn, J. C. Richmond, J. A. Wiebelt, *Ellipsoidal Mirror Reflectometer*, J. Res. Nat. Bur. Stand. 70C, 75, 1966.
221. M. P. Fuller, P. R. Griffiths, *Diffuse Reflectance Measurements by Infrared Fourier Transform Spectroscopy*, Anal. Chem. 50, 1906–1910, 1978.
222. H. Maulhardt, D. Kunath, *Diffuse Reflectance Spectroscopy in the Infrared*, Talanta 29, 237–241, 1982.
223. E. H. Korte, *Figures of Merit for a Diffuse Reflectance Accessory Using an On-axis Ellipsoidal Collecting Mirror*, Appl. Spectrosc. 42, 428–433, 1988.
224. E. H. Korte, A. Otto, *Infrared Diffuse Reflectance Accessory for Local Analysis on Bulky Samples*, Appl. Spectrosc. 42, 38–43, 1988.
225. A. Otto, *Infrarotspektroskopie mit diffus reflektierter Strahlung: In-situ Messungen an schwach streuenden Proben*, Dissertation Universität-GHS Essen, publiziert als Fortschr.-Ber. VDI Reihe 8, Nr. 146, VDI-Verlag, Dusseldorf, 1987.
226. W. T. Welford, R. Winston, *The Optics of Nonimaging Concentrators—Light and Solar Energy*, Academic Press, New York, 1978.
227. T. Hirschfeld, *Optimization of Diffuse Reflectance Infrared Spectroscopy Accessories*, Appl. Spectrosc. 40, 1082–1085, 1986.
228. R. Marbach, H. M. Heise, *Novel Design of an Ellipsoidal Diffuse Reflectance Accessory with Improved Throughput*, 8th International Conference on Fourier Transform Spectroscopy, H. M. Heise, E. H. Korte, H. W. Siesler (eds.), Proc. SPIE 1575, 288–289, 1992.
229. G. Schroeder, *Technische Optik: Grundlagen und Anwendungen*, 6th Ed., Vogel-buchverlag (Kamprath-Reihe: Technik), Würzburg, 1987.
230. siehe Katalog der Fa. Spectra-Tech, Stamford, CT, USA, in Europa vertreten durch: Spectra-Tech Europe Ltd., Genesis Centre, Science Park South, Warrington WA3 7BH, England.
231. W. J. Smith, *Modern Optical Engineering*, McGraw-Hill, New York, 1966.

232. J. Hecht, *The Laser Guidebook*, McGraw-Hill, New York, 1986.
233. DIN-VDE 0837, *Strahlungssicherheit von Laser-Einrichtungen*, 1986 (Übersetzung der internationalen Norm IEC 825, 1984).
234. C. H. Reinsch, *Smoothing by Spline Functions*, Numer. Math. 10, 177–183, 1967.
235. H. Spaeth, *Algorithmen für elementare Ausgleichsmodelle*, R. Oldenbourg Verlag, München, 1973 (Anm.: Vorzeichenfehler in Eq. 2.7.12).
236. O.-A. Neumueller, *Rompps Chemie-Lexikon*, 8th Ed., Franckh'sche Verlagshandlung, Stuttgart, 1979.
237. G. Yoon, A. J. Welch, M. Motamedi, M.C.J. van Germert, *Development and Application of Three-Dimensional Light Distribution Model for Laser Irradiated Tissue*, IEEE J. Quantum Electron. 23, 1721–1733, 1987.
238. DIN 5030, Teil 3: *Spektrale Strahlungsmessung: Spektrale Aussonderung-Begriffe und Kennzeichnungsmerkmale*, December 1984.
239. M. Born, E. Wolf, *Principles of Optics*, 6th Ed., Pergamon Press, Oxford, 1989.
240. G. Hansen, *Abbildung von Volumenstrahlern in Spektrographen*, Optik 6, 337–347, 1950.